Università degli Studi di Ferrara

DOTTORATO DI RICERCA IN
FISICA

CICLO XXI

COORDINATORE Prof. Filippo Frontera

Foreground Implications in the Scientific Exploitation of CMB Data

Settore Scientifico Disciplinare FIS/05

Dottorando	**Tutore**
Dott. Pietro Procopio	Prof. Nazzareno Mandolesi

Co-Tutori
Dr. Carlo Burigana
Dr. Jacques Delabrouille

Anni 2006/2008

Preface

The Cosmic Microwave Background (CMB) represents one of the main sources of information of modern cosmology. Through the CMB it is possible to probe the Universe till the very primordial stages of its evolution. This is done thanks to the observables characterizing the CMB: the spectrum, the temperature anisotropies and the polarization anisotropies. The first part of this thesis focuses on the spectral distortions of the CMB: the deviations from the Planckian shape of the CMB photon distribution function. Those may arise in different epochs: from the early Universe, much more before recombination, until the reionization phase at relatively recent redshifts. The observation of this cosmological signal is complicated by astrophysical foregrounds. In the context of a CMB experiments, the foregrounds represent unwanted signals and, in order to study the CMB signal, they are subtracted from the observations during the data analysis phases. Anyway, this is even a way to study them, because the better you know the component to subtract the better is performed the subtraction itself.

In this thesis, the impact of the foreground in CMB data analysis will be mainly discussed, focusing on some aspects about foregrounds modeling and subtraction.

Foregrounds affects any observables of the CMB. CMB features and characteristics are discussed in Chap. 2 and in particular the generation and evolution of spectral distortions are treated deeply.

All the work on the CMB was done at the Istituto di Astrofisica Spaziale e Fisica Cosmica in Bologna (IASF-Bo). In Chap. 3, the code named KYPRIX will be presented. It is a code for the solution of the Kompaneets equation in cosmological context and the detailed phases of the implementation and the upgrade of the code, the tests done on it and some cosmological applications are discussed in the same chapter.

For what it concerns experiments aiming to the observations of spectral distortions, I was involved in the Italian Vision for Moon Exploration, belonging the proposal *Observation of the Universe from the Moon*, in which two mission ideas, of two different size are proposed, allowing to lower dramatically the upper limits on the parameters characterizing the spectral distortions and probably to detect them.

The *Planck* satellite is dedicated to the study of the other two CMB observables: the anisotropies in temperature and polarization. Being a

member of the Low Frequency Instrument (LFI) team in Bologna gave me possibility to better know the instrument's features. In Chap. 4, after a review of the past, on going, and future CMB dedicated missions, I'll briefly highlight the peculiar technical and instrumental characteristics of the Low Frequency Instrument aboard the *Planck* satellite. The amount of data that the LFI and the High Frequency Instrument (HFI) will provide on the temperature anisotropies represents the ultimate leap forward to explore the Universe in different stages of its evolution: from epochs antecedent the recombination to the more recent reionization process. The latter is a crucial phase in which the Universe passed through. Indeed, reionization leaves imprints on every CMB observables, for example it may give rise to free-free distortions of the spectrum or it can suppress the peaks in the temperature anisotropy power spectrum.

In Chap. 5, an overview about the foregrounds in the microwave range will be given. Their modeling and in particular in the context of the Planck Sky Model (PSM) will be also discussed. Thanks to its wide frequency coverage, *Planck* will also provide detailed maps of the foregrounds affecting the CMB. Extragalactic, Galactic and local foregrounds will be modeled with greater precision. The PSM is an ensemble of tools dedicated to the prediction and simulation of the sky at microwave frequencies, in particular to those at which *Planck* will observe the sky.

Being a student of the International Doctorate in Astro-Particle Physics (IDAPP), I had the opportunity to go working in Paris, at APC within the ADAMIS group, for two times during my PhD. During the second stage in Paris in 2008, I performed some validation tests on the PSM, in particular on the models of the Galactic foreground emission. Some of the results of these tests are shown in Chap. 5.

During the first stage in Paris, in 2007, I started studying a component separation method. These techniques are treated in Chap. 6. They consist in separating a component of interest from the others, in maps where all the emissions are mixed. The method I worked with is called SMICA and it is a performing tool for diffuse sources component separation. In particular, once back in Bologna, I used this tool, jointly with a Fourier filter made on purpose, in order to subtract the Zodiacal Light Emission (ZLE) residual from the complete IRIS map set. This is a set of maps catching the sky in the far-infrared in four frequencies. The results of the subtraction are presented in Chap. 7.

Acknowledgements

I warmly thanks my direct supervisor Dott. Carlo Burigana, a guide and a friend, ever available for useful discussions and for providing me a constant support. I am grateful to Prof. Nazzareno Mandolesi for the constructive discussions on CMB physics and experiments and for giving me the possibility to work at the Istituto di Astrofisica Spaziale e Fisica Cosmica in Bologna for all the duration of my PhD. A special thanks goes to Prof. Giovanni Fiorentini, director of the International Doctorate of Astro-Particle Physics, and Prof. Yves Charon, department head of the University Paris Diderot, that made me to belong to the IDAPP program, having in this way the opportunity to go studying in Paris. Thanks to Dott. Jacques Delabrouille, my co-tutor in Paris, that gave me the occasion to learn more about signal processing. I would like also to thank Moude Le Jeune, her *numerical support* was very important.

Thanks to Claudio Gheller, for its collaboration and for giving me the access to CINECA resources in order to develop and run my codes. Thanks to Alessandro Simonetto, at Istituto di Fisica dei Plasmi in Milano, that until two years ago supplied me the necessary computational resources. A constant support on computational resources is also provided by Matteo Genghini, at IASF-Bologna. I would like also to thank Lucio Vittori and Mick Pont, for their support on NAG numerical libraries. I acknowledge the use of the Planck Sky Model. Some of the results in this thesis have been derived using the HEALPix package. I acknowledge the use of the Legacy Archive for Microwave Background Data Analysis (LAMBDA). Support for LAMBDA is provided by the NASA Office of Space Science. I acknowledge the use of the IRIS maps.

The biggest thought goes to my whole family and to Laura: their love and their constant support are of vital importance. Thank you very much. Last but not least, many many thanks to all my friends, in a way or in another all of you helped me.

Contents

Chapter 1

Introduction

Since its discover, the Cosmic Microwave Background (CMB) represents one of the main sources of information on which the modern cosmology is based. Seen as the strongest proof of the Hot Big Bang cosmological model, the CMB arise in the first stages of life of the Universe, because of the tight coupling between matter and radiation that established the thermal equilibrium between themselves. CMB became *visible* only after the baryon-photon decoupling, when its photons were diffused at the Last Scattering Surface (LSS). A wealth of informations can be extracted from the CMB, not only on the early Universe but also on its subsequent evolution up today. The detection and the study of the CMB goes through the observation of three physical observables: the CMB photon distribution function, the temperature anisotropies and the polarization anisotropies.[1]
The first of these represents the frequency spectrum of the CMB radiation, well fitted by a Planckian spectrum at the actual temperature of 2.725 ± 0.002 K [94]. Anyway, in various stages of the history of the Universe several kinds of physical processes out of the equilibrium might have produced energy injection in the radiation field (like radiative particles decaying or energy dissipation due to viscosity, diffusion from turbulent matter movements or other non-linear effects). It is then possible that these energy dissipation could leave signatures of the CMB spectrum, leading to the not yet observed *spectral distortions*. Hence, spectral distortions represent a tool to investigate the thermal history of the Universe and allow to push observational cosmology beyond the last scattering surface. The precise measurement obtained through the COBE-FIRAS instrument [50] allow us to put strong constraints to the energy injection parameters characterizing spectral distortions [56].

---

[1]See Chap. 2 for a deeper treatment of the CMB features.

The CMB temperature anisotropies pattern encrypts information directly related to the origin of the large-scale structures that we observe today. These anisotropies consist in fluctuations from the CMB mean temperature at various angular scales (at level of $\Delta T/T \simeq 10^{-5}$), which are related to the density contrast at the epoch of recombination. Given that the CMB photons traveled almost unperturbed from the LSS to now, the CMB temperature anisotropies pattern represents a snapshot of the Universe at that epoch, allowing us to extract informations, at various angular scales, on the gravitational potentials and instabilities that generated the density inhomogeneities and the large density contrast that we observe today [150]. More detailed informations can be extracted from the pattern of polarization anisotropies of the CMB radiation. The CMB polarization arises during the recombination phase [128]. If the incident radiation were isotropic or had only a dipole variation (on 180° scale), the scattered radiation would have no net polarization. However, if the incident radiation from perpendicular directions (separated by 90°) had different intensities, a net linear polarization would result. These diffused photons could scatter only while free electrons are present. Thus, polarized radiation could be produced only during a short period near the end of recombination. Only a small fraction of the CMB radiation is therefore polarized.

The polarization angular power spectrum of the CMB is thus a direct snapshot of physical conditions at the last scattering surface and it can substantially improve the accuracy level at which parameters are measured by breaking the degeneracy between certain parameter combinations. Furthermore, it allows a much detailed probe of the reionization history of the Universe.

Observing the fine structures of the CMB is not easy at all. Many astrophysical processes emit in the microwave range: a detector looking at the sky sees a superposition of emissions that come from different sources. In the context of CMB experiment, everything that is not CMB has to be considered as a foreground emission, affecting the measure of the CMB itself and it must be subtracted from the maps.

A first attempt of classification could be done on the basis of the involved angular scale. According to this, one can discern between *diffuse* and *discrete* foreground emissions. The diffuse foreground is characterized by large scale template, with non-sharp bounded regions, while the discrete emissions are represented by discrete sources or point sources, for example.

A subsequent subdivision can be done on the basis of the environment in which the foreground is generated: local foregrounds are in general represented by Solar System emissions, like the Zodiacal Light; Galactic foregrounds are the emission processes raising from our own Galaxy, like the synchrotron radiation, free-free emission and dust emission; extra-galactic foregrounds are instead generated out of our Galaxy and they involve different kinds of emission mechanisms, more relevant in radio and far-IR sources or the Sunyaev-Zel'dovich effect from galaxy clusters.

These emissions contribute in confusing the signals of all the CMB observables. Fortunately, foreground most prominent emissions shows a minimum in their intensity around 70 GHz, where the CMB emission is still relatively strong. Anyway, the contamination level, even at this frequency, is non-zero and the subtraction of the unwanted emissions from the sky map is necessary. As we will see, to do this we have to model these emissions as better as possible, hence full-sky surveys at several frequencies are a fundamental basis on which to build a model for the relevant physical processes.

In order to achieve the high level of accuracy that we reached in observing the CMB, many efforts have been done since its first official detection by A. Penzias and R. Wilson. Furthermore, the observation technics depend on which observable of the CMB one is going to measure.[2]

The aim of a direct measurement of the CMB spectrum is to determine the absolute temperature of the radiation at a given wavelength. More in details, what is done is to compare the sky temperature to that of a source of known temperature, the reference calibrator. The calibrator must have an emissivity as near as possible to 1 and its temperature must be comparable to the CMB temperature (in order to avoid a possible non-linear response of the instrument). The accuracy of the measurement depends strongly on the control of systematics and on the accuracy of the calibration. As an example, the most precise measurements of the CMB absolute temperature were obtained by the FIRAS instrument, aboard the COBE satellite, based an a Michelson interferometer. More precisely, FIRAS was a dual-input differential device. In this concept, the instrument output power is proportional to the difference of the two inputs: the input that looks at the sky is a horn antenna, cryogenically cooled, the other is a similar reference antenna looking to a temperature-controlled blackbody. This temperature

---

[2]Results from past, on going and future experiments are presented in Chap. 4

can be adjusted in order to obtain a null output interferogram, minimizing instrument uncertainties. Finally, FIRAS had a precision calibrator which can be inserted in front of the sky antenna, allowing a precise external calibration in flight.

Because of its *limited* precision, such kind of observations do not reach the needed accuracy for precisely mapping the angular distribution of the CMB. Differential measurements represent a performing method to reach the necessary level of sensitivity. This instrument concept consists in measuring the difference between the radiation intensity observed in two different directions. This method dramatically reduces the systematic errors related to absolute measurements, but it provides no informations regarding the CMB absolute temperature. A performing technic involves the use of two symmetrical antennas, separated by a fixed angle, that simultaneously observe the sky. The successful WMAP satellite is based on this technic, but the antennas are substituted by reflecting mirrors, allowing to increase angular resolution. On the other hand, the forthcoming *Planck* mission will map the CMB anisotropies using only one telescope and will provide results of unprecedented accuracy, thanks to the great control and minimization of systematic errors.

Polarization observations are challenging as well: they require a very high sensitivity together with an extreme control of the systematic effects to highest level. Two classical detection techniques are being used to observe the CMB polarisation: imaging and interferometer experiment that can be either heterodyne or bolometric (radiometers can be also used for this purpose, like in the *Planck* LFI). For example, the measurement of Stokes parameters with bolometers is obtained by subtracting the signals from two perpendicular polarized detectors. This method induces instrumental systematic effects since the two detection chains do not behave exactly in the same way. CMB polarization detection is recently dated (2002) and it was performed by DASI: a compact interferometric array optimized for the measurement of CMB temperature and polarization anisotropy.

The contamination level could be reduced using prior information on the emissions, in order to lower their impact on the data. This could be done by: an adequate selection of the region of observation, masking some regions in the sky, selecting the *right* frequency bands of the instrument and subtracting an estimate of the contamination.

For full-sky CMB observations, there is obviously no region to select, but

for ground-based and balloon-borne experiments a good choice of the sky region to observe is perhaps the most obvious solution to minimize contamination by foreground (at least *extra-terrestrial* emissions). The choice is based on existing observations of foreground emissions, hence it is possible to select regions in which their emission is known to be low. Anyway, there is a drawback in this strategy: observing a poor contaminated sky region puts dramatic limitations on the estimate that could be done on the foregrounds themselves (level of contamination, properties of the contaminants), because of the lack of collected data about them.

On the other side, in all-sky experiments the masking strategy is widely used. Highly contaminated regions are masked and the CMB properties are recovered in the regions with low foreground contamination level. With this strategy it is also possible to collect more informations about foregrounds. The frequency (or frequencies) of observation are chosen on the basis of more than one criterion. The *cosmological window* around 70 GHz represents a frequency range in which the foreground emission is minimal, that is to say a stronger relative CMB signal with respect to the contaminants.[3]

The foreground cleaning is strictly related to this. In order to subtract the foregrounds from a sky map and recover a clean CMB map, it is necessary to model the involved astrophysical emissions. For example, for a frequency range going from tens of MHz to few GHz, an absolute measurement of the sky temperature could be decomposed as a superposition of components:

$$T_{sky}(\mathbf{r}, \nu) = T_{Gal}(\mathbf{r}, \nu) + T_{CMB}(\nu) + T_{ers}(\nu) \, .$$

Here, ν is the frequency, T_{Gal} is the Galactic contribution, depending also on the direction of observation $\mathbf{r}$, that is partially polarized and anisotropically distributed, T_{CMB} is the background temperature and T_{ers} is a blend of unresolved extragalactic radio sources isotropically distributed. Any of these quantities is of particular astrophysical importance, but for disentangling each contribution precise models for foregrounds must be available. It is easy to understand why multi-frequency observations cover a key-role in foreground modeling. The available surveys around the microwave frequency range supply fundamental informations on which model the components and optimize the model parameters of the involved

---

[3]For ground-based and balloon-borne experiments atmospheric emission must be taken into account, considering the related best windows frequency bands for observation (30, 90, 150 and 240 GHz). For ground-based observations also ground emission at ~ 300 K contributes in contaminating the CMB signal.

processes. Up to now, it is possible to find in literature maps of sky temperature, around 1 GHz and also in the far-IR. These maps can present some artificial defects like *stripes*, due to instrumental and observational issues and to the fact that maps are a combination of data collected at different sites or at different time. Moreover, if there are no observation at a determined frequency, the data extrapolation to CMB frequencies is an useful tool to estimate the foreground contribution. Of course, the more detailed and likely is the emission model the more reliable is the estimate obtained by extrapolation.

From the early 90's, component separation technics had a rapid improvement in performances, especially in context of CMB anisotropies/polarization data reduction. To date, there are different technics operating with different methods and each of them has particular advantages and limitations. A preliminary rough classification could be done separating *non-blind* from *blind* component separation technics. The former are so called because they require some a-priori information on the signal to be separated (e.g. spatial templates and frequency dependences of the underlying components), while the blind approach is characterized from the absence of priors.

Different algorithms are used for the analysis of diffuse sources and for the extraction of point sources.[4]

In this work some of the current component separation technics will be also reviewed and the application of one of them to infrared maps is presented.

---

[4]Methods for SZ clusters extraction, based on the knowledge of SZ spectral shape, can also be added to this list.

Chapter 2

The Cosmic Microwave Background

2.1 Introduction

In the last century, our knowledge about the evolution and the origin of the Universe had a tremendous growth. The wide accepted model of the Hot Big Bang, with a period of inflationary expansion, is the by-product of the great effort carried out in theoretical and experimental fields of cosmology. According to this model, after the Big Bang, in the first 3.8×10^5 yr matter and radiation were tightly coupled. After that period, at a redshift $z \sim 1000$, the temperature cooled down to about 3000K, permitting in this way the decoupling of the baryon-photon fluid. From that time, photons have travelled almost undisturbed, feeling only gravitational effects on themselves. Today we can observe this cosmological relic radiation as a blackbody at a temperature of 2.725 ± 0.002 K [94], as measured by COBE/FIRAS, whose emission, in all directions in the sky, peaks in the microwave region of electromagnetic spectrum. Because of the tight coupling between matter and radiation at the *recombination* era, faint anisotropies in the CMB angular distribution are the traces of density inhomogeneities at that time. Due to this unique chance to have a snapshot of primordial Universe, CMB anisotropies have caught the interest of many experimental cosmologists, since their first detection by COBE/DMR [133] and even before, and have become the target of more and more advanced experiments.

In this chapter, a brief review regarding the Cosmic Microwave Background will be given. After a short introduction on the standard cosmological scenario, the main features of any observable related to the CMB are discussed, with particular attention to its spectrum, the related spectral

distortion and the physical processes that contribute to these phenomena.

2.2 The cosmological scenario

The large scale geometry of the Universe is well described [78, 89, 105], within the General Relativity framework, by the Robertson-Walker metric:

$$ds^2 = dt^2 - a^2(t) \left[\frac{dr^2}{1 - kr^2} + r^2(d\theta^2 + \sin^2\theta d\phi^2) \right] . \tag{2.1}$$

Here the dynamics of the expanding Universe is implicitly contained in the time dependance of the so called *scale factor* $a(t)$. The curvature parameter k can assume $-1, 0$ or $+1$ values corresponding to a hyperbolic, flat or spherical three dimensional space. Solving the Einstein field equation with such a metric, one obtains the Friedmann equations:

$$\frac{\dot{a}^2}{a^2} + \frac{k}{a^2} = \frac{8\pi G}{3}\rho + \frac{\Lambda}{3} \tag{2.2}$$

$$\frac{\ddot{a}}{a} = -\frac{4\pi G}{3}(\rho + 3p) + \frac{\Lambda}{3} \tag{2.3}$$

where G is the gravitational constant, ρ and p are the energy density and pressure of the Universe components, related by the typical equation of state $p = w\rho$, where w is a constant typical of each particle species. The *cosmological constant*, Λ, is an additional vacuum energy component in the stress-energy tensor. Eq. (2.3) together with the stress-energy conservation, $d(\rho a^3) = -pd(a^3)$, contains relevant informations about the evolution of our Universe. The expansion rate of the Universe is defined by the Hubble parameter $H = \dot{a}/a$.

If we assume $\Lambda = 0$, the first of the Friedmann equations can be recast as

$$\frac{k}{H^2 a^2} = \frac{\rho}{3H^2/8\pi G} - 1 \equiv \Omega_{tot} - 1 \tag{2.4}$$

Where Ω_{tot} is the ratio of the density to the critical density ρ_c

$$\Omega_{tot} \equiv \frac{\rho}{\rho_c} \tag{2.5}$$

$$\rho_c \equiv \frac{3H^2}{8\pi G} . \tag{2.6}$$

The meaning of the critical density is given by analyzing Eq. (2.4). The value of the parameter Ω_{tot} is related to the curvature parameter k. If $\Omega_{tot} > 1$ the curvature is positive; the density of the Universe is greater than

the critical density and it will begin to decelerate and finally collapse. So $\Omega_{tot} = 1$ ($\Omega_{tot} < 1$) means a *flat* (*open*) Universe. The expansion of the Universe decrease the frequency of a travelling photon. The *redshift* $z = v_{obs} - v_{em}/v_{em}$ describing this effect is related to the scale factor as $z + 1 = a(t_0)/a(t)$, where t_0 and t are, respectively, the time when we observe radiation and when it is emitted. In Tab. 2.1 are reported relevant relations describing the evolution of different contribution to the total energy.

Radiation	Matter	Vacuum
$\rho \propto a^{-4}$	$\rho \propto a^{-3}$	$\rho \propto const$
$a \propto t^{1/2}$	$a \propto t^{2/3}$	$a \propto e^{H_0 t}$
$T \propto a^{-1}$	$T \propto a^{-2}$	$-$

Table 2.1: Main relations driving the evolution of parameters for the expanding Universe depending by the energy contribution form of the equation of state.

2.2.1 Thermal history

The expansion of the primordial plasma led to a cooldown, according to the Tab.2.1. The rate of change of temperature is set by the expansion rate $\dot{T}/T = -H$. A key to understand the thermodynamics of the early Universe is the comparison of the interaction rates of the activated processes to the expansion rate, H. As long as the interactions necessary for particle distribution functions to adjust to the changing temperature are fast enough compared to the expansion rate, particles are tightly coupled and our Universe will evolve through a succession of quasi-steady thermal states. As interaction rates are usually depending on temperature, the Universe expansion and cooling passed through some typical temperature scales where different particles decoupling occurred. Two of the main steps of the thermal history of the Universe, which have left relevant observable traces we now use to recover the features of its early stages, are the nucleosynthesis and the photon-matter decoupling.

- Nucleosynthesis started about 1 sec after the Big Bang when the temperature dropped below the scale of weak interaction (1 MeV), which interconverted neutrons to protons. This allowed the formation of the first nuclei of ^{2}H and, in the subsequent three minutes, of other species of light elements. Abundances of such elements observed today fit well this model.

- After about $3 \cdot 10^5$ years, at a temperature of about $3000K$ ($z \simeq 1100$), decoupling between photons and electrons occurred, followed by the *recombination* of electron and protons into neutral hydrogen atoms.

2.2.2 Inflation

In spite of its success in giving account to most part of the Universe history since nucleosynthesis up to date, the cosmological standard model leaves some open questions. One of these problems is the *horizon problem*. In the expanding Universe every particle has a growing causal horizon, defined by:

$$d_H(t) = a(t) \int_0^t \frac{dt'}{a(t')} \ , \qquad (2.7)$$

which represents the maximum proper distance which could have been in causal contact with the particle at a given epoch. This implies, for instance, that at the *recombination* time 10^5 regions contained in the present Hubble volume were causally disconnected. As the CMB is isotropic up to a part in 10^5, on a large angular scale, classical cosmology does not explain a such singular scenario.

Another open issue left unsolved by the standard cosmology is the so-called *flatness problem*. In fact from its definition (see Eq. (2.6)) the Ω parameter changes with time as $\Omega(t) = 1/[1 - x(t)]$ where

$$x(t) = \frac{k/a^2}{8\pi G\rho/3} \qquad (2.8)$$

It could be found that $x(t)$ varies as a^2 (a) in a radiation (matter) dominated universe. This implies that, since the Ω parameter is very close to unity today, as confirmed also by recent CMB measurements, at the very early stages of the Universe, such as the Planck time (10^{-43} sec), it should have been much more close to one, better than a part in 10^{60}. This strong *fine tuning* has no explanation in classical cosmology. Both these issues are solved by the inflationary theory [62, 86].

Inflation is based upon the basic idea that there was an epoch when vacuum energy, parametrized by a scalar field called inflaton, was the dominant component of the energy density of the Universe, so that the scale factor grew exponentially. During such an epoch a small causally coherent patch of the sky could grow to become the current observable horizon. This large and quick expansion would dilute existent inhomogeneities, assuming that in our local patch the spatial gradients are small, and

smooth the curvature at a relevant level fitting the actual observed flatness. Quantum fluctuations generated at the inflaton epoch, are stretched by the accelerated expansion to become density perturbations. Inflationary models predict fluctuations almost Gaussian with a power spectrum described to first approximation by a power law $P(k) \propto k^{n_s}$, close to a scale-invariant spectrum, i.e. with $n_s \approx 1$ when density fluctuations of scales k re-enters the horizon. Therefore inflation offers a natural physical mechanism for the origin of primordial density fluctuations, which have subsequently grown by gravitational instability, providing the seed of current discrete structures, such as galaxies and clusters. Furthermore they left their signatures in the CMB angular anisotropy, which is a rich source to understand both early stages of the Universe history and late stages of its evolution during the structure formation.

2.2.3 Models for structure formation

Once the background cosmology has been defined and an acceptable mechanism generating the fluctuations has been suggested (inflation paradigm), the way in which structure grows depends on the amount and type of dark matter present. Three models have been proposed: *i*) *cold dark matter* (CDM): the currently standard model assumes that a minor fraction of the matter density is due to baryons, while the rest is in non-relativistic dark matter. Including the contribution of the vacuum energy density (e.g. the cosmological constant) the total energy density corresponds to $\Omega_{tot} = 1$ i.e. to vanishing curvature.[1] Under these assumptions the matter power spectrum shows a turnover from $P_{mat} \propto k$ at large scales (small k) to a k^{-3} fall-off at small scales (large k), which occurs at $k \simeq 0.03h$ Mpc. The reason for this turnover is that perturbations enter the horizon before the universe becomes matter-dominated, so the growth of perturbations on small scales, which spend longer periods inside the horizon in the radiation dominated era, is retarded. Dark matter produces potential wells due to gravitational instability; baryons fall into them when the photon drag becomes small enough; *ii*) *hot dark matter* (HDM): in this model the difference between Ω_b and Ω_m is made up of relativistic particles. These have a minimum scale on which gravitational instability can cause overdensities, due to their free streaming. This leads to a large-scale (small k) cut-off; *iii*) *mixed dark matter* (MDM): a combination of hot and cold dark matter may account for extra

---

[1]The actual standard cosmological scenario consists in a ΛCDM model.

power on large scale structure measurements over predictions of standard CDM (but this difference may also be made up by the cosmological constant).

2.2.4 Dark energy

In 1998 two independent groups, observing Type Ia Supenovae, pointed out that the expansion of the Universe is accelerating [107] [120]. They observed the luminosity distance of high redshift SN. The apparent magnitude m, of a source with an absolute magnitude M, is related to the luminosity distance d_L through

$$m - M = 5\log_{10}\left(\frac{d_L}{\text{Mpc}}\right) + 25 \tag{2.9}$$

and the luminosity distance, in a flat geometry, is given by

$$d_L = \frac{(1+z)}{H_0} \int_0^z \frac{\text{d}z'}{\sqrt{\sum_i \Omega_i^0 (1+z')^{3(1+w_i)}}} \, , \tag{2.10}$$

where w_i represents the equation of state for each component. The belief is that SN Ia are formed and evolve in the same way wherever they are in the Universe and this is translated in the idea that they have a common absolute magnitude M, independent of the redshift. The supernova cosmology project (SCP) and the high-z supernova team (HSST) collected in total fluxes from almost 70 SN Ia, with redshift ranging in the interval $0.16 < z < 0.83$. In 2004, thanks the study of 16 SN Ia with redshifts $z > 1.25$ it turned out [121] that the Universe exhibits a transition from deceleration to acceleration at > 99% confidence level.

Another evidence for the existence of a cosmological constant emerges comparing the age of the oldest stellar population with the age of the Universe. The latter must obviously be greater than the former, but it is difficult to satisfy this condition for a flat cosmological model with normal form of matter [30].

Further and more recent observations provided other proofs for an additional component in the Universe dynamics: observations of CMB anisotropies and of large scale structures independently support the idea of a dark energy dominated Universe.

From the point of view of particle physics, the cosmological constant naturally arises from an energy density from the vacuum and it corresponds to a fluid with a constant equation of state $w = -1$. To date, the observations

say very little about the evolution of w, so it is possible to consider situations in which the equation of state of dark energy changes with time. Among the others, these ideas include: quintessence, phantoms, K-essence, tachyon, ghost condensate.

Let now see just some features of one of this model. Quintessence is described by an ordinary scalar field Φ minimally coupled with gravity, but with a particular potential that lead the late time inflation. The action for quintessence [30] is given by:

$$S = \int d^4x \sqrt{-g} \left[-\frac{1}{2}(\nabla\Phi)^2 - V(\Phi) \right] , \qquad (2.11)$$

where $(\nabla\Phi)^2 = g^{\mu\nu}\partial_\mu\Phi\partial_\nu\Phi$ and $V(\Phi)$ is the potential of the field. In a FLRW space-time the variation of the action with respect to Φ is gives

$$\ddot{\Phi} + 3H\dot{\Phi} + \frac{dV}{d\Phi} = 0 . \qquad (2.12)$$

Computing energy density and pressure of the scalar field in a Friedmann background, it is possible then to obtain the following equations for the cosmic evolution:

$$H^2 = \frac{8\pi G}{3}\left[\frac{1}{2}\dot{\Phi} + V(\Phi) \right] , \qquad (2.13)$$

$$\frac{\ddot{a}}{a} = -\frac{8\pi G}{3}\left[\dot{\Phi}^2 + V(\Phi) \right] . \qquad (2.14)$$

2.3 CMB anisotropies

The inflationary model predicts Gaussian fluctuations for CMB temperature anisotropies. If this condition holds, their statistical content is hold in the 2-point temperature correlation function, or equivalently in its angular decomposition into Legendre moments C_l, commonly called *power spectrum*.

The details of the cosmological model cannot be shaped through the informations encrypted in the thermal nature and isotropy of the CMB. Temperature anisotropies anisotropies bear the imprint, filtered through the dynamics and geometry of the expanding universe, of the fluctuations which eventually led to structure formation in the universe.

In this section, a light description on the origins and characteristics of the CMB temperature anisotropies will be given, focusing with more details on its statistical description.

2.3.1 Primordial perturbations

In order to analyze the origin of primordial fluctuations we have to go back in time until the actual model is consistent. At this stage of life of the Universe, quantum gravity effects start to be important and General Relativity is no longer a *safe theoretical probe*. The moment after which this happens is named *Planck time*: the age of the universe was $t \sim 10^{-43}$ sec and its temperature was about 10^{19} GeV. At present, a firm understanding of the elementary particles and their interactions only extends to energies of the order of 100 GeV, which corresponds to a time of the order of 10^{-11} sec. An ascertain truth is that at temperature of about 100 MeV – 200 MeV ($t \sim 10^{-5}$ sec) there was a transition from quark/gluon plasma to very hot hadronic matter, and that some kind of phase transition associated with the simmetry breakdown of the electroweak theory took place at a temperature of the order of 300 GeV.

In this primordial era, two kind of perturbation are of interest: adiabatic perturbations and isocurvature perturbations

2.3.2 Adiabatic perturbations

Adiabatic (or isentropic) modes are fluctuations in the energy density, or the number of particles, such as the specific entropy is constant for any species i. If these species are non-relativistic:

$$\delta\left(\frac{n_\gamma}{n_i}\right) \propto \frac{\delta\rho_i}{\rho_i} - \frac{3}{4}\frac{\delta\rho_\gamma}{\rho_\gamma} = 0.$$

In terms of the perfect fluid stress-energy tensor of general relativity, the assumption of an adiabatic perturbation is equivalent to assuming that the pressure fluctuation is equivalent to the energy density perturbation. The adiabatic condition implies:

$$\frac{\Delta T}{T} = \frac{1}{4}\frac{\delta\rho_\gamma}{\rho_\gamma} = \frac{1}{3}\frac{\delta\rho}{\rho}$$

On the other hand, because an over-density gives a larger gravitational potential that photons must climb out of, the gravitational effect and the adiabatic effect partially cancel, leaving

$$\frac{\Delta T}{T} = -\frac{1}{3}\delta\phi$$

where $\delta\phi$ is the fluctuation in the gravitational potential and the minus sign means that the CMB hot spots are matter under-densities. Inflation naturally predicts adiabatic perturbation.

2.3.3 Isocurvature perturbations

Isocurvature modes are fluctuations in the number density of particles which do not affect the total energy density. They perturb the specific entropy or the equation of state:

$$\delta s = \delta\left(\frac{n_\gamma}{n_b}\right) \propto \frac{\delta\rho_b}{\rho_b} - \frac{3}{4}\frac{\delta\rho_\gamma}{\rho_\gamma} \neq 0$$

While these perturbations are outside the horizon, causality precludes them from becoming an energy density perturbation. Inside the horizon, however, pressure gradients can convert an isocurvature perturbation into an energy density fluctuation. For isocurvature fluctuations, a positive fluctuation in the matter density (and therefore in the gravitational potential) is compensated by a negative fluctuation in the photon temperature. The gravitational effect (Sachs-Wolfe) and the initial temperature fluctuation therefore add each other (rather than cancel, as in the adiabatic case), giving rise to six times more large $\Delta T/T$ for a given matter perturbation.

2.3.4 Statistics and angular power spectrum

Since the tight coupling between matter and radiation in the primordial Universe it is possible to recover the gravitational potential at the Last Scattering Surface (LSS), which wrap detailed features of the recombination epoch [70, 106, 139]. In the context of a CMB observation, it is usual to describe te temperature distribution on the sky through a spherical harmonics decomposition:

$$T(\bar{x}_0, \theta, \phi) = \sum_{\ell=0}^{\ell=\infty} \sum_{m=-\ell}^{m=\ell} A_{\ell m}(\bar{x}_0) Y_{\ell m}(\theta, \phi) \tag{2.15}$$

where $\bar{x}_0$ represents *our* location in the Universe, and the two angles θ and ϕ define the pointing direction in the sky. The dependence from $\bar{x}_0$ should always appear but this will be omitted in the continuation since it is somewhat implicit in the measurement: we are clearly able to do measurement only from our location and this is the only realization of Universe that we can observe. This obviousness is translated in what is called *cosmic variance*, that is described at the end of this section.

The multipole moments, $A_{\ell m}$, represent the collection of numerical values necessary to describe the observed sky pattern. The first term, the *monopole*, represents the mean sky temperature: $T_0 = 2.725 \pm 0.002$ K [94].

The second term, the *dipole*, has an amplitude of about $\Delta T \sim 3.365 \pm 0.027$ mK and it results from the Doppler-shifted Planck spectrum due to the Solar System's motion with respect to the rest of frame of the CMB, towards the direction of the Virgo cluster with a velocity of about 370 km/s.

Since CMB spectrum is an extremely good blackbody the observable is generally described in terms of a temperature fluctuation $\Delta T(\theta, \phi) = T(\theta, \phi) - T_0$ and $a_{\ell m} = A_{\ell m}/T_0$:

$$\frac{\Delta T(\theta, \phi)}{T_0} = \sum_{\ell=1}^{\ell=\infty} \sum_{m=-\ell}^{m=\ell} a_{\ell m} Y_{\ell m}(\theta, \phi). \tag{2.16}$$

The observed quantities are the RMS value of temperature fluctuations:

$$\left\langle \left(\frac{\Delta T}{T_0}\right)^2 \right\rangle = \frac{1}{4\pi} \int_{4\pi} \left(\frac{\Delta T(\theta, \phi)}{T_0}\right)^2 (\theta, \phi) \, d\Omega$$

$$= \frac{1}{4\pi} \sum_{\ell} \sum_{m} a_{\ell m} a_{\ell' m'}^* \int_{4\pi} Y_{\ell m}(\theta, \phi) Y_{\ell' m'}^* \, d\Omega. \tag{2.17}$$

Since $\int_{4\pi} Y_{\ell m}(\theta, \phi) Y_{\ell' m'}^* \, d\Omega = \delta_{\ell \ell'} \delta_{m m'}$ it results:

$$\left\langle \left(\frac{\Delta T}{T_0}\right)^2 \right\rangle = \sum_{\ell} \sum_{m} \frac{\left\langle |a_{lm}^2| \right\rangle}{4\pi}. \tag{2.18}$$

In an isotropic universe a rotational invariance of the coefficients $\langle |a_{lm}|^2 \rangle = \langle |a_{lm'}|^2 \rangle$ is aspected and:

$$\left\langle \left(\frac{\Delta T}{T_0}\right)^2 \right\rangle = \sum_{\ell} \frac{(2\ell + 1) C_\ell}{4\pi} \tag{2.19}$$

where the coefficients $C_\ell = \left\langle |a_{lm}^2| \right\rangle$, named *power spectra*, are the quantities related to the physical phenomena. The multipole ℓ is related to the angular scale θ by the relationship $\ell \sim \pi/\theta$.

The average in Eq. 2.17 should be computed over all possible locations $\bar{x}$ but of course is not. For this reason what we measure is not C_ℓ but:

$$\tilde{C}_\ell(\bar{x}_0) = \sum_{m=-l}^{\ell} \frac{|a_{\ell m}(\bar{x}_0)|^2}{2\ell + 1}. \tag{2.20}$$

Usually is plotted the value $\ell(\ell + 1) C_\ell / 2\pi$ versus the multipole ℓ because in the standard CDM this quantity is aspected to be constant for multipoles larger than the horizon ($\ell \lesssim 50$). The cosmological models predict only the statistical distribution of temperature fluctuations and, as said, if such a

distribution is Gaussian then the power spectrum completely describes the models.

How accurately could the spectra ultimately be measured had been defined by the mentioned *cosmic variance* due to the fact that there are only $(2\ell + 1)$ $m-$samples of the power in each multipole moment. This leads to an unavoidable error of:

$$\sigma_\ell \sim \sqrt{\frac{2}{2\ell + 1}C_\ell} \qquad (2.21)$$

Allowing for further averaging over ℓ in bands of $\Delta\ell \sim \ell$, the precision in the power spectrum determination scales as ℓ^{-1}, i.e. $\sim 1\%$ at $\ell = 100$ and $\sim 0.1\%$ at $\ell = 1000$.

There are two general caveats to these scalings. The first is that any source of noise, instrumental or astrophysical, increases the errors. If the noise is also Gaussian and has a known power spectrum, the power spectrum on the right-end-side of Eq. 2.21 can be simply replaced with the sum of the signal and noise power spectra. This explains why the errors for the PLANCK satellite increase near its resolution scale. Because astrophysical foregrounds are typically non-Gaussian it is usually necessary to remove heavily contaminated regions, e.g. the Galaxy. If the fraction of covered sky is f_{sky}, then the errors increase by a factor of $f_{sky}^{-1/2}$ and the resulting variance is usually dubbed *sample variance*.

Another observation related topic that must be considered is the *window function* W_ℓ. This is characteristic of the instrument involved in the measurement of the power spectrum and it is due to its discrete angular resolution:

$$C_{\ell,meas} = C_\ell \cdot W_\ell \qquad (2.22)$$

For a Gaussian beam with angular resolution equal to FWHM the window function is:

$$W_\ell \sim e^{-\frac{\ell^2\sigma^2}{2}} \qquad (2.23)$$

with $\sigma = $ FWHM $/(2\sqrt{2\ln 2})$. Therefore, the drop of the window function makes an instrument sensitive only to $\ell \lesssim \pi/$PFWHM.

2.3.5 Primary anisotropies

When the universe was about 3×10^5 years old the CMB was a thousand times hotter ($T \simeq 3 \times 10^3$ K, $z \simeq 10^3$), and jointly to the high number of photons it was able to keep separated baryons and leptons. Before that epoch, the strength of the Coulomb interactions establish a baryon-photon

fluid. Fluctuations in the total matter density (including dark matter and possibly neutrinos) have effects on the photons through the gravitational potential they create. The anisotropies formation are due also to the presence of these fluctuations in the early Universe.

The following discussion will be done in Fourier space, in units in which $c = 1$ and the gravity is neglected, for the moment. If Θ is the photon temperature, the decomposition of the temperature field monopole is then:

$$\Theta_{\ell=0,m=0}(\mathbf{x}) = \int \frac{d^3k}{(2\pi)^3} e^{i\mathbf{k}\mathbf{x}} \Theta(\mathbf{k}) ,$$

where the subscript 00 in the Fourier amplitude is omitted. In the Fourier space the temperature perturbations obey

$$\dot{\Theta} = -\frac{1}{3}kv_\gamma , \tag{2.24}$$

where the derivative is done with respect to the conformal time η and the photon fluid velocity v_γ is written as a scalar because in the early Universe only the velocity component parallel to the wavevector $\mathbf{k}$ is important. [2] The factor 1/3 comes from the fact that continuity preserves photon number but not the temperature and the number density $n_\gamma \propto T^3$. Now, if we consider that the momentum density of the photons is $(p_\gamma + \rho_\gamma)v_\gamma$, with a photon pressure $p_\gamma = \rho_\gamma/3$ and neglect gravity and fluid imperfections, the pressure gradients represent the only force $\nabla p_\gamma = \nabla \rho_\gamma/3$ and since $\rho_\gamma \propto T^4$, this becomes $4k\Theta\bar{\rho}_\gamma/3$ in Fourier space.

With these assumptions, the Euler equation, that for a fluid represents the momentum conservation, can be written as

$$\dot{v}_\gamma = k\Theta . \tag{2.25}$$

Differentiating Eq. 2.24, that represents the continuity equation in Fourier space and inserting Eq. 2.25, it is possible to achieve to the most basic form of the oscillator equation:

$$\ddot{\Theta} + c_s^2 k^2 \Theta = 0;, \tag{2.26}$$

where $c_s \equiv \sqrt{\dot{p}/\dot{\rho}} = 1/\sqrt{3}(= c/\sqrt{3})$ is the sound speed in the fluid (considered dynamically baryon-free for now). The pressure gradients act to any initial perturbations and make them oscillate at the speed of sound. The

---

[2]Specifically, it must be written as $\mathbf{v}_\gamma = -iv_\gamma\hat{\mathbf{k}}$ and it represents the induction of a dipole moment directed along $\mathbf{k}$

temperature oscillations physically represent the heating and the cooling of a fluid in the phases of compression and rarefaction respectively. This mechanism is well described through the action of acoustic waves and it lasts until recombination occurs.

Acoustic Oscillations

Acoustic oscillations result inside the fluid since the gravity tries to compress the fluid in potential wells generated by energy density fluctuations and photon pressure resists the compression. Ignoring, as first approximation, time variations in the two potentials Ψ and Φ and the contribution of baryons to the sound speed, that can be considered $c_s \simeq c/\sqrt{3}$, the oscillator equation then reduces to:

$$\ddot{\Theta} + k^2 c_s^2 \Theta = -\frac{1}{3}k^2\Psi \tag{2.27}$$

where Θ is the isotropic temperature fluctuation and the derivative are done with respect to the conformal time $\eta \equiv \int dt/a(t)$. This is a simple harmonic oscillator under the constant acceleration provided by gravitational infall and can be solved as:

$$\Theta(\tau_c) = [\Theta(0) + (1+R)\Psi]\cos(kr_s) + \frac{1}{kc_s}\dot{\Theta}_0(0)\sin(kr_s) - (1+R)\Psi, \tag{2.28}$$

where the sound horizon $r_s = \int c_s d\eta = c_s \eta$. The two initial conditions $\Theta(0)$ and $\dot{\Theta}_0(0)$ govern the form of the acoustic oscillation.

Gravitational infall and redshift

In the early universe photons dominate the fluid and $R \to 0$. In this limit the oscillation becames an even simpler form. For the adiabatic mode, $\dot{\Theta}(0) = 0$ and

$$\Theta(\eta) = [\Theta(0) + \Psi]\cos(kr_s) - \Psi . \tag{2.29}$$

This represents an oscillator with a zero point which has been displaced by gravity. The zero point represents the state at which gravity and pressure are balanced. This displacement $-\Psi > 0$ yields hotter photons in potential well since gravitational infall not only increases the number density of photons but also their energy through gravitational blueshifts. However, photons also suffer a gravitational redshift from climbing out of the potential well after the last scattering. This precisely cancel the $-\Psi$ blueshift and the

effective temperature perturbation is

$$\Theta(\eta) + \Psi = [\Theta(0) + \Psi]\cos(kr_s) \,. \tag{2.30}$$

The phase of the oscillation at last scattering determines the effective fluctuation. Since the oscillation frequency $\omega = kc_s$, the critical wavenumber $k = \pi/r_s(\eta^*) \approx \pi/c_s\eta^*$ is essentially at the scale of the sound horizon (asterisks denote evaluation at recombination). If there is a spectrum of k-modes, there will be a harmonic series of temperature fluctuation peaks with $k_m = m\pi/r_s(\eta^*)$ for the m-th peak. Odd peaks represent the compression phase (temperature crests), while even peaks represent the rarefaction phase (temperature troughs), inside the potential well. As first calculated by Sachs & Wolfe [?], the effective temperature in the matter dominated limit goes to

$$\Theta + \Psi = \frac{1}{3}\Psi \,. \tag{2.31}$$

Thus this effect, named *Sachs & Wolfe effect*, is a combination of intrinsic temperature and gravitational redshift.

Baryon drag

The baryons contribution must be also taken into account. Even if they are effectively pressureless, baryons contribute in decreasing the sound speed. Considering consider the photon-baryon momentum density ratio

$$R = \frac{p_b + \rho_b}{p_\gamma + \rho_\gamma} \approx 30\Omega_b h^2 (z/10^3)^{-1} \,,$$

it is possible to quantify the sound speed decrease: $c_s = 1/\sqrt{3(1+R)}$. Because baryons play a fundamental role in the calculation of the inertial and gravitational mass of the fluid, they change also the balance of pressure and gravity. The gravitational infall in a potential well is now characterized by a greater compression of the fluid and this involves a displacement of the zero point of the oscillations. In order to better understand the contribution of the baryons, let consider the limit in which R, Φ and Ψ are constant. Maintaining the formalism of Eq. 2.27 and considering $\Theta \rightarrow \Theta + (1+R)\Psi$, the solution of the *revised oscillation equation* is

$$[\Theta + (1+R)\Psi](\eta) = [\Theta + (1+R)\Psi](\eta_{md})\cos kr_s \,. \tag{2.32}$$

Lowering the sound speed, baryons decrease the sound horizon and they have two further effect: to let the oscillations reach larger amplitude and to
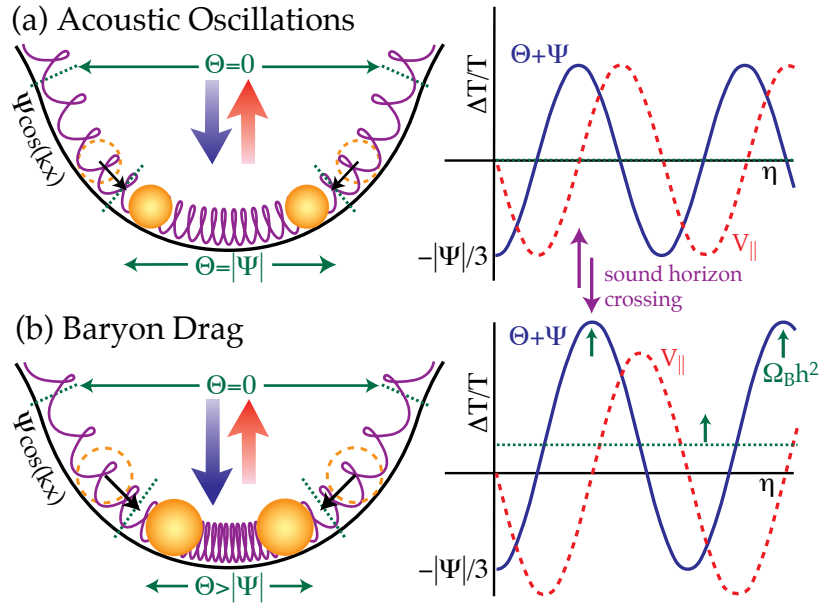
Figure 2.1: Top panel: radiation pressure from the photons resists the gravitational compression of the fluid into potential wells and sets up acoustic oscillations in the fluid. Bottom panel: baryons increase the effective mass of the fluid and the gravitational infall leads to a greater compression of the fluid in the potential well. Figure from [3]

shift the zero point of oscillations themselves. This shift breaks the symmetry of the oscillations, leading the baryons to enhance only compressional phases (odd peaks on the APS). It means that the baryons supply the extra gravity to make compressions became potential wells.

It is possible to consider the case of a time-variable mass, that causes the adiabatic damping of an oscillator and since the frequency (and so the energy) of an oscillator is an adiabatic invariant, the amplitude must decay as $(1 - R)^{-1/4}$.

Doppler effect

Since the oscillation turning points are at the extrema, the fluid velocity oscillates 90 degrees out of phase with the density. Its motion relative to the observer causes a Doppler shift. Whereas the observer velocity creates a pure dipole anisotropy on the sky, the fluid velocity causes a spatial temperature variation on the last scattering surface from its line of sight component.

The velocity contribution is equal in amplitude to the density effect. The addition of baryons significantly changes the relative velocity contribution. As the effective mass increases, conservation of energy requires that the velocity decreases for the same initial temperature displacement. Thus the relative amplitude of the velocity scales as c_s. Velocity oscillations are symmetric around zero unlike the temperature ones. Thus compressional peaks will rise clearly above the velocity oscillations if R is large. Even in a universe with $\Omega_b h^2$ given by nucleosynthesis, R is suffciently large to make velocity contributions subdominant.

Including radiation

It is possible to take into account the contribution of the energy density of the radiation. The matter-to-radiation ratio scales as $\rho_m/\rho_\gamma \approx 24\Omega_m h^2 (z/10^3)^{-1}$. At he epoch of recombination $z \sim 10^3$, so this ratio is of the order of unity (for reasonable cosmological parameters). It also happened that fluctuations corresponding to higher peaks, entered the sound horizon during the radiation dominated era.

Further, the inclusion of the radiation of course changes the Universe evolution and so the physical scale and the sound horizon at recombination. The effect of the radiation on the power spectrum is to drive the acoustic oscillations by making the gravitational force to evolve with time. In particular, in the radiation dominated era once pressure starts to oppose to gravity at the first compressional maxima of the wave, the Newtonian gravitational potential and the spatial curvature must decay. The oscillations are then driven, because the decay leaves the fluid maximally compressed without any gravitational potential to oppose.

Anyway, once the Universe becomes matter dominated the gravitational potential is no more determined by the photon-baryon density but by the cold dark matter and the amplitude of the acoustic peaks increases as the cold dark matter-to-radiation ratio decreases. So radiation density perturbations won't grow anymore around the horizon crossing. It is worth noting that not considering gravitational potential leads to eliminate the alternating peaks heights caused by the baryon loading. Indeed, the height of the third peak is an indication that cold dark matter exists and dominates the energy densities at recombination.

Damping

Even id it is characterized by particular regimes, the baryon-photon fluid is not a perfect fluid. Heat conduction and shear viscosity may perturb the acoustic oscillations. The effect consists in damping the oscillations. Considering that the number of photons and baryons is conserved, the continuity equation, for each of the two species, are written as

$$\dot{\Theta} = -\frac{k}{3}v_\gamma - \dot{\Phi} ,$$

$$\dot{\delta}_b = -kv_b - 3\dot{\Phi} , \tag{2.33}$$

where δ_b and v_b are the density perturbation and the fluid velocity of the baryons respectively. It is possible now to write the Euler equations for the two species, considering also the new terms:

$$\dot{v}_\gamma = k(\Theta - \Psi) - \frac{k}{6}\pi_\gamma - \dot{\tau}(v_\gamma - v_b) ,$$

$$\dot{v}_b = -\frac{\dot{a}}{a}v_b + k\Psi + \dot{\tau}(v_\gamma - v_b)/R . \tag{2.34}$$

Here $\dot{\tau} \equiv n_e\sigma_T a$ is the differential Thomson optical depth and the term of the equation containing it takes into account the momentum exchange during the Thomson scattering between photons and electrons. Further, the presence of the scale factor a in the Euler equation for baryons ensures that momenta decay as a^{-1}. These terms represent the origin of the heat conduction imperfections.

Anisotropic stress gradients or radiation viscosity add an extra force in the Euler equation for the photons. The viscosity and the heat conduction terms can be written the form of damping terms and included in the oscillator equation, that takes the following form:

$$c_s^2\frac{\mathrm{d}}{\mathrm{d}\eta}(c_s^{-2}\dot{\Theta}) + \frac{k^2c_s^2}{\dot{\tau}}[A_V + A_h]\dot{\Theta} + c_s^2K^2\Theta = -\frac{k^2}{3}\Psi - c_s^2\frac{\mathrm{d}}{\mathrm{d}\eta}(c_s^{-2}\dot{\Phi}) . \tag{2.35}$$

Here $A_h = R^2/(1 + R)$ is the heat conduction coefficient, while A_V takes into account the anisotropic stress gradients. The damping scale, k_d, is of the order of $\sqrt{\dot{\tau}/\eta}$, that corresponds to the geometric mean between the horizon and the mean free path, $\lambda_C = \dot{\tau}^{-1}$. At the recombination k_d/η is of the order of few %, so in the CMB power spectrum all the peaks after the third one are expected to be affected by dissipation.

completare con massa di silk

2.3.6 Secondary anisotropies

After recombination, CMB photons travel until us, traversing large scale structures in the Universe. From the decoupling and along all their journey they pick up secondary anisotropies in temperature and polarization anisotropies as well.

Contributions to these anisotropies come from several parts: dark matter, dark energy, temperature and density distribution of the baryonic gas and even the existence of gravitational waves could play a role in this phenomena. Anyway, there are some limitations related to the precise determination of these effects: on one side the non-linear regime of these processes and the uncertainties on them put some limitations on the predictions of their effects, while on the other precise measurements are limited by cosmic variance and by the important contamination that Galactic and extragalactic foregrounds bring on CMB measurements.

The secondary anisotropies can be divided in two main classes on the basis of the source of the anisotropy itself: gravitational secondaries and scattering secondaries. What follows is a brief description of the secondary anisotropies.

Gravitational effects

Integrated Sachs Wolfe effect

In a cosmological model in which $\Omega_m < 1$, at the epoch in which the Universe from matter-dominated becomes dark energy-dominated, it is possible that potentials on a given scale may decay. This happens whenever the expansion is dominated by a component whose effective density is smooth on that scale. The effect consists in the relation that is between the decaying of a potential well and the crossing of it by a photon while it is decaying. If it decay during the photon crossing, this latter gets a boost in temperature of $\delta\Psi$, due to differential gravitational redshift and $-\delta\Phi \approx \delta\Psi$ due to the contraction of the wavelength.

A potential decay due to dark energy is characterized by a long time interval on which the potential decays and today this is of the order of the Hubble time. Anyway, the distance on which photons feel the effect is much shorter than the wavelength of the potential fluctuation.

On the power spectrum the contribution of the ISW effect is generally seen at large angular scale (low ℓ). Since the effect is very sensitive to the dark

energy, it is very important, because it can provide informations of the amount, on the equation of state and on the clustering properties of the dark energy. Unfortunately, being concentrated to low multipoles, the ISW effect suffers very much from the cosmic variance.

The ISW effect is called *early* ISW if the time evolution of the anisotropy perturbation is due to the radiation content, while it is called *late* ISW if it is due to expansion.

Rees-Sciama effect

The cancellation of the ISW effect on small scales, due to the fact that photons travel through many peaks and valleys, generates second order and non-linear contributions to the anisotropies. The evolution of the density profile of a isolated structure can cause changes in the potential along the line of sight and a more prominent effect comes from the bulk motion of the structure along the line of sight. The bulk motion of dark matter halos contributes to this effect, that consists in low levels of anisotropies: it is never the major level of secondary anisotropies on any scales.

Gravitational waves and gravitational lensing

The contribution of the gravitational waves to the generation of anisotropies is generated by a time-variable tensor metric perturbation [123]. The effect is that of a standing gravitational wave: the raise of a quadrupolar distortion in the spatial metric and its changing in time leaves a quadrupolar distortion in the CMB temperature distribution. Once the perturbation crosses the horizon, the amplitude of a gravitational wave starts oscillating and decaying and given that this process happen before the recombination, the Thomson scattering deletes any developing quadrupole anisotropies. On the power spectrum only the contribution for large scales remains, while later than the first peak any effect is suppressed. Since the effect is limited to low moltipoles, the isolation of the gravitational waves contribution is strongly limited by cosmic variance (see Fig. 2.2)

A further effect of the large-scale gravitational potential consists in lensing the CMB photons. This is a second order effect because the lensing holds the surface brightness and affects only anisotropies.

Scattering effects

Reionization

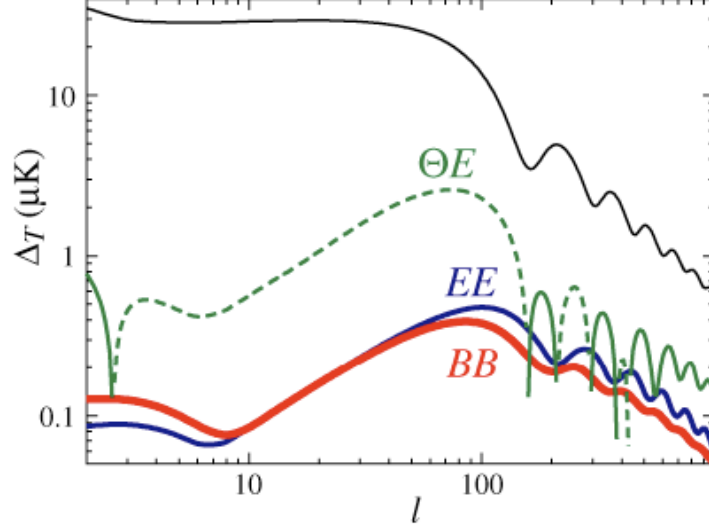CMB anisotropies can be suppressed if photons are scattered again in

Figure 2.2: Temperature and polarization spectra from an initial scale invariant gravitational wave spectrum. Figure from [2]

relatively late epochs, like in the case of a reionization of the Universe. This process has some major impact on all the observables of the CMB. In particular, if a reionization occurs the temperature anisotropies will be suppressed by an amplitude strictly related to the fraction of photons rescattered. The optical depth for photons plays here a fundamental role and an important epoch is when it is equal to unity. Since Thomson scattering is independent of frequency, is quite simple to calculate the reionization redshift from the following formula

$$\tau = -\int_0^z \bar{n}_e(z)\sigma_T c \left(\frac{\mathrm{d}t}{\mathrm{d}z}\right)\mathrm{d}z \; , \qquad (2.36)$$

where σ_T is the Thomson cross section, c is the speed of light and $n_e(z)$ takes into account the number density of electrons at different epochs. For a geometrically flat Universe with a constant ionized fraction, Eq. 2.36 can be written as:

$$\tau \simeq 0.035\Omega_b h x_e z^{3/2} \; . \qquad (2.37)$$

Here, x_e is the ionized fraction of the electrons. The important effects of reionization on anisotropies are at arc-minute scales, in particular, where primary anisotropies are expected to be erased. These will be suppressed proportionally to $e^{-\tau}$.

Doppler effects

After the Compton drag epoch baryonic gravitational instability can no

longer be prevented by the photons. Collapse of the baryon density fluctuations implies that baryon peculiar velocities will create a Doppler effect in the CMB. However, the photon traverses many crests and troughs of the perturbation at last scattering and these contributions are suppressed in the same way as the late ISW effect: photons that last scattered off opposite sides of the perturbation get Doppler shifted by equal and opposite amounts. Thus for wavelengths far below the thickness of the last scattering surface, Doppler contributions tend to cancel leaving a negligible net effect (see Fig. 2.4).
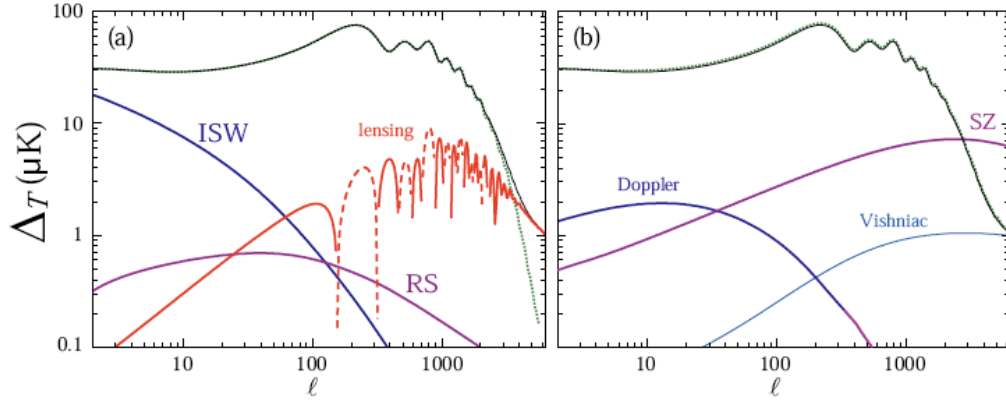
Figure 2.3: Secondary anisotropies. Gravitational secondaries: ISW, lensing and Rees-Sciama effects (*left side*). Scattering secondaries: cancelled Doppler effect, Vishniac effect, and the thermal SZ effect (*right side*). Figure from [2]
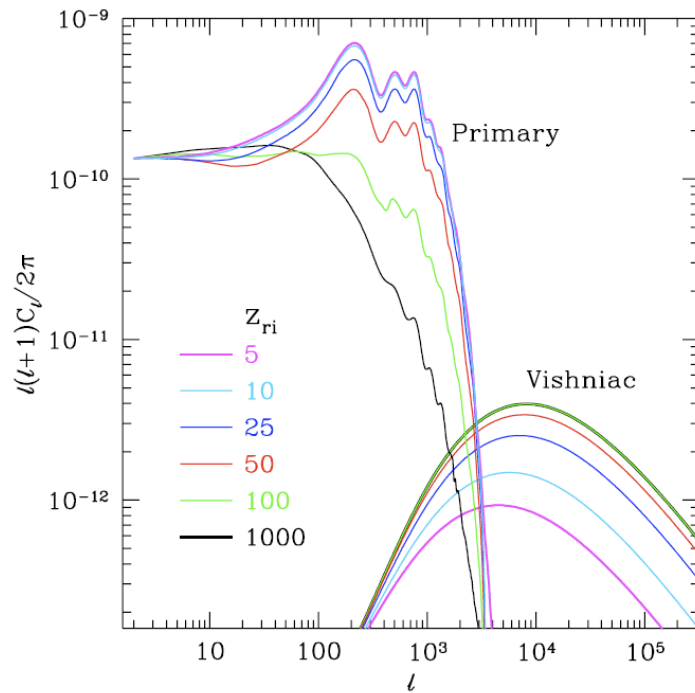
Figure 2.4: Primary and Vishniac contributions for a range of possible ionization histories in the standard CDM model. Note that even for minimally ionized $z_{ri} = 5 - 10$, where first order anisotropies are nearly indistinguishable from the standard recombination case, the Vishniac effect contributes a significant fraction of its total in temperature fluctuations. Because standard CDM has more small scale power than measurements suggest, these calculations are expected to be an upper limit for CDM-like models. Figure from [2]

Vishniac

Since the first order Doppler fluctuation is severely suppressed due to coincidental geometrical reasons other effects may dominate the anisotropy at small scales. Variations in the optical depth due to density fluctuations across the last scattering surface may allow the Doppler effect to avoid severe cancellation. The increased probability of scattering causes a preferential generation of Doppler fluctuations in overdense regions. A coupling between large scale velocity perturbations with small scale density perturbations is thus established; it is not as severely damped as the first order contribution. Vishniac contributions are expected to peak on sub-arcmin scales.

Sunyaev-Zel'dovich effect

Clusters provide a non-linear analogue of the Vishniac effect. Here the hot cluster provides the variation in the optical depth which causes preferential scattering. The Doppler effect due to the peculiar velocity of the cluster yields an anisotropy known as the *kinematic Sunyaev-Zeldovich effect* (SZ) [151]. For an individual cluster the temperature fluctuation is of order $\tau_c v_c$, where the optical depth through a cluster is of order $\tau_c \approx 0.1 - 0.01$ and the peculiar velocity $v_c \approx$ few $\times 10^{-3}$. This provides an interesting way of measuring the peculiar velocity of a cluster without introducing the problems associated with determining the distance scale. The average effect is much smaller however and probably does never dominates the anisotropy spectrum. Anyway, this non-linear Doppler effect is small in comparison to the second order Doppler effect.

Approximately 10% of the total mass of rich clusters of galaxies is in the form of hot ($\sim 10^8$ K) ionized plasma. Compton scattering of CMB photons by electrons in this intra-cluster plasma can result in an optical depth as high as 0.02, resulting in a distortion of the CMB spectrum at the mK level named *thermal Sunyaev-Zeldovich* effect.

2.4 CMB polarization

The temperature anisotropies that we observe are the result of primordial fluctuations. On the LSS, Thomson scattering of temperature anisotropies generates a linear polarization pattern on the sky that can be simply read off from their quadrupole moments. These quantities correspond directly to the fundamental scalar (compressional), vector (vortical), and tensor (gravitational wave) modes of cosmological perturbations.

Thomson scattering, driving baryon-photon interactions at the recombination era, is represented by a polarization-dependent differential cross-section:

$$\frac{d\sigma}{d\Omega} = \frac{3\sigma_T}{8\pi} \, |\widehat{\epsilon}\,' \cdot \widehat{\epsilon}|^2 \tag{2.38}$$

where σ_T is the total cross section, while $\widehat{\epsilon}$ and $\widehat{\epsilon}\,'$ are unit vectors in the planes perpendicular to the propagation directions of incoming and outgoing radiation scattered by an electron. The unpolarized scattered photon gain a residual polarization from this interaction. Then if we integrate the effects for photons interacting with the electron through all directions, polarized component is averaged out. The presence of a local quadrupole component in the distribution of photons at last scattering generates a net linear polarization in the CMB [2]. This causal process leads to polarization spectrum peaks at angular scales smaller than the horizon size at last scattering. Furthermore, the polarized fraction of the temperature anisotropy is small, since only those photons that last scattered in an optically thin region could have possessed a quadrupole anisotropy (multiple scattering causes photon trajectories to mix and hence erases anisotropy). This fraction, which depends on the duration of last scattering, is expected to be of $5 - 10\%$ on a characteristic scale of tens of arcminutes. Polarization spectrum is related with fluid velocity induced local quadrupole and then out of phase with temperature power spectrum.

2.4.1 Statistical description

More formally, let call I_{ij} the 2×2 intensity tensor characterizing the CMB radiation field. This quantity is a function of the direction on the sky $\mathbf{n}$ and the two directions perpendicular to $\mathbf{n}$: $\widehat{\mathbf{e}}_1, \widehat{\mathbf{e}}_2$. The Stokes parameters are defined as $Q = (I_{11} - I_{22})/4$ and $U = I_{12}/2$, while the temperature anisotropies

is given by $T = (I_{11}+I_{22})/4$. Generally one represents the polarization through the definition of the quantities $P = \sqrt{Q^2 + U^2}$, the magnitude, and the angle $\alpha = \arctan\left(\frac{U}{Q}\right)$. The Stokes parameter V that describes circular polarization is not included because it could not be generated through Thomson scattering. In the plane perpendicular to $\mathbf{n}$, under a right handed rotation of an angle ψ, Q and U transform as

$$Q' = Q\cos 2\psi + U\sin 2\psi$$

$$U' = -Q\sin 2\psi + U\cos 2\psi \tag{2.39}$$

where $\widehat{\mathbf{e}}_1' = \cos\psi\widehat{\mathbf{e}}_1 + \sin\psi\widehat{\mathbf{e}}_2$ and $\widehat{\mathbf{e}}_2' = -\sin\psi\widehat{\mathbf{e}}_1 + \cos\psi\widehat{\mathbf{e}}_2$. From the Stokes parameters, it is then possible to construct two quantities having a definite value of spin:

$$(Q \pm iU)'(\hat{n}) = e^{\mp 2i\psi}(Q \pm iU)(\hat{n}) . \tag{2.40}$$

As for the temperature, also these quantities can be decomposed through spherical harmonics:

$$(Q + iU)'(\hat{n}) = \sum_{lm} a_{2,lm}\,_2Y_{lm}(\hat{n})$$

$$(Q - iU)'(\hat{n}) = \sum_{lm} a_{-2,lm}\,_{-2}Y_{lm}(\hat{n}) , \tag{2.41}$$

where the $_sY_{lm}(\theta,\phi)$ are the so called spin-s spherical harmonics. This sets of function satisfy the same completeness and orthogonality relations of the usual spherical harmonics.

The Q and U parameters are easily calculated in a coordinate system where the wavevector $\mathbf{k}$ is parallel to $\hat{z}$. The fact that the Stokes parameters are not invariant under rotations in a plane perpendicular to $\hat{n}$, complicate the calculation of the superposition of different modes. For each wavevector $\mathbf{k}$ and direction on the sky $\hat{n}$ one has to rotate the Q and U parameters from the $\mathbf{k}$ and $\hat{n}$ dependent basis into a fixed basis on the sky. This process is well defined only in the small scale limit. However, it is possible to use the spin raising and lowering operators $\eth$ and $\bar{\eth}$ on $Q \pm iU$ and from Eq. 2.41 one reaches

$$\bar{\eth}^2(Q + iU)(\hat{n}) = \sum_{lm}\left[\frac{(l+2)!}{(l-2)!}\right]^{1/2} a_{2,lm}Y_{lm}(\hat{n})$$

$$\bar{\eth}^2(Q - iU)(\hat{n}) = \sum_{lm}\left[\frac{(l+2)!}{(l-2)!}\right]^{1/2} a_{-2,lm}Y_{lm}(\hat{n}) \tag{2.42}$$

The expansion coefficients are then expressed by

$$a_{2,lm} = \int d\Omega \, _2Y^*_{lm}(\hat{n})(Q+iU)(\hat{n}) = \left[\frac{(l+2)!}{(l-2)!}\right]^{-1/2} \int d\Omega \, _2Y^*_{lm}(\hat{n})\bar{\eth}^2(Q+iU)(\hat{n})$$

$$a_{-2,lm} = \int d\Omega \, _2Y^*_{lm}(\hat{n})(Q-iU)(\hat{n}) = \left[\frac{(l+2)!}{(l-2)!}\right]^{-1/2} \int d\Omega \, _2Y^*_{lm}(\hat{n})\bar{\eth}^2(Q-iU)(\hat{n}) \ .$$

$$(2.43)$$

It is possible to introduce the linear combination of $a_{2,lm}$ and $a_{-2,lm}$

$$a_{E,lm} = -(a_{2,lm} + a_{-2,lm})/2$$

$$a_{B,lm} = i(a_{2,lm} + a_{-2,lm})/2 \ , \qquad (2.44)$$

that have a different behavior under parity transformation: while E remains unchanged B changes the sign, in analogy with electric and magnetic field. With these quantities, together with the temperature power spectrum, it is possible to characterize the statistics of the CMB perturbations with only four power spectra: those for T, E, and B and one for the cross correlation between T and E. These spectra are defined as rotationally invariant quantities

$$C_l^{TT} = \frac{1}{2l+1}\sum_m \langle a^*_{T,lm}a_{T,lm}\rangle$$

$$C_l^{EE} = \frac{1}{2l+1}\sum_m \langle a^*_{E,lm}a_{E,lm}\rangle$$

$$C_l^{BB} = \frac{1}{2l+1}\sum_m \langle a^*_{B,lm}a_{B,lm}\rangle$$

$$C_l^{TE} = \frac{1}{2l+1}\sum_m \langle a^*_{T,lm}a_{E,lm}\rangle \qquad (2.45)$$

and the following relations can be obtained

$$\langle a^*_{T,l'm'}a_{T,lm}\rangle = C_l^{TT}\delta_{l'l}\delta_{m'm}$$

$$\langle a^*_{E,l'm'}a_{E,lm}\rangle = C_l^{EE}\delta_{l'l}\delta_{m'm}$$

$$\langle a^*_{B,l'm'}a_{B,lm}\rangle = C_l^{BB}\delta_{l'l}\delta_{m'm}$$

$$\langle a^*_{T,l'm'}a_{E,lm}\rangle = C_l^{TE}\delta_{l'l}\delta_{m'm}$$

$$\langle a^*_{B,l'm'}a_{E,lm}\rangle = \langle a^*_{B,l'm'}a_{T,lm}\rangle = 0 \ . \qquad (2.46)$$

For real space calculation, it is worth introducing two scalar quantities:

$$\tilde{E}(\hat{n}) \equiv -\frac{1}{2}\left[\bar{\eth}^2(Q+iU) + \eth^2(Q-iU)\right] = \sum_{lm}\left[\frac{(l+2)!}{(l-2)!}\right]^{1/2}a_{E,lm}Y_{lm}(\hat{n})$$

$$\tilde{B}(\hat{n}) \equiv -\frac{1}{2}\left[\bar{\eth}^2(Q + iU) - \eth^2(Q - iU)\right] = \sum_{lm}\left[\frac{(l+2)!}{(l-2)!}\right]^{1/2} a_{B,lm}Y_{lm}(\hat{n}) . \quad (2.47)$$

These variables are rotationally invariant, but they are not the invariant version of Q and U, because $\eth^2$ and $\bar{\eth}^2$ are differential operators. Finally, in l space, the quantities defined in 2.47 are related by

$$a_{(\tilde{E},\tilde{B}),lm} = \left[\frac{(l+2)!}{(l-2)!}\right]^{1/2} a_{(E,B),lm} . \quad (2.48)$$
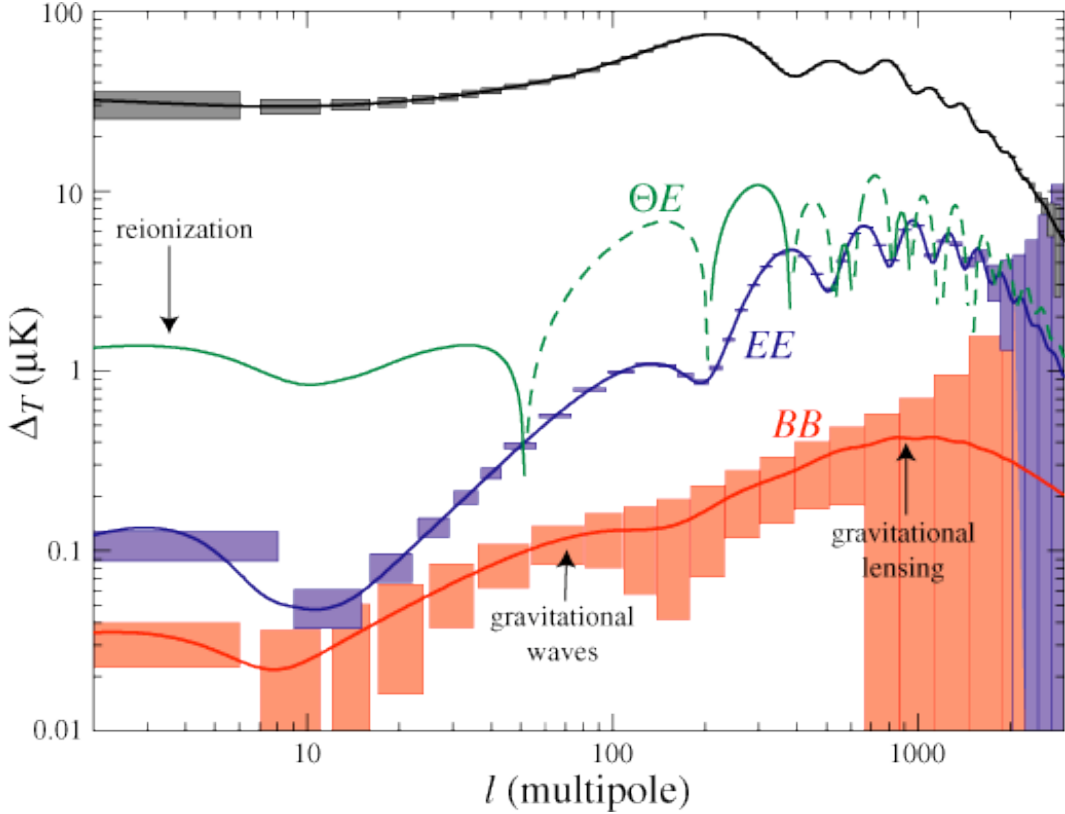
Figure 2.5: Temperature and polarization spectra. Figure from [2]

CMB polarization provides an important tool for reconstructing the model of the fluctuations from the observed power spectrum. Indeed polarization probes the epoch of last scattering directly unlike the temperature fluctuations, which may evolve between last scattering surface and the present. Further, different sources of temperature anisotropies (scalar, vector and tensor) give different patterns in the polarization, both in its intrinsic structure and in its correlation with the temperature fluctuations themselves. That is why different power spectra are attainable from CMB polarization measurements: discerning between scalar polarization modes E, and curl component mode B, we can construct a temperature-polarization

cross correlation spectrum TE and two different polarization power spectra, EE and BB (Fig.2.5).

Due to its generation mechanism, one interesting feature of polarization power spectrum is a low ℓ bump, appearing in the case of a Universe reionization at low redshifts (see Fig. 2.5). At this epoch the process coherence scale, the causal horizon, is at large angular scales in the sky.

2.5 Physical processes in the primordial plasma

For the following analysis, we consider true that: 1) the Universe has a FRW metric; 2) the CMB nature is the one predicted by the standard Hot Big Bang model; 3) in the primordial plasma the number of protons is equal to the number of electrons: $n_e = n_p$.

Let assume that the photon distribution function at equilibrium is a Planckian one:

$$\eta(v) = \frac{1}{e^{hv/k_B T} - 1}.$$ (2.49)

The differential number of photons is given by

$$dN_\gamma = 2\eta(\mathbf{r}, \mathbf{k}) \frac{d^3 r\, d^3 k}{(2\pi\hbar)^3},$$

where $\mathbf{k}$ is the moment of the particle. If the radiation field is isotropic and homogeneous, the photons differential density is given by

$$dn_\gamma(v) = 2\eta(v) \frac{d^3 k}{(2\pi\hbar)^3} = \frac{8\pi}{c^3} \eta(v) v^2 dv,$$

where $|\mathbf{k}| = hv/c$, and the evolution of the photons occupation number is described by

$$\frac{\partial \eta}{\partial t} = \frac{\partial \eta}{\partial t}\bigg)_c + \frac{\partial \eta}{\partial t}\bigg)_s,$$

where c and s stands for collisions and sources contribution respectively.

2.5.1 Compton Scattering

Compton scattering consists in the diffusion of photons by free electrons $(e^- + \gamma \rightarrow e^{-'} + \gamma')$ and so it permits the exchange of energy between electrons and radiation. Let consider a collision between an electron, with moment $\mathbf{q}$ and energy u (including the mass m_0 corresponding to the rest frame energy) and a photon with moment $\mathbf{k}$ and energy $\omega = hv$. From the energy-moment conservation law we have

$$\mathbf{q} + \mathbf{k} = \mathbf{q}' + \mathbf{k}' \quad , \quad u + \omega = u' + \omega',$$

where ′ indicates the particle features after the collision. Using the following substitutions $\mathbf{k} = \frac{\omega}{c}\hat{\mathbf{e}}$ and $\mathbf{k}' = \frac{\omega'}{c}\hat{\mathbf{e}}'$, one can obtain the quantity

$$\omega' - \omega = -\frac{\omega c \mathbf{q}(\hat{\mathbf{e}} - \hat{\mathbf{e}}') + \omega^2(1 - \hat{\mathbf{e}} \cdot \hat{\mathbf{e}}')}{\omega(1 - \hat{\mathbf{e}} \cdot \hat{\mathbf{e}}') - c\mathbf{q}\ \hat{\mathbf{e}}' + u}\ ,$$

where $\hat{\mathbf{e}}$ represents the photon direction. In relativistic regime (($h\nu, |\mathbf{q}|c \ll m_e c^2$), we have

$$\omega' - \omega \sim -\omega\left[\frac{\mathbf{q}}{m_e c}(\hat{\mathbf{e}} - \hat{\mathbf{e}}') + \frac{\omega}{m_e c^2}(1 - \hat{\mathbf{e}} \cdot \hat{\mathbf{e}}')\right].$$

In the rest of frame of the electron, the photon energy decrease is represented by the term in square brackets, while the first term is related to the change of frequency of the same photon due to Doppler effect (in the *laboratory* rest frame). If the electron velocities are randomly distributed, averaging on angles, in the limit where $T_e \gg T_r$, we obtain that, for a single diffusion, the energy variation rate of the photons is given by the mean variation of ω times the collisions number in the time unit, is given by

$$\frac{dN}{dt} = \sigma_T n_e c\left(1 - \frac{\mathbf{V}}{c}\hat{\mathbf{e}}\right), \tag{2.50}$$

where $\mathbf{V}$ is the electron velocity. Considering only Doppler effect it is possible to write

$$\left(\frac{d\omega}{dt}\right)_D \simeq \omega\frac{\mathbf{q}}{m_e c}(\hat{\mathbf{e}} - \hat{\mathbf{e}}')\frac{dN}{dt}\ . \tag{2.51}$$

Substituting in Eq. (2.51) the expression for dN/dt (Eq. 2.50) and averaging on electrons' momenta, we can obtain the time scale for considerable changements in the photons distribution function

$$\tau_C \simeq \frac{\omega}{\langle\frac{d\omega}{dt}\rangle} \simeq t_{\gamma e}\frac{mc^2}{k_B T_e} \simeq 4.5 \times 10^{28}\left(\frac{T_0}{2.7K}\right)^{-1}\phi^{-1}\widehat{\Omega}_b^{-1}(1+z)^{-4}\ \text{s} \tag{2.52}$$

where $t_{\gamma e} = 1/(n_e \sigma_T c)$ is the photon-electron collision time, $\phi = T_e/T_r$. The isotropic distribution of photons and electrons allow us to write newly the kinetic equation like

$$\left(\frac{\partial\eta}{\partial t}\right)_C = -2\int\frac{d^3q}{h^3}\int d\sigma_L v_{rel}\{f(u_k)\eta(\omega)[1+\eta(\omega')]-f(u_k+\omega-\omega')\eta(\omega')[1+\eta(\omega)]\}\ , \tag{2.53}$$

where $d\sigma_L$ is the differential cross section in the comoving rest frame, v_{rel} is the relative velocity between electron and photon in the moving direction of the photon, the factor 2 takes into account the possible spin state of the electron and the function $f(u_k)$ is the electrons distribution function (assumed to be

Maxwell like).

Expanding Eq. (2.53) to the second order in $(\omega' - \omega)/(k_B T_e)$, in the non-relativistc regime and substituting $d\sigma_L$ with the differential Thomson cross section, it is possible to obtain (Kompaneets, 1956) the Kompaneets equation

$$\left(\frac{\partial \eta}{\partial t}\right)_C\bigg|_{x_e=cost} = n_e \sigma_T c \frac{k_B T_e}{mc^2} \frac{1}{x_e^2} \frac{\partial}{\partial x_e}\left\{x_e^4\left[\frac{\partial \eta}{\partial x_e} + \eta(1+\eta)\right]\right\}, \qquad (2.54)$$

where $x_e = h\nu/k_B T_e$, $\sigma_T = (8\pi/3)(e^2/m_e c^2)^2 = 6.65 \times 10^{-25}\text{cm}^2$ is the Thomson cross section. Given that x_e is not an invariant, it is useful to redefine ?? in terms of the usual dimensionless frequency $x = h\nu/k_B T_r$, that is invariant thanks to T_r.

If we also define

$$y \equiv \int_{t_h}^t \frac{dt}{\tau_C} = \int_z^{z_h} a_c t_{exp} \frac{dz}{z} ,$$

where $a_c = \tau_C^{-1}$ e z_h suggests the redshift at which the energy injection happened (or started). In the case of $z = 0$ e $z_h = z$ Eq. (2.5.1) becomes

$$y = \int_0^z \frac{dz}{z} \frac{t_{exp}}{\tau_C} , \qquad (2.55)$$

and the Kompaneets equation can be write as

$$\frac{\partial \eta}{\partial y} = \frac{1}{x_e^2} \frac{\partial}{\partial x_e}\left\{x_e^4\left[\frac{\partial \eta}{\partial x_e} + \eta(1+\eta)\right]\right\}. \qquad (2.56)$$

The terms that appear in the eqution are:

$$\frac{1}{x_e} \frac{\partial}{\partial x_e}(x_e^4 \eta)$$

the contribution of ordinary scattering, more important in presence of high energy photons and with a low numeric density;

$$\frac{1}{x_e} \frac{\partial}{\partial x_e}(x_e^4 \eta^2)$$

describes the contribution of the induced scatterig, that dominates both at low frequencies, where $\eta \gg 1$, and in condition where the thermodynamic temperature is much higher than electrons temperature;

$$\frac{1}{x_e^2} \frac{\partial}{\partial x_e}\left(x_e^4 \frac{\partial \eta}{\partial x_e}\right)$$

describes the inverse Doppler effect and photons heating. It dominates if $T_e \gg T_\gamma$.

2.5.2 Bremsstrahlung

It is a process characterized by the acceleration of a charge passing through the Coulombian field of another charge: electrons dipped in the electrostatic field of ions produce photons by spontaeous emission; on the other hand, a radiation field stimulates an inducted emission as well, whose efficiency, at a given frequency, is given by multiplying by η.

Here, a classic treatment with quantum corrections will be provided.

If the process involves identical particles then there is no radiation emission in the dipole approximation, because the dipole moment $\sum e_i \mathbf{r}_i$ is proportional to the mass center $\sum m_i \mathbf{r}_i$, that is constant. So let's consider an electron moving in a fixed field of an ion and we assume that the electron is moving at such a velocity that we can neglect the direction deviations during the whole process.

The electron is in tight interaction with the ion for a characteristic time given by the collision time $\tau_{coll} = b/v$, where b is the impact parameter. Let's consider the electron velocity variation

$$\Delta v = \frac{Ze^2}{m_e} \int_{-\infty}^{\infty} \frac{b\,\mathrm{d}t}{(b^2 + v^2t^2)^{3/2}} = \frac{2Ze^2}{mbv} \,, \tag{2.57}$$

where Z is the atomic number of the specie considered. From eq. 2.57 it is possible to recover the emission for a single collision in the limit of small angles

$$\frac{\mathrm{d}W(b)}{\mathrm{d}\omega} = \begin{cases} \frac{8z^2e^6}{3\pi c^3 m_e^2 v^2 b^2} \,, & b \ll v/\omega \\ 0 \,, & b \gg v/\omega \end{cases} .$$

From this it is possible to recover the entire spectrum for a medium with more ions and electrons, at a given electron velocity. The emission per time unit, volume unit, frequency unit, and valid for every regime and corrected with the Gaunt factor is

$$\frac{\mathrm{d}W}{\mathrm{d}\omega \mathrm{d}V \mathrm{d}t} = \frac{16\,\pi e^6}{3\sqrt{3}c^3 m_e^3 v} n_e\, n_i\, Z^2 g_{ff}(v,\omega) \,,$$

where $g_{ff}(v,\omega) = \frac{\sqrt{3}}{\pi} \ln\left(\frac{b_{max}}{b_{min}}\right)$ while n_e and n_i are the electrons and ions density respectively.

For thermal bremsstrahlung it is possible to obtain the expression for total emission per volume unit, per time unit

$$\frac{\mathrm{d}W}{\mathrm{d}t \mathrm{d}V} = \left(\frac{2\pi k_B T_e}{3m_e}\right)^{1/2} \frac{2^5 \pi e^6}{3 h m_e c^3} Z^2 n_e\, n_i g_{ff}(v, T_e) \,,$$

where the Gaunt factor is averaged on velocities. For absorption the relation is

$$\frac{dW}{dtdVd\nu} = 4\pi j_\nu^{ff},$$

where $j_\nu^{ff} = \alpha_\nu^{ff} B_\nu(T)$ (Birchhoff's law). The free-free absorption coefficient is

$$\alpha_\nu^{ff} = \frac{4e^6}{3mhc}\left(\frac{2\pi}{3k_B m_e}\right)^{1/2} T^{-1/2} Z^2 n_e\, n_i\, \nu^{-3}(1 - e^{-h\nu/k_B T})g_{ff}(\nu, T_e).$$

For non-relativistic Maxwellian electrons, the bremsstrahlung contribution for a variation of the photons distribution function, is given by

$$\left.\frac{\partial\eta}{\partial t}\right)_{ff} = K_0 g_{ff}(\nu, T_e)\frac{e^{-x_e}}{x_e^3}[1 + \eta(1 - e^{x_e})],$$

with

$$K_0 = \frac{8\pi}{3}\frac{e^6 h^2 n_e(n_H + 4n_{He})}{m_e(6\pi m_e k_B T_e)^{1/2}(k_B T_e)^3} \simeq \tag{2.58}$$

$$\simeq 2.1 \times 10^{-25}\phi^{-7/2}\left(\frac{T_0}{2.7\,K}\right)^{-7/2}(1 + z)^{5/2}\Omega_b^2 h^4\ \mathrm{s}^{-1},$$

where n_H and n_{He} are the hydrogen and helium density respectively. For the Gaunt factor the following approximations are considered

$$g_{ff}(\nu, T_e) = g_{ff}(x_e) = \begin{cases} \frac{\sqrt{3}}{\pi}\ln\left(\frac{2.25}{x_e}\right), & x_e \ll 1 \\ \left(\frac{3}{nx}\right)^{1/2}, & x_e \gg 1. \end{cases}$$

Now let's put

$$K_{ff} = \alpha_\nu^{ff} c = K_0 g(x_e)x_e^{-3}(1 - e^{-x_e}), \tag{2.59}$$

and let define the optical depth like

$$\tau_{ff} = \int_t^{t_{ric}} K_{ff}dt' = \int_{z_{ric}}^z K_{ff}(x_e, z)\frac{t_{exp}}{1 + z'}d(1 + z') \simeq \tag{2.60}$$

$$\simeq 3.3 \times 10^{-5}\phi^{-7/2}\left(\frac{T_0}{2.7^\circ K}\right)^{-11/2} h^4\Omega_b^2 \cdot \frac{1}{K}g(x_e)x_e^{-3}(1 - e^{-x_e})$$

$$[\quad (k_B z + z_{eq})^{1/2} - (k_B z_{ric} + z_{eq})^{1/2}], $$

$$\tag{2.61}$$

where K represents the neutrinos contribution to the universe evolution ($K = 1.68$ for 3-species massless neutrinos). It is interesting to find x_{eB} when $\tau_{ff} = 1$, that roughly corresponds to the maximum frequency at which bremsstrahlung process can thermalize a spectrum distorted at redshift z. In the limit for $x_{eB} \ll 1$

$$x_{eB} = 5.7 \times 10^{-3}\phi^{-7/4}\left(\frac{T_o}{2.7\,K}\right)^{-11/4}\widehat{\Omega}_b\frac{1}{K^{1/2}}.$$

$$\cdot g_{ff}^{1/2}(x_{eB})[(k_B z + z_{eq})^{1/2} - (k_B z_{ric} + z_{eq})]^{1/2} \, ,$$

from which we can obtain values for $z \gg z_{eq}$ regime

$$x_{eB} = 5.7 \times 10^{-3} \phi^{-7/4} \left(\frac{T_0}{2.7\,K} \right)^{-11/4} \widehat{\Omega}_b \cdot g^{1/2}(x_{eB}) z^{1/4}$$

and for $z \ll z_{eq}$ regime

$$x_{eB} = 4.1 \times 10^{-4} \phi^{-7/4} \left(\frac{T_0}{2.7\,K} \right)^{-15/4} \Omega_b \, h^{3/2} \, \Omega_{tot}^{-1/4} \, g_{ff}^{1/2}(x_{eB})(z - z_{ric})^{1/2}$$

from which can be stated that bremsstralung is efficient in thermalizing distorted spectra only at low frequencies.

2.5.3 Radiative Compton

Photons production by radiative Compton rises up quickly increasing the redshift. In fact, its emission dominates the bremsstrahlung emission for $z \gtrsim 10^5 \div 10^6$ [36], [85].

Consider an ionized plasma in non-relativistc regime, the time scale for photons emission and the time scale for reaching a Planckian distribution will grow like the inverse of the square of the electrons number density. In this case, the radiative scattering, $e^- + \gamma \rightarrow e^- + \gamma + \gamma$, will dominate on free-free emission. One of the main features of this process is that electron density rise up almost sponentially in time, until equilibrium is reached.

In the following treatment, we will assume that electrons have such a temperature that $kT \ll mc^2$.

So, consider the process $\nu' + e^- \leftrightarrows \nu_1 + \nu_2 + e^-$ in the rest of frame of the electron. If $h\nu' < mc^2$ then the total cross section, in the direct process, is strongly dominated by the contribution of one of the outgoing photons, if, for example, ν_2 is produced at low energies: $\nu_2 \ll \nu_1$ [118]. In this limit, integrating on the solid angle of ν_2 we obtain

$$\frac{d\sigma_{DC}}{d\nu_2} = \frac{4\alpha}{3\pi} \left(\frac{h\nu'}{mc^2} \right)^2 (1 - \cos\theta_1) \frac{1}{\nu_2} d\sigma_e \, ,$$

where $d\sigma_e$ is the differential Compton cross section and θ_1 is the angle between the directions of ν' and ν_1. Computing at the lowest order $d\sigma_e$, ignoring the change of frequency $\Delta\nu_1/\nu_1 \sim h\nu_1/mc^2 \ll 1$ and integrating on the solid angle Ω_1 (the solid angle corresponding to ν_1) we have

$$\frac{d\sigma_{DC}}{d\nu_1 d\nu_2} = \frac{4\alpha}{3\pi} \sigma_T \left(\frac{h\nu'}{mc^2} \right) \frac{1}{\nu_2} \delta(\nu_1 - \nu'), \tag{2.62}$$

where $\sigma_T = (8\pi/3)r_0^2$ is the Thomson cross section.

We can recover an equation for the evolution of the photons occupation number, $\eta(\nu)$. The number density fo the photons in the gap between ν and $\nu + d\nu$ is $\frac{dN}{dV}d\nu = 8\pi\eta(\nu)\frac{\nu^2}{c^3}d\nu$.

The total spontaneous production rate of photons per volume unit in the frequency range between ν_2 and $\nu_2 + d\nu_2$ is given by

$$8\pi\frac{\nu_2^2}{c^3}d\nu_2\frac{\partial\eta(\nu_2)}{\partial t} = \iint n_e\frac{d\sigma_{DC}}{d\nu_1 d\nu_2}cd\nu_1 d\nu_2\left(8\pi\eta(\nu')\frac{\nu'^2}{c^3}d\nu'\right)$$

where n_e is the number electron density. If we add the stimulated emission to this expression, then we have

$$\left.\frac{\partial\eta(\nu_2)}{\partial t}\right|_{spont+stim} = n_e c\iint\frac{d\sigma_{DC}}{d\nu_1 d\nu_2}d\nu_1 d\nu'\left(\frac{\nu'}{\nu_2}\right)^2\left[1+\eta(\nu_1)\right]\left[1+\eta(\nu_2)\right]\eta(\nu'). \quad (2.63)$$

The absorption process must be proportional to $\eta(\nu_1)\eta(\nu_2)[1 + \eta(\nu')]$ and it must delete the contribution of eq. 2.63 when all the photons reach a Planckian distribution, $\eta(\nu) = \left(e^{h\nu/k_B T} - 1\right)^{-1}$. If we consider that the frequency shift of the photons, due to the continuous scattering, dominates the corrections of the total equation for $\partial\eta/\partial t$ and substituting eq. 2.62 in eq. 2.63, we obtain the well known expression for the radiative Compton contribution to the evolution of the photons occupation number [85]:

$$\left.\frac{\partial\eta}{\partial t}\right)_{DC} = K_{DC}\frac{g_{DC}}{x_e^3}\left[1 - \eta\left(e^{x_e} - 1\right)\right],$$

where

$$K_{DC}(z) = \frac{4\alpha}{3\pi t_{\gamma e}}\left(\frac{k_B T_e}{mc^2}\right)^2 I(t), \quad (2.64)$$

$\alpha = e^2/\hbar c$ is the fine structure constant, T_e is the electrons temperature, $t_{\gamma e} = (n\sigma_T c)^{-1}$ is the collision time photon-electron, x is the dimensionless frequency and

$$I(t) = \int_0^\infty x_e^4(1 + \eta)\eta dx_e.$$

The Gaunt factor is given by [60]

$$g_{DC}(x_e) = \frac{\int_{2x_e}^\infty x_e'^4[1 + \eta(x_e' - x_e)]\eta(x_e')[wF(w)/2]dx_e'}{\int_0^\infty (1 + \eta)\eta x_e'^4 dx_e'}, \quad (2.65)$$

where w represents the ratio between the frequency of the new produced photon and the frequency of the old one. A good approximation for the Gaunt factor, in the case of a Bose-Einstein like spectrum, is given by [18]:

$$g_{DC}(x_e) \simeq \exp(-x_e/2).$$

2.6   The Spectrum of the CMB

The CMB spectrum emerges from the thermalization redshift, $z_{therm} \sim 10^6 - 10^7$, with a shape very close to a Planckian one, owing to the tight coupling between radiation and matter through Compton scattering and photon production/absorption processes, radiative Compton and bremsstrahlung. These processes were extremely efficient at early times and able to re-establish a blackbody (BB) spectrum from a perturbed one on timescales much shorter than the expansion time (see, e.g., [35]). Fig 2.6 show the spectrum of the CMB radiation recovered through different type of measurements. The resulting shape follows a Planckian one in any measured band. The value of z_{therm} [18] depends on the baryon density parameter, Ω_b, and the Hubble constant, H_0, through the product $\widehat{\Omega}_b = \Omega_b(H_0/50)^2$ (H_0 expressed in Km/s/Mpc). On the other hand, physical processes occurring at redshifts $z < z_{therm}$ may lead imprints on the CMB spectrum. Therefore, the CMB spectrum carries crucial informations on physical processes occurring during early cosmic epochs (see, e.g., [33] and references therein) and the comparison between models of CMB spectral distortions and CMB absolute temperature measures can constrain the physical parameters of the considered dissipation processes.

The timescale for the achievement of kinetic equilibrium between radiation and matter (i.e. the relaxation time for the photon spectrum), t_C, is

$$t_C = t_{\gamma e} \frac{m_e c^2}{k T_e} \simeq 4.5 \times 10^{28} \, (T_0/2.7\,K)^{-1} \, \phi^{-1} \widehat{\Omega}_b^{-1} \, (1+z)^{-4} \, \sec , \qquad (2.66)$$

where $t_{\gamma e} = 1/(n_e \sigma_T c)$ is the photon–electron collision time, $\phi = (T_e/T_r)$, T_e and $T_r = T_0(1+z)$ being respectively the electron and the CMB radiation temperature; $k T_e/m_e c^2$ (being m_e the electron mass) is the mean fractional change of photon energy in a scattering of cool photons off hot electrons, i.e. $T_e \gg T_r$; T_0 is the present radiation temperature related to the present radiation energy density by $\epsilon_{r0} = a T_0^4$ (here $a = 8\pi I_3 k^4/(hc)^3$, $I_3 = \pi^4/15$); a primordial helium abundance of 25% by mass is here assumed. It is useful to introduce the dimensionless time variable $y_e(z)$ defined by

$$y_e(z) = \int_t^{t_0} \frac{dt}{t_C} = \int_1^{1+z} \frac{d(1+z)}{1+z} \frac{t_{exp}}{t_C} , \qquad (2.67)$$

where t_0 is the present time and $t_{exp} = 1/H = 1/[(da/dt)/a]$ is the expansion time, $a = 1/(1+z)$ is the cosmic scale factor normalized to the present time.
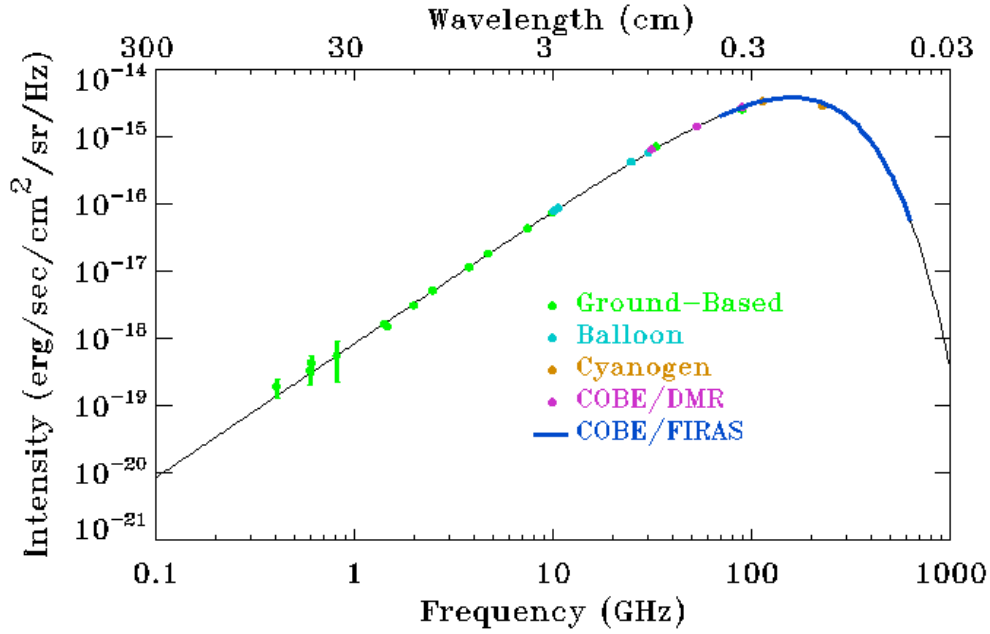
Figure 2.6: This plot shows measurements of the intensity of the cosmic microwave background as a function of observing frequency (or wavelength). The CMB follows the expected blackbody curve over more than 5 orders of magnitude in intensity. Figure from [1]

As particular cases, by neglecting the cosmological constant (or dark energy) contribution we have

$$t_{exp} \simeq 6.3{\times}10^{19} \left(\frac{T_0}{2.7\,K}\right)^{-2} (1+z)^{-3/2} \left[\kappa(1+z) + (1+z_{eq}) - \left(\frac{\Omega_m-1}{\Omega_m}\right)\left(\frac{1+z_{eq}}{1+z}\right)\right]^{-1/2} \text{sec}\,,$$
(2.68)

where $z_{eq} = 1.0 \times 10^4 (T_0/2.7\,K)^{-4}\widehat{\Omega}_m$ is the redshift of equal non relativistic matter and photon energy densities and $\kappa = 1 + N_v(7/8)(4/11)^{4/3}$, N_v being the number of relativistic, 2–component, neutrino species (for 3 species of massless neutrinos, $\kappa \simeq 1.68$), takes into account the contribution of relativistic neutrinos to the dynamics of the universe[3], while assuming $\Omega_K = 0$, $\Omega_\Lambda = 1 - \Omega_m$, and neglecting the radiation energy density, as possible at relatively low redshifts, we have

$$t_{exp} \simeq (1/H_0)\left[\Omega_m(1+z)^3 + 1 - \Omega_m\right]^{-1/2} \text{sec}\,, \qquad (2.69)$$

---

[3]Strictly speaking the present ratio of neutrino to photon energy densities, and hence the value of κ, is itself a function of the amount of energy dissipated. The effect, however, is never very important and is negligible for very small distortions.

where $1/H_0 \simeq 3.1 \times 10^{17} h^{-1}$ sec ($h = H_0/100$).

The time evolution, $\partial \eta / \partial t$, of the photon occupation number, $\eta(\nu, t)$, under the combined effect of Compton scattering (resulting into a second order, linear partial differential equation of parabolic type) and of photon production processes, namely radiative Compton (RC) [60], bremsstrahlung (B) [122], [71] plus other possible contributions (EM), is well described by the complete Kompaneets equation [80], [17]:

$$\frac{\partial \eta}{\partial t} = \frac{1}{\phi} \frac{1}{t_C} \frac{1}{x^2} \frac{\partial}{\partial x} \left[x^4 \left[\phi \frac{\partial \eta}{\partial x} + \eta(1 + \eta) \right] \right] + \left[\frac{\partial \eta}{\partial t} \right]_{RC} + \left[\frac{\partial \eta}{\partial t} \right]_B + \left[\frac{\partial \eta}{\partial t} \right]_{EM} . \quad (2.70)$$

This equation is coupled to the time differential equation governing the electron temperature evolution for an arbitrary radiation spectrum in the presence of Compton scattering, energy losses due to radiative Compton and bremsstrahlung, adiabatic cooling, plus possible external heating sources, $q = a^{-3}(dQ/dt)$,

$$\frac{dT_e}{dt} = \frac{T_{eq,C} - T_e}{(27/28)t_{e\gamma}} - \frac{2T_e}{t_{exp}} + \left[\frac{dT_e}{dt} \right]_{RC,B} + \frac{(32/27)q}{3n_e k} ; \quad (2.71)$$

here $T_{eq,C} = [h \int \eta(1 + \eta)\nu^4 d\nu]/[4k \int \eta \nu^3 d\nu]$ is the Compton equilibrium electron temperature [108], [152], $t_{e\gamma} = 3m_e c/4\sigma_T \epsilon_r$, $\epsilon_r \simeq \epsilon_{r0}(1 + z)^4$ being the radiation energy density, and x is the dimensionless frequency $x = h\nu/kT_0$ (ν being the present frequency).

2.7 Spectral Distortions

In the primordial plasma, the main processes that contributed to form the presently observed spectrum are: Compton scattering ($e^- + \gamma \rightarrow e^- + \gamma$), Bremsstrahlung (absorption or emission of photons in presence of charges, $e^- + p \rightarrow e^- + p + \gamma$) and radiative Compton ($e^- + \gamma \rightarrow e^- + 2\gamma$). These processes are able to thermalize a spectrum distortion, caused by an energy injection arbitrarily big, at the condition that this occurred before a certain period. We can refer to this epoch by z_{therm}. After z_{therm} these processes are not effective enough to ensure a thermodynamic equilibrium. Anyway, if an energy exchange occurs in epochs not too far from z_{therm}, the matter-radiation interaction processes are able enough to establish a kinetic equilibrium. We can indicate with z_{BE} the epoch until this is true. So, after an energy injection, at epochs such to have $z_{therm} < z \lesssim z_{BE}$, there will be a photons redistribution pointing to a Bose-Einstein (BE) like spectrum with $\mu \neq 0$

(every distortion occurred between z_{therm} and z_{BE} must be drive the photons distribution function from a Planckian shape to a BE one). It is possible to show that for an energy injection $\Delta\epsilon$ we find $\mu \approx 1.4\Delta\epsilon/\epsilon_i$, where ϵ_i is the energy density just before the heating and $\Delta\epsilon$ is the variation.

After z_{BE}, even if the interactions are not effective enough to maintain a Bose-Einstein spectrum, if an energy injection occurs and this is able to increase the electrons temperature to very high value ($T_e \gg T_\gamma$), the same interactions can increase the photons temperature through the comptonization process. In this case, a typical distortion of the CMB spectrum will appear: the comptonized spectrum well describes by Sunyaev and Zel'dovich [138] characterized by $y \simeq (1/4)(\Delta\epsilon/\epsilon_i)$.

After recombination, free-free interaction can play a fundamental role in the spectrum evolution, given that it is a process producing low energy photons and so it has the capacity to distort the spectrum itself.

Fig. 2.7 shows typical shapes of CMB spectral distortions with respect to the Planckian distribution observed, the flat line at $T = 2.725$ K.
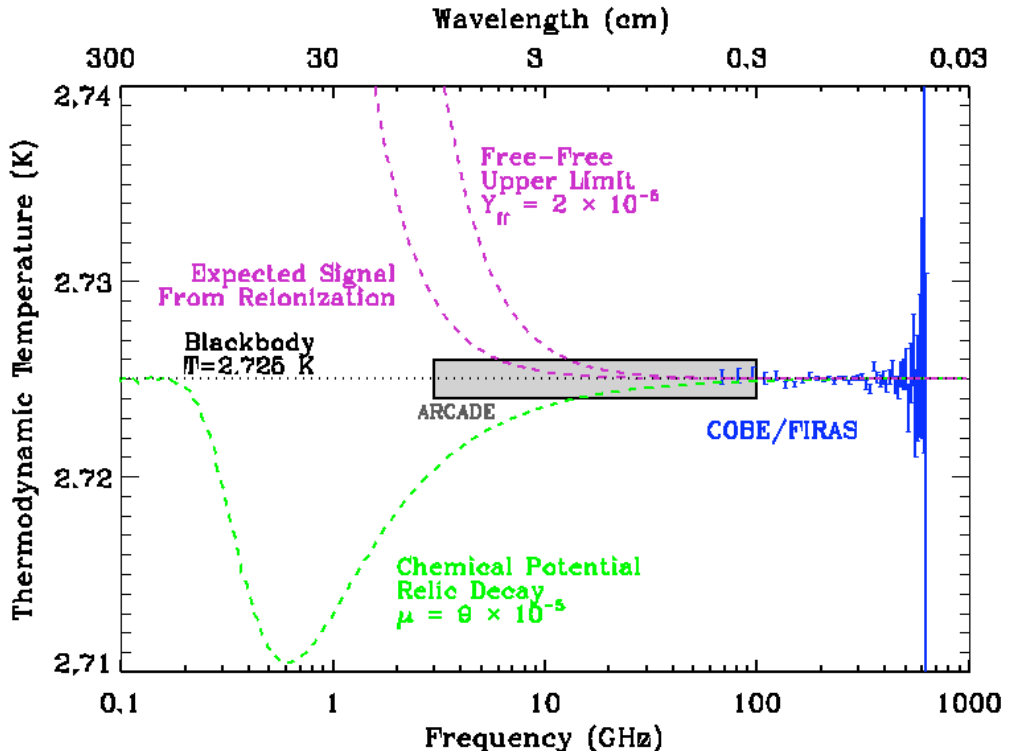

Figure 2.7: Typical spectral distortions that could occur at various cosmic epochs. In particular typical shapes of free-free, chemical potential related and reionization related distortions are showed. Arcade first flight coverage and COBE/FIRAS measurements are also shown. Figure from [1]

When a population of particles, i, is in thermal equilibrium, the corresponding moments distribution function is given by quantum statistics that depend on the baryonic or fermionic nature of the examined species. The distribution takes this form

$$n_i(q)dq = \frac{4\pi h^{-3} g_i q^2 dq}{e^{E(q) - \frac{\mu}{k_B T}} \pm 1} \tag{2.72}$$

that provides the number of particles, per volume unit, having a moment between q and $q + dq$ (here it is $E(q) = (m^2 c^4 + q^2 c^2)^{1/2}$ with $m = 0$ for photons). The sign discriminate between a Fermi-Dirac statistic (sign +) for fermions and a Bose-Einstein one (sign −) for bosons; the factor g_i provides the number of the possible spin states for each species.

Let consider now photons and let look at the occupation number as a function of frequency ν. For matter and radiation in thermodynamic equilibrium $\mu = 0$. The mean number of photons of frequency ν, or the occupation number η_ν, is described by

$$\eta_\nu = \frac{1}{e^{(h\nu/kT) + \mu} - 1} \tag{2.73}$$

that is the standard expression for a Bose-Einstein statistic (please note the difference between the notation in eq. 2.72 and eq. 2.73: in the latter it was introduced the dimensionless potential, that here after will be used). When $\mu = 0$ the spectrum is a planckian one.

It is possible to associate to the radiation field his brightness $I_\nu = (2h\nu^3/c^2)\eta_\gamma$. There are two well known regimes: the high frequencies limit ($h\nu \gg k_B T$), described by the Wien law

$$I_\nu^W = \frac{2h\nu^3}{c^2} e^{-\frac{h\nu}{k_B T}}$$

and the low frequencies limit ($h\nu \ll k_B T$), described by the Rayleigh-Jeans (RJ) law

$$I_\nu^{RJ} = \frac{2\nu^2 k_B T}{c^2}.$$

From the formula that defines the Planckian spectrum it is possible to recover a quantity that can characterize the radiation intensity, the thermodynamic temperature

$$T_{thd} = \frac{h\nu}{k_B \ln\left(1 + \frac{2h\nu^3}{c^2 I_\nu}\right)}.$$

Thanks to this formula, it is possible to analyze the photons distribution in terms of little shifts from a given temperature, related to the intensity

deviation by

$$\Delta T_{thd} \equiv T_{thd} - T_r = \frac{(e^x - 1)^2}{x^2 e^x} \frac{c^2 \Delta I_\nu}{k2\nu^2} ,$$

with $x = h\nu/k_B T$.   Another interesting relation is that between the thermodynamic temperature and the antenna temperature, defined as the temperature of a source in the RJ regime that irradiates the same power, with a value defined by

$$T_{antenna} = \frac{Tx}{e^x - 1} \approx T\left(1 - \frac{x}{2} + \frac{x^2}{12}\right) \tag{2.74}$$

(plus higher order terms).

2.8   The complete Kompaneets equation and evolution of the electrons temperature

Considering all the reviewed processes, we can now write the equation for the photons distribution function like

$$\frac{\partial \eta}{\partial t} = \frac{\partial \eta}{\partial t}\bigg)_C + \frac{\partial \eta}{\partial t}\bigg)_{ff} + \frac{\partial \eta}{\partial t}\bigg)_{DC} . \tag{2.75}$$

It is possible to add a further term: $(\partial \eta/\partial t)_s$, that takes into account the photons emission that can joins to the energy release (like in the case of radiative particle decays).

The variations of T_e are related with the interactions of the primordial plasma.   During epochs in which it is possible to neglect emissions or dissipations of energy caused by the matter in the radiation field, electrons reach the equilibrium temperature in a time scale much shorter than the expansion time. This equation describes its evolution

$$\frac{dT_e}{dt} = \frac{T_{eq,C} - T_e}{t_{e\gamma}} + \frac{q}{3n_e K} - \frac{2T_e}{t_{e\gamma}} - \frac{8\pi(k_B T_e)^4}{3n_e k_B h^3 c^3} . \tag{2.76}$$

$$\cdot \left\{ K_0 \int_0^\infty g(x_e)e^{-x_e}[1 + \eta(1 - e^{x_e})]dx_e + C(t) \int_{x_{e.min}}^{x_{e,max}} [1 + \eta(1 - e^{x_e})]dx_e \right\},$$

where $T_{eq,C}$, in a radiation field isotropic and not polarized, with an arbitrary spectrum, is given by

$$T_{eq,C} = \frac{h}{4k} \frac{\int_0^\infty \nu^4 \eta(1 + \eta)d\nu}{\int_0^\infty \nu^3 \eta d\nu} .$$

The quantity q in Eq.   (2.76) represents the energy disssipation rate for electron heating due to an external source and it depends on the specific

process considered.[4]

The terms in braces in eq. 2.76 describes the variation of T_e caused by double Compton and bremsstrahlung: if the spontaneous and stimulated emission dominates on absorption there will be electrons cooling and vice versa. The third term represents the temperature variation in the pure adiabatic expansion, showing that in absence of interations T_e will cool down as R^{-2}. Furthermore, from the same equation it is possible to recover the time scale t_{ff} and t_{DC}, resulting to be greater than $t_{e\gamma}$, so is quite safe to assume $T_e = T_{eq,C}$ (only if $q = 0$).

In many case of interest, the CMB spectrum (immediately after the energy injection, for processes occurred at $y_h \ll 1$) can be described by a superposition of black bodies, so the electrons temperature at equilibrium will be given by

$$\phi_{eq} \simeq 1 + 5.4\, y^*\,,$$

where the comptonization parameter is y^*. This quantity can be related to the exchanged energy amount through this formula

$$y^* \simeq (1/4)\Delta\epsilon/\epsilon_i\,, \tag{2.77}$$

where ϵ_i indicates the radiation field energy before the energy exchange.

Until it is possible to neglect injection and exchange of energy between matter and radiation, the evolution of the electrons temperature depends only on the epoch at which the injection occurs. For injection occurred at epochs such to have $y_h \ll 1$, the Compton scattering is no longer effective to modify the perturbed spectrum, so, just before the decoupling, the electrons temperature is similar to ϕ_{eq}. Instead, if the injection occurred at epochs corresponding to $y_h \gtrsim 5$, the Compton scattering could re-establish the kinetic equilibrium corresponding to a Bose-Einstein spectrum, while the final value for the electrons temperature is given by

$$\phi_f(y_h \gtrsim 5) = \phi_{BE} \simeq (1 - 1.11\mu_0)^{-1/4}\,,$$

where $\mu_0 \ll 1$. The evolution of $\mu(z)$ and the relation between itself and the value of the injected fractionary energy $\Delta\epsilon/\epsilon_i$ depend on the epoch of the

---

[4]It is possible to use a numerical application in order to describe the behaviour of q. If we consider a Gaussian behaviour, then for q it's valid the following [18]:

$$\tilde{q} = q\left|\frac{dt}{dz}\right| = \frac{\Delta\epsilon}{\sigma_\omega(2\pi)^{1/2}(1+z)}\exp\left[-\frac{1}{2}\left(\frac{\omega - \bar{\omega}}{\sigma_\omega}\right)^2\right],$$

where $\omega = \ln(1+z)$ and σ_ω is chosen to be so little to determine a characteristic time variations for T_e much shorter than t_{exp} (defined from eq. **??**). In this way, it is possible to neglect the adiabatic cooling and so to have a good approximation for T_e.

injection, z_h. If $y_h \lesssim 5$ the value of ϕ_f is about in the middle between ϕ_{BE} and ϕ_{eq}, because Compton scattering tends to produce a Bose-Eintesin like spectrum. In this case, the following is valid [35] $\mu_0 \simeq 1.4\,\Delta\epsilon/\epsilon_i$, while for ϕ_f a good fit of the numerical results is given by

$$\phi_f(y_h) = \frac{k}{5}\frac{5 - y_h}{k - y_h}(\phi_{eq} - \phi_{BE}) + \phi_{BE}\,,$$

where $k = 0.146$. This result does not depend on $\widehat{\Omega}_b$ directly, according to the fact that the electrons temperature is essentially controlled by Compton scattering. The last equation permits to compute the evolution of ϕ and in Chap. 3 it will be used to test the numerical evaluation of the same quantity.

2.9   Recombination

During the so-called *recombination* era, the cooling down of the Universe allowed the nuclei and electrons contained in it to form neutral atoms [105]. This era is important for more than one reason: recombination sets up the initial conditions for the chemistry of the early Universe, for example. Anyway, here we are interested to CMB science and the recombination era plays a fundamental role in CMB chronicles.
According to the standard cosmological model, the physical environment during this epoch is not complicate at all thanks to the isotropy and homogenousity of the universe in those ages. However, the precision calculation we make about this era arise from the fact that during recombination CMB photons were last scattered (from here the name of Last Scattering Surface). Contributions to the relation between cosmological parameters and CMB temperature APS come also from detailed calculations and an accurate knowledge of the processes at work during recombination. Another interesting aspect is related to the CMB polarization: this did arise when the Universe was sufficiently transparent to permit quadrupole anisotropy but yet sufficiently opaque to scatter photons and to convert temperature anisotropies into polarization. Indeed, the CMB polarization is more sensitive to the mechanism involved in recombination.
The recombination process is all but istantaneous: in the period between $8000 \gtrsim z \gtrsim 5000$ the transition from He III→He II takes place; between $3500 \gtrsim z \gtrsim 1600$ the recombination for He II→He I; between $2000 \gtrsim z \gtrsim 500$ takes place the hydrogen recombination [137]. The main limitations for understanding and reproducing the ionization history and the cosmological

recombination spectrum lies in our knowledge of the atomic processes and the associated transition rates.

A simple treatment of this era could be based equilibrium thermodynamics. This implies that the rates of the reactions involved have a scale time shorter than the expansion time, $t_{reactions} \ll H^{-1}$. However, the equilibrium assumption is approximative, even if it provides some details on some basic questions. Given that, in thermodynamic equilibrium, the abundances of the elements involved in this process are recovered by standard equilibrium arguments, the ratio between one exited state and another for a single species is given by the Saha formula:

$$\frac{n_q n_e}{n_q - 1} = \frac{2g_q (2M_e T)^{3/2}}{g_{q-1}(2\pi)^3} e^{-\chi_q/T} , \qquad (2.78)$$

where g_q are statistical weight related to the state degeneracy, χ_q the ionization energy, n_i the abundance of the specie i, M_e the electron mass and T is the temperature. Considering only the predominant elements in the primordial Universe, H and He, the relative amounts of them are generally specified by the primordial helium mass fraction Y_P, that derives from nucleosynthesis calculations:

$$Y_P = \frac{n_{He} m_{He}}{n_{He} m_{He} + n_H m_H} = \frac{f_{He}}{f_{He} + m_H/m_{He}} , \qquad (2.79)$$

where $f_{He} = n_{He}/n_H$. Let rewrite the Saha equation for hydrogen. In this case, $g_H = 2, g_{H^+} = 1$ and $\chi_{HI} = 13.59844$ eV and the formula can be written as

$$\frac{x_e x_p}{x_{HI}} = \frac{(2M_e T)^{3/2}}{n_H (2\pi)^3} e^{-\chi_{HI}/T} , \qquad (2.80)$$

where x_i are the ionization fraction normalized to the density of neutral hydrogen.

One can note that at very high temperature ($T \gg \chi$) the exponential term becomes unity the equilibrium shifts to favor more ionized states (this is true in the regime of non-degenerate densities). Instead, at low temperature the exponential strongly favors the lower ionization state, the neutral state in this case.

From Eq. 2.80 it is possible to derive the redshift at which recombines. Substituting T with $T_0(1 + z)$ and the number density $n_H = n_{H0}(1 + z)^3$ we reach the form:

$$1 + z = \frac{\chi_{HI}}{T_0} \left[\ln \frac{(2M_e T)^{3/2}}{n_{H0}(2\pi)^3} - \frac{3}{2}\ln(1 + z) + \ln \frac{x_{HI}}{x_e x_p} \right]^{-1} . \qquad (2.81)$$

Substituting $T_0 = 2.725$ K and using the relation $n_{H0} = \rho_c \Omega_b (1 - Y_P)/m_H$ the previous equation could be written as:

$$1 + z = 57940 \left[40.33 - \ln \left(\frac{\Omega_b h^2 (1 - Y_P)}{0.0167} \right) - \frac{3}{2} \ln \left(\frac{1 + z}{1000} \right) + \ln \frac{x_{HI}}{x_e x_p} \right]^{-1} . \quad (2.82)$$

In the previous $h = H_0/(100\text{Km/s/Mps})$ is the reduced Hubble constant. Again, this is a valid treatment if the rates of recombination and ionization have a scale time much shorter than the Hubble time.

Detailed calculations showed that, taking into account precise transition rates related to the recombination process, both in the Wien and the Rayleigh-Jeans regions of the CMB blackbody spectrum distortions could grow. Unfortunately, for regions near the Lyman-α line, even if the relative distortion exceed unity by several orders of magnitude, the cosmic infra-red background due to sub-millimeter, dusty galaxies makes a direct measure of this feature impossible.

2.10 Reionization

An early reionization of the Universe is indicated by the recent WMAP polarization measurements. With the three-year data on CMB temperature and its polarization power spectra,WMAP produced a more accurate determination of the electron scattering optical depth, downwarding its value from $\tau = 0.17 \pm 0.08$ [134] obtained with the first-year data to $\tau = 0.09 \pm 0.03$ [104] consistent with an abrupt reionization at redshift $z_{re} \simeq 11$, significantly later than $z_{re} \simeq 17$ as implied by first-year data.

Further refinements to this parameter came from the five-year WMAP data that, in combination with Type Ia supernovae and the Baryon Acoustic Oscillations in the distribution of galaxies, provide a more stringent limit on the optical depth: $\tau = 0.084 \pm 0.016$ [58].

In this theoretical and experimental frame, the *Planck* mission will be crucial to test the robustness of the ΛCDM concordance model since the relevant cosmological parameters will be measured with much better sensitivity. Furthermore, through E-mode CMB polarization power spectrum measurements, *Planck* will have the sensitivity to distinguish among different reionization history models even when they imply the same optical depth to electron scattering and degenerated temperature anisotropy power spectra, constraining some properties of the ionizing sources [110]. It

is well known that the principal observational objective of the *Planck* mission is to measure the temperature fluctuations of the CMB with an accuracy set by the fundamental astrophysical limits, but all the LFI channels and four of the HFI channels will also measure the linear polarization of the CMB which encodes not only a wealth of cosmological information, but also provides a crucial probe of the ionization history of the Universe during the time when the first stars and galaxies formed.

The polarization signal depends more directly than the temperature signal on the fluctuations at the last scattering surface and thus encloses a wealth of cosmological information, some of which being complementary to those derived from the temperature anisotropies. The polarization anisotropy at large angular scales is generated by the subsequent rescattering as the Universe reionized, providing a crucial probe of the ionization (and, possibly, thermal) history of the Universe at the end of dark ages, when the first stars and galaxies formed.

The mean ultraviolet radiation background (UVB) intensity responsable for the cosmological reionization, $J(\nu_0, z_0)$, observed at the frequency ν_0 and the redshift z_0 produced by a population of sources characterized by the comoving emmisivity $\epsilon_\nu(z)$ can be written as [111]:

$$J(\nu_0, z_0) = \frac{c}{4\pi} \int_{z_0}^{\infty} \epsilon_\nu(z) e^{-\tau_{eff}(\nu_0, z_0, z)} \frac{dt}{dz} dz,$$

$$\epsilon_\nu(z) = \bar{L}(z) \bar{\tau}_{lf} f_* \frac{\omega_b}{\omega_m} \frac{d}{dt} \int_{M_{min}(z)}^{\infty} \frac{dn}{dM_h}(M_h, z) M_h dM_h. \tag{2.83}$$

In the above equation $\nu = \nu_0(1 + z)/(1 + z_0)$, $(dt/dz)^{-1} = -H_0(1 + z)\sqrt{\Omega_m(1 + z)^3 + \Omega_\Lambda}$ is the line element in our ΛCDM cosmological model, τ_{eff} is the IGM effective optical depth, $n(M_h, z)$ is the comoving number density of halos of mass M_h at redshift z given by Press-Shechter formalism, $\bar{L}(z)$ is the mean specific luminosity of the ionizing sources, $\bar{\tau}_{lf}$ is their mean lifetime and f_* is the star formation efficiency.

Fig. 2.8 presents few reionization histories obtained for different UVB models chosen to investigate the effects of Thomson optical depth in the range τ_{es} = 0.050.1 and to study the possibility to distinguish between models with the same values of τ_{es}. The corresponding CMB anisotropy temperature, $C_T(\ell)$, and E-mode polarization, $C_E(\ell)$, power spectra are presented in Fig. 2.9 One should note in Fig. 2.9 that while $C_T(\ell)$ power spectra are almost degenerated, the differences in different
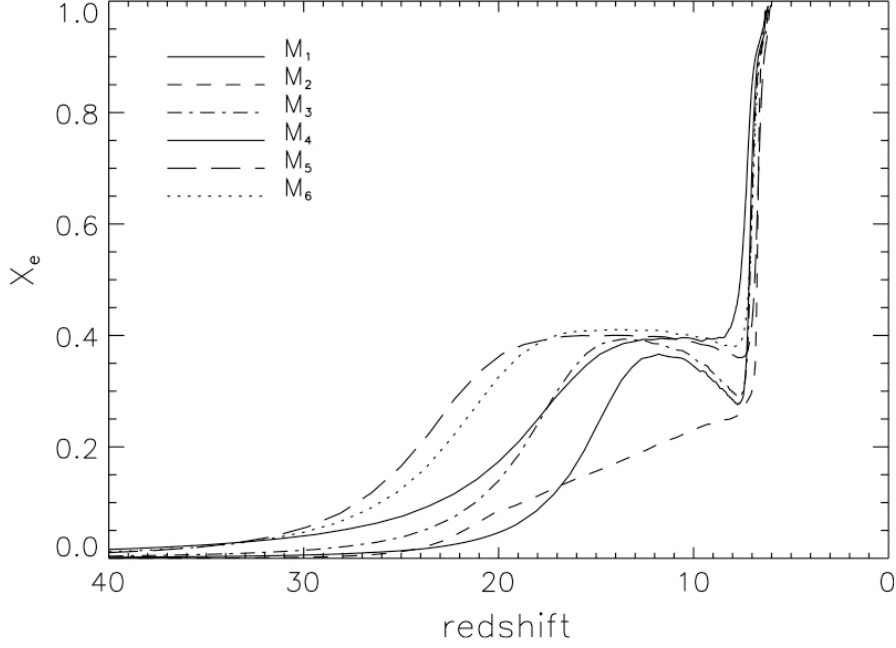
Figure 2.8: The evolution with redshift of the ionization fraction obtained for different UVB models chosen to investigate the effects of Thomson optical depth in the range $\tau_{es} = 0.050.1$. Figure from [111].

reionization histories produce non-degenerated signatures on $C_E(\ell)$ power spectra at low multipoles ($\ell \lesssim 50$). This can be explained by the fact that while polarization is projecting from the epoch of reionization at angular frequencies $\ell = k(\eta_0 - \eta_{ri})$ (here k is the wavenumber, η_0 and η_{ri} are the conformal times today and at the epoch of reionization) the temperature is projecting from the (further) last scattering surface.

The differences between the reionization models in comparison with the expected sensitivity of the future *Planck* mission can be expressed in terms of relative difference between the power spectra $C_E(\ell)$ of the E-mode polarization component as [101]:

$$D_{i,j}(\ell) = \frac{2[C_{E,i}(\ell) - C_{E,j}(\ell)]}{C_{E,i}(\ell) + C_{E,j}(\ell)} \,, \tag{2.84}$$

where the indices i and j denote different reionization models. We compare the amplitude of the function $D_{i,j}(\ell)$ with the expected relative error of the $C_E(\ell)$ anisotropy power spectrum for the *Planck* experiment. If systematic and foreground effects are successfully removed, the corresponding error

bar is given by:

$$\frac{\Delta C_E(\ell)}{C_E(\ell)} = \frac{1}{\sqrt{f_{SKY}(\ell + \frac{1}{2})[1 + w^{-1}C_E^{-1}]}} .$$ (2.85)
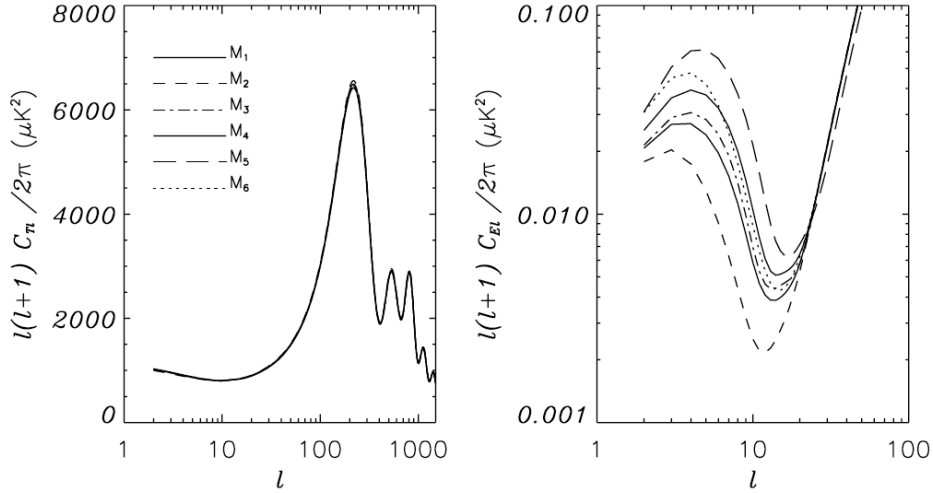

Figure 2.9: The CMB angular power spectra, CT(l) and CE(l) for the reionization histories presented in 2.8. Figure from [111]

The effects of a global reionization of the Universe would leave imprints on any osservable feature of the CMB. In fact, such a process will produce, to our eyes, a secondary Last Scattering Surface, with a consequent new photons diffusion: temperature anisotropies at high ℓ will be suppressed, because in the absence of motion for electrons, there will be no preferred directions and the diffusion will make the photons distrubution more isotropic and more homogeneus. The effects would be not negligible also in polarization anisotropies: growth of the anisotropies power in the cross-correlation temperature-polarization and of the E mode power spectrum, with the possibility that the growth could be more stressed at low/mid multipoles depending on the epoch at which the reionization occurs. On the photon distribution function, the effect is that to generate free-free and comptonization spectral distortion, related to the heating of the electronic temperature of the interstellar medium.

Chapter 3

KYPRIX

3.1 Introduction

In the previous chapter, we saw how it is possible to use the Kompaneets equation to compute the evolution of the photon occupation number, taking into account the photon production processes also. Now I will present KYPRIX, a performing Fortran based code capable of such computation. The details on the update of the code will be presented, followed by the tests done on it and some interesting cosmological applications.

3.2 Setting up the problem

Partial differential linear equations are divided in three classes: elliptic, parabolic and hyperbolic. The Kompaneets equation is a parabolic partial differential equation [144]. Solutions to this equation under general conditions have to be searched numerically, because it is impossible to find analytical solutions that accurately take into account the many kinds of cosmological scenarios and the great number of relevant physical processes. The numerical code KYPRIX [18] was written to overcome the limited applicability of analytical solutions and to get a precise computation of the evolution of the photon distribution function for a wide range of cosmic epochs and for many cases of cosmological interest. KYPRIX makes use of the NAG libraries. Besides these libraries, a lot of numerical algorithms are used in this code: we used some of the routines available for the scientific community, but often we did write routines dedicated to a specific task. Among the formers, the D03PCF routine (of the current version of the NAG release, corresponding to D03PGF routine used the first versions of KYPRIX), has been used to reduce the Kompaneets equation into a system of ordinary differential equations. In order to use this routine, we have to put the

Kompaneets equation in the form

$$\sum_{j=1}^{NPDE} P_{i,j} \frac{\partial U_j}{\partial Y} + Q_i = X^{-m} \frac{\partial}{\partial X}\left(X^m R_i\right); \qquad (3.1)$$

where Y is the time variable, X the spatial variable, $P_{i,j}, Q_i, R_i$ depends on $x, t, U, \partial U/\partial x$, the vector U is defined as above. In our case, $P_{i,j} = 1$ and $m = 0$ (Cartesian coordinates). Note that $P_{i,j}, Q_i, R_i$ do not depend on $\partial U/\partial t$.

The variables that enter in this equation are introduced and used in logarithmic form, to have a good and essentially uniform accuracy of the solution in the whole frequency range considered. These variables are X=log(x) and U=log(η), where x and η are the dimensionless frequency and the photon occupation number, respectively. Hereafter, the following notation will be used for the variables: X, U, Y for what concerns the informatic aspect of the problem, x, η, y for physical problems treatment. The function R_i is determined only by the inverse Compton term while the other physical processes, i.e. at least Compton scattering, bremsstrahlung, and radiative Compton, are included in the function Q_i. In order to reduce Eq. (3.1) into a system of ordinary differential equations, the D03PCF routine uses the method of lines: pratically, the right member of Eq. (3.1) is discretized, reducing the calculation of partial derivatives in terms of finite values of the solution vector U at all the points of the X axis grid. Spatial discretization is made by the method of finite differences [96]. The choice of the time parameter was driven by the need to have a very simple form of the Kompaneets equation. Finally, a "temperature independent" (time) Comptonization parameter

$$Y = y(t) = \int \frac{dy_e}{\phi} = \int_{t_i}^{t} n_e \sigma_T c \frac{kT_r}{mc^2} dt', \qquad (3.2)$$

has found to be particularly advantageous [18].

3.2.1 Boundary conditions

Integrating equations of the type of Eq. (3.1) means calculating the time evolution of the function $U(X, Y)$, for a given initial condition $U(X, 0)$ (in fact, the problem is also called "problem at initial conditions"). Numerically, the derivatives of U are replaced by finite differences between values of U computed for a grid of points (in X, Y) and the differential equation is replaced by a system of more simple equations. However, in presence

of the only initial condition, this system is singular [112]. For this reason, resolving partial differential parabolic equations needs boundary conditions: the problem is at initial values for the Y variable and at the boundary values for the X variable. In general, boundary conditions mean additional relations written to be joined to the system derived from the discretization to finite differences.

Therefore, a good statement of the problem requires the definition of appropriate boundary conditions and, possibly, the capability of a refresh of this conditions along the time integration leads more stability to the solution evolution because of the evolution of the radiation field. Thanks to the opportunity of having the correct value of ϕ for each time step, the update of the boundary conditions can be physically motivated (see Sect. 3.3.2). The limits of the frequency range considered are: $X_{min} = \log(x_{min}) = -4.3$ and $X_{max} = \log(x_{max}) = 1.7$. Of course, we want a solution of the Kompaneets equation over all the frequency range where it is possible to measure the CMBR and, in addition, a frequency range large enough to contain, in practice, all the energy density of the cosmic radiation field.

Also, the frequency range is so wide for two other reasons. During the time evolution, some spurious oscillations of the solution at points close to the boundaries may appear (these effects, that could also occur independently of the need of refreshing ϕ – for example for cases at constant ϕ –, may be partially amplified if, for computational reasons discussed in the following, the necessary refresh of the electronic temperature is not made for every time step). Fixing the frequency integration range limits far from the interval where we are interested to compute the photon distribution function allows to prevent the "contamination" of the solution by this possible spurious oscillations in the frequency range of interest.

Finally, since we can generally assume that a Planckian spectrum at x_{min} is formed before recombination in a timescale shorter than the expansion time and, on the contrary, at x_{max} the shape of the spectrum is unknown, it has been implemented in the code the possibility to adopt a particular case of Neumann boundary conditions: the requirement that the current density, in the frequency space, is null at the boundaries of the integration range [29]:

$$\left[\phi \frac{\partial \eta}{\partial x} + \eta(1 + \eta) \right]_{x=x_{min}, x_{max}} = 0. \tag{3.3}$$

This choice of boundary conditions formally satisfies the requirement of the problem when we integrate the Kompaneets equation in the case of Bose-

Einstein like distortions (with a frequency dependent chemical potential, $\mu = \mu(x)$, vanishing at very low frequencies). In fact, such distorted spectra are indistinguishable from a blackbody spectrum at sufficiently high and at low frequencies.

Of course, it is possible to make a different choice of the boundary conditions by selecting Dirichlet like conditions. In this case the photon occupation number at the boundaries of the integration interval does not change for the whole integration time. (In general cases, keeping constant conditions at the boundaries could be dangerous for the continuity of the solution. Nevertheless, for some specific problems this condition can work – typically for problems with constant ϕ).

3.3   A detailed view on KYPRIX

The code KYPRIX has been written to solve the Kompaneets equation in many kinds of situations. The physical processes that can be considered in KYPRIX are: Compton scattering, bremsstrahlung, radiative Compton scattering, sources of photons, energy injections without photon production, energy exchanges (heating or cooling processes) associated to $\phi \neq 1$ at low redshifts, radiative decays of massive particles, and so on. Being very versatile, this code could be easily implemented to consider other kinds of physical processes. Just to have an idea, KYPRIX is fully capable to simulate scenarios in which the initial condition is: a pure Planckian spectrum; a Planckian spectrum with several ways to include an istantaneous heating; a pure Bose-Einstein (BE) spectrum or a BE spectrum modified to become a Planckian one at low frequencies (this option is worth using in the case one would integrate the Kompaneets equation with a constant Φ and constant boundary conditions); a grey body spectrum; a superposition of black bodies.

The data are saved into five files.

DATI. This file contains the information about the specific parameters of the problem considered with a general description of its main aspects.

DATIP. In this file we give the evolution of interesting quantities, like time, redshift, ϕ, and many another quantities inherent to physical and numerical aspects of the problem.

DATIG. It contains: the points grid for the X axis used by the main program (remember that we are using a dimensionless frequency), a Planckian

spectrum at temperature T_0 and the solution vector U (that is to say $\log(\eta)$) at $y = 0$ (starting time).

DATIDE. This is the fundamental output file: it gives the solution of the Kompaneets equations at the desired cosmic epochs.

DATIT. It is similar to the file DATIDE, but it contains the solution in term of brightness temperature (i.e. equivalent thermodynamical temperature, see Eq. 3.6 in Sect. 3.3.2).

3.3.1 Main subdivisions

The code is divided in several sections and, from a general point of view, is structured as described here below.

1. Main program, in which many actions can be carried out: choice of the physical processes, choice of the cosmological parameters, characteristics of the numerical integration (accuracy, number of point of the grid, ...), time interval of interest, choice of the boundary conditions, and so on.

2. Subroutine PDEDEF. It is the subprogram where the problem is numerically defined. This subroutine is also divided in subsections to allow modifications in a simple and practical way.

3. Subroutine BNDARY. Here the boundary conditions are numerically specified.

4. Subroutines and auxiliary functions to perform specific operations.

3.3.2 Technical specifications and code implementation

The first version of KYPRIX[1] worked with the Mark 8 version of the NAG numerical library and were based on the routine D03PGF. The version of the NAG numerical library currently distributed is the Mark 21. Therefore an update of the KYPRIX code is necessary to adapt it to this new package.

When KYPRIX starts running it asks all the input data: from the declarations of the output files' names to the integration accuracy and features. In the following subsections we give a description of the various aspects of the code (and of its update), trying to give relevant hints about computational aspect fo the code.

---

[1]Written in 1989 by Carlo Burigana

Grid

The frequency integration interval is divided in a grid of points (the mesh points): larger the number of points smaller the adopted frequency step.

It is possible to used a very dense grid (for example 36001 mesh points corresponding to 36000 frequency steps). In general, it is necessary to use at least 3001 mesh points to have a solution accurate enough.

We found an important difference between the two NAG versions, not reported in the documentation of the routine D03PCF. In the first version (D03PGF), the subroutine where the partial differential equation is defined adopted the same mesh points defined in the main program. In the Mark 21 version the calculation is carried out in a different manner: the mesh points used in the subroutine PDEDEF is shifted of half spatial step with respect to the mesh defined in the main program. In this way, the mesh points in the PDEDEF subroutine will be exactly in the middle of the steps defined in the grid of the main program. For this reason, the limit of the integration interval are not considered in the mesh points in the subroutine PDEDEF and they are used only for the boundary conditions.

The effect of this feature implies the definition of new parameters that play a fundamental role in the subroutine PDEDEF. The integral quantities in the Kompaneets equation (necessary to define the radiative Compton term in the kinetic equations and the electron temperature) are computed once for any time step, inside the PDEDEF subroutine. For this computation, arrays of dimension equal to the number of mesh points of the x variable as defined in the PDEDEF subroutine are used. Therefore, particular care must be taken in the definition of the dimension of the arrays defined in KYPRIX. Those used in the main program have dimension equal to the number of points of the mesh defined in the main program. The same dimension is given for the arrays defined for the boundary conditions. On the other hand, the major number of arrays are used in the PDEDEF subroutine to compute the integral quantities. The inner grid adopted in the PDEDEF subroutine is based on mesh points in the middle of the spatial steps of the main program grid, so the two grids can not work with the same point number; in fact, the arrays used in the PDEDEF subroutine have dimension $NPTS-1$. Therefore, in the main program and in the subroutine BNDARY we have to work with

arrays based on the formula:

$$X(I) = A + (I - 1) \times \frac{(B - A)}{(NPTS - 1)},$$

(3.4)

$$\text{with } 1 \leq X \leq NPTS,$$

to define the correspondence between the grid of $NPTS$ points and the X position, while we need another expression able to shift of half step the grid in the PDEDEF subroutine and based on $NPTS - 1$ mesh points:

$$X(I) = \left(A + (I - 1) \times \frac{(B - A)}{(NPTS - 1)}\right) + \left(\frac{(B - A)}{2(NPTS - 1)}\right),$$

(3.5)

$$\text{with } 1 \leq X \leq NPTS - 1.$$

For continuity reasons, we need to define (according to the choices made in the main program) the solution vector, containing the photon initial distribution function, at the beginning of the integration also according to this grid definition. This vector is used by the PDEDEF subroutine as initial spectrum adopted for the computation of the rates of the physical processes and, of course, it is then renewed at every time step incrementation.

Output

Concerning the output files, the update version of KYPRIX stores a new vector containing the inner X grid used by the PDEDEF subroutine, XXGR (XGR refers to the main program X grid).

In addition, we preferred to have the possibility to perform the conversion of the solution into equivalent thermodynamic temperature directly into the code and save it in a new output file (DATIT). The conversion relation is:

$$T_{term,equiv} = \frac{x T_0}{\ln(1 + 1/\eta)}$$

(3.6)

(we remember that in the code $X = \log_{10}(x)$ and $U = \log_{10}(\eta)$).

The fundamental reason to perform this conversion directly in the code is associated to the extreme accuracy required for the solution in the case of very small distortions, of particular interest given the FIRAS results [51]. During the first tests, the conversion of the solution in brightness temperature was performed at the same time as the solution visualization, through the IDL visualization program. The saving of the solution into files

is typically performed not for all the points of the grid but for a reduced grid of, for example, 300 equidistant points along the original grid to avoid to store files of large size, unuseful for our scope, given the interest for the CMB continuous spectrum (by definition, the Kompaneets equation is not appropriate to treat recombination lines). If the considered distortions were very small then the solution at each specific "inner" grid point could be affected by a numerical uncertainty not negligible in comparison with the very small deviations from a Planckian spectrum relevant in this cases. This numerical error is greatly reduced (becoming negligible for our purposes) by the averaging over a suitable number of grid points. Of course, the storing of the solution directly on a limited number of grid points makes this averaging no longer possible on the stored data. It were then necessary to average the solution values in intervals corresponding to the output X grid directly into the code. Anyway, in many circumstances the diagram shape derived applying the conversion to brightness temperature only on the stored averaged solution still deviates at high frequencies from the effectively computed solution displayed by considering all the "inner" grid points because of the high gradients in the photon distribution function and/or in the brightness temperature that makes difficult, or impossible, to find a general rule for the solution binning that simultaneously works properly for the two solution representations. This problem is avoided converting the solution vector in equivalent thermodynamic temperature before of the binning of its values and then applying the binning to the equivalent thermodynamic temperature. The result is then a brightness temperature diagram very clean and precise, even for very small distortions. Other minor changes are made about the output data, where we passed from real to double precision, and for the saving frequency into the output files.

Equation formalism

A necessary update of the code has been performed to adapt it to the different formalism adopted by the new version of the NAG routine [116]. This regards the expression of the Kompaneets equation in the PDEDEF subroutine. In particular, the D03PGF routine adopted the following expression of the partial differential equation:

$$C_i \frac{\partial U_i}{\partial Y} = X^{-m} \sum_{j=1}^{NPDE} \frac{\partial}{\partial X} \left[X^m G_{ij} \frac{\partial U_j}{\partial X} \right] + F_i ,$$ (3.7)

where $i = 1, 2, ..., NPDE$ (number of partial differential equations); C_i, F_i depends on $X, Y, U, \partial U/\partial X$; $G_{i,j}$ depends on X, Y, U and U is the set of solutions values $(U_1, U_2, ..., U_{NPDE})$.

The expression now adopted by the D03PCF routine is represented by eq. 3.1.

Translating the code from the old to the new formalism is not very difficult. In the considered case $NPDE = 1$. In this case, we have simply that R_1 contains both the function G_1 and the vector solution derivative with respect to X according to:

$$R_1 = G_{11} \times \frac{\partial U_1}{\partial X} . \tag{3.8}$$

At this point, it is necessary to apply only the following substitutions:

$$Q_1 = -F_1 \qquad \text{and} \qquad P_{11} = C_1 . \tag{3.9}$$

With respect to this formalism, it is not so difficult to adapt the various terms of the Kompaneets equation to the D03PCF routine. The terms that describe Radiative Compton, bremsstrahlung, (optional) electromagnetic processes and part of the contribution of the Compton scattering are counted in the funtion Q_1. Instead, the second derivative of the solution vector with respect to X, which represents part of the inverse Compton rate, is counted in the function R_1. So, according to this settings, we can write:

$$Q_1 = FC + FBREM + FRAD + FDEC , \tag{3.10}$$

where FC stands for the contribution of the Compton scattering, $FBREM$ the bremsstrahlung one, $FRAD$ the radiative Compton one and $FDEC$ represents the contribution of radiative decaying of particles. In details, these equation are written like this:

$$FC = \left[\Phi \frac{\partial U}{\partial X} \left(\frac{\partial U}{\partial X} + 3 \right) + 10^X \left(\frac{\partial U}{\partial X} + 4 \right) + 2 \times 10^X 10^U \left(\frac{\partial U}{\partial X} + 2 \right) \right] \frac{1}{ln(10)} \tag{3.11}$$

and

$$FBREM + FRAD = \frac{\left(e^{10^X} \right)^{\Phi}}{10^{3X}} \times \left\{ \frac{1}{10^U} - \left[\left(e^{10^X} \right)^{\Phi-1} - 1 \right] \right\}$$

$$\times \left(FF0 \times W \times 1.5\Phi^{-1/5} \times FGAUNT + \frac{DC0}{W} I_1 \times GDC \right) , \tag{3.12}$$

where $FF0$ and $DC0$ are the coefficients for the rates of bremmstrahlung and radiative Compton respectively; $FGAUNT$ and GDC represent the Gaunt

factor corrections for bremsstrahlung and radiative Compton respectively; I_1 is an integral quantity refreshed at every time step.

The inverse Compton goes in R_1 in this way:

$$R_1 = \frac{\partial U}{\partial X} \times \Phi \times ln(10)^{-2} \, . \tag{3.13}$$

Finally, we can put $P_{11} = 1$.

Furthermore, it is possible to add a term in Eq. (3.10). For example, an already implemented utility would generate a term here called *FDEC*, to be added in Eq. 3.10. In this term are included the contributions of possible radiative decaying of particles in the primordial universe. Anyway, it is possible to add terms representing other kinds of electromagnetic processes.

Boundary conditions

Also notable are the differences between the input expressions defining the boundary conditions. The D03PGF routine adopted an expression of the form:

$$P_i(Y)U_i + Q_i(Y)\frac{\partial U_i}{\partial X} = R_i(Y, U) \, , \tag{3.14}$$

where $i = 1, 2, ..., NPDE$ and $P_i(Y), R_i(Y, U), Q_i(Y)$ are functions to be defined. A quite different notation is used to provide the boundary conditions in the D03PCF routine:

$$\beta_i(X, Y)R_i(X, Y, U, U_X) = \gamma_i(X, Y, U, U_X) \, , \tag{3.15}$$

where $i = 1, 2, ..., NPDE$ and $\beta_i(X, Y)R_i(X, Y, U, U_X)$ and $\gamma_i(X, Y, U, U_X)$ are functions to be defined ($U_X \equiv \partial U/\partial X$).

As a consequence of this notation, Neumann like boundary conditions can be now specified according to the expression:

$$\beta(1) = 1 \tag{3.16}$$

$$\gamma(1) = -XVA \times (10^{U(1)} + 1) \times \ln 10^{-2} \tag{3.17}$$

where $XVA = \eta$ computed in A and the dimension of both the equations corresponds to the differential equation number. Similar conditions are defined for the other extreme of the integration interval [A,B].

Accuracy parameters

Another considerable difference between the two library versions regards the definition of the integration accuracy parameter. D03PGF used three parameters for monitoring the local error estimate in the time direction, supplying a good versatility. RELERR and ABSERR were respectively the quantity for the relative and absolute component to be used in the error test. The third parameter, INORM, was used to define the error test. If $E(i, j)$ is the estimated error for U_i (the vector solution) at the $j - th$ point of the X grid, then the error test was:

- $INORM = 0 \Longrightarrow | E(i, j) | \leq$ ABSERR $+$ RELERR$\times | U(i, j) |$

- $INORM = 1 \Longrightarrow | E(i, j) | \leq$ ABSERR $+$ RELERR $\times \max_y | U(i, j) |$

- $INORM = 2 \Longrightarrow \|E(i, j)\| \leq$ ABSERR $+$ RELERR $\times \|U(i, j)\|$.

Instead, according to the new library version we have to define only one parameter ACC, a positive quantity that monitors the local error in the time integration. If $E(i, j)$ is defined as above, then the error test is:

$$| E(i, j) |= \text{ACC} \times (1+ | U(i, j) |) . \tag{3.18}$$

Electron temperature

During the numerical integration, some subprograms use the distribution function calculated at that time to compute ϕ. The integrals to be computed are those appearing in the expression for $\phi_{eq,C}$:

$$\phi_{eq,C} = \frac{T_e}{T_\gamma} = \frac{\int_0^\infty \eta(\eta + 1)x^4 \mathrm{d}x}{4 \int_0^\infty \eta x^3 \mathrm{d}x} . \tag{3.19}$$

In this calculation, the integration range is obviously the integration interval considered for the problem: $A \leq X \leq B$ (that, in terms of mesh ordering, corresponds to the range between 1 and $NPTS$ or $NPTS - 1$). For computing these integrals, all the points of the grid are used. The integration is based on the NAG D01GAF routine, suitable for tabulated functions. Of course, the update value of ϕ is also used in the boundary conditions.

In the previous version of the KYPRIX code, the computation of integral quantities were performed through a specific modification of the NAG package implemented by the KYPRIX code author that allowed to recover the whole vector solution at each time step in the subroutines (and in

particular in PDEDEF), while the original package maked only available in PDEDEF the solution separately at each grid point (being in fact the package originally designed for "pure" partial differential equation, without terms involving integrals of the solution). This modification, possible thanks to the availability of the NAG sources (and, in practice, thanks to the relative simplicity of the early library versions), permitted to update the integral quantities perfectly according to the implicit scheme adopted by the code for the integration in time. This is no longer feasible, because the sources file are no longer delivered with the libraries (and in addition they are very expensive now). Therefore, the update of the integral quantities must be now performed with an alternative scheme, saving the solution at the previous time step in a proper vector and using it in the computation at the given time step. This alternative scheme may be less stable than implicit schemes. And, in fact, we verified the difficulty of the D03PCF routine to work implementing the update of the quantities corresponding to the integral terms in the Kompaneets equation (and in particular of ϕ) for each time step. The latter, depending on the accuracy required, may be very small. This issues were likely due to numerical instabilities.

We have then introduced a new integer control parameter into the code: STEPFI. It determines the frequency for the update the dimensionless electron temperature ϕ, relevant, of course, in the case we want to perform an integration with a variable ϕ. We have checked that updating the integral terms in the Kompaneets equation not at every time step, but after a suitable number of time steps does not affect the accuracy of the solution. This is due to the fact that the time increasing in the code is performed with very small steps while the physical variation of ϕ occurs on longer timescales [2].

Radiative Compton

In the computation of the radiative Compton term there is an integral term, so it is necessary to harmonize its update according to the parameter STEPFI discussed in the previous subsection. In fact, a possible asynchronous update of it and ϕ could create numerical instabilities and the crash of the code run, as physically evident from the great relevance of both radiative Compton term and electron temperature for the evolution of the

---

[2]Of course, for physical processes with a stronger variation of the electron temperature, the accuracy parameter (see previous subsection) should be good enough to force the code to adopt sufficiently small time steps.

low frequency region of the spectrum.

Integration routines

Different numerical integration routines can make similar tasks, but this is made with different algorithms. Inside KYPRIX we find a practical example: in the early release of the code the NAG D01BDF routine was used to calculate integrals of a function over a finite interval. The same task can be carried out by the D01AJF routine. Anyway, this code offers a better accuracy than D01BDF (D01AJF is in fact suitable also to integrate functions with singularities, both algebric and logarithmic). After the routines substitution, the results showed a great increasing of accuracy. In particular, this improvement offers the possibility to investigate also very small distortions that requires a very precise determination of all the relevant quantities because the absolute numerical error of the integration must be much smaller than the (very small) quantities of interest in these cases. In particular, the quantity $\Delta \epsilon_r / \epsilon_i$ (where ϵ_r is the density energy and ϵ_i is the energy density corresponding to the imperturbed distribution function just before the energy injection) must be constant during all the integration process in the absence of energy injection terms, according to the energy conservation. The precision increase on the computation of this quantity was noteworthy: now it is always inside a few percent of the physical value (and its possible physical variation) of the same quantity independently of the magnitude of the considered distortion. This allows to accurately check the global accuracy of the code and to assure that the integral terms appearing in the Kompaneets equation are properly computed (this is a remarkable result, because the code can now be used also for very small distortions).

3.4   New physical options

3.4.1   The introduction of the cosmological constant

Up to about 10 years ago the favourite cosmological models were CDM or CHDM models. In the recent years the relevance of the cosmological constant term (or of dark energy contributions) has been renewed by a wide set of astronomical and cosmological observables

[107, 120, 79]. The numerical integration code KYPRIX has been then updated to include the cosmological constant in the terms controlling the general expansion of the universe [117][116]. In particular the input background cosmological parameters considered in the code are now: $T_0, \kappa, h[= H_0/(100\text{Km/s/Mpc})], \Omega_m, \Omega_b, \Omega_\Lambda, \Omega_K$, i.e. the present CMB temperature, the contribution of massless neutrinos, the Hubble constant, the (non relativistic) matter and baryon energy density, the energy densities corresponding to cosmological constant and curvature terms.

In order to compute the proper cosmic evolution of the various terms we introduced a scale factor parameter ω [129], defined by:

$$\omega = \frac{a}{a_1} \equiv \frac{m_e c^2}{kT_0} \frac{1}{1+z} = 1.98 \times 10^9 \Theta (1+z)^{-1}, \tag{3.20}$$

with $\Theta \equiv T_0/3°K$ and the index 1 is referred to a particular epoch, when the CMB energy density was equal to the electron mass[3]: $k_T(a_1) = m_e c^2$. To write a suitable expression for its time evolution we have to introduce two new key parameters

$$\beta = \frac{\rho_{m1}}{\rho_{r1}} = 3.5 \times 10^{-6} \frac{h^2}{\Theta^3} \Omega_{tot} \tag{3.21}$$

that is the initial ratio between matter energy density and radiation energy density, and

$$\frac{1}{\tau_{g1}} = \left(\frac{8\pi}{3} G \rho_{r1}\right)^{1/2} = \left[\frac{8\pi}{3} G \frac{a}{c^2} \left(\frac{m_e c^2}{k}\right)^4\right]^{1/2} = 0.076 \text{s}^{-1} \tag{3.22}$$

defined as ana initial gravitational time scale. The quantities with the index 1 refer to the epoch when $a = a_1$, with the index 0 when $t = t_0$ (today); ρ_{r1} and ρ_{m1} are related to ρ_r and ρ_m by

$$\rho_r = \rho_{0r}\left(\frac{\omega_o}{\omega}\right)^4 = \rho_{r1}\frac{1}{\omega^4}; \quad \rho_m = \rho_{0m}\left(\frac{\omega_0}{\omega}\right)^3 = \rho_{m1}\frac{1}{\omega^3}, \tag{3.23}$$

respectively.

Now we can define an equation for the evolution of ω:

$$\frac{\dot\omega}{\omega} = \left[\frac{8\pi}{3} G \rho(\omega)\right]^{1/2} = \tag{3.24}$$

$$\frac{8\pi}{3} G \left[\frac{\rho_{r1}\kappa}{\omega^4} + \frac{\rho_{m1}}{\omega^3} + \frac{\rho_{K1}}{\omega^2} + \rho_\Lambda\right],$$

where we have included the contribution of massless relativistic neutrinos in the term κ (see also footnote 1; the term κ should be properly evaluated

---

[3]So, the parameter ω is analogous to the scale factor a, but normalized at the epoch in which $a = a_1$, that is to say when $kT = m_e c^2$.

considering also possible energy injections after neutrino decoupling).
After some calculations (see Appendix A), we can write the final expression
of $\frac{dt}{d\omega}$ implemented in the new code version:

$$\frac{1}{\dot{\omega}} = \frac{\tau_{g1}\,\omega}{\left[1 + \beta\,\omega\left(1 + \frac{\Omega_{K/m}\,\omega}{2.164\times10^9} + \frac{\Omega_{\Lambda/m}\,\omega^3}{2.164\times10^{27}}\right)\right]^{1/2}}\,, \tag{3.25}$$

where $\Omega_{x/y} = \frac{\Omega_x}{\Omega_y}$.

The equation for $\dot{\omega}$ has to be inserted in the expression giving $dy = a_c dt$. The latter is involved in the integral used to compute the time variable $y(\omega) = \int_{\omega_{start}}^{\omega} dy$ because we set $y = 0$ when the integration starts at $\omega = \omega_{start}$ (or equivalently at $z = z_{start}$). Finally, the expression for the time evolution of ω and y are related by the variable change:

$$dy = a_c dt = a_c\,\frac{dt}{d\omega}\,d\omega = a_c\,\frac{\omega}{\dot{\omega}}\,\frac{1}{\omega}\,d\omega\,, \tag{3.26}$$

where $a_c = \phi/(\tau_{c1}\omega^4)$ $(\tau_{c1} = 2.638 \times 10^{-9}\,\Theta^3/(h^2\Omega_b))$.

Introducing the cosmological constant and curvature terms, the code KYPRIX is suitable to be applied to interesting cases at low redshifts, where Λ supplies the greatest contribution to the expansion rate of the universe (remarkable examples are spectral distortions associated to the reionization of the universe). For sake of completeness, a few words about the computation of the time evolution in the code. The subroutine called WDIY0 is the core of the time evolution in KYPRIX: it computes the value of ω given a value of y. This process takes advantages of the definition of y as integral of dy and, of course, it happens at each time step. To do this, we make use of a double precision version of the function ZBRENT, from Numerical Recipes.

3.4.2 Chemical abundances

As a consequence of the fact that now it is possible to choose the primordial abundances of H and He a different number of effective electrons, n_e^{eff}, are involved in the different physical processes. Before this was possible, in the code was assumed a fixed abundance of H and He and also the maximum level of ionization of the elements was assumed. With a primordial He abundance of the 25%, the number of the effective electrons was given by

$$n_e^{eff} = n_e^{tot} \simeq \frac{\rho_b}{m_b}\frac{7}{8}\,, \tag{3.27}$$

where ρ_b is the baryon density and m_b the mean mass of a baryon. Now, if we call f_H the fraction of primordial H and considering that $n_e = n_H + 2n_{He}$, after some calculation, we have:

$$n_e^{eff} = \frac{1 + f_H}{2} \frac{\rho_b}{m_b} .$$

(3.28)

Of course it is necessary to newly calculate the rates of the physical processes involved in the code.In fact, both Compton scattering and bremsstrahlung depends directly from n_e^{eff}.

3.4.3 Including recombination and reionization processes

The high accuracy reached in the last years in observations on CMB is bringing us a lot of informations regarding temperature anisotropies and spectrum. So, a detailed understanding of the recombination process is crucial for modeling the power spectrum of CMBR anisotropies with such a precision. Future missions, dedicated to the masurement of the absolute temperature of the cosmic background, must have an high sensitivity and accuracy in order to bring the level of measurements adequate to the physic knowledge that we reached on this axpect of the CMBR.

The past versions of KYPRIX included the recombination process as an istantaneous phenomenon and characterized by fully ionized elements. This is a very semplified scenario and a more precise calculation was needed.
The first implemenation about that was to include the ionization fraction in the equation for the rates of bremsstrahlung and Compton scattering, by allowing a more realistic calculation of the spectral distortions that could accurred during this phase transition [117].
This upgrade permits to take into account the ionization fraction of the elements involved in the physical processes during recombination in three different ways: the simplest is a *toy model* in which, once the ionization fraction of electrons, χ_{e^-}, is given (that is to say a recombination history), the code assumes that hydrogen and helium has the same degree of ionization.
In order to include new precise calculation regarding the processes involved in phenomena like reionization or recombination, we performed another remarkable implementation in KYPRIX. This is related to the contribution that each state of ionization of the elements involved in the processes could now give in the considered scenario. More precisely, independent ionization fractions are introduced in the code for each element that takes

part in the processes. Before this implementation, the code was able to simulate reionization only considering the species involved as totally ionized. Now there are different way by which the code can handle the ionization parameters related to the ionization fractions of the elements.

The effects of this implementation are totally negligible for the Radiative Compton, because during the epochs this process is active, the medium is totally ionized thanks to the high energy scale of the primordial universe. Instead, Compton scattering and bremsstrahlung feel strongly the influence of the implementation, although in different way: Compton scattering depends of course on the number of free electron n_e, so if we have a medium not fully ionized the number of active electrons will be different; bremsstrahlung shows also a dependence from the baryon density and, again, the fact that the medium could be considered not fully ionized will have deep effects on this process evolution.

Now, once introduced an electron ionization fraction in the code, χ_e, which represents the effective number of electrons that take part in the physical processes, we can choose different way by which the active fractions of elements can play their roles in the phenomena. Given χ_e, from the charge conservation law, we have constraints on the number of the free baryon in the considered plasma. The simplest way to take count of them, in the code, is to assume: an equal fraction of ionization for H and He and a totally ionized plasma. Of course, this is a toy model, but a parametrization like this would be very useful to test the code, and also it is just enough to newly write the rates for the Compton scattering and for bremsstrahlung.

A more accurate treatment of the physics of reionization/recombination processes, consists in introducing the Saha equation for every degree of ionization of the considered species:

$$\frac{n_{i+1}n_e}{n_i} = \frac{2}{\Lambda^3} \frac{g_{i+1}}{g_i} e^{-\frac{\epsilon_{i+1}-\epsilon_i}{k_B T}} \,, \tag{3.29}$$

where n_i is the density of atoms in the i-th state of ionization, n_e is the electron density, g_i is the degeneracy of states for the i-ions, ϵ_i is the energy required to remove i electrons from a neutral atom and Λ is the thermal de Broglie wavelength of an electron, defined by

$$\Lambda = \sqrt{\frac{h^2}{2\pi m_e k_B T}} \,. \tag{3.30}$$

Thanks to this equation it is possible to obtain the concentration of each ionization state of the considered elements: there is no more degeneracy

about the ionization states of *He*. Providing the electron ionization fraction χ_e, we find unknown parameters, $\chi_H, \chi_{H^+}, \chi_{He}, \chi_{He^+}, \chi_{He^{++}}$, that are the relative abundances of the different states of the elements. The Saha equation provides the ratio between two state of ionization of a single specie, once given the electron density and the temperature. This means that we can easily calculate these ratio:

$$\frac{n_{H^+}}{n_H} \ , \ \frac{n_{He^+}}{n_{He}} \ , \ \frac{n_{He^{++}}}{n_{He^+}} \ , \tag{3.31}$$

where n_X indicates the particles number for the element X. To recover all the unknows we need to couple some other relations to the Saha equation. These additional conditions are provided by the charge conservation law and the nuclei conservation. If we write these latter two relations in function of the ionization fractions of the elements considered, we approach to this form for the nuclei conservation law:

$$n_b^{TOT} = \frac{\rho_b}{m_b} \left[f(\chi_H + \chi_{H^+}) + \left(\frac{1-f}{4} \right) (\chi_{He} + \chi_{He^+} + \chi_{He^{++}}) \right] \tag{3.32}$$

and to this form for the charge conservation law:

$$n_e^{eff} = \frac{\rho_b}{m_b} \left[\chi_{H^+} f + 2 \left(\frac{1-f}{4} \right) (\chi_{He^+} + \chi_{He^{++}}) \right] . \tag{3.33}$$

These two relations, plus those ones that gives us the ratio shown in 3.31, complete a sistem of five unknowns and five equations that we need to recover all the effective abundances of the various elements.

Another way to perform the exact calculation and integration of the processes rates in scenarios involving reionization/recombination is to use a co-running code, coupled to KYPRIX, able to supply the ionization fraction for all the species.

3.5 Tests carried out

Once termined the updating of the numeric integration code, we have carried out many accuracy and performance tests [117][113]. A code of good quality requires at least: high numerical precision compared to the knowledge, both theoretical and observational, of the considered problem and physical meaning of the results obtained from the numerical integration based on a specific NAG routine (D03PCF for the update version – D03PGF

for the original version) for partial differential equations. Moreover, for several specific computations some other routines, mainly from the NAG package albeit also from the Numerical Recipes [112] package, are used in the code. Since different routines can solve the same mathematical problems using different numerical methods and/or implementations, typically with different settings and different input parameters, we have also verified that the adopted routines allow an appropriate efficiency and accuracy.

In order to evaluate the global CPU time of the code we performed many runs with very different settings. These times are carried out testing the code on a Digital machine with 4 Alpha CPUs, but effectively using only one CPU (now we are running the code on IBM Power5 Processors). The global CPU time interval ranges from few minutes for cases in which the integration starts at low redshifts to about 5 hours for cases starting at very high redshifts ($y(z) \simeq 5$). There are many factors that take role in determining the global CPU time. The complete Kompaneets equation [17] is in fact composed by several terms. In the KYPRIX code we can select the physical processes to be considered in the numerical integration and the global CPU time increases with the number of activated processes.

Of course, the global CPU time depends on the parameters related to the numerical integration characteristics. The number of points adopted for the x grid has a great influence on the global CPU time. The integration interval starts from a point, A, and ends to a point, B, and it is discretized in a number of spatial steps given by the parameter $NPTS$. Clearly, the integration accuracy improves with $NPTS$ because of the increasing of the density of the adopted mesh point grid. In most of the cases $NPTS$ is set up to a very large value. We find that the global CPU time is approximately proportional to $NPTS$ ($t_{CPU} \propto NPTS$).

The parameter that plays the most relevant role in determining the global CPU time is the accuracy required for the time integration. The final solution precision depends on the value of the corresponding parameter ACC. Only for very high accuracy (ACC $\lesssim 10^{-12} - 10^{-14}$) the CPU time reaches the duration of some hours while keeping ACC $\sim 10^{-5}$ the integration is carried out in few minutes. Anyway, the limits imposed by CMB spectrum observations drive us to investigate in particular on small distortions. It is then necessary to work with low values of ACC (in general, $\lesssim 10^{-10}$).

Once termined the better choice of the various numerical routines and fixed the characteristics of the time integration, we have carried out several

tests in order to verify the physical validity of the results given by the code KYPRIX.

3.5.1 Energy conservation test

In the code output file DATIP we store values of several parameters of interest. Two of them provide very useful information on the goodness of the numerical integration. The first one is the ratio, ϵ_r/ϵ_i, between the radiation energy density today and the energy density corresponding to the unperturbed distribution function before the distortion[4]. In absence of dissipation processes, the perfect energy conservation is represented by the constance of this ratio at all the times during the integration. To determinate the accuracy supplied by KYPRIX, the values of ϵ_r/ϵ_i are stored at the starting of the integration and at many following times. In order to estimate the precision of the energy conservation, we define the quantity:

$$ERR_\epsilon = \frac{|(\epsilon_r/\epsilon_i)_{t=t_{start}} - (\epsilon_r/\epsilon_i)_{t>t_{start}}|}{(\epsilon_r/\epsilon_i)_{t=t_{start}} - 1} , \qquad (3.34)$$

that gives the relative error induced by the numerical uncertainty on the initial value of the amount of fractional injected energy, $\Delta\epsilon_r/\epsilon_i$.

A typical result is reported in Fig. 3.1.

Since the same absolute numerical integration error corresponds to a larger relative error for a smaller distortion, i.e. for smaller $\Delta\epsilon_r/\epsilon_i$ in these models, we could in principle expect a degradation of the energy conservation for decreasing distortions. Our tests indicate in fact that the maximum induced error shows an increasing of the degradation of the energy conservation for decreasing distortions adopting the same accuracy parameters. On the other hand, one can select them according the specific problem. We find that for suitable choices of the integration accuracy parameters, the above relative error can be kept always below $\simeq 0.05\%$ without requiring a too large computational time. Finally, we note that in some circumstances the scheme for the electron temperature evolution in the new version of KYPRIX (backward differences), different from that used in the original one (implicit scheme), could imply some small discontinuities in the evolution of the electron temperature and of $\Delta\epsilon_r/\epsilon_i$. They are localized only to few time steps and do not propagate along the evolution. We have

---

[4]For example, for a Bose-Einstein distorted spectrum $\epsilon_r/\epsilon_i = \phi^4 f(\mu)/[\phi_0^4 \varphi_0^{4/3}(\mu)]$ (see, e.g., [138] [35]).
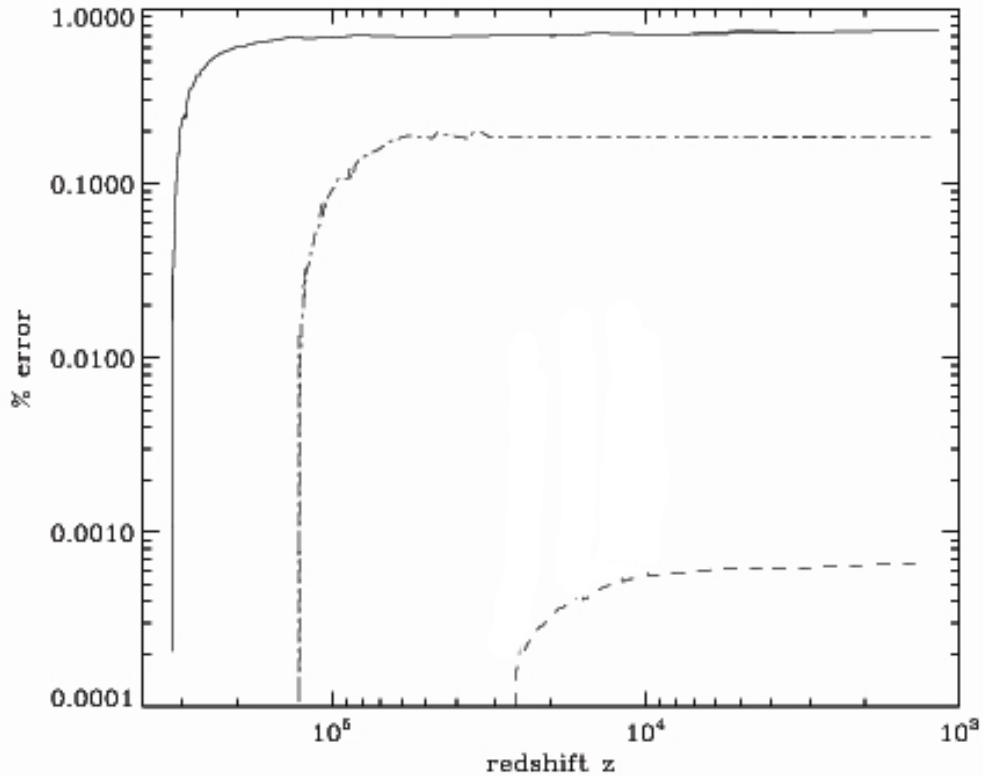
Figure 3.1: Error in the energy conservation expressed in terms of relative (%) deviation from its input value of the quantity $\Delta\epsilon_r/\epsilon_i$. See the text for further details on computation parameters. Thin solid, dot-dashed, and dashed lines refer to an energy injection occured respectively at $y_h(z) \simeq 1.5, 0.25, 0.01$. Obviously, this error further decreases improving the accuracy parameter adopted in the numerical integration.

verified that this effect does not affect the very good accuracy of the solution, because of the very small amplitude of these discontinuities and of the corresponding energy conservation violation.

3.5.2 Comparative tests

Comparing solutions

The first kinds of tests consisted simply in comparing the results obtained with the update version of KYPRIX with those obtained with the original version for the same sets of input parameters (see Fig. 3.2).

To this purpose, we have considered some interesting cases carried out in the past. In particular we used the input parameters adopted in Burigana et al. (1995) where also semianalytical descriptions of the

numerical solutions of the Kompaneets equation were reported. Relatively small distortions have been assumed in the tests reported here: the amount of exchanged fractional energy is $\Delta\epsilon_r/\epsilon_i = 10^{-4}$ and we started the integration from a redshift corresponding to $y_h(z) \simeq 0.25$ in one of the two cases and $y_h(z) \simeq 0.01$ for the other case. The input cosmological parameters are: $H_0 = 50$, $\widehat{\Omega}_b = 0.03$, $k = 1.68$, $T_0 = 2.726$ K. Clearly, the results given by the update version of KYPRIX are fully consistent with the those reported in [17]. Moreover, since in that paper a seminalytical description of the solution of the Kompaneets equation is given, it is clear that a good agreement of the numerical results obtained with the original and update code represents a further confirmation of the analytic solution validity.
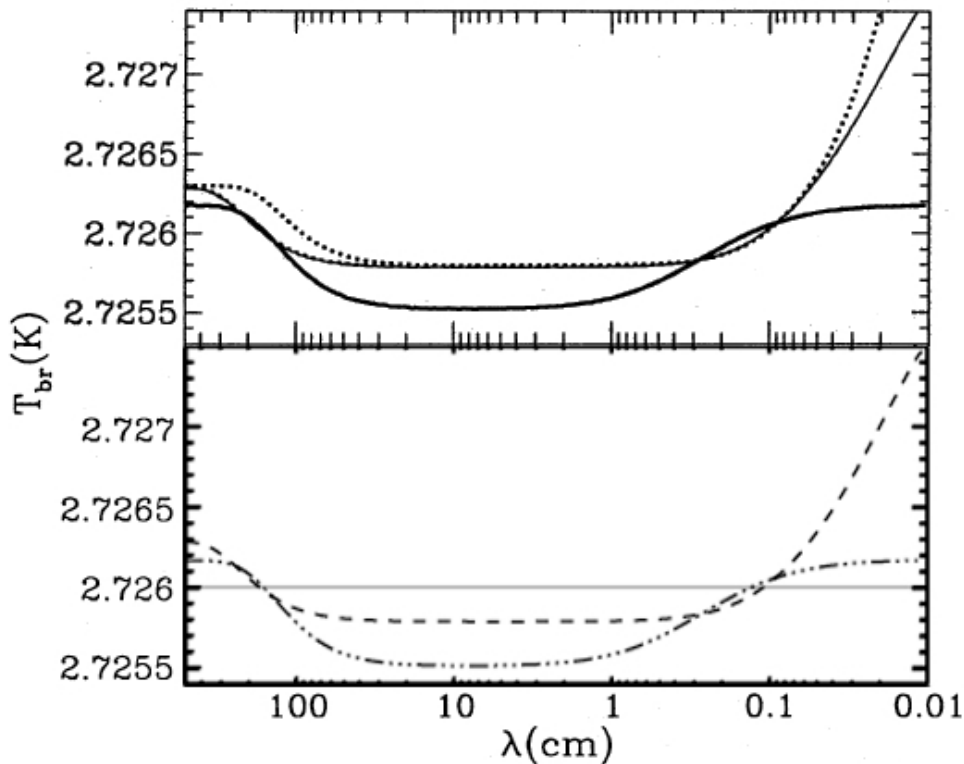
Figure 3.2: Comparison between the present time solution for the CMB spectrum obtained from the old version of the numerical code (upper lines; adapted from panel a of Fig. 1 in [17]) and the current one (lower lines). See the text for further details on computation parameters. Dashed (dot-dashed) line refers to an energy injection occured at $y_h(z) \simeq 0.01$ ($y_h(z) \simeq 0.25$). Note the excellent agreement between the results of the two codes. In the case of the old version of the code we report also the analytical approximation (dotted line) described by a Comptonization spectrum plus a free-free distortion (see Eq. (33) in [17]).

Comparing the analytical description of the behaviour of ϕ with the numerical one

While the energy exchange between matter and radiation is led by Compton scattering (in the absence of external energy dissipation processes), electrons reach the equilibrium Compton temperature (Peyraud 1968, Zeldovich & Levich 1968), $T_{e,eq}$, in a time shorter than the expansion time. For $y_h \ll 1$, (non primordial heating processes) Compton scattering is no longer able to significantly modify the shape of the perturbed spectrum and the final electronic temperature ϕ_f (remember that $\phi = T_e/T_r$), immediately after the decoupling, is very close to $\phi_{eq} = T_{e,eq}/T_r$. On the other hand, we know that for energy injections at redshifts corresponding to $y_h \gtrsim 5$ Compton scattering can estabilish kinetic equilibrium between matter and radiation. This corresponds to a Bose-Einstein spectrum, with a final electron temperature given by (Sunyaev & Zeldovich 1970, Danese & De Zotti 1977):

$$\phi_f(y_h \gtrsim 5) = \phi_{BE} \simeq (1 - 1.11\mu_0)^{-1/4}, \tag{3.35}$$

where $\mu_0 (\ll 1)$ is the dimensionless (initial) chemical potential. Moreover, in this case the evolution of the chemical potential, $\mu(z)$, the relation between it and the amount of fractional energy injected, $\Delta\epsilon/\epsilon_i$, depends on the energy injection epoch.

For the intermediate energy injection epochs, corresponding to $y_h \lesssim 5$, the final value of ϕ (a function depending on y_h) is between the values of ϕ_{BE} and ϕ_{eq}, because the Compton scattering works to produce a Bose-Einstein like spectrum anyway (Burigana et al. 1991). At these epochs the relation between the chemical potential and the amount of fractional injected energy injected is simply given by (Sunyaev & Zeldovich 1970, Danese & De Zotti 1977):

$$\mu_0 \simeq 1.4 \frac{\Delta\epsilon}{\epsilon_i}. \tag{3.36}$$

By exploiting the numerical results, Burigana et al. (1995) found a simple formula for ϕ:

$$\phi_f(y_h) = \frac{k}{5} \frac{5 - y_h}{k + y_h} (\phi_{eq} - \phi_{BE}) + \phi_{BE}, \tag{3.37}$$

where $k = 0.146$. Moreover, this expression represents an accurate description of the evolution of ϕ for any value of y_h. In facts, for a value of y ($y < y_h$) we have:

$$\phi(y, y_h) = \phi_f(y_h - y). \tag{3.38}$$

In the considered cases, as in many situations of interest, the perturbed spectrum of the radiation (immediately after the heating process) could be described by a superposition of blackbodies and the equilibrium temperature is given by (Zeldovich & Sunyaev 1969, Zeldovich et al. 1972, Burigana et al. 1995):

$$\phi_{eq} \simeq (1 + 5.4\, y^*)\phi_i\,, \tag{3.39}$$

where $\phi_i = T_i/T_r = (1 + \Delta\epsilon/\epsilon_i)^{-1/4} \simeq 1 - y^*$ and the Comptonization parameter y^* could be related to the amount of fractional energy exchanged by (Zeldovich & Sunyaev 1969, Zeldovich et al. 1972, Burigana et al. 1995):

$$y^* \simeq (1/4)\Delta\epsilon/\epsilon_i\,. \tag{3.40}$$

Through Eqs. (3.37) and (3.38) we can test the behaviour of the electron temperature during the numerical integration of the Kompaneets equation carried out with the new code version. With the increasing of the time variable, the values of ϕ are saved into the file DATIP, from the initial time step to the final one. Fig. 3.3 shows the two behaviours of ϕ (the numerical one and the analytical expression given by Eqs. (3.37) and (3.38)).

This test is of particular importance for the check of the validity of the results. In fact, the numerical computation of ϕ during time evolution of the system is of crucial relevance because of the role of ϕ in the Kompaneets equation. As remembered in the previous section, in the new version of the code a different scheme is used with respect to that implemented in the original version. The verification of the very good agreement of the above behaviours of ϕ further supports the substantial equivalence of the two code versions, their reliability, and, in particular, the negligible impact of the approximation implemented into the new numerical scheme adopted for the evolution of ϕ (in principle less stable than the implicit scheme) with respect to the old one.

3.5.3 Tests on the free-free distortion

As already discussed by Sunyaev & Zeldovich (1970), accurate measures of the CMB spectrum in the Rayleigh-Jeans region could provide quantitative informations about the thermal history of the universe at primordial cosmic epochs. On the other hand, photon production processes (mainly radiative Compton at earlier epochs and bremsstrahlung at later epochs) work to
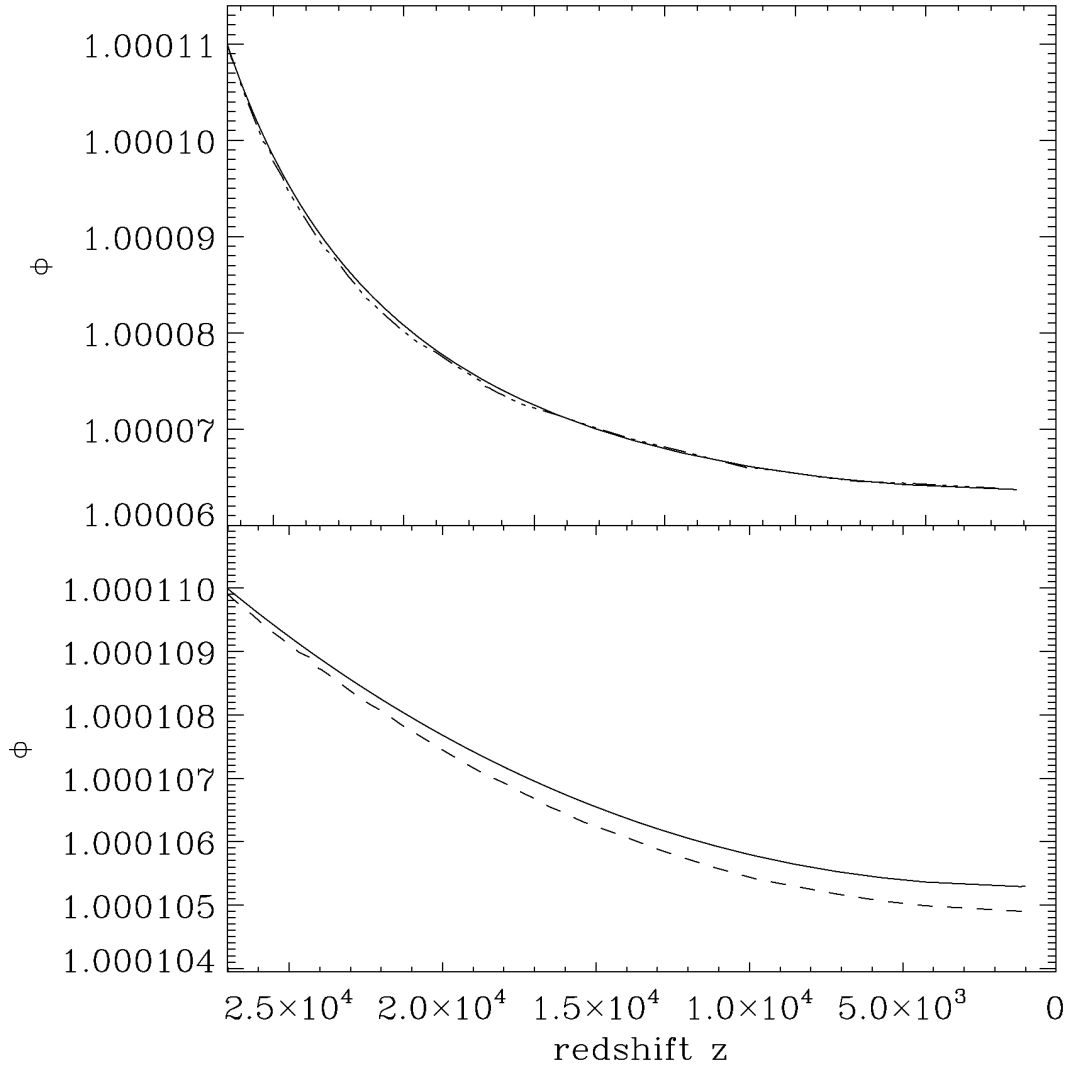
Figure 3.3: Evolution of ϕ as derived from the numerical code compared with that defined by Eq. **??**. The parameters adopted for the computation are the same as in Fig. 3.1 as well as the adopted kinds of lines. Note that the differences in ϕ between the numerical results (solid lines) and those based on Eq. **??** are less than 10^{-6} and the relative differences in $(\phi_{numerical} - \phi_{analytical})/(\phi - 1)$ are less than 1% at each time.

reduce the CMB spectrum depression at long wavelengths [34] since they try to estabilish a true (Planckian) equilibrium. For $z < z_p$ [34] [18] with

$$z_p \simeq 2.14 \times 10^4 \left(\frac{T_0}{2.7\,K}\right)^{1/2} \left(\frac{k}{1.68}\right)^{1/4} \widehat{\Omega}_b^{-1/2}\,, \tag{3.41}$$

low frequency photons are absorbed before Compton scattering brings them to higher frequencies.

In case of small and late distortions ($z_h \lesssim z_p$), a good approximation of the whole spectrum is given by [17]

$$\eta(x, \tau) = \eta_i e^{-(\tau - \tau_h)} e^{-(\tau - \tau_h)} \int_{\tau_h}^{\tau} e^{(\tau' - \tau_h)} \frac{1}{e^{x/\phi(\tau')} - 1} d\tau'$$

81

$$+u \frac{x/\phi_i e^{x/\phi_i}}{(e^{x/\phi_i}-1)^2}\left(\frac{x/\phi_i}{\tanh(x/2\phi_i)}-4\right), \tag{3.42}$$

where the index i denotes the initial value of the corresponding quantity and u is the Comptonization parameter. This expression provides also an exhaustive description of continuum spectral distortions generated in various scenarios of (standard or late) recombination or associated to the cosmological reionization. For an initial blackbody spectrum, at dimensionless frequencies $x_B \ll x \ll 1$ the above equation can be simplified and reduces to [17]

$$\eta \simeq \eta_{BB,i} + \frac{y_B}{x^3} - u\frac{2}{x/\phi_i}\,; \tag{3.43}$$

here y_B, an optical depth of the universe for bremsstrahlung absorption (radiative Compton can be neglected at late epochs), is analogous to the Comptonization parameter and it is given by

$$y_B = \int_{t_h}^t (\phi - \phi_i)\phi^{-3/2} g_B(x,\phi) K_{0B} dt = \tag{3.44}$$

$$\int_{1+z}^{1+z_h} (\phi - \phi_i)\phi^{-3/2} g_B(x,\phi) K_{0B} t_{exp} \frac{d(1+z)}{1+z}\,;$$

x_B is the frequency at which $y_{abs,B} = 1$ [151] [39]. The dependence of the Gaunt factor ([71],[122],[18]) on x and ϕ at very long wavelengths is weak: $g_B \propto \ln(x/\phi)$.

In terms of brightness temperature, the distortions at low frequencies (at any redshift) could be written as

$$\frac{T_{br} - T_r\phi_i}{T_r} \simeq \frac{y_B}{x^2} - 2u\phi_i\,, \tag{3.45}$$

where $T_r = T_0(1+z)$. This approximation holds at low frequencies but not at extreme low frequencies, where the brightness temperature obviously approaches the electron temperature because of the extreme efficiency of bremsstrahlung still able to generate a Planckian spectrum at electron temperature.

In order to show that our numerical solution follows the behaviour described by the last equation, we can compute y_B from the brightness temperature derived from the numerical solution:

$$y_B \simeq x^2\left(\frac{T_{br} - T_r\phi_i}{T_r} + 2u\phi_i\right). \tag{3.46}$$

The reported numerical result (see Fig.3.4) refers to a heating process corresponding to a full reionization starting at $z \simeq 20$ with $\phi = 10^4$ K,

producing a final Comptonization parameter $u \simeq 4 \times 10^{-6}$ compatible with FIRAS upper limit. As shown in Fig.3.4, at low frequencies y_B approaches an almost constant value with varying frequency. This is correct only for $\lambda > 200 - 300$ cm while at higher frequencies y_B is no longer almost constant because of the dependence of the Gaunt factor on x and ϕ as expressed in the definition of y_B. We can also write an expression describing the brightness temperature through a constant parameter $\bar{y}_B$, derived from Eq. **??** (see Fig.3.4 bottom panel) averaged over the range at very long frequencies before the y_B declining shown in the lower panel of Fig.3.4, to verify the accuracy of the below expression

$$T_{br,y_B} = \left(\frac{\bar{y}_B}{x^2} - 2u\phi_i + \phi_i \right) \cdot T_r \tag{3.47}$$

in comparison with the numerical results. Note that where the Gaunt factor dependence on x and ϕ produces a significantly varying y_B (see Fig.3.4 top panel), the Comptonization decrement is more relevant than the free-free excess in determining the brightness temperature, as evident from the good agreement of the two curves in Fig.3.4 (bottom panel). Clearly, the brightness temperature derived in this way works only up to frequencies (~ 100 GHz) approaching that at which the excess in the brightness temperature produced by the Comptonization begins (at ~ 220 GHz, $\lambda \sim 0.13$ cm see Fig.3.4 bottom panel). Note also that, the uses of $\bar{y}_B$ is Eq. (3.47) implies a slight excess with respect to the accurate numerical results since y_B decreases with the frequency (see Fig.3.4 upper panel). In this representative test, the excess is ~ 0.02 mK. This error is clearly negligible for the analysis of current data (see, e.g., [124]) It is also negligible for the analysis of future measures at $\lambda \gtrsim 1$ cm with accuracy comparable to that proposed for DIMES [74, 25].

On the contrary, it could be relevant for a very accurate analysis of future measures at $\lambda > 1$ cm with accuracy comparable to that proposed for FIRAS II [56, 26]. This calls for a complete frequency and thermal history dependent treatment of the free-free distortion in the accurate analysis of future data of extreme accuracy.

3.6 Some cosmological applications

We saw that before the thermalization redshift, $z_{therm} \sim 10^6 - 10^7$ (the exact epoch depends on the baryon density and on H_0), any kind of energy injection has no consequences on the spectrum of the CMB. More
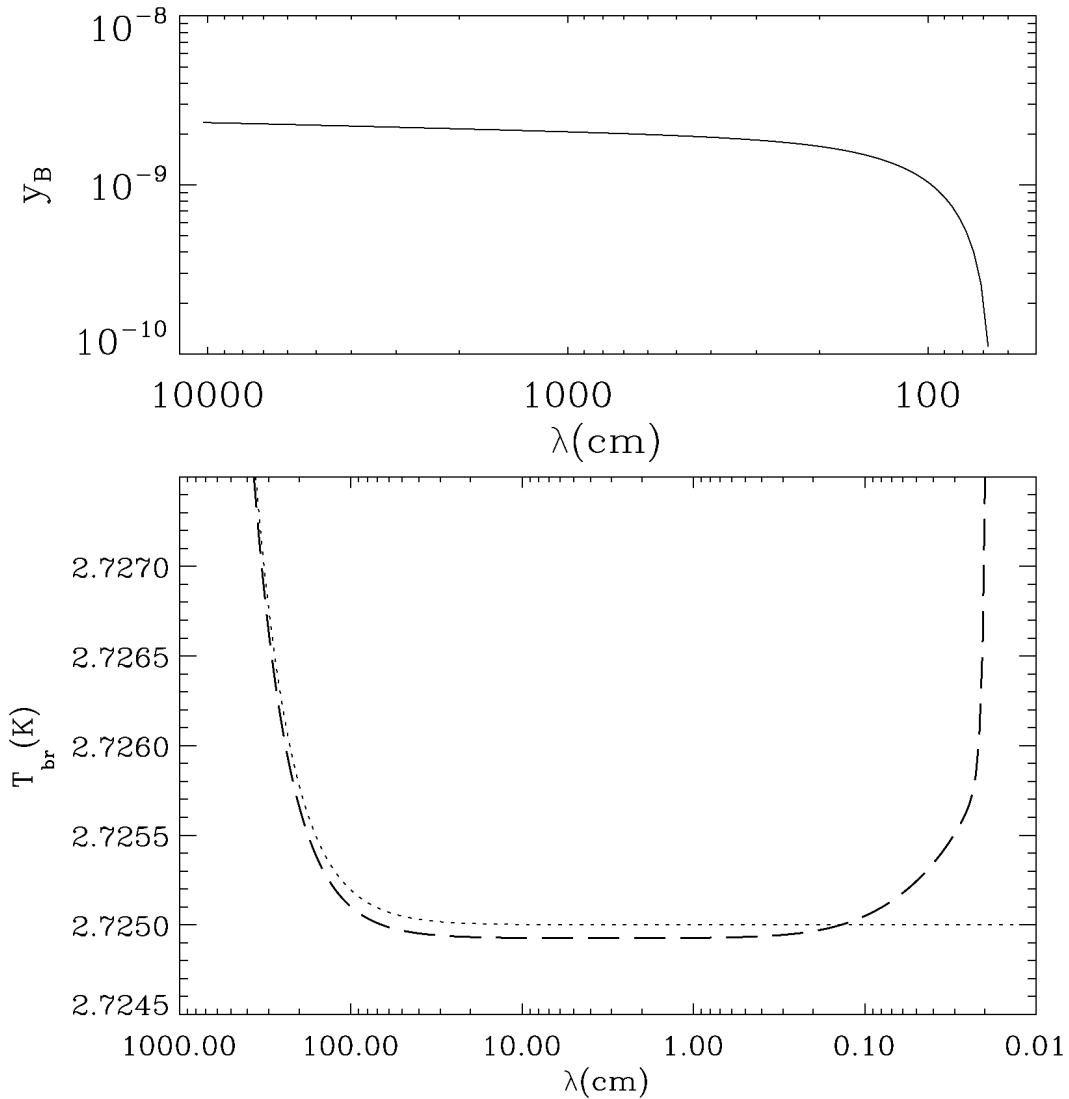
Figure 3.4: Top panel: y_B as derived from Eq. 3.46. Bottom panel: comparison between the numerical (long dashes) solution and the analytical approximation represented by Eq. 3.47. See the text for further details.

in detail, even if a big amount of energy is injected, the thermodynamic equilibrium between matter and radiation is soon re-established because of the high efficiency of the photons production processes, coupled to the photons migration to high frequency due to Compton scattering. After that particular redshift (that corresponds approximately to the first year of life of the Universe), if an energy injection occurs, the features of the distortion induced depends strongly on the epoch of the injection. Indeed, an energy release occurred at a redshift $z_{therm} < z < z_{BE}$ could leave an imprint on the CMB spectrum and the resulting one is well described by a Bose-Einstein spectrum, while if the heating occurs before recombination, but not near to z_{BE} in time, then the resulting spectrum is described by a

superposition of blackbodies. These two are the only two asymptotic limit in which the Kompaneets equation could be resolved analytically. In this section, starting from the most primordial possible energy injections, I will show some interesting applications of the code KYPRIX [114][115].

3.6.1 Distortions at $z \gtrsim z_{BE}$

Once the *thermalization epoch* termined, in case of energy injection, the CMB spectrum is described by

$$\eta_{BE} = \frac{1}{e^{x/\Phi_{BE}+\mu} + 1} \tag{3.48}$$

where $\mu(x) = \mu_0 e^{-x_c(z_{BE})/(x/\Phi_{BE})}$ is the dimensionless chemical potential, $\Phi_{BE} \simeq (1 - 1.11\mu_0)^{-1/4}$ and $\mu_0 \simeq 1.4\Delta\epsilon/\epsilon_i$ in the limit in which $\mu_0, \Delta\epsilon/\epsilon_i \ll 1$. The characteristic dimensionless frequency x_c is the solution of the equation $t_{abs} = t_C$, computed at z_{BE}, where t_{abs} is the joined absorption time for Bremsstrahlung and radiative Compton, while t_C is the time scale to reach the kinetic equilibrium between matter and radiation.

The contribution of the radiative Compton is very effective at high redshifts. The following results come from integrations starting at a redshift corresponding to $y(z) \simeq 5$

3.6.2 Distortions at $z_{BE} > z \gg z_{rec}$

For energy injections occurring in the period between the two asymptotic limit cases, the solution of the Kompaneets equation can be found only numerically and even if some analytical approximations were found [17], these are true only under determined conditions.

Just after the heating process, the initial spectrum of the photons is assumed to be a superposition of blackbodies:

$$\eta(x, y^*) = (4\pi y^*)^{-1/2} \int_0^\infty \eta_0(x')\exp\left[- \frac{(\ln(x/x') + 3y^*)^2}{4y^*} \right]\frac{dx'}{x'}, \tag{3.49}$$

where $\eta_0 = 1/[exp(x'/\phi_i) - 1]$, $\phi_i = T_i/T_r \simeq (1 + \Delta\epsilon/\epsilon_i)^{-1/4}$, and ϵ_i is the CMB energy density before the heating and y^* the comptonization parameter. Eq. 3.49 represents a comptonized spectrum, from a Planckian one, by hot electrons and, in case of small distortions, the shape of the spectrum is completely independent from a detailed description of the distribution function of the temperature.

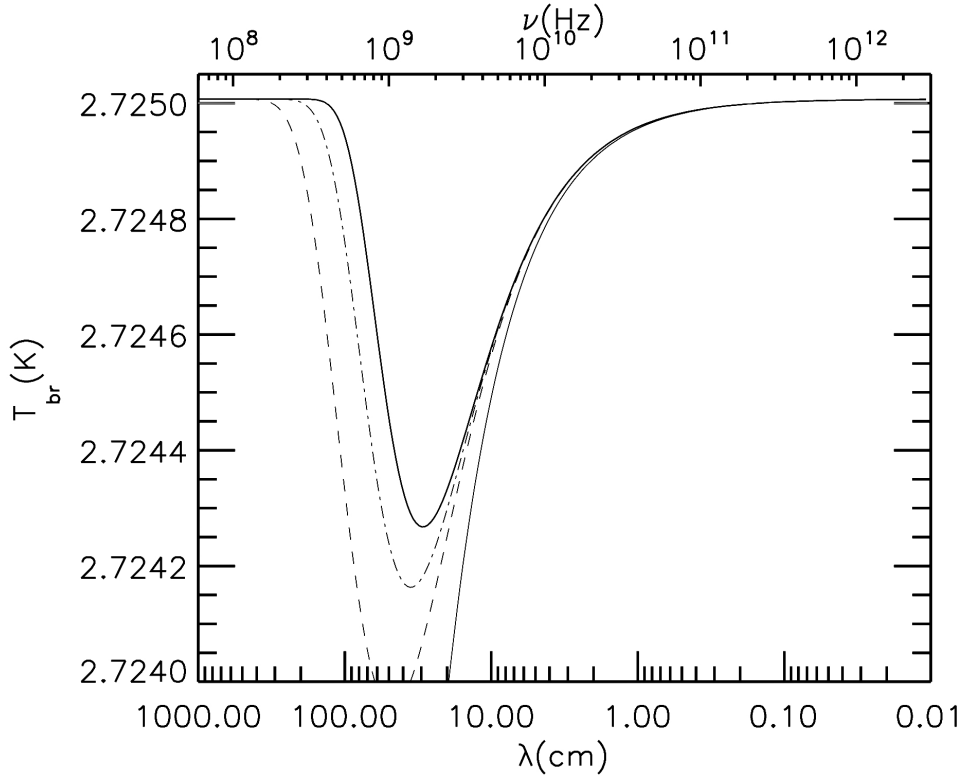The redshifts range in which this kind of distortion could occur is wide. From

Figure 3.5: Final distorted spectrum starting from a Bose-Einstein one. The related chemical potential is $\mu = 1 \times 10^{-5}$. An early energy injection occurred at redshift $z \sim 2.85 \times 10^5$, corresponding to an $y_h \simeq 4$. Cosmological parameters: $\Omega_b = 0.047, \Omega_\Lambda = 0.73, \Omega_m = 0.23, H_0 = 70$. For this simulation, the recombination process is assumed to be instantaneous.

the numerical integrations, the final spectrum results to have an intermediate shape, a sort of *mix* between a Bose-Einstein spectrum and a comptonized one. The presence and the depth of the well that recalls a chemical potential distortion depends strongly from the epoch at which the heating occurs.

3.6.3 Distortions at $z_{rec} \lesssim z \ll z_{BE}$

In this limit, the analytical results fits very well with the values for η obtained through the numerical integration. The integrations I made starts from redshifts corresponding to $y(z) < 1$. The initial spectrum is assumed to be a superposition of blackbodies. In this case, the low frequency *filling* due to Bremsstrahlung, depends strongly from the epoch at which the heating occurs and from the amount of fractional energy injected. With reference to the case treated in the next section, it turned out that at the epoch corresponding to the run of Fig. the recombination history had a negligible impact on the final spectrum.
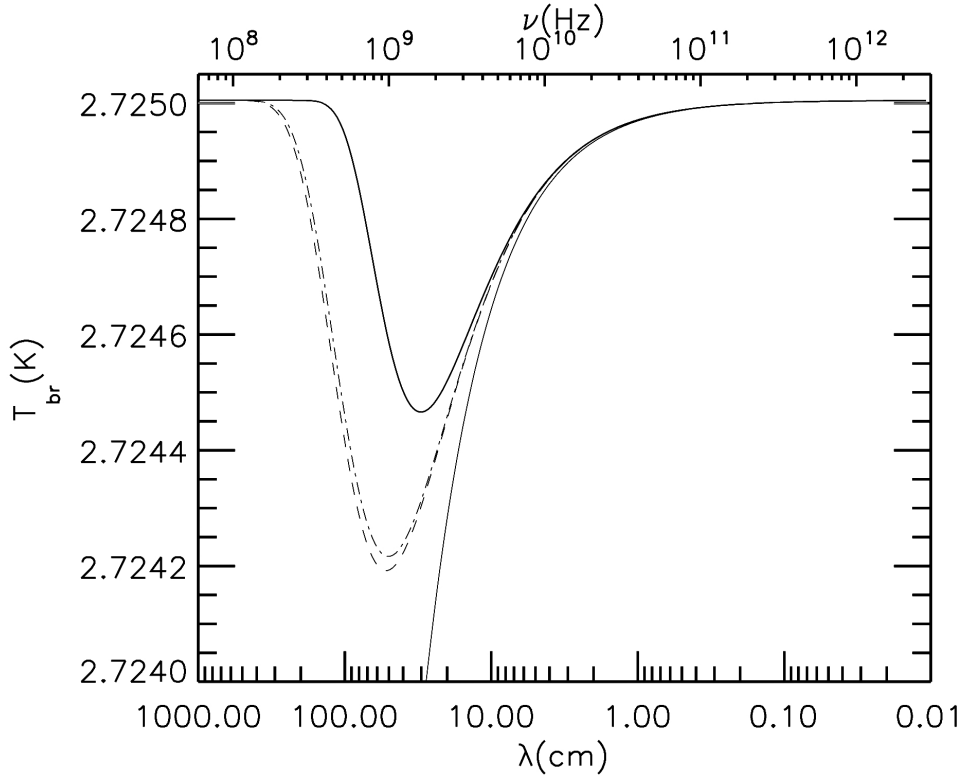
Figure 3.6: Final distorted spectrum starting from a Bose-Einstein one. An early energy injection of $\Delta\epsilon = 5 \times 10^{-6}$, that corresponds to a chemical potential $\mu = 7 \times 10^{-6}$, occurred at redshift $z \simeq 2.5 \times 10^{5}$, corresponding to an $y_h \simeq 3$. Cosmological parameters: $\Omega_b = 0.047, \Omega_\Lambda = 0.73, \Omega_m = 0.23, H_0 = 70$. For this simulation, the recombination process is assumed to be instantaneous.

3.6.4   Distortions at $z \sim z_{rec}$: impact of a recombination history

The principal results of the latest implementations to the code are those to probe in a more precise way the contribution of the photons production processes during the recombination.

The introduction of the ionization fractions for Hydrogen, Helium and electrons permitted to create an interface between KYPRIX and codes capable to provide a reionization history. In our case the code RECFAST was chosen. In particular, for the case here showed, I modified the output of RECFAST in order to have an ionization fraction history for each of the involved elements. Acting in this way, it is only necessary to create a crowded web for these values e redshifts coming from RECFAST, in order to have continuity of solutions for whatever values can take the redshift inside the integration routine of KYPRIX.

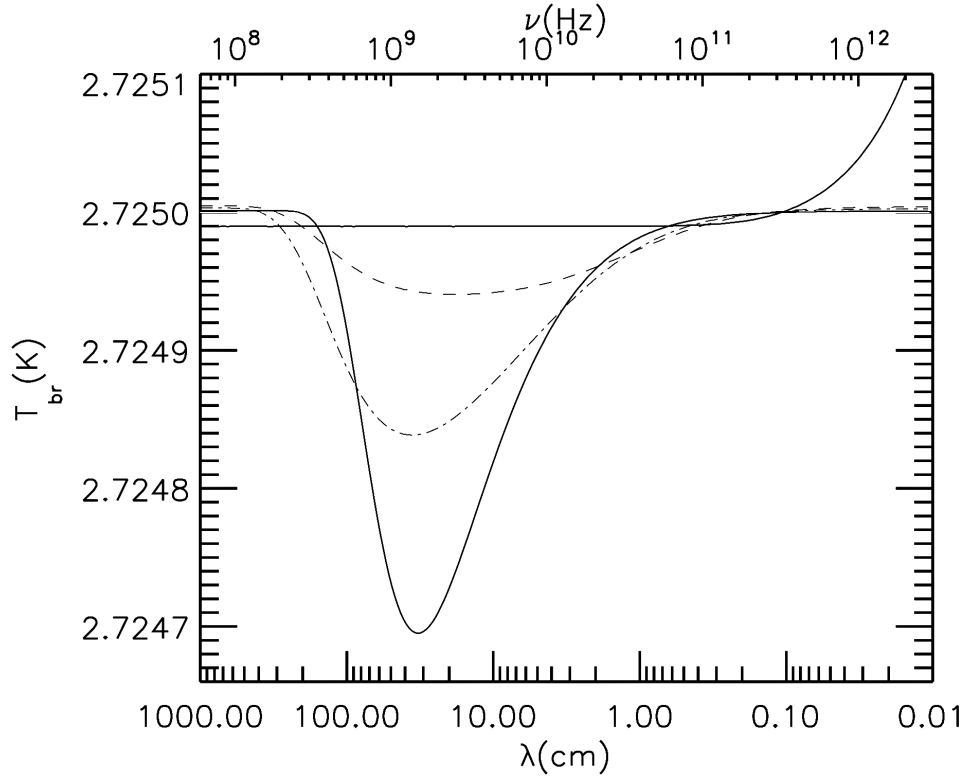The difference between Fig. 3.9 and Fig. 3.10 lies in the *type* of

Figure 3.7: Intermediate (dashed and dot-dashed lines) and final (solid line) distorted spectrum in the case of an energy injection occurred at $z < z_{BE}$, at an epoch corresponding to $y_h = 2.5$. The initial spectrum is represented by a superposition of blackbodies. The fractional energy injected is $\Delta\epsilon/\epsilon_i = 5 \times 10^{-6}$. The cosmological parameters are the same of the case in Fig. 3.6.

recombination used in the code. The non-instantaneous recombination used to simulate the spectrum in Fig. 3.10 allows the active processes to act with different effectiveness. In particular, Fig. 3.11 shows the difference of this two kind of history: it is the result of subtracting the final spectrum of the case with a gradual recombination from the case in which is activated an instantaneous recombination. The excess of photons at lower frequencies finds easily an interpretation: in the case of instantaneous recombination, the photon production process (at these epochs, only bremsstrahlung is effective) works with the maximum possible rate until recombination redshift is reached, because the species involved are assumed to be fully ionized; instead, the rate of photon production of the same process in the case of a recombination history is not so effective because the role of the ionization fraction, that allow a weaker production of photons (the production rate is proportional to the density of ions and electrons).

At higher frequency an similar argumentation could be found to explain the well that starts at the right end in Fig. 3.11. The Compton scattering
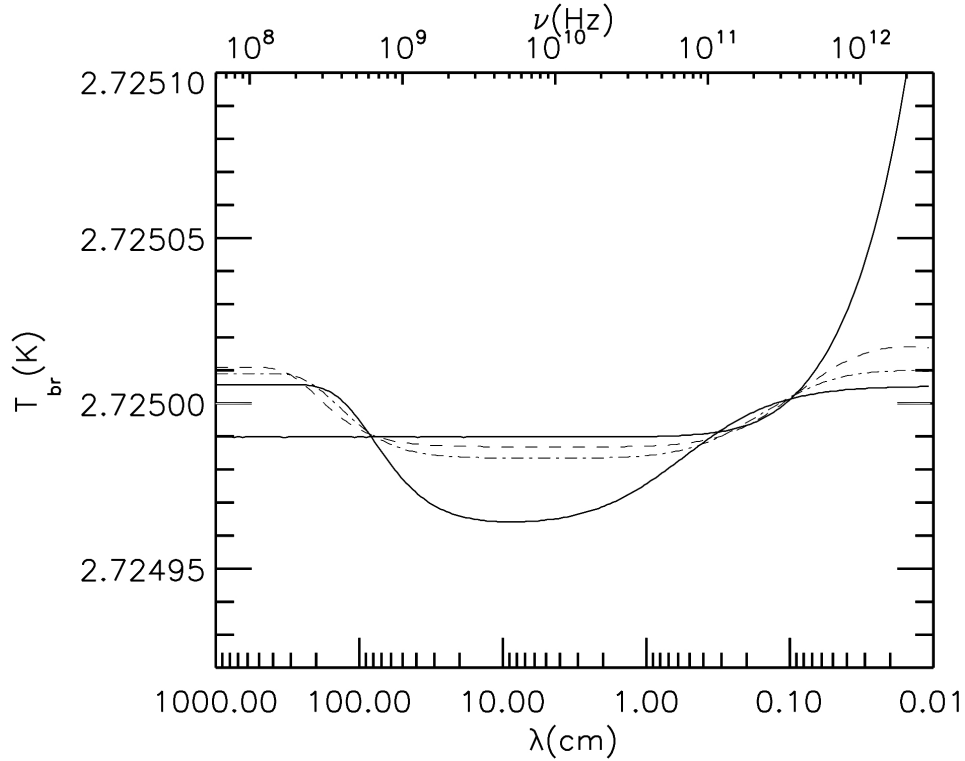
Figure 3.8: Intermediate (dashed and dot-dashed lines) and final (solid line) distorted spectrum in the case of an energy injection occurred at $z_{rec} \lesssim z \ll z_{BE}$, at an epoch corresponding to $y_h = 0.5$. The initial spectrum is represented by a superposition of blackbodies. The fractional energy injected is $\Delta\epsilon/\epsilon_i = 5 \times 10^{-6}$. The cosmological parameters are the same of the case in Fig. 3.6.

is more effective, in shifting photons to higher frequencies, in the case of a instantaneous and *fully ionized* recombination, while it loses effectiveness when the ionization fraction are considered (its rate is proportional to the free electrons). That's why the spectrum in Fig. 3.10 shows more photons at high frequency.

3.6.5 Distortions due to reionization process

In the previous chapter we saw that if the Universe pass through a phase of reionization this could leave imprints on any CMB observable. The available data from the WMAP satellite suggest a global reionization occurred at a redshift $z_{reion} = 11.0 \pm 1.4$. This epoch is derived from the observed optical depth $\tau = 0.087 \pm 0.017$ (WMAP data only). The reasons of the rise of this phenomenon can be traced in the context of a primordial star formation, such the one related to Population III stars, for example. The thermonuclear reaction caused by the matter gravitational collapse could heated the Universe, allowing reionization around the collapsed regions. To
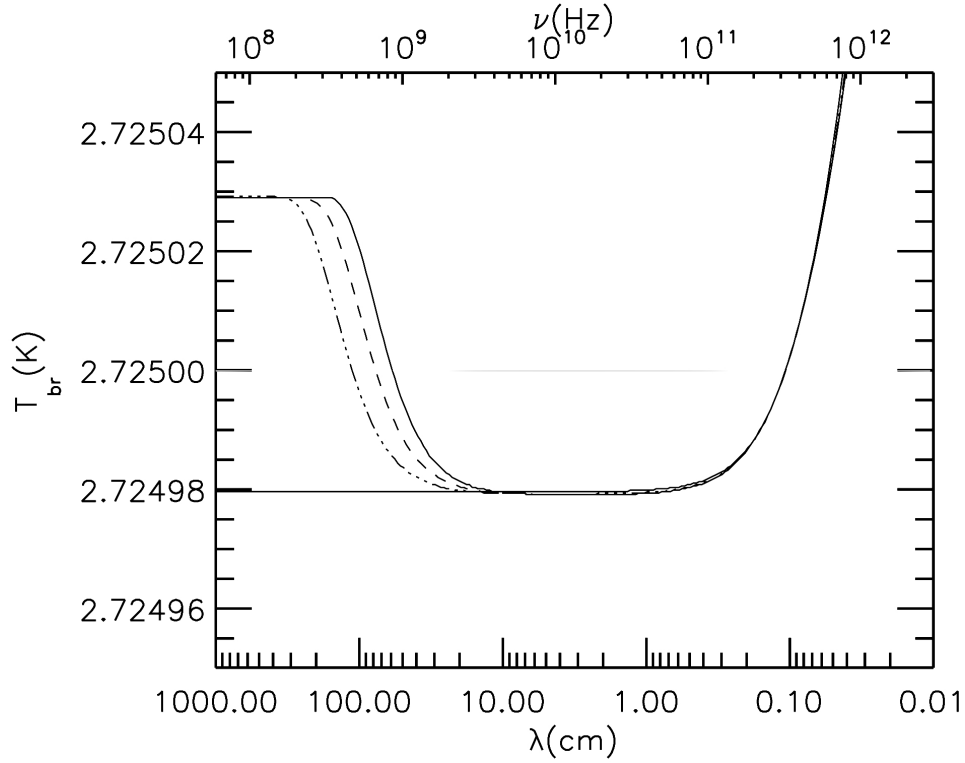
Figure 3.9: Final spectrum (solid line) for an energy injection occurred at redshift $z = 10^4$. The initial spectrum is a superposition of blackbodies and the amount of fractional energy injected is $\Delta\epsilon/\epsilon_i = 1 \times 10^{-5}$. Here an instantaneous recombination process is considered.

our eyes, the effect of such a event is that to move forward in time the LSS, because an heating of the photons implies a dramatic re-distribution of their energies and a consequent loss of informations regarding their previous *configuration*.

On the CMB spectrum the effects consist in formation of free–free and comptonization like distortions, related to the heating of the electrons of the ISM during the reionization phase. Furthermore, these distortions depends strongly on the thermal history of the ISM also and not only from the degree of ionization: the exchanges of energy between matter and radiation depend directly on the electronic temperature.

Here a reionization toy model was used to produce the results presented. The process is simulated through an instantaneous heating of the electrons, characterized from a fixed value for $\Phi = 10^4$.

The effect of a contribution of $\Lambda \neq 0$ is well visible through the tests done. The difference of depth between the two final spectra is $\Delta T \simeq 5 \times 10^{-5}$. The interpretation of such difference lies in the huge contribution that a $\Lambda \neq 0$ gives to he Universe evolution, during late epochs like the one considered
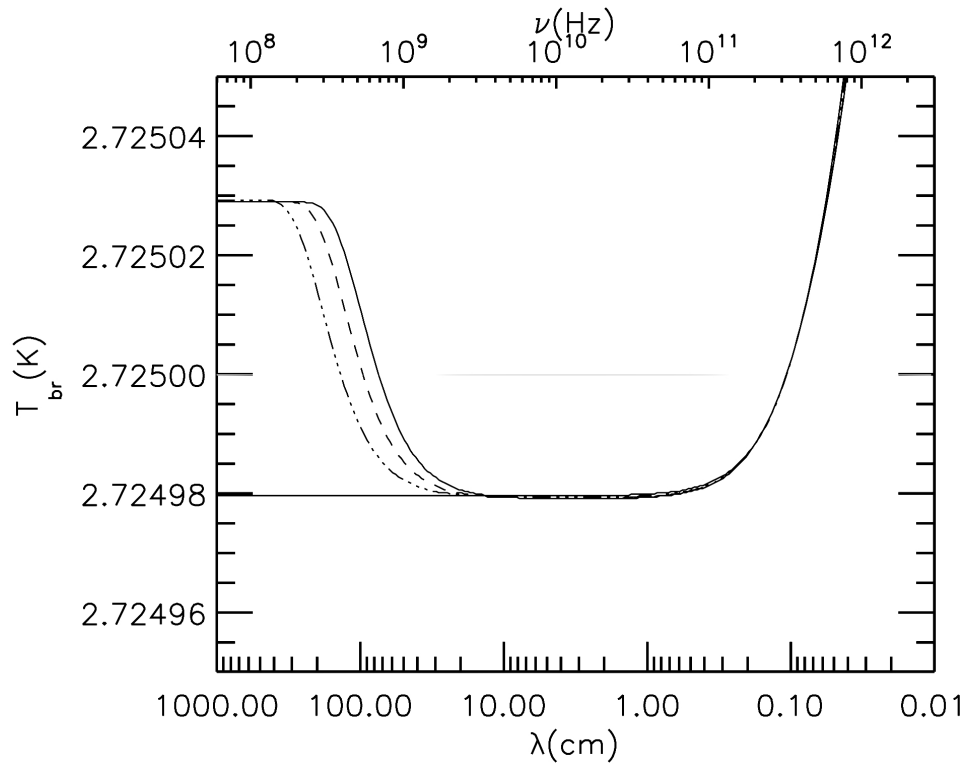
Figure 3.10: Same of FIg. 3.9, but the recombination process. A RECFAST simulation was used to recover the recombination history of the ionization fraction of electrons, H and He. See text for details.
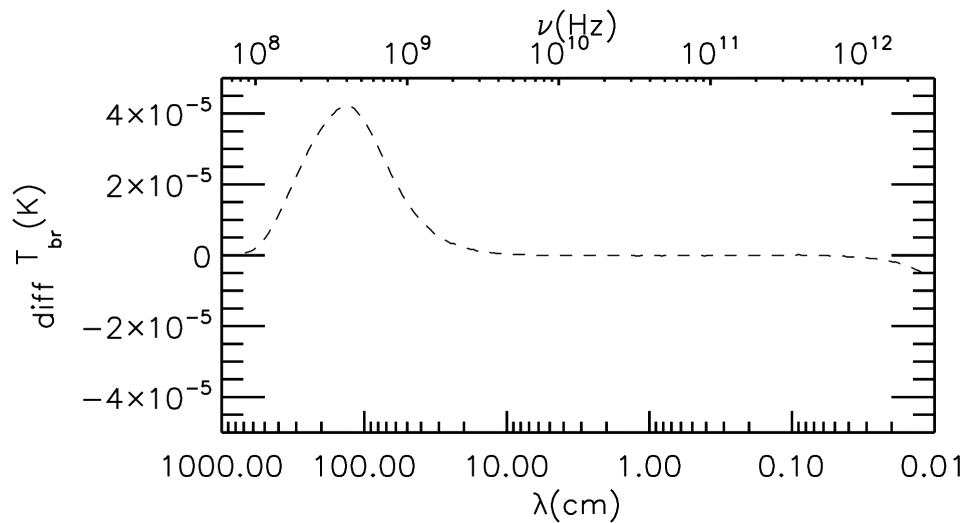

Figure 3.11: Result of the subtraction of the final spectrum of Fig. 3.10 from the final spectrum of Fig. 3.9. See text for details.

($z_{reion} \simeq 20$). Practically, the processes have more time to act, producing in this way a more prominent distortion.
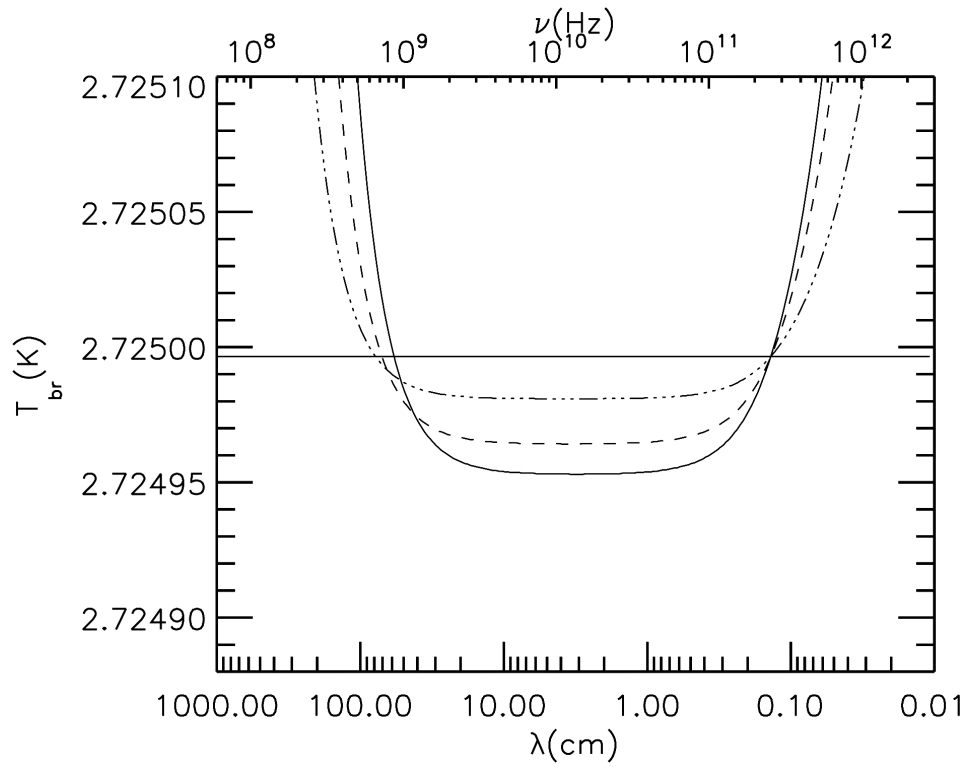
Figure 3.12: Reionization process simulation in an Universe with no Λ contribution. The initial spectrum is Planckian and a fractional energy injection $\Delta\epsilon/\epsilon_i = 5 \times 10^{-6}$ occurs during reionization. The final spectrum is represented by the solid line. The process starts at redshift $z \simeq 20$.
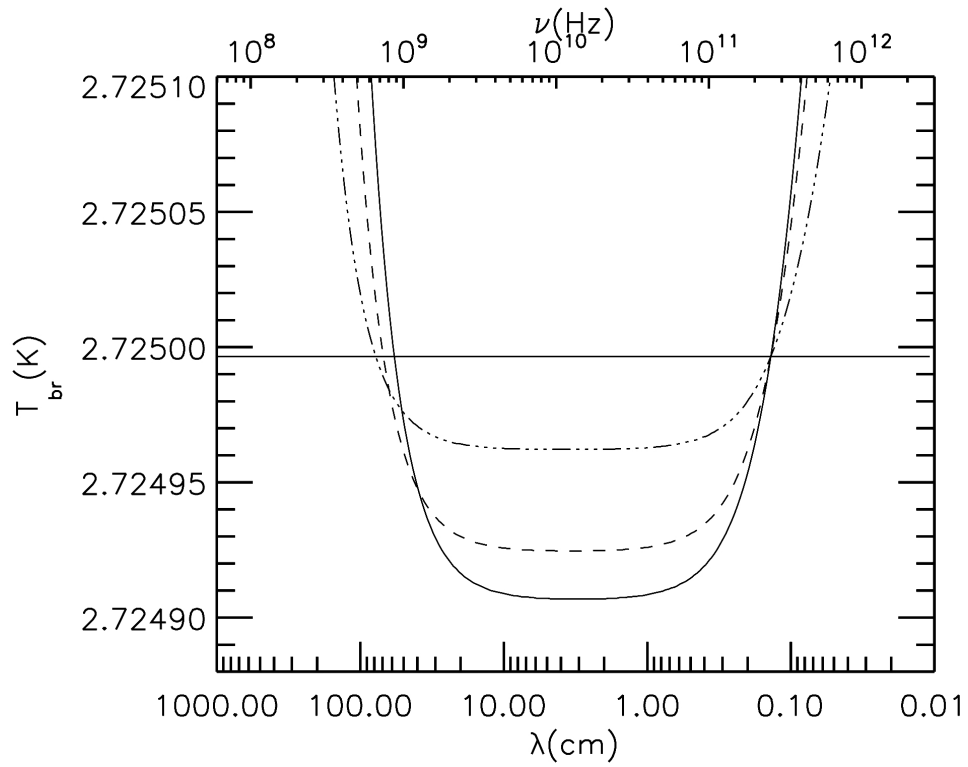
Figure 3.13: Reionization process simulation in an Universe with Λ contribution. Same integration characteristic of Fig. 3.12.

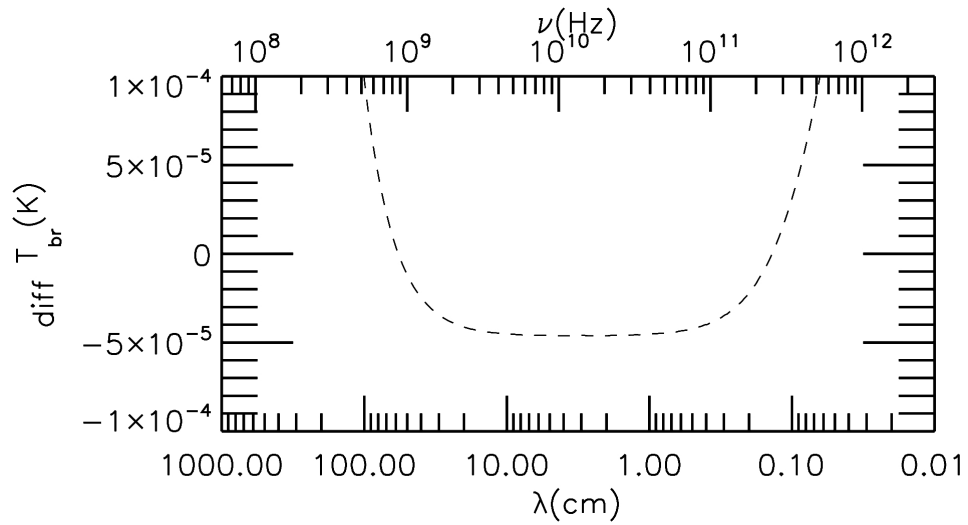

Figure 3.14: Difference in thermodynamic temperature between the two previous cases. See text for details.

Chapter 4

CMB measurements

4.1 Introduction

As previously said, definitive, very precise maps of the CMB are fundamental to fully characterize cosmological parameters and to constrain theories. Small error bars in the power spectrum and on the frequency spectrum let us to provide answers to recently rising questions about the nature and content of the Universe.

The observation of the CMB is crucial for more than one reason. First of all, its signal is weak, as said, its absolute temperature is measured to be 2.725 ± 0.002 K. No detection of spectral distortions is recorded to date, the upper limit imposed by FIRAS measurements on the key parameters for possible spectral distortion are: $|\mu| < 9 \times 10^{-5}$ for the chemical potential (characterizing a Bose-Einstein like spectrum) and $|y| < 15 \times 10^{-6}$ for what concern the Comptonization parameter (that characterize a superposition of black bodies or a Comptonized spectrum) [56].

On the other hand, the detected fluctuations from the mean temperature are on a scale of $\Delta T/T \sim 10^{-5}$ and after the first detection, by the COBE Differential Microwave Radiometer [133], the missions that followed aimed to observe these fluctuations with an ever better resolutions, in order to probe the smallest angular scale possible, with the consequent results on constraining the cosmological parameters of the standard model.

The *newest* discover about CMB observables is its polarization. The CMB was predicted to be weakly polarized (5-10 %). The first detection came out in 2002, through the observation made by the DASI interferometer [81]. A further indirect indication of the polarized signal was detected from the one-year WMAP data [76], through the cross-correlation with temperature anisotropies, followed by a polarization analysis made on the WMAP three-

years data [104].

Another complication regarding CMB measurements is the signal that came from spurious and unwanted emissions raising from our Galaxy and from extragalactic sources: the *foregrounds*. These emissions are the main limiting factors in the new generation CMB experiments and we will see the reasons of that in the next pages.

In this chapter, after a review of the past and future CMB dedicated experiments, it will be given an overview of the *Planck* mission, focusing on some details about the importance of monitoring foreground, to be followed in the next chapter, by a more deep presentation of the foregrounds features.

4.2 Observing the Background

Spectrum measurements

In Fig. 4.1 all the measurements done on the CMB absolute temperature are shown. The first observations of the CMB spectrum were made through ground based experiments. The signal coming out from the instrument of such experiments contains the combined contribution of Galactic and extra-Galactic sources' radiation, atmospheric emission, ground radiation and the cosmic background radiation (neglecting instrumental losses). The presence of an absorbing atmosphere degrades the received signal for two reasons: a reduction of the signal power is due to simple absorption, while a re-radiation at the atmosphere ambient temperature introduces a signal. Many results from ground-based experiments are collected in [35], and treating the errors on measures as standard deviations, a simple statistical analysis gives a CMB absolute temperature of 2.69 ± 0.08 K.

Before the coming of the COBE space mission, and before the COBRA rocket measurements [61], the observations based on the analysis of the molecular absorption lines, provided measurements of the CMB absolute temperature with good precision. It must be noticed, that this method allows to probe, in a direct way, the homogeneity of the CMB: in a FRW Universe, the temperature of the background scales with redshift as $T_{CMB}(z) = T_{CMB}(0)(1 + z)$, where $T_{CMB}(0)$ is the nowdays CMB temperature. Anyway, to measure the blackbody temperature at redshifts higher than 1, it is better to use atomic fine-structure transitions in absorbers toward high redshift quasars [9]. Many observations used the C I, because the energy levels in its fine structure levels are closer compared to other abundant

species. The main difficulties in this kind of measurements are: on one side, the fact that the absorption lines of the C I ground state are often weak and difficult to detect in quasar absorbers at high redshifts, on the other side, non-cosmological sources can also populate the excited fine-structure levels interested. Also for these reasons, the excitation temperature derived in such way, is an upper limit to the CMB temperature, unless the *degeneracy* due to the source of excitation is broken.

Another kind of measurements involve the observation of the rotational energy states of some molecules, common in the interstellar medium, like CN, CH and CH^+: these energy states are so low that can be populated by CMB thermal radiation. In general, it is calculated the ratio between two population with different rotational states through the Boltzmann equation:

$$\frac{N_b}{N_a} = \frac{g_b}{g_a} \exp[(E_a - E_b)/kT] \,, \tag{4.1}$$

where a and b are the two states, k the Boltzmann's constant, T the temperature and and N, g, E are the particles number, the statistical weight and the energy of the related state. Anyway, there is the possibility that other processes might alter the population ratios, like collisions between electrons and the CN molecules and this could bring to overestimate the excitation temperature and so T_0.

The COBRA instrument was launched in 1990. It started observing the sky when the rocket was at 150 km altitude in the ascent phase until it was 100 km in descent phase, with a maximum value for the altitude of 250 km. COBRA measured the CMB temperature in the frequency range $90 < \nu < 500$ GHz. The instrument compared the temperature of the sky T_{sky} with the radiation of a blackbody calibrator T_{ref} in this way: T_{sky} was directed to one side of a differential polarizing symmetric two-beam interferometer, while the other side of the instrument looked to the blackbody calibrator, through an identical telescope. The internal black body was calibrated after the launch, filling the the aperture of the sky telescope by an additional black body whose emissivity was more than 0.999 and whose temperature was possible to set between 1.8 and 4.2 K. The limit on the accuracy of the measures was determined by the discrepancy of these two calibrators, that is lower than ± 5 mK. The mean temperature observed from the rocket is 2.736 ± 0.017 K, in good agreement with the FIRAS data.

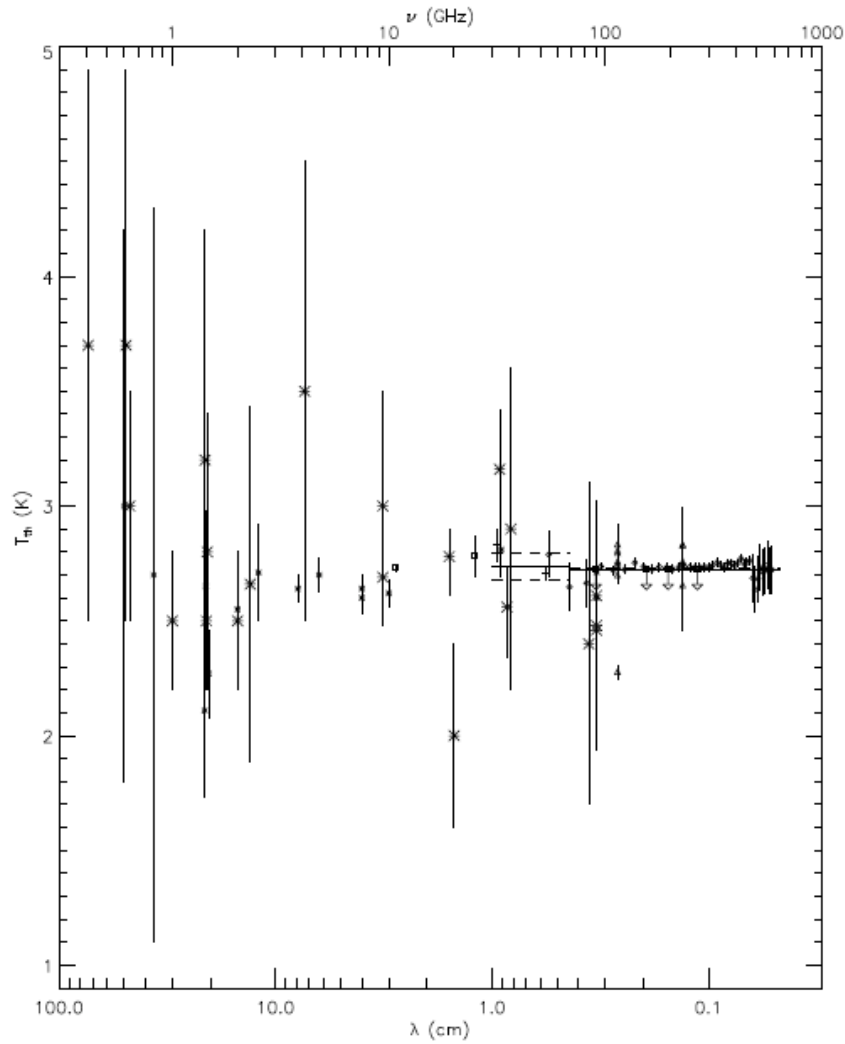To date, the best measurements of the CMB spectrum are those made

Figure 4.1: Plot of all measures of the CMB thermodynamic temperature. The big stars are the early ground measurements, the small stars the recent ground measurements, the squares the balloon measurements, the triangles the experiments with the CN molecular and the diamonds the COBRA data. The FIRAS data are plot as a solid line. Figure from [124]

through the FIRAS instrument (Far Infrared Absolute Spectrometer), aboard the COBE (COsmic Background Explorer) satellite. FIRAS was a polarizing Michelson interferometer operated differentially, with two input and two output ports, calibrated with an external black body having an estimated emissivity of better than 0.9999 [50]. One of the input ports, received signals from the sky horn, while the other from the reference horn, seeing an internal reference calibrator with an emissivity of $\simeq 0.98$. For the calibration, the sky horn was completely filled by the external calibrator, isothermal to better than 1 mK at 2.7 K, with a consequent uncertainty on the spectrum of approximatively 10 parts per million.
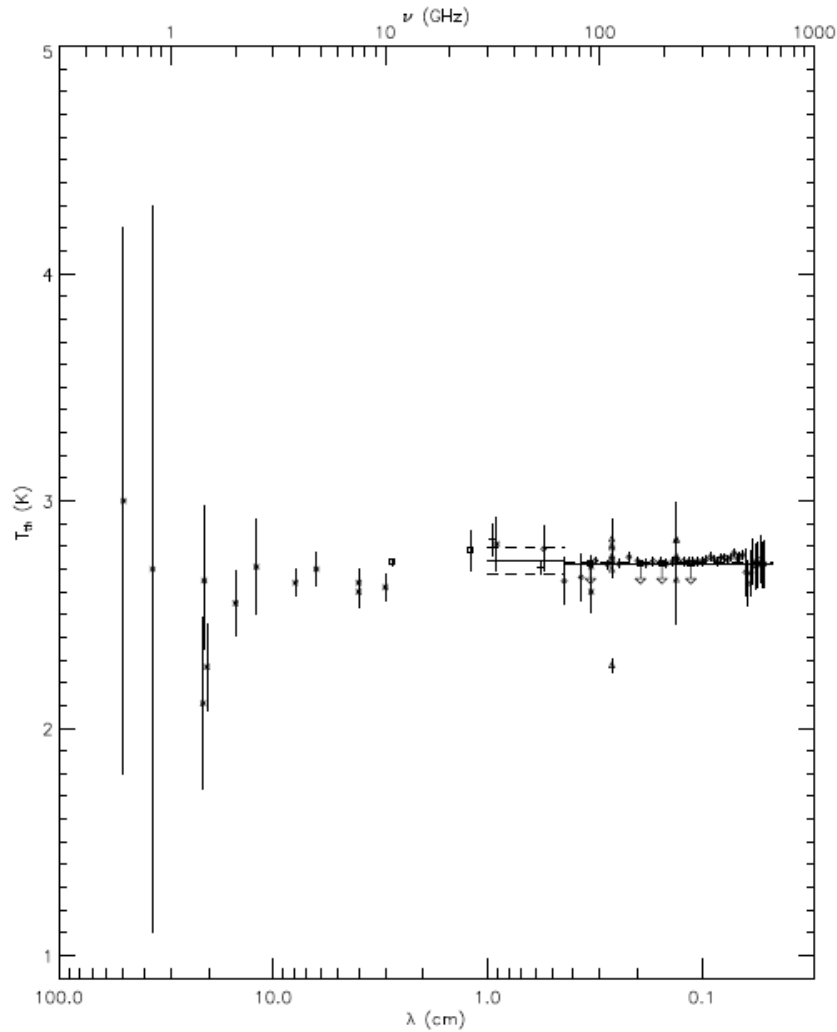
Figure 4.2: Plot of the more recent measures of the CMB thermodynamic temperature. The small stars the recent ground measurements, the squares the balloon measurements, the triangles the experiments with the CN molecular and the diamonds the COBRA data. The FIRAS data are plot as a solid line. Figure from [124].

The first analysis of the FIRAS data was made on a frequency range spanning from 1 to 20 cm^{-1} and it gave a temperature of 2.735 ± 0.06 K [92]. Successive more refined analysis improved the calibration (bias of some pixels corrected, effects of Cosmic Rays hits removed, different weighting for the pixels mostly affected by glitches) and gave an absolute temperature of 2.726 ± 0.004 K (95% CL) [93].

A following re-processing of the FIRAS data supplied a CMB temperature of 2.728 ± 0.004 K (95 % CL) [52]. The derivation of this value was obtained by the combination of three methods used on the dataset. One of these consisted in using the preflight calibration of the external calibration thermometers

and it gave a temperature of 2.730 ± 0.004 K and the error is practically determined and dominated only by the absolute calibration error on the external calibrator. Another method used the collected data to determine the temperature scale. The uncertainty on the frequency, 0.03%, generates an uncertainty on the temperature of 0.82 mK. This way provided a value of 2.7255 ± 0.0009 K. In the third method, the CMB itself was used. The basic assumption is that the dipole is the result of a Doppler shift. As consequence, that the shape of the differential spectrum should be dB_ν/dT, where $B_\nu(T)$ is the Planck function and the derived temperature showed a value of 2.717 ± 0.007 K, with the uncertainty dominated by the ones concerning the fitting of the Galaxy radiation, which contributes in a modulation of the dipole (see Fig. 4.3 for an example of two subsequent FIRAS calibrations).
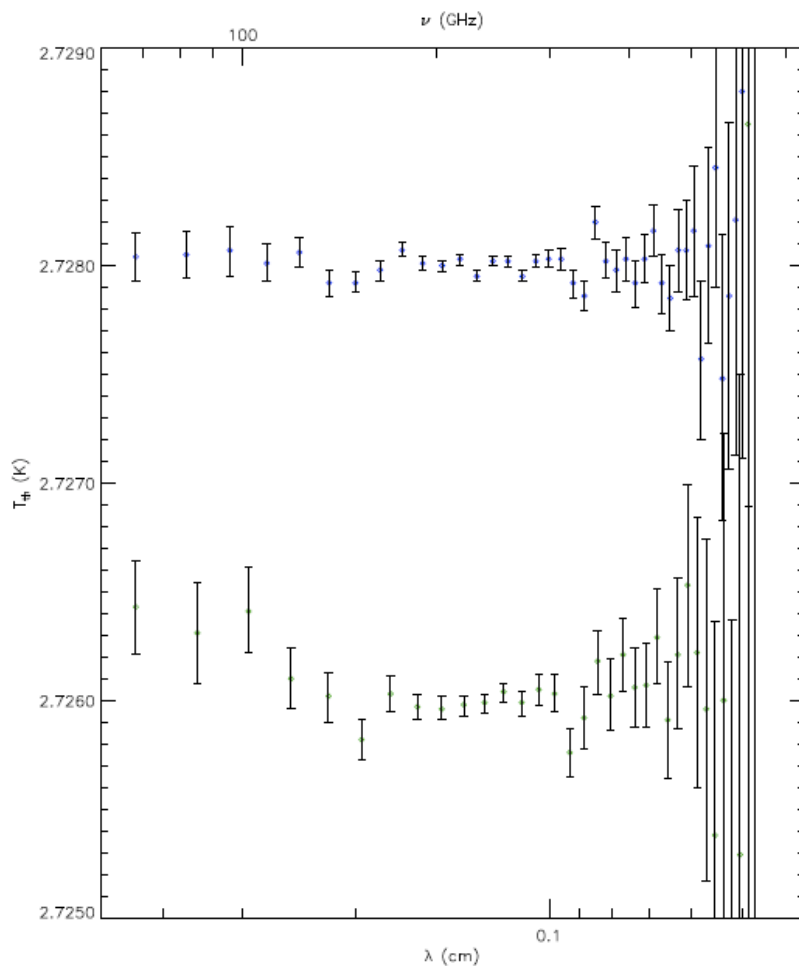

Figure 4.3: A comparation between the FIRAS data reported by Mather et al. (1994) and the more refined analisis of these by Fixsen et al. (1996). Figure from [124]

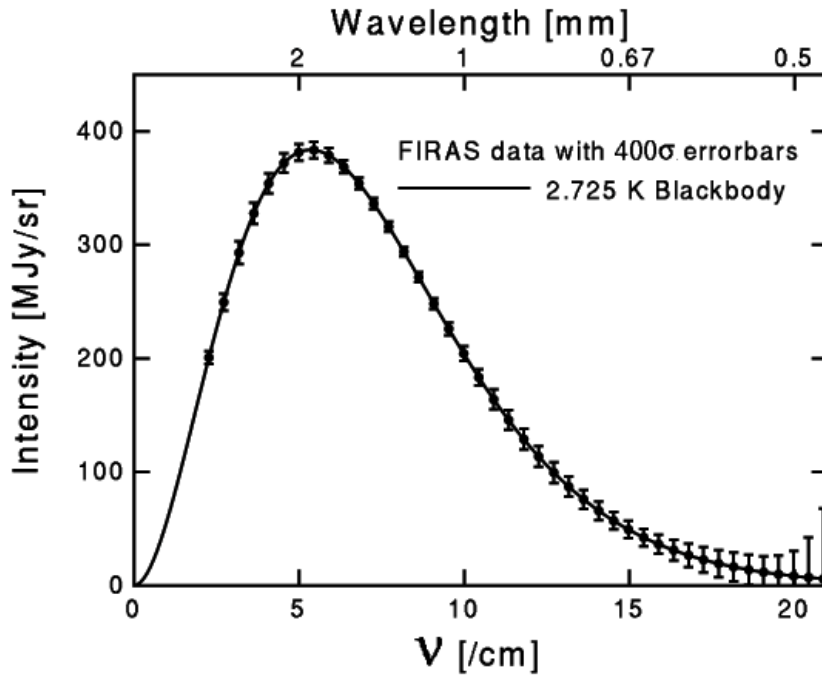The most recent re-processing of the calibration data provided an

Figure 4.4: The COBE/FIRAS spectrum overplotted on a 2.725 K. Error bars are magnified by a factor 400. Figure from [7]

absolute temperature of 2.725 ± 0.002 K [94] (see FIg. 4.4). They newly analyzed the performance of the FIRAS black body calibrator and reduced the estimate of systematic errors. The final constraints on the distortions parameters are: $|\mu| < 9 \times 10^{-5}$ and $|y| < 15 \times 10^{-6}$. Anyway, these parameters, and the observational limits on them, depend on the shape of the spectrum and not on the value of the absolute temperature.

The Absolute Radiometer for Cosmology, Astrophysics, and Diffuse Emission (ARCADE) is one of the most recent mission dedicated to the observation of the CMB spectrum. It is a balloon-borne instrument which measured the radiometric temperature of the sky at 10 and 30 GHz (ARCADE), and at six frequencies, ranging from 3 to 90 GHz (ARCADE II) [130]. The measurements done during the first scientific flight of ARCADE gave an absolute CMB temperature of 2.721 ± 0.01 K at 10 GHZ and 2.694 ± 0.032 K at 30 GHz [55].

The goal was not only to measure the CMB signal, but also to observe Galactic diffuse emission. The sky was observed at Galactic latitude of $13° < b < 83°$ and most of the observations were taken at $b > 35°$. The models mainly used to estimate the Galactic contaminations are those derived from the WMAP data for synchrotron, free-free and dust emissions, scaled for ARCADE

frequencies using the spectral index derived from the WMAP 23 and 33 GHz. Considering the frequency coverage of the mission, the uncertainty on the zero level of the foreground emission is dominated by the uncertainty on the synchrotron spectral index β: simply scaling the synchrotron zero level as $T_{sync}(\nu/408\text{MHz})^\beta$ with $-3.2 < \beta < -2.7$ the estimates on the temperature give values between 0.7 and 3.5 mK at 10 GHz. The free-free emission from ionized gas was traced and estimated through the H_α emission from the same gas [47], whose contribution is rated to be 0.04 mK at 10 GHz, while the thermal dust emission estimates, at the same frequency, suggest a temperature of 1μK at $|\beta| > 75°$ [48].

The newest results from ARCADE II suggest an excess at low frequencies [54]. In particular the excess is seen in the 3.3 and 8 GHz channels. The amount is of 50 ± 7 mK at 3.3 GHz and it is interpreted as an unknown extragalactic contribution. The exclude the effects of systematic errors, thanks to the high control on them; the radio sources count is not responsible for this signal as well, because it is expected to rise at lower frequencies. Anyway, in their paper they also exclude the possibility of a free-free distortion of the CMB spectrum because their models don't fit the data.

Temperature anisotropies measurements

The initial theoretical estimates of temperature fluctuations can be dated in the 60′ s and in the following years, characterized by a predicted contrast scale to an upper limit of $\Delta T/T < 10^{-3}$. The first detection was claimed in 1992, by the COBE DMR team [133] and it was the ticket for the Nobel prize for G.F. Smoot and J.C. Mather (2006). The COBE satellite was launched November 18, 1989 and carried three instruments, a Diffuse Infrared Background Experiment (DIRBE) to search for the cosmic infrared background radiation, a Differential Microwave Radiometer (DMR) to sensitively map the cosmic radiation anisotropies, and a Far Infrared Absolute Spectrophotometer (FIRAS) to compare the spectrum of the cosmic microwave background radiation with a precise blackbody. Each of these instruments gave a huge contribution to the richness of our cosmological model. The already mentioned FIRAS features and results are not mentioned here.

- With its ten frequencies, ranging from 1.25 to 240 μm, the DIRBE instrument was designed to carry out a search for the cosmic infrared background (CIB), providing maps of the infrared absolute sky brightness. The CIB was detected both by DIRBE and FIRAS. This

signal contains the cumulative emissions of stars and galaxies dating back to the epoch when these objects first began to form.

- The CMB was found to have intrinsic "anisotropy" for the first time, at a level of a part in 100,000. These tiny variations in the intensity of the CMB over the sky show how matter and energy was distributed when the Universe was still very young. These early structures, seen by DMR, are the seeds from which born galaxies, galaxy clusters, and the large scale structure that we see in the Universe today.

The results from COBE opened the road for a new cosmology era. Before the coming of the second generation CMB dedicated space mission, many other ground based and balloon borne experiments were realized.
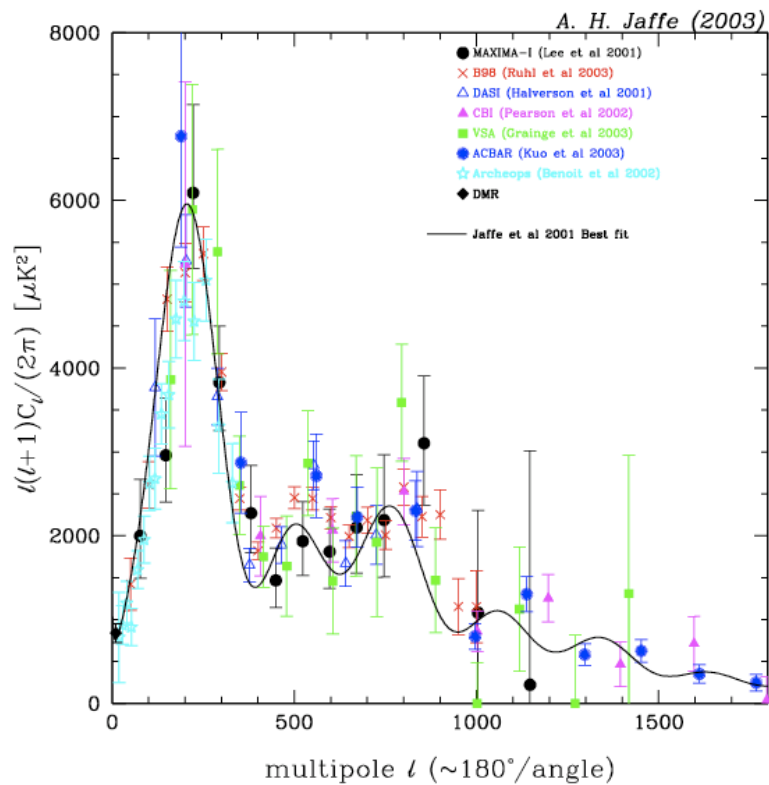

Figure 4.5: Measurements on the temperature angular power spectrum of the CMB from various experiments.

Among the others, big results have been obtained from: ARCHEOPS [11], a balloon borne experiment based on bolometers receivers at frequencies of 143, 217, 353, 545; ACBAR [119], a ground based bolometer array receiver capable of measuring the CMB anisotropies from angular scales corresponding to $\ell = 200$ to $\ell \sim 3000$. It extended the frontier of CMB

anisotropy measurement to angular scales more than a factor of two finer than that achieved with previous experiments; BOOMERANG [31], [38], [37], a balloon borne experiments, flown around Antarctica in two separate flights (the first in 1998, the second in 2003) to map the CMB, providing with the first flight data the first *high resolution* map of the CMB anisotropies, for a patch of the sky with low foreground emissions; COSMOSOMAS [57], dedicated to mapping COSMOlogical Structures On Medium Angular Scales and diffuse emission of our Galaxy, provided considerable results at 11,12, 13, 15 and 17 GHz, showing also an anomalous emission at high Galactic latitude [64]; MAXIMA [136], evolved from the successful MAX experiment. To date, the most precise measurements on temperature anisotropies (and on polarization) are the datasets provided by the WMAP team [65], [104]. WMAP produced the first full-sky map of the microwave sky with a resolution of under a degree, producing a convincing consensus on the contents of the universe, confirming the existence of dark energy, and severely limiting the density of hot dark matter. The telescope's primary reflecting mirrors are a pair of Gregorian 1.4m $\times$ 1.6m dishes (facing opposite directions), that focus the signal onto a pair of 0.9m $\times$ 1.0m secondary reflecting mirrors, while the receivers are differential radiometer, sensitive to polarization. The five frequencies at which WMAP operates (23, 33, 41, 61, 94 GHz) permit a good measurement and a consequent effective subtraction of the foregrounds contributing at these frequencies (mainly synchrotron, free-free and dust emission) and providing the possibility to realize the more accurate full sky map of CMB anisotropies. The last release of cosmological parameters derived from WMAP data is shown in Fig. 4.6.

Polarization measurements

Predicted by the cosmological standard model, the first signal of polarization in the CMB radiation was detected in 2002 through the Degree Angular Scale Interferometer (DASI), observing from the NSF Amundsen-Scott South Pole station. DASI is an interferometer based on cooled HEMT amplifiers running between 26-36GHz, in ten 1 GHz channels. DASI has an instrumental response to E and B modes that is symmetric and nearly independent. For this reason, even if the B mode spectrum is predicted not to have a E mode like shape, in the analysis reported in [84] they assumed the modes to have the same spectrum, to preserve this symmetry.

A more precise measurements comes from WMAP data. The satellite has

WMAP Cosmological Parameters			
Model: lcdm+sz+lens			
Data: wmap5			
$10^2\Omega_b h^2$	2.273 ± 0.062	$1-n_s$	$0.037^{+0.015}_{-0.014}$
$1-n_s$	$0.0081 < 1-n_s < 0.0647$ (95% CL)	$A_{\rm BAO}(z=0.35)$	0.457 ± 0.022
C_{220}	5756 ± 42	$d_A(z_{\rm eq})$	14279^{+186}_{-189} Mpc
$d_A(z_*)$	14115^{+188}_{-191} Mpc	$\Delta_{\mathcal{R}}^2$	$(2.41 \pm 0.11) \times 10^{-9}$
h	$0.719^{+0.026}_{-0.027}$	H_0	$71.9^{+2.6}_{-2.7}$ km/s/Mpc
$k_{\rm eq}$	0.00968 ± 0.00046	$\ell_{\rm eq}$	136.6 ± 4.8
ℓ_*	$302.08^{+0.83}_{-0.84}$	n_s	$0.963^{+0.014}_{-0.015}$
Ω_b	0.0441 ± 0.0030	$\Omega_b h^2$	0.02273 ± 0.00062
Ω_c	0.214 ± 0.027	$\Omega_c h^2$	0.1099 ± 0.0062
Ω_Λ	0.742 ± 0.030	Ω_m	0.258 ± 0.030
$\Omega_m h^2$	0.1326 ± 0.0063	$r_{\rm hor}(z_{\rm dec})$	286.0 ± 3.4 Mpc
$r_s(z_d)$	153.3 ± 2.0 Mpc	$r_s(z_d)/D_v(z=0.2)$	0.1946 ± 0.0079
$r_s(z_d)/D_v(z=0.35)$	0.1165 ± 0.0042	$r_s(z_*)$	146.8 ± 1.8 Mpc
R	1.713 ± 0.020	σ_8	0.796 ± 0.036
$A_{\rm SZ}$	$1.04^{+0.96}_{-0.69}$	t_0	13.69 ± 0.13 Gyr
τ	0.087 ± 0.017	θ_*	0.010400 ± 0.000029
θ_*	0.5959 ± 0.0017 °	t_*	380081^{+5843}_{-5841} yr
$z_{\rm dec}$	1087.9 ± 1.2	z_d	1020.5 ± 1.6
$z_{\rm eq}$	3176^{+151}_{-150}	$z_{\rm reion}$	11.0 ± 1.4
z_*	1090.51 ± 0.95		

Figure 4.6: Cosmological parameters derived from WMAP data only for a ΛCDM model. Figure from [?]

mapped the full sky in Stokes I, Q, and U parameters at frequencies of 23, 33, 41, 61, and 94 GHz. They firstly detected correlations between the temperature and polarization maps significant at more than 10σ [77], then, with the increasing observations and statistics, they delivered a detailed polarization analysis [104]. Furthermore, WMAP detected a significant polarization level from foreground emission, in particular from Galactic synchrotron radiation and thermal dust emission. In the analysis they applied a Galactic mask, cutting out the 25.7% of the sky and showed that the high Galactic latitude rms polarized foreground emission ranges from $\approx 5\mu$K at 22 GHz to $\lesssim 0.6\mu$K at 61 GHz. In order to compare the magnitude of the CMB signal, the level of intrinsic CMB polarization for a ΛCDM model, considering an optical depth of $\tau = 0.09$ and a tensor to scalar ratio $r = 0.3$, are $\approx 0.3\mu$K for E-mode polarization and 0.1μK for the B-mode. In the foreground corrected maps, they detect $\ell(\ell+1)C^{EE}_{\ell=<2-6>}/2\pi = 0.086 \pm 0.029(\mu$K$)^2$ and they interpreted it as the result of the re-scattering of CMB photons by free electrons released during an

instantaneous reionization occurred at $z_r = 11.0^{+2.6}_{-2.5}$. No evidence for B-modes was seen, but a more stringent upper limit was derived, that is $\ell(\ell+1)C^{BB}_{\ell=<2-6>}/2\pi = 0.04 \pm 0.03(\mu\text{K})^2$ [104].

Further results were presented with the BOOMERanG 2003 flight, observing the 0.22% of the sky. The instrument was formed by four pairs of polarization sensitive bolometers operating in bands centered at 145, 245 and 345 GHz (the first CMB polarization detection made with bolometers) [99]. Using two independent analysis pipelines, they found a non-zero $\langle EE \rangle$ signal, for angular scales corresponding to $100 < \ell < 1000$, with a significance of 4.8σ, and estimated the $\langle EE \rangle$ APS. A 2σ upper limit for any $\langle BB \rangle$ contribution was derived to be 8.6μ (K)^2, while a 2σ upper limit of 7.0μ (K)^2 was fixed for the $\langle EB \rangle$ spectrum.

Among the others, previous upper limits were fixed with POLAR [72]: 10μK on both E- and B- mode polarization on angular scales greater than $7°$; PIQUE, a ground-based polarimeter operating at 90 GHz, yielded to a 95% confidence level flat band power limits of 14 and 13 μ(K)^2 on the amplitudes of the E- and B-mode angular power spectra, respectively [63].

4.3   Future missions

The possibility to measure or to provide upper limits on the distortions related parameters y and μ at level of 10^{-7} was hypothesized with the proposal of the FIRAS II mission [56]. Likely, it would be feasible to measure deviations from the Planckian shape with an accuracy and precision of 1 ppm, reaching the astrophysical limit set by our location in the Galaxy. The analysis of the main limitations to FIRAS is a key point for the new possible mission. An improved detector characterization, a more accurate control of the calibrator reflectance of light, a wider frequency band, a better control of the cosmic rays contamination, the use of reflectors to obtain a smaller beamwidth are some of the features that FIRAS II must have to be a leap forward than FIRAS. The proposed frequency coverage is from 2 to 120cm^{-1} (60-3600 GHz), with a resolution of 0.2cm^{-1} (6 GHz). A FIRAS like design limits the resolution, so an external off-axis parabolic mirror with 1 m of aperture would be provided. The mirror must be surrounded by absorbing walls of controlled temperature and the parabolic shape is to ensure that the beam spillover onto the black walls is extremely small. Detector would
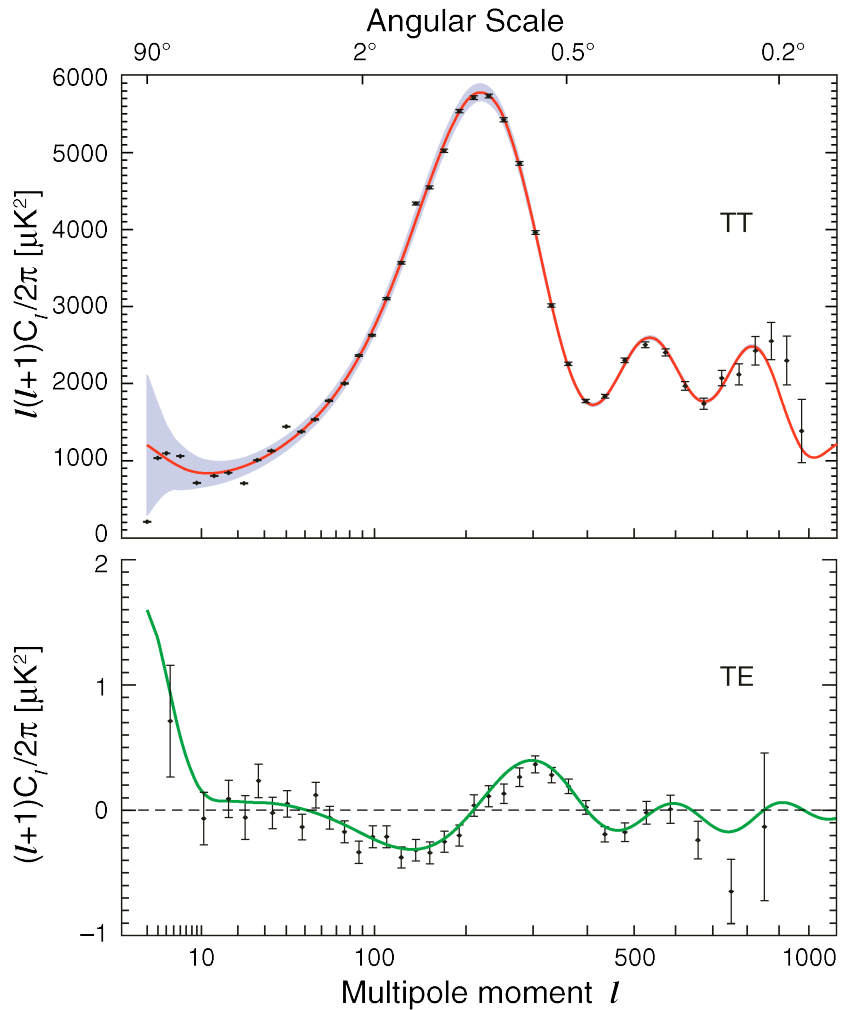
Figure 4.7: The WMAP five-year TT and TE power spectra. Figure from [4]

be four spiderweb bolometers, one for each polarization, and with optical efficiencies of 10% each of them would achieve a cosmic background photon noise-limited sensitivity of 10^{-17} W Hz$^{-1/2}$, that is about 100 times better than the FIRAS one.

The Diffuse Microwave Emission Survey (DIMES) [74] represents a complementary proposal to FIRAS II. The complementarity lies in the fact that the frequency coverage would fill the gap between the full-sky surveys at radio frequencies ($\nu < 2$ GHz) and the mm and sub-mm measurements done by COBE. The instrument consists of a set of narrow-band cryogenic radiometer ($\Delta\nu/\nu \sim 10\%$), each of them measures the power difference between sky through a beam-defining antenna of FWHM $\sim 6°$ and an internal reference load of controlled temperature. Further, each antenna sees alternatively the sky and a full-aperture target with an emissivity of $\epsilon > 0.9999$. This will eliminate instrumental signatures. The sensitivity

reached in 100 sec of integration is 0.1 mK.

For measures at wavelength $\lambda < 1$ cm, the equipment is not so large and as seen more could be gained by using dedicated satellites. For measurements at $\lambda > 1$ cm the instrument starts to be quite big and a satellite is no longer reasonable. Indeed, in the context of the Observation of the Universe from the Moon campaign the Italian Vision for Moon Exploration proposal [27] (in which I'm involved) include two possible missions with different *size* [24]. The large size experiment proposal consists in a multi-channels receiver with a frequency range coverage of $0.4 - 50$ GHz, a spectral resolution of 10%, an angular resolution of $7° - 8°$ (FWHM), a sensitivity < 1 mK sec$^{-1/2}$, leading to a final sensitivity better than 0.1 mK for resolution element. The frequency range coverage is determined by the proposed scientific target and it permits to separate in a good way the different components that contribute to the CMB spectral distortions. The obvious advantages of basing such an instrument on the Moon can be summarized in two points: the more long is the wavelength of observation the bigger is the radiometer needed and it is not possible to realize it on a satellite; secondly, on the Moon there is no atmosphere, which is an effective source of contamination for ground based measurements.

A small instrument mission design is also proposed. The motivation consists in the fact that free-free and Bose-Einstein like distortions, although more remarkable at $\lambda > 10$ cm, can reach levels of some 0.1 mK even at λ of some cm where they can be detected with an experiment with ultimate sensitivity comparable to that of COBE/FIRAS, as that proposed [23]. In addition, although experiments at centimetre wavelengths are more devoted to (earlier) Bose-Einstein like distortions and to (later) free-free ones, a very careful absolute calibration accuracy such that of the proposed experiment could have also relevant implications for our understanding of (later) Comptonization like distortions.

4.4   The *Planck* Mission

Planck, whose launch is foreseen in 2009, is the third generation space mission, after COBE/DMR [133] and WMAP [103], devoted to image the CMB anisotropies. The Low Frequency Instrument (LFI) [147, 142] will simultaneously observe the sky in three frequency bands centered at 30, 44

and 70 GHz. It is composed by 11 pseudo-correlation receivers, actively cooled to 20 K, able to detect both orthogonal polarisation of the incoming signal. The LFI will be located, along with the High Frequency Instrument (HFI), in the focal region of a 1.5 m aperture telescope. The LFI will produce full-sky maps of the anisotropies of the CMBR with a FWHM angular resolution of 33′, 27′ and 13′ for the 30, 44 and 70 GHz LFI bands, respectively. While WMAP is not sensitive at frequency higher than ~100 GHz, the *Planck* instruments will produce cross calibrated full sky maps spanning a very large frequency range. The HFI, operating between 100 and 857 GHz, is able to monitor, for instance, the dust contamination, the LFI, covering from ~27 to ~77 GHz, is sensitive to the synchrotron and freefree emission. The combination of the two instruments will therefore produce the cleanest image of the CMB anisotropies ever obtained. Moreover, the wide frequency range covered, delivering all-sky maps for each channel, will provide at the same time a gold-mine of astrophysical information.

Comparing the three generation of space mission devoted to the CMB anisotropies, COBE/DMR first mapped the temperature anisotropies; WMAP, after successful ballon-borne and ground-based experiments (see among others [37]; [43]) determined with high accuracy the temperature power spectrum up to the third peak and improved [102] the first determination of the TE and EE power spectrum. *Planck* will not only extend the high precision determination of the TT-spectrum up to $\ell \sim 2000$, but it will determine the EE-spectrum with high sensitivity up to $\ell \sim 1000$ and has a chance to detect primordial B-modes, depending on the tensor-to-scalar ratio of primordial perturbations (The Scientific Programme of *Planck*, 2005).

4.4.1 Some details about the satellite

The design philosophy for the LFI is to minimise any systematic effect, from instrument intrinsic effects and from astrophysical origin, in the design of the instrument instead of removing it in data reduction. It results in a very complex instrument, especially for the radiometric [127], optical [21] and thermal aspects [95]. Moreover a big effort is made to model the impact of any known effect on the final maps. The LFI is an array of 22 pseudo-correlation receivers [13], based on radio detectors [32]. They are continuously comparing the signal of the sky and of a stable reference load. LFI design minimises systematic effects such as thermal instabilities [95], 1/f
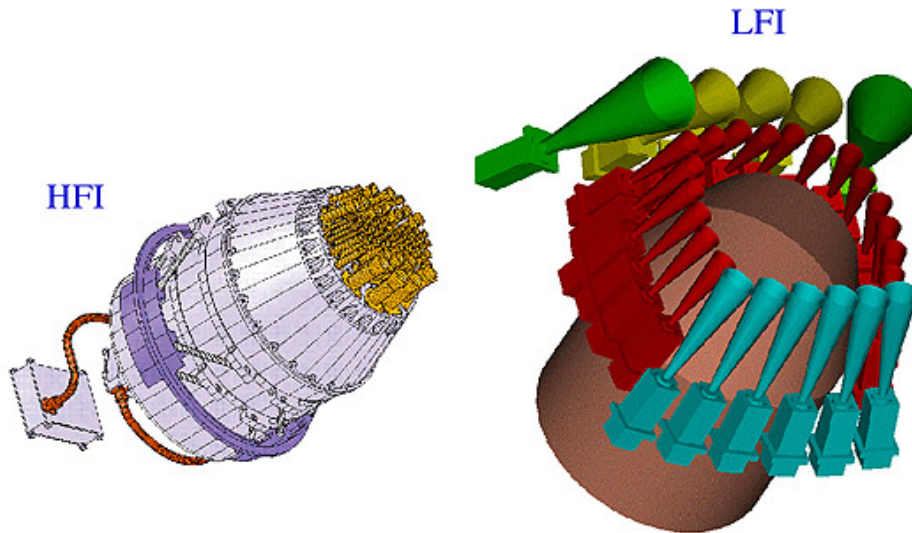
Figure 4.8: The High Frequency Instrument and the Low Frequency Instrument that will be aboard the *Planck* satellite.

[127] noise. To minimise the effects of power dissipation in the critical focal plane area, the receivers are split into two parts, the Front-end and the Back-end. The former is placed in the focal plane unit (FPU) at 20 K, and the latter at 300 K on the top part of SVM (the service module). The radiation focused by the telescope [148] is coupled to the radiometers by double profiled, corrugated feed-horns. Feed-horn, in particular, are optimised for angular resolution as a trade-off with straylight rejection and low sidelobes [21], minimal beam ellipticity [125].

The reference signal for the LFI radiometers is provided by the 4K reference load (4KRL) unit [146], which uses the HFI outer shield to reach an operating temperature expected less than 5 K. The overall design of the 4KRL was driven by high-level constraints: total heat load on the HFI less than 1 mW and the small allowed volume within the two instruments. Among the possible options, it was chosen to have a mechanical separation (only radiative thermal coupling) and a minimum clearance to prevent any contact between the LFI and the HFI due to vibrations at launch. Two figures-of-merit were used in designing the 4KRL unit: reflectivity and leakage. Since the LFI radiometers are comparing the signal from the CMB (whose temperature is known with an accuracy of about 1%) and the reference signal from the 4KRL, the loads emissivity should be better than $\epsilon = 0.99$. The leakage is defined as the spillover signal that can enter the horn-target gap (< 1.5).

Particular care is posed on thermal aspects, which could be an important source of systematic effects: thermal fluctuations, induced mainly by the HFI 4K cooler, are propagated in the LFI radiometer global model up to the final effect expected on the sky maps [95].

Another main limiting factors in terms of systematic effects in a CMB space-borne experiment is the optical system, because main beam distortions and sidelobes are two of the main sources of systematic errors [20]. The former degrades the angular resolution, limiting the reconstruction of the anisotropy power spectrum at high multipoles, the latter drives unwanted radiation not coming from the boresight direction (the so-called straylight) into the feed horn, contaminating the measurement mainly at large and intermediate angular scales (i.e. at multipoles ℓ less than ≈ 100). Accurate predictions and measurements of the beam shape are essential both during the instrument development phase (to design and to properly locate each feed horn) and for an in-depth knowledge of the whole-instrument response in the development of the data reduction pipeline (to remove residual systematic effects by software) [126].

The Planck sorption cooler [100] is a closed-cycle, continuous cryocooler designed to provide more than 1 W of heat lift at a temperature of less than 20 K using isoenthalpic expansion of hydrogen through a JouleThompson valve (JT). Some of this cooling power will be provided to cool the low-frequency instrument onboard the Planck spacecraft. The remaining heat lift will be used as a pre-cooling stage for two further cryogenic refrigerators (He JT cooler to 4 K; Dilution cooler to 0.1 K) that will in turn maintain the high-frequency instrument (HFI) at 100 mK.

Since the performance of the LFI radiometers, sensitive also to polarization, is the best ever obtained in a CMB space mission at $\nu \lesssim 70$ GHz, LFI data will play a crucial role in the context of the Planck scientific aims and, possibly, in the context of future CMB space missions dedicated to a more precise measure of CMB polarization anisotropies.

On the other hand, at $\sim$ 70 GHz all the three (two) main Galactic diffuse components in temperature (polarization), synchrotron, free-free and dust (synchrotron and dust) are in principle relevant, with a consequent increasing of the number of needed fit parameters for a precise component separation between CMB and foreground. It is then required to combine
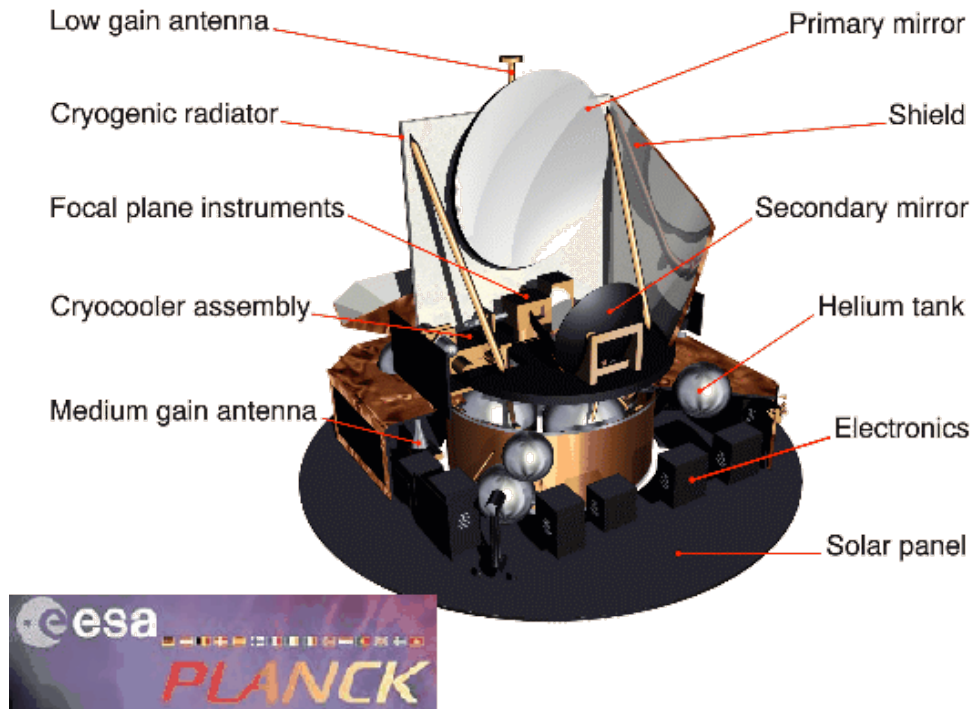
Figure 4.9: A schematic and simple view of the *Planck* satellite. HFI and LFI are placed at the focal plane instruments.

data at different microwave frequencies and, possibly, to add auxiliary information (Galactic templates) from radio to far-IR. The 30 and 44 LFI bands are crucial to determine the foreground contribution at low frequency. In fact, if the Galactic foreground close to the Galactic plane can be excluded by applying dedicated masks to the all-sky maps, the determination and careful subtraction of the Galactic synchrotron and the free-free contribution [46] at intermediate Galactic latitudes is critical to avoid a significant loss of statistical information. Finally, we note that the LFI information on Galactic foreground polarization will be useful to understand the level of accuracy needed in future high accuracy CMB satellite polarization missions dedicated to the B-mode. In the case in which they will include frequency channels at $\nu \lesssim 50$ GHz, LFI will contribute to appropriately define their sensitivity, In the case in which they will operate only at $\nu \gtrsim 50$ GHz, it will constitute the best uniformly calibrated all-sky survey for the intercalibration of collections of future dedicated observations of Galactic polarized synchrotron emission.

4.5 The key-role of the foregrounds

As it will be stressed in the next chapter, foreground emissions are by now the main limitations to a space mission devoted to observation of any of the features of CMB. More precisely, this limitation consists in two facts: the narrow band that corresponds to the minimum of the foregrounds emissions (especially that from Galactic foregrounds), found to be around 70 GHz, limits us to measure *directly* the CMB radiation in few frequency channels, limiting a wider spectral coverage that potentially could bring more informations from the first years of life of our Universe; on the other side, the lack of knowledge necessary to outline the precise characterization of these unwanted emissions.

For what concerns the first factor, we can not do so much: this is a matter of facts, we observe that there is a minimum and the only thing we can do is to not forget to provide our instruments of frequency channels lying in this spectral range. It is clear that on the sky there are regions less contaminated and regions that are more. Indeed, a basic strategy, characterizing a *non-full sky* experiment devoted to observe the CMB signal, consists in choosing one or, better, more regions on the sphere with a low level of contamination. This is the observing strategy that owned to every experiment from ground or from balloon, given that is not possible to observe the whole sky with such experiments.

In order to plan observations like this, it is clear that sky surveys and available data from previous observations and estimates of the foregrounds patterns and signals have the fundamental role. Clearly, the *bigger* and the better is this database, the cleanest will be the region chosen. Anyway, observing a foreground free region of the sky, and consequently a less contaminated CMB signal, has a drawback: this kind of observations do not permit to estimate the level of contamination effectively. Furthermore, it is not possible to estimate the properties of the foreground itself. Of course the lack of an uniform frequency coverage of collected data and statistics about the *contaminants* is a result of the trade-off between the observation of the clean CMB signal and the observation of the foreground itself.

On the other hand, the inaccurate knowledge and characterization of these emissions is due to different factors. Multi-frequency observations are a must if one wants to model the foregrounds spectral behavior. As we will see in the next chapter, it is usual to model Galactic emissions through a

power law, characterized by a spectral index β. A wide multi-frequency monitoring could of course lead to a more precise estimate of β for every emission process. However, there are some issues about determining β. For example, it was found that the spectral index of a particular emission could vary along the sky, depending on the region one is observing. Clearly, this has a potentially deep impact when it is necessary to extrapolate the emission law of the foreground to frequencies where there is a total lack of observations, leading to a bad estimation of its contributions and with a consequent non-optimal CMB signal after a foreground subtraction process. In addition to this, a sort of degeneracy among processes emitting in a particular frequency range could drive to a bad estimation of their single contributions. Sometimes, it is possible to disentangle the two emissions: synchrotron and free-free emissions both dominates on CMB in the low frequency part of the spectrum. In this case, the degeneracy is broken first of all thanks to the polarization signal from synchrotron, while no detection of polarization from free-free is registered to date. Furthermore, free-free can be traced through H_α line emission. Instead, in some other cases, to separate contributions could be more tricky: the *anomalous dust* emission contributes to Galactic foregrounds signals at low frequency as well. The emission mechanism related to this anomalous contribution is well not understood (more details in the next chapter). However, the key point is that foreground estimation of the WMAP team fits the 90% of the sky with a 3-components model (synchrotron, free-free and thermal dust), while on the Galactic plane, where this model doesn't work very well, it is necessary a further tuning. Indeed, in this region, an additive component like *spinning dust* or a steepening of the synchrotron contribution gives the same results.

All that means that we have to push further on this phenomena, also because polarization experiments are the next challenge and, as we will see, the disentanglement between foregrounds and CMB is much crucial on this aspect.

The contamination doesn't spare any CMB observable. In addition to this, CMB spectral distortions are characterized by a very weak signals and they likely could lie in critical spectral regions. Furthermore, the contaminating processes are characterized by temperature higher than the CMB one. Just think about thermal dust: it dominates from $\nu \lesssim 70$ GHz and its emission is well modeled by a grey body (a modified black body) of few tens of degrees.

In the following chapter, we will see how and how much the foregrounds contaminate any CMB observable.

Chapter 5

Foregrounds and models

5.1 Overview

Any instrument trying to measure the intensity (or anisotropy) of the CMB sees many other mixed signals in the sky, which cannot be avoided by instrumental or observational techniques, and must be accounted for and subtracted from the data during the analysis. It is crucial to determine which fraction of the observed signal is due to some foreground contaminant.

The foregrounds could be divided in two main classes: Galactic and extra-Galactic foreground. In addition to these, there are other local foregrounds, like the Zodiacal Light Emission (ZLE), and if we consider ground-based experiments and balloon experiments, the atmospheric contamination is not negligible.

The main physical processes that contribute to the Galactic foreground contamination are: synchrotron emission, bremsstrahlung and the dust emission (thermal and anomalous emission). At lower radio frequencies the synchrotron emission is usually dominant, with flux decreasing at higher frequencies. In terms of brightness temperature, a power law model would have an average index $\beta \sim -3$. Free-free emission has a flux that is nearly constant with frequency and its emission temperature is well fitted by a power law with an index $\beta \sim -2.1$. It becomes relatively more important than synchrotron at higher frequencies, let say 60 GHz at higher latitudes, but at a fixed frequency its domination varies on the sky (also because the synchrotron has a varying spectral index).

At frequencies larger than 60 GHz it is possible to begin to probe the spectrum tail of vibrational dust emission, $\beta \sim 2$, which becomes dominant around 70 GHz. In addition to these three foregrounds, there is the possibility to have another contribution of foreground at lower frequencies, in the 10-30 GHz

range. The nature of this source is still unknown, but many think that are some hints to point at rapidly rotating dust grains.

The uncertainties in the maps and in the frequency dependence of the galactic emission at radio and microwave frequencies have become the limiting factor in the accuracy and interpretation of the low frequency measurements of the spectrum of the CMB and anisotropies as well.
In the following sections, the main foreground features will be presented, in the context of CMB experiments. This will be followed by a brief overview of the impact that the *PLANCK* satellite will have in the context of foregrounds and by a description of the Planck Sky Model, coming with the report of some tests I've done on it.

5.2 Extragalactic foregrounds

Extragalactic sources emit in several frequency ranges. The extragalactic foregrounds include: radio sources, the Sunyaev-Zel'dovich effect from galaxy clusters, and infrared-bright dusty galaxies.
The spectral energy distribution (SED) of most of them shows a minimum around 1-2 mm. This is the results coming from the superposition of two emission mechanisms: the radio emission, that dominates for lower frequencies with respect to this minimum, and the thermal dust emission, that starts dominating at frequency $\nu \gtrsim 70$ GHz. Consequently, this determines also a difference in the populations of the bright sources observed above and below ~ 1 mm.
The synchrotron emission is likely to be the primary emission mechanism of all radio sources. According to the model of Blandford & Rees (1974), supported by observational evidence, the frequency of this spectral break, ν_b, that coincides with the frequency at which the synchrotron spectrum steepens, is related to the magnetic field and the *synchrotron age*, t_s, by

$$\nu_b \simeq 96\left(\frac{30\mu G}{B}\right)^3 t_s^{-2} \text{ GHz} \tag{5.1}$$

where t_s is expressed in Myr. In concordance with this, a systematic multifrequency study, that will be possible to do with the multifrequency *Planck* data-set, will provide a statistical estimate of the source ages and of the evolution of their spectra.
Synchrotron is also known to be strongly polarized, while most of the radio

sources observed in MHz and GHz ranges are not. This lack of polarization could be due to random alignment of the magnetic field in the source, or to Faraday depolarization of the emergent radiation.

However, the observed spectra of radio sources can be not a power law with a fixed index. This departure from a simple power law depends mainly on two facts: the *aging* process: the higher the energy of an electron, the less time it takes to radiate a given fraction of that energy; the *opacity*: a peak may appear in the SED, centered roughly at the frequency where the optical depth reaches unity.

A particular class of objects that shows clearly this behavior is that of the so-called gigahertz peaked spectrum (GPS) sources [135]. These objects could represent very young stages of the evolution of a radio source and this would provide an insight into the genesis of this sources class. They can be also very compact sources in the ISM of host galaxies, characterized by unusual conditions like high density or turbulence.

In many galaxies, a very cold dust component is observed ($6 \lesssim T \lesssim 15$ K). When SCUBA started observing the sky with unprecedented sensitivity in the sub-millimeter waveband three years ago, it unveiled vigorous star-forming activity in the early Universe and hundreds of otherwise invisible galaxies were seen. Radiation from dust in distant star-forming galaxies contributes in the sub-mm frequency range through thermal emission (see Sec. 5.3.3).

Concerning anisotropy observations a consideration must be done. The first space mission for CMB anisotropies observation, DMR aboard the COBE satellite, was basically not affected by extragalactic foreground sources [10]. That's because its large beam size. In fact, the contribution of a point source increases with the inverse of the solid angle of the beam. From this statement follows that observations at high angular resolution (i.e. the *Planck* mission) are more sensitive to extragalactic foregrounds, than a mission with lower resolution.

Clusters of galaxies play another important role among the astrophysical foregrounds. A systematic shift of photons from the Rayleigh-Jeans to the Wien regime is caused by the inverse Compton scattering of CMB photons against the hot and diffuse electron gas trapped in the potential well of clusters of galaxies (also responsible of their X-ray emission). This contribution, the thermal Sunyaev-Zel'dovich (SZ) effect, arises from the thermal motion of the electrons and it is described by the Kompaneets

equation which, in the non relativistic limit, leads to the formula for the spectral intensity changes across a cluster:

$$\Delta I_v = 2 \frac{(kT_{CMB})^3}{(hc^2)} yg(x) \,, \tag{5.2}$$

where x is the usual dimensionless frequency and $g(x)$ is the function that describes the spectral form of this effect

$$g(x) = x^4 e^x [x\dot{\coth}(x/2) - 4]/(e^x - 1)^2 \,. \tag{5.3}$$

$g(x)$ is negative for $x < x_0 = 3.83$ (corresponding to $v_0 = 217$ GHz) and positive for $x > x_0$.

Hence, CMB absolute temperature measurements are affected by extragalactic foregrounds: the astrophysical monopole must be subtracted from the total monopole observed and this is a crucial step.

The sky brightness can be decomposed as follow:

$$T_{sky}(v, \alpha, \delta) = T_{CMB}(v) + T_{Gal}(v, \alpha, \delta) + T_{ext}(v) \,, \tag{5.4}$$

where $T_{Gal}(v, \alpha, \delta)$ is the emission of our Galaxy and $T_{ext}(v)$ the contribution of the unresolved extragalactic sources. An estimate of their contribution could be done on the current knowledge of their amplitude and spectrum [87], recovered through CMB observations carried out in the past. These estimates could be done at 600, 800, 1400 and 2500 MHz, for example, and their contribution is 810 ± 180 mK, 340 ± 80 mK, 79 ± 19 mK and 16 ± 4 mK respectively [131]. Using the current 178 MHz normalization [87] it turns out that the uncertainty associated with the unresolved extragalactic contribution is potentially higher than instrumental systematic errors. This is particularly important for low frequency measurements, which is the most interesting frequency range for looking for CMB spectral distortions.

In the sub-mm range, the extragalactic contribution is expected to overwhelm the differences between a distorted spectrum or a blackbody one with the same, or very similar, T_0, permitting a relatively simple subtraction of it. The submillimetric extragalactic foreground derived in [53] is given by

$$I \simeq 1.3 \times 10^{-5} [v/(c/0.01 \text{cm})]^{0.64} B_v(18.5\text{K}) \,. \tag{5.5}$$

These results support an active phase of star formation rate at high redshift ($z \simeq 2.1 - 3.8$) and dust reprocessing [19].

5.3 Galactic Foregrounds

In the following sections will be given a description of the Galactic diffuse foreground emission. In order to explain the relation between foreground and CMB pattern, the problem will be considered under temperature and polarization aspect, given that many efforts are being done to face the challenge related to the amount of data that the Planck mission will provide. On the other side, foregrounds are crucial also for absolute temperature measurements and so, after the T and P overview, I will focus on the contaminations related to the monopole moment.

5.3.1 Synchrotron emission

Synchrotron emission is widespread in the Galaxy and it arises from the acceleration of cosmic ray electrons in the magnetic field of our Galaxy. Concerning CMB experiments, the synchrotron emission is the dominant Galactic foreground at low frequencies, i.e. below 30 - 40 GHz (for polarization it starts to be dominant from higher frequencies, given that free-free is considered un-polarized) and its intensity depends on the Galactic magnetic field, on the energy spectrum of the electrons and on their spatial distribution.
The Galactic synchrotron emission (like the other two Galactic emissions) is generally described by a power-law spectrum

$$T(\nu) \sim \nu^{-\beta_{sync}} \tag{5.6}$$

where β_{sync} is the synchrotron spectral index, with typical values in the range $2.6 - 3.4$. This is a varying spectral index: it varies with frequencies, depending on the details of the cosmic ray electron propagation, including energy loss, and as a consequence it varies with position on the sky. Electrons with energy between 3 and 170 GeV, accelerated in magnetic field with an intensity between 0.2 and 2.5 μG, will have a spectrum ranging from 400 MHz and 100 GHz. Furthermore, synchrotron radiation could reach a theoretical intrinsic degree of polarization of about 75%. In order to better understand this foreground process, some observations have been performed in the typical frequency range of synchrotron emission: the Leiden surveys are linear polarization surveys covering the Northern Celestial Hemisphere at five frequencies between 408 MHz and 1411 MHz, with an angular resolution ranging from 2.3° to 0.6° [16], the DRAO

polarization survey at 1.4 GHz [149] with a FWHM resolution of 36′ and the Villa Elisa polarization survey [143], with the same resolution. The latest two survey covered respectively the Northern and the Southern sky and both were sensitive to the Stokes parameter Q and U.

The total intensity template of the radio sky appears very different from the polarization one. Furthermore, the polarized intensity is characterized by important structures at high Galactic latitude, while on the Galactic plane it results to be less bright than in total intensity. From the statistical analysis in [22] results also that E and B polarization modes show a very similar behavior and are well fitted by a power law, with typical slopes ringing from -2.5 to -3, confirming previously results at $\ell \lesssim 200$ obtained through analysis on the Leiden survey at 1.411 GHz [82].

Other available high resolution data, in radio band, is approximately 10 arcmin and data are limited to a low - medium Galactic latitude, $|b| \lesssim 20°$ [45]. More than one times, these templates were used to evaluate the synchrotron angular power spectrum in the radio band up to arcmin scale.

In terms of C_ℓ, for $\ell \gtrsim 200$, other efforts come from independent groups. For the Galactic region they considered, Tucci et al. [145] estimated $C_\ell^{E,B} \propto \ell^{-1.5 \div -2}$ and the same behavior was claimed by Tegmark [141]. Furthermore, Baccigalupi et al. [8] confirmed this results up to $|b| \simeq 20°$ and they also found out that the level of Faraday depolarization is quite important, but not so much to affects and masks the true synchrotron emission.

A multifrequency analysis of these surveys resulted in a series of angular power spectra, that when fitted with a power law ($C_\ell \sim k\ell^\alpha$) give spectral indices that steepen with increasing frequency [82]: from $\alpha \sim -(1-1.5)$ at 408 MHz to $\alpha \sim -(2-3)$ at 1411 MHz for $10 \lesssim \ell \lesssim 100$ and from $\alpha \sim -0.7$ to $\alpha \sim -1.5$ for lower multipoles (the exact values depending on the considered sky region and polarization mode). Anyway, it is possible that Faraday depolarization effects can play a fundamental role in the determination of the effective degree of polarization for the synchrotron emission.

Even if it is subject to a degeneracy with the free-free emission, synchrotron radiation results to be stronger than dust emission in WMAP frequencies [58]. They claim a strong synchrotron depolarization toward the Galactic plane. Indeed, a decrement in polarization intensity can be caused by the superposition, along the line of sight, of two synchrotron regions having their polarization angles oriented nearly orthogonally. Moreover, if the two regions have different spectral indices the loss of power in polarization is

maximized at the frequency where the individual polarization amplitudes match. Also because of that, total intensity and polarization synchrotron template appears quite different.
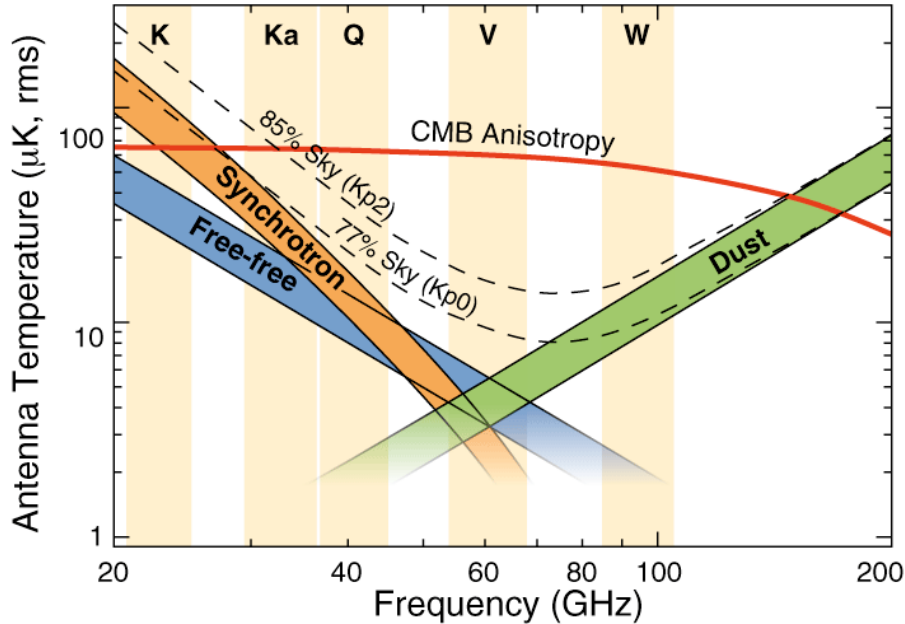

Figure 5.1: The frequency dependence of the expected CMB anisotropy (red band) and of three known sources of foreground emission from our Galaxy, in units of antenna temperature. The five bands of WMAP are indicated, while the dotted lines labeled with Kp0 and Kp2 represent the level reached after a Galactic cut with the two different masks. The residual fraction of sky after the cut is also indicated. [6]

5.3.2 Bremsstrahlung

Free-free emission arises from the collisions between thermal electrons and other ions. Typically this process takes place in regions with hot gas, with temperature around 10^6 Kelvin. The spectral index is fixed through the atomic physic laws: $\beta_{ff} \sim 2 - 2.1$ (in the formalism of Eq. (5.6)), and it varies with the frequency. Like synchrotron, the main contribution of the free-free emission is visible at low frequencies, below 70 GHz. Anyway, synchrotron emission dominates over free-free for frequencies below 30 GHz. This foreground emission is also a tracer of star formation, that is a process able to ionize the abundant interstellar hydrogen and consequently, the ionized component, locks all the gas to the magnetic field through collisions. This hot ionized gas can be traced, in the optical regime, by recombination lines

of hydrogen, principally the H-alpha line.

It is possible to estimate the brightness temperature for free-free emission. Theoretically, one considers an electrically neutral medium consisting of ions and electrons. The estimate of the temperature T_{ff} at a given frequency ν is given by

$$T_{ff} \simeq 0.08235 T_e^{-0.35} \nu^{-\beta} \int_{l.o.s.} N_e N_i \mathrm{d}l , \qquad (5.7)$$

where the line of sight integral of electron and ion density must be expressed in cm^{-6} pc.

However, free-free emission has a weak signal if compared to the others Galactic emissions and it cannot be directly observed. A good tracing of the source of its emission it could be reconstructed out through hydrogen recombination emission lines, in particular H_α emission. This is due to the fact that both processes are emitted by the same ionized medium and both have intensities proportional to the line of sight integral of the free electron density squared, $\propto \int N_e^2 \mathrm{d}l$. For $T \leq 2.6 \times 10^4$ K, the intensity of $H\alpha$ emission is given by

$$I_\alpha = 0.36 R \left(\frac{T}{10^4 \mathrm{K}} \right)^{-\gamma} \frac{\int N_e N_i \mathrm{d}l}{cm^{-6} pc} , \qquad (5.8)$$

where γ varies from 0.9 to 1.2 for higher temperatures and

$$1R \equiv 1 Rayleigh \equiv \frac{10^6}{4\pi} \mathrm{photons}/(cm^2 \mathrm{s \ ster}) = 2.41 \times 10^{-7} \mathrm{photons}/(cm^2 \mathrm{s \ ster}) ,$$

at $\lambda = 6563$ Å.

The connection between this two processes has been widely discussed [75, 47, 132] and an $H\alpha$ intensity based estimate of the free-free brightness temperature could be given as follows:

$$\frac{T_{ff}}{I_\alpha} \simeq 10.4 \nu^{-2.14} T_4^{0.527} 10^{0.029/T^4} (1 + 0.08) . \qquad (5.9)$$

Here, T_{ff} is expressed in mK, I_α is the H_α surface brightness in Rayleigh and T_4 is the temperature of the ionized medium in unit of 10^4 K.

Free-free emission is observed to be not polarized (at least to the first order), because it is generated by incoherent emissions from individual electrons scattered by nuclei in a partially ionized medium.

5.3.3 Dust emission

In the most general scenario, the Inter-Stellar Medium (ISM) contains molecular and atomic cold clouds and hot ionized cavities likely generated

by supernovae. Observations suggest that atomic gas (HI) could be part of the warm neutral medium, with $T \approx 10^4$, and also of the cold neutral medium, with $T \approx 100K$. The warm ionized medium is in part ionized gas ($T \approx 10^4$K), while a small fraction of the ISM gas is in the hot ionized medium ($T \approx 10^6$K).

What we know about interstellar dust, comes from observation in the infrared and beyond and from the extinction observation from UV to infrared. It is also known, that dust is susceptible to magnetic fields, showing indeed a certain degree of polarization. The dimensions of the grains could vary from few nanometers for the smallest, to several hundreds of nanometers for the biggest grains. In addition, to this it is possible to classify the variety of materials of which dust is thought to be composed: large polycyclic aromatic hydrocarbon molecules, carbonaceous compounds and silicates.

The thermal dust emission is usually modeled by a spectrum of a modified black-body (a grey-body):

$$I(\nu, T_d) \approx \nu^{\beta_d} B(\nu, T_d) \approx \nu^{\beta+2} \qquad (5.10)$$

where $B(\nu, T_d)$ is the emission law of a black-body and $\beta = 2$ (recovered from FIRAS and WMAP data).

In total intensity, an all sky map at 100 μm and with a resolution of 6 arcmin, is available and it is possible to scale this map down to microwave frequencies, in order to be compared with the CMB [48]. For what concerns the dust polarization, a great leap forward was made through the results obtained by the *Archeops* experiment, at 353 GHz, based on observations of the $\sim 20\%$ of the sky [12], [109]. Extrapolation at 353 GHz of the IRAS and DIRBE data are in good agreement with the dust power spectrum recovered through *Archeops*. On large scales and for Galactic latitudes $|b| \geq 5°$ is detected a temperature-polarization cross-correlation $(\ell + 1)C_\ell^{TE}/2\pi = 76 \pm 21\mu K_{RJ}^2$ at 4 σ. They set also upper limits on E and B polarization modes at $11\mu K_{RJ}^2$. For Galactic latitude $|b| \geq 10°$ they report also a TE cross-correlation $(\ell + 1)C_\ell^{TE}/2\pi = 24 \pm 13\mu K_{RJ}^2$ at 2 σ. The extrapolation of these data down to 100 GHz gives interesting results [109]: if the dust properties detected are the same significant for a whole sky representation and if the upper limits recovered on E and B modes are near to the dust polarization level, then the dust contribution to the polarized foreground at 100 GHZ is the most important spurious signal when recovering the polarization power spectra

of the CMB.

In recent times, dust emission is likely decomposed in two components that contribute in different ways: one is the classical thermal emission, the other is the so called *anomalous emission*. It came out from cross-correlation studies of CMB and far-IR data. This emission shows a spectral index typical of the free-free emission, but evidence from experiments (COBE, Saskatoon, Tenerife experiment) indicates is high level correlated to the dust emission, instead of free-free like thought before. Draine & Lazarian [44] suggested that this emission may originate from very small spinning dust grains, but it is still an open question (that's why this source is often also called *spinning dust emission*). They also showed how this emission can't be attributed to an anomalous emission related to bremsstrahlung.

5.4 Local foregrounds

Foregrounds can arise also from our Solar System. Planets, asteroids owing to the Main Belt and NEO, comets and comets trails, all of these are compact or narrow featured objects from the Solar System.

The diffuse local foreground is instead known as Zodiacal Light and the thermal emission arising from the Interplanetary Dust Particles (IDPs) is known as Zodiacal Light Emission (ZLE). The ZLE is the far-IR counterpart of the more known Zodiacal Light, due to scattering of the solar light by IDPs.

This dust cloud consists of a population of micron to millimeter size particles, distributed mainly between the Sun and the orbit of asteroid belt at 2 AU (the tail of the distribution may be more far). ZLE shows a significant emission component at infrared wavelengths. In fact, depending on the distance from the Sun, these particles have temperatures from 240 to 280 K.

Many leaps forward were done in our understanding the complex geometry and the dust properties of the ZLE, thanks to the infrared and far-infrared space-borne missions like IRAS, COBE and ISO, that observed the emission below 300 μm. The peak of the ZLE is at $\lambda \approx 10\mu$m, so it is one of the major contributors to the sky background in the far-IR domain at low ecliptic latitude. It is important to study the ZLE not only through maps and templates, but also using the time ordered data stream coming from a CMB satellite mission. That's because its surface brightness depends not only on the pointing direction, but also on the instantaneous position of the observer

with respect to the Sun.

Under determined assumptions, it is possible to write a relatively simple general expression for estimating the ZLE brightness at a frequency ν. For a space-born experiment and for a given population c of the IDPs cloud, this is represented by [91]

$$I_{\nu,c}(\mathbf{P}, \mathbf{R}_P) = K_\nu E_{\nu,c} n_{0,c} \times \int_0^{+\infty} \mathrm{d}s B_\nu(T_c(\mathbf{r}(s))) N_c(\mathbf{r}(s)) , \qquad (5.11)$$

where $\mathbf{P}$ is the observing direction, s the distance from the observer along $\mathbf{P}$, $\mathbf{R}_P$ the position of the observer with respect to the Sun, $\mathbf{r}(s)$ the position within the Solar System with respect to the Sun along the line of sight, $T_c(\mathbf{r}(s))$ the thermodynamic temperature of the grains of the population c, B_ν the blackbody emissivity, $N_c(\mathbf{r}(s))$ the spatial distribution of the grains, K_ν is a color correction that takes into account the effect of the frequency response of the instrument in a given bandwidth, $n_{0,c}$ the optical density for the dust component c and E_ν is an emissivity correction that takes into account features related to the size distribution and composition of the grains. In general E_ν is normalized to a reference frequency ν_0. This operation implies a further renormalization of the optical density ν_0. As said, Eq. (5.11) is valid only under determined conditions: the grain size distribution and their optical properties must not depend on $\mathbf{r}$; a symmetrical beam is assumed and it has no variations with ν inside the bandwidth of each channel; the beam is small compared to the typical scale on which the properties of the ZLE show variations.

Fig. 5.2 shows the spectrum of the Zodiacal Dust cloud from 10 to 1000 μm, normalized to a 240 K blackbody spectrum. It is clear a break in the emission at ~ 150 μm: below this wavelength, the Zodiacal Dust spectrum is roughly represented by a 240 K blackbody with a grey emissivity of $\sim 3 \times 10^{-7}$, while above the break wavelength the emissivity shows a dependent behavior with respect to λ and it falls off as λ^{-2} [49]. Even if this is a simple model, it helped to recover informations about size and mass distribution of the grains in the main cloud: the spectrum is dominated by emission from grains with radii smaller than ~ 30 μm, characterized by the λ^{-2} decline, while a larger population is responsible of the normalized flat spectrum below 150 μm.

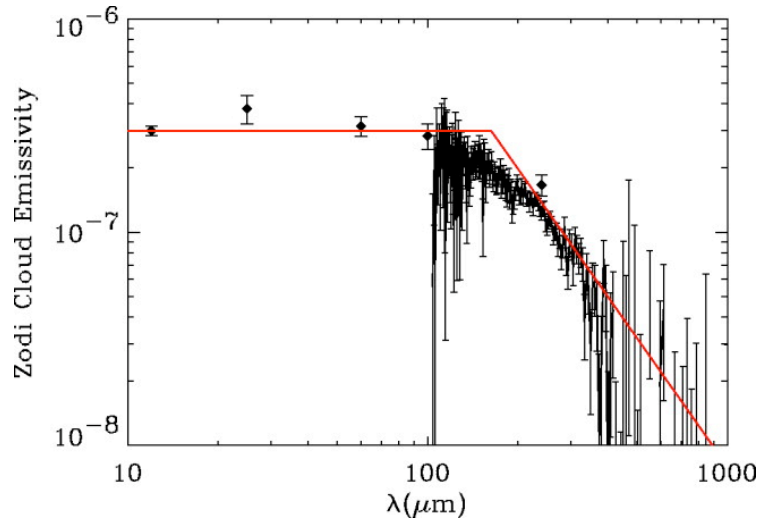Figure 5.2: The $10 - 1000$ μm annually averaged spectrum of the zodiacal dust cloud normalized to that of a 240 K blackbody. Diamonds represents the DIRBE data and the solid error bars represent the FIRAS spectrum. See text for more details. Figure from [49].

5.5 Observing and monitoring foregrounds with *PLANCK*

5.5.1 Galactic study

The LFI and HFI maps of the Galactic foregrounds (synchrotron, free-free and dust emission) will have a measurement accuracy comparable to that achieved on the CMB, with orders of magnitude lower noise than any current data, and at least 3-4 times better sensitivity than WMAP. Methods of blind and non blind component separation applied to these high resolution maps could be a very valuable tool for understanding the different sources of Galactic emission. Also polarization measurements could be very useful in singling out the synchrotron emission whose percentage polarization can be expected at a level of $30 \div 50\%$ at the frequencies sampled by *PLANCK*/LFI, where Faraday depolarization will be minimal. Maps of the synchrotron emission of the Galaxy will give information about:

- the structure of the magnetic field;

- the spatial and energy distribution of relativistic electrons;

- the variations of electron density, of electron energy and of magnetic field induced by supernova shocks and winds from OB stars.

The maps will explore correlations between magnetic fields and the matter distribution more systematically and often on much smaller scales than

ground-based surveys. Free-free emission from ionized gas in the Galaxy is not easily identified at radio frequencies, except near the Galactic plane. It may, however, be the dominant foreground at $30 \div 80$ GHz. The multifrequency all-sky *PLANCK*/LFI maps, coupled with X-ray maps and *Hα* surveys, will therefore be a very valuable tool for investigating the structure, distribution and physical conditions in the hot regions of the interstellar medium. Galactic dust emission is expected to be important, or even dominant, at frequencies higher than 100 GHz, and to fade rapidly at lower frequencies. *PLANCK*/HFI measurements will contribute to investigate the distribution and nature of cold dust in the Galaxy. The simultaneous study of dust and free-free emission will be very useful to investigate the relationships between different phases (HI and HII gas) of the interstellar medium. *PLANCK* measurements will also detect and provide spectral information on the brightest discrete Galactic radio sources, including a relatively large sample of supernova remnants. These data will be unique in allowing a search for extremely compact bremsstrahlung or synchrotron sources, self-absorbed up to tens of GHz and therefore unobservable in existing surveys.

5.5.2 Extragalactic sources

Although *PLANCK*'s instruments have sensitivities near fundamental physical limits, CMB optimized instrumental properties lead to an overall sensitivity of *PLANCK* to compact sources which is poor compared to dedicated ground based instruments, as well as to space missions such as HERSCHEL. Nevertheless, because *PLANCK* will observe the entire sky, it will be able to detect a large number of compact sources. As a result, the LFI surveys will provide unique information on the frequency range they explore; the data sets they will produce will be important in several areas of extragalactic radio astronomy, particularly since *PLANCK* covers just the frequency range where the shape of the spectral energy distribution of Active Galactic Nuclei is least well known. The LFI is expected to detect mostly flat spectrum radio-sources (compact radio-galaxies, radio loud QSOs, BL Lacs, blazars), in a frequency region where spectral features carrying essential information on physical conditions of sources show up. These features include:

- spectral breaks related to the synchrotron age of the source;

- spectral steepening corresponding to the transition between optically thick and optically thin synchrotron emission;

- spectral turnovers due to self absorption of extremely compact flaring components.

Sources with strongly inverted spectra, peaking at mm wavelengths would either be missing or strongly under-represented in low frequency surveys. Recent studies of GHz Peaked Spectrum radio sources (GPS) have revealed a flat distribution of peak frequencies extending out to 15 GHz in the rest frame. This suggests the existence of an hitherto unknown population of sources with a spectral peak at high frequencies. GPS sources are important because they may be the youngest stages of radio source evolution and may thus provide insight into the genesis and evolution of radio sources; alternatively, they may be sources which are kept very compact by unusual conditions (high density and/or turbulence) in the interstellar medium of the host galaxy.

Using COBE/FIRAS and IRAS observations, it is possible to have a good data-set to be compared to the predictions of the level of extragalactic foregrounds. Most of the far-IR sources detected by IRAS are inactive spiral galaxies, while some are quasars, starburst galaxies and Seyfert galaxies. Gawiser and Smoot compared the location of more than 5000 galaxies, from the IRAS data, with a thousand of the brightest radio sources. They found only 7 possible matching results. This lack of coincidence shows that radio-loud galaxies can be treated separately.

The forthcoming *Planck* satellite will detect many low-redshift spiral galaxies and moderate starburst galaxies already detected by IRAS, but his long-wavelength coverage will provide many informations on cold dust, that were unavailable from IRAS.

5.5.3 Clusters of galaxies

The Sunyaev-Zel'dovich (SZ) effect is the result of the Compton scattering of the CMB radiation by non-relativistic electron gas, either in the intergalactic space or within clusters of galaxies. This effect, arising from the thermal motions of the electrons, results in a systematic shift of photons from the Rayleigh-Jeans to the Wien side of the spectrum. With respect to the

incident radiation field, the change of the CMB intensity across a cluster can be viewed as a net flux emanating from the cluster. The flux is negative below the crossover frequency, $\nu_0 = 217\,\text{GHz}$, and positive above this characteristic frequency. While the main emphasis so far has been on the measurement of the SZ effect in individual clusters, the ability to observe a large number of clusters in a satellite survey at millimetric wavelengths enhances interest in cluster number counts using the SZ signal. Because of its angular resolution and sensitivity, *PLANCK* will observe a large number of clusters. While the model dependence of the number and amplitude of cluster SZ signals makes predictions of the cluster foreground contamination difficult, *PLANCK* observations provide a splendid opportunity to get information on the intracluster medium complementary to the X-ray observations. In fact, the SZ surface brightness is proportional to n_e (electron density), while the X-ray surface brightness is proportional to n_e^2. Thus, SZ measurements are much better suited than X-ray observations to probe the less dense regions, further away from the cluster core. The comparison of SZ and X-ray measurements will yield an independent measure of the Hubble constant. On the other hand, if we make use of the cosmological parameter estimation derived from the C_l's, *PLANCK* detection of several hundred individual clusters will certainly result in an enhanced knowledge of the population of clusters and of the properties of their hot gas.

5.6 The Planck Sky Model

5.6.1 An overview

The Planck Sky Model (PSM) is a complete and versatile set of programs and data, to be used for the simulation or the prediction of sky emission in the frequency range of typical CMB experiments, and in particular of the upcoming Planck sky mission (the 10-1000 GHz range). It is being developed as part of the activities of Planck Working Group 2 (WG2) on component separation, and of the ADAMIS team at APC.

With the PSM, It is possible to have a reconstruction of the sky, at a given frequency, in two different ways:

- *prediction*: it is the case in which the sky provided by the PSM is the best guess of what the sky emission could be at a certain frequency. For this option, the models involved are deterministic and there are few tunable parameters (where possible);

- *simulation*: in this second case, on the contrary, the realization of the sky is widely tunable, offering the possibility to test and evaluate algorithm and tools (i.e. component separation, for example).

The PSM package is mainly composed by IDL script and it is continuously updated and implemented. It contains and uses a certain number of templates and catalogs, like: Galactic template, non Gaussian CMB maps, WMAP-constrained CMB maps, thermal SZ, IR point sources, radio sources, and others. From summer 2007 the PSM includes a 4-components Galactic model (thermal dust, synchrotron, free-free and spinning dust) and also Galactic polarization has been improved.

During the set up of a PSM run it is possible to choose several options and parameters: first of all, one decides if the run will be a simulation or a prediction and if it will involve temperature or polarization or both; then it is possible to determine the parameters of the output format (resolution of the maps, the maximum multipole order ℓ, the maps coordinate system, etc.); then the cosmological environment must be set up; the emission model for the CMB; the diffuse Galactic emission model; the extra-Galactic foregrounds options.

It is clear that such a package is of primary importance in the context of the *PLANCK* mission, for testing the softwares that will used for the data reduction for example, but it is not excluded that it could have some repercussions on other field of astrophysics: just think about the PSM Galactic model and at the possibility to implement it with multifrequency templates and data, it would be used from astrophysicist from different areas.

The Galactic model emission of the PSM, is discussed in the next section and, in particular, I will give an overview of the tests I did on it.

5.6.2 Tests carried out

I carried out some tests on the PSM galactic models aiming to a validation of the models themselves. In particular, I performed several comparative tests between the two last realizations of diffuse Galactic emission model in the PSM: the mamd2008 model (the last release) and the mamd-dickinson model (the previous one). In addition, the models were compared with the corresponding real Galactic emissions derived from the WMAP 3yr data, estimated through the Maximum Entropy Method (MEM).

The models were tested both in temperature and in polarization.

Here, I will report only a fraction of the tests done, showing few plots about the differences between the two PSM Galactic models and some others about the validation of the model in relation with the MEM predicted foreground maps from WMAP. Every map or plot here is at a frequency of 23 GHZ (K band), unless differently specified.

Have been also used the Galactic mask used to identify point sources (PS) by the WMAP team and a low foreground, full sky, new CMB map release [42].
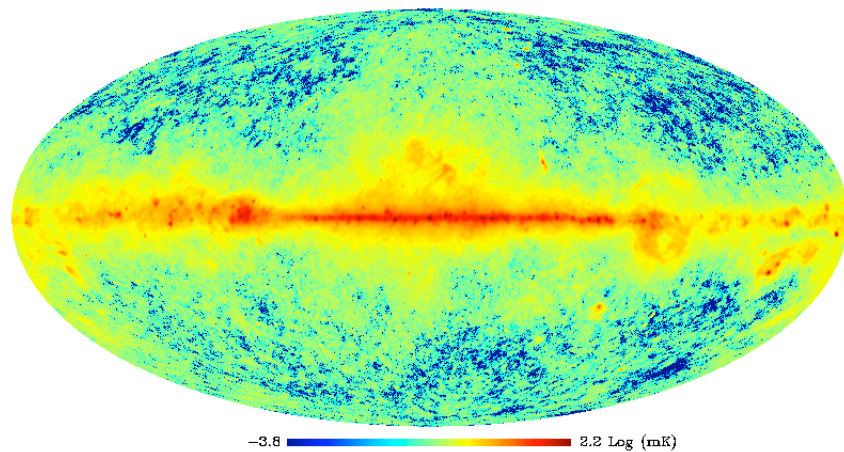
Figure 5.3: Full sky map of the 23 GHz channel of WMAP. The log scale was used to emphasize the details. Temperature in mK.
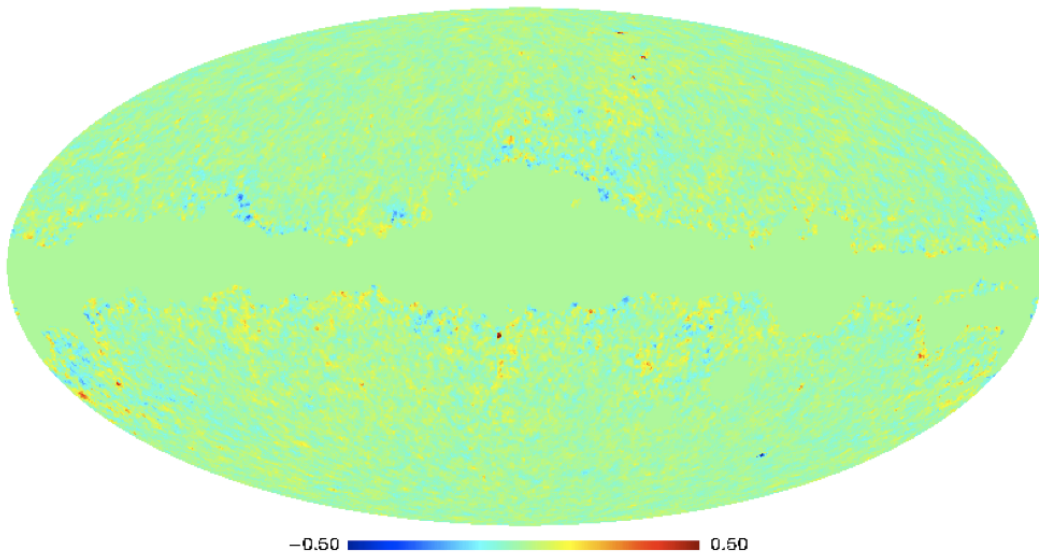
Figure 5.4: Full sky map of the results of the subtraction of the mamd2008 model and the CMB map from the WMAP coadded map in K band. The results was multiplied for the Galactic mask used for the identification of PS by the WMAP team. Flux is constrained from −0.5 to 0.5 mK.
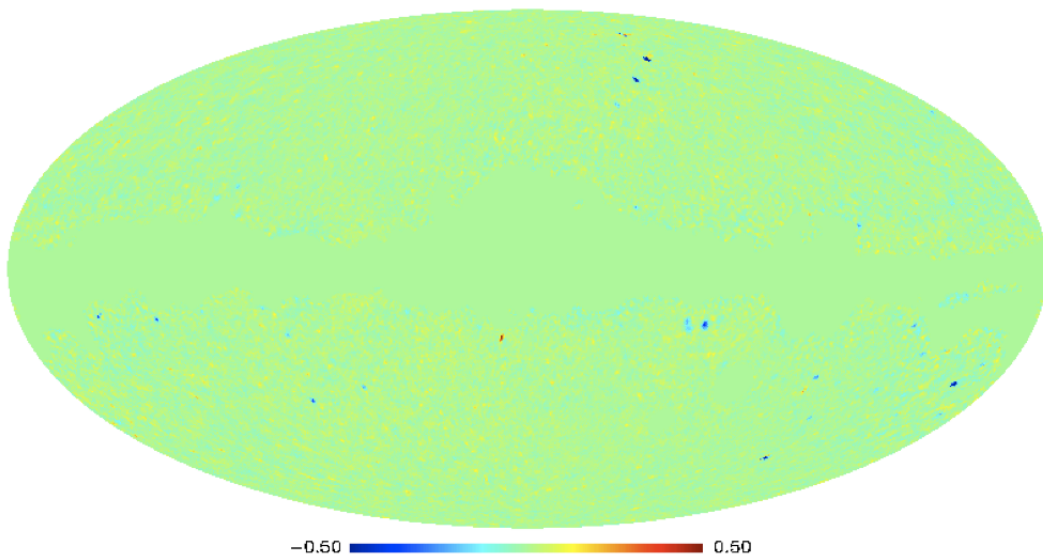
Figure 5.5: Same of Fig. 5.4, but the model subtracted is the mamd-dickinson one.

Several validation tests were carried out also between the PSM Galactic models themselves: both considering the coadded maps and considering the single emission process. In particular, the Galactic models considered are 4-components models, that is to say that synchrotron, free-free, thermal and spinning dust emission processes are considered. The next double panel figure shows the subtraction of the mamd2008 model from the mamd-

dickinson one. more details in the caption.
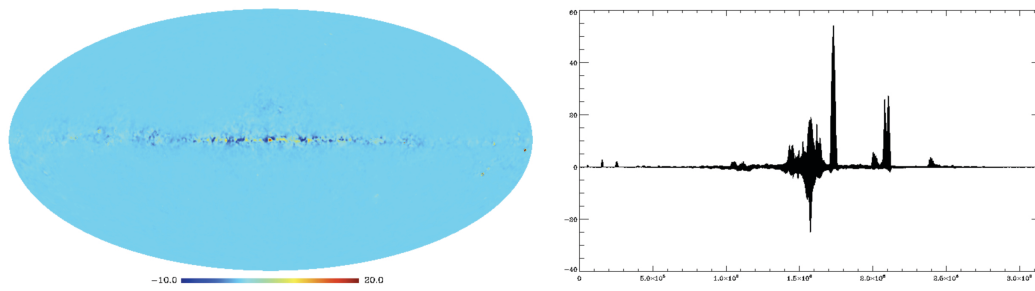
Figure 5.6: Left panel: mollview projection of the difference of the two model (see text), with flux constrained between two arbitrary values in order to emphasize the differences. Right-panel: plot of the same quantity. More precisely: on the x axis there is the pixel number for a ring numbering scheme in HEALPix[2] [59] environment, on the y axis the pixel power. With this kind of plot the North Galactic Pole is on the left of the graph, the South Galactic Pole on the right, while the Galactic plane stays in the middle.

5.6.3   Results from the tests

In total intensity it turned out that the main discrepancies between the models stays on the Galactic plane, even if some other confined zones out of the Galactic disk seem to mismatch between the two models. These seem to be compact regions, mostly known, and it would be not so hard to include them in the model.

It is clear that if one wants to validate a software, let's say a certain component separation technique, the lack of precision in the PSM is of course transmitted in some way to validation criterion used to test the software. Hence. there is the need of some improvements for what concerns the temperature template, at least at low frequency. At higher frequencies the features of the templates of the Galactic emission of the two model converge, showing the same amplitude and spatial template. Also in the Galactic plane, at high frequencies, the residuals start to be comparable to those left when one subtract the MEM foreground realization to a sky map at a determined frequency. For what concerns polarization the results of the validation test were optimal, in the sense that the new model takes better into account the polarized signal of the foreground emissions, with respect to the mamd-dickinson model.
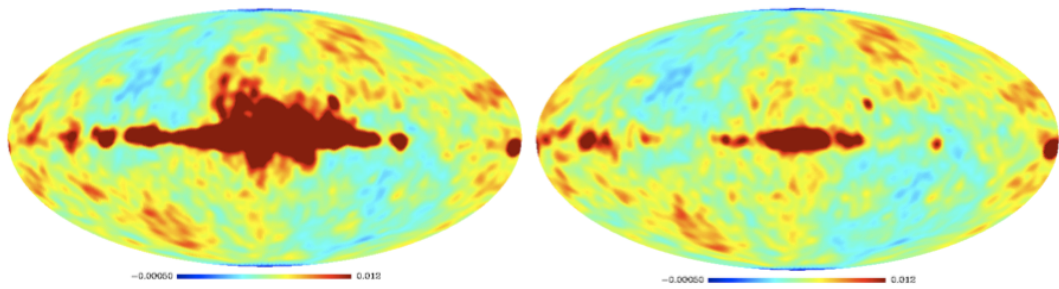
Figure 5.7: Left panel: mollview projection of the residuals for the Q Stokes parameter, in K band, obtained subtracting the mamd.dickinson model from the WMAP map. No CMB was taken into account. Right panel: same thing, but the Q parameter from the mamd2008 model was subtracted. The scale is in mK.
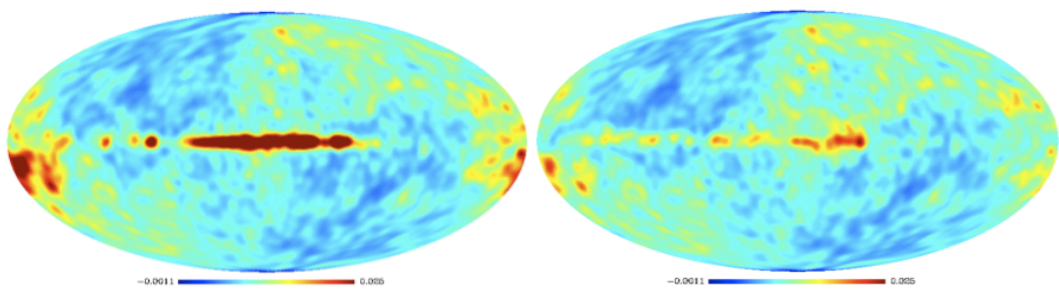

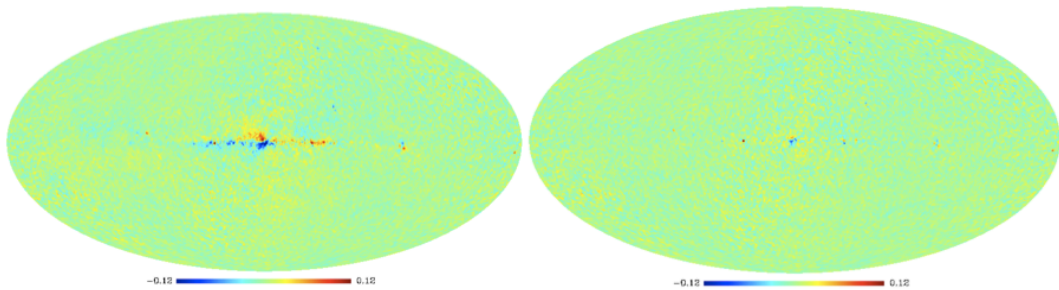Figure 5.8: Same of previous figure, but in W band.

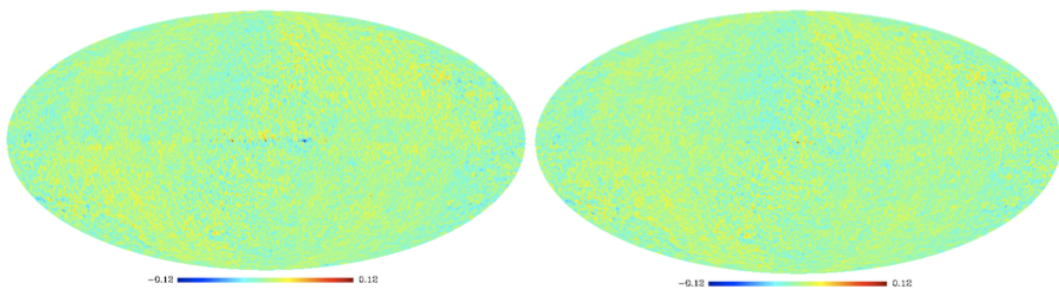Figure 5.9: Same of Fig. 5.7, but for U Stokes parameter.

Figure 5.10: Same of previous figure, but in W band.

136

Chapter 6

Component Separation

6.1   Introduction

Looking forward for the *Planck* mission, some considerations on the techniques that will be used to recover all about CMB features have to be done.

To recovery the CMB anisotropy pattern (and the consequent Angular Power Spectrum representation) one must disentangles the CMB component from the foregrounds. In this process, two factors determine the quality of the whole analysis: on one side the knowledge of the Galactic and extragalactic emissions, of the physical processes involved in these and the need to have a good database about their spectral behavior, on the other side the development of precise algorithms capable of separating the CMB patterns from the other contributions. Of course it is worth complementing all of these by ancillary data and informations at other frequencies.

Moreover, if we are looking for collecting polarization data, with respect to the case of temperature, it turns out a relevant intrinsic complication: observations show that the Galactic foregrounds components are typically polarized up to $5 - 50\%$, while CMB anisotropies are weakly polarized, around few %. In addition to this, the CMB B-mode polarization is much weaker than the E-mode, differently from the case of foregrounds where the two polarization modes have almost the same amplitude.

6.2   Component separation technics

In the previous chapter we saw how impressive is the contamination of CMB by foregrounds and so, in order to study CMB features, it is worth (not to say necessary) to separate the astrophysical emissions. This is done

through *component separation* techniques: the aim is indeed to isolate the emission of interest (or more than one) from all the rest, in the best possible way. Usually, for each component, the best map estimation, is obtained minimizing the total error variance [40]

$$\chi^2 = \sum_p |\hat{s}(p) - s(p)|^2 \, , \tag{6.1}$$

where $s(p)$ is the true component emission, $\hat{s}(p)$ is its estimated value, p is an index for the space of interest (it could be a set of pixels, or modes of a spherical harmonic decomposition, etc).

Let overview now a simple method to consider in a stand alone set an average of the measurements obtained at different frequencies: the Internal Linear Combination (ILC) method. It assumes few informations about the components. One of them is considered to be the emission of interest (for example, the CMB), while all the other emissions are considered foregrounds, unwanted signal. In the ILC component separation method, the component of interest has the same emission template at every frequency and the observations are calibrated on the component of interest. For each frequency channel i we have

$$y_i(p) = s(p) + f_i(p) + n_i(p) \, , \tag{6.2}$$

where $f_i(p)$ is the foreground contribution and $n_i(p)$ is the noise, for each channel i. Practically, it is possible to consider that, during the observation, the detector is measuring $s(p)$ with an error $f_i(p) + n_i(p)$, so it is quite natural to average all the measurements giving to each of them a specific weight w_i

$$\hat{s}(p) = \sum_i w_i(p) y_i(p) \, . \tag{6.3}$$

Of course, the choice of the weights is driven by the maximization of some criterion on the estimate of $s(p)$. This means that for all p, the sum of the coefficients $w_i(p)$ must be equal to 1.

It is so possible to minimize the variance σ^2 of the map $\hat{s}(p)$ using weights independent of p, in order to have $w_i(p) = w_i$ and $\sum_i w_i = 1$. The estimate takes the following form

$$\hat{s}(p) = \sum_i w_i y_i(p) = s(p) + \sum_i w_i f_i(p) + \sum_i w_i n_i(p) \, . \tag{6.4}$$

If the signal $s(p)$ is non-correlated with foregrounds $f_i(p)$ and with noise $n_i(p)$, the variance of the error is minimum when the variance of the ILC map is

minimum.

The ILC method is widely used to obtain CMB maps, but it could be used to obtain emission maps also for other emission processes. In this case, it is necessary to remember that the data must be calibrated with respect to the component of interest (that is to say, the emission template of this component should not change significantly with the frequency of observation) and the component itself must be uncorrelated with other components. Anyway, as demonstrated in [40], there are some issues caused by this non-correlation problem that could complicate the separation process. The ILC could indeed bias the results if the assumption on the component of interest are correlated with other components for some reason or if the data-set is significantly small (e.g., if the analysis is done on small region on the sky).

Hence, even if the ILC method is powerful when nothing is known about the data, it is not the optimal procedure when prior informations are available.

6.2.1 A more detailed view

In the context of CMB experiment, in order to handle observations derived data, the most used model is probably the *linear mixture*. In this model, the emission of each component could be decomposed as the product of two parts: a spatial template independent of the frequency and a spectral emission that does not depend on the pixel. The total emission of an emission process j, at the frequency v, in the pixel p is given by

$$x_j(v, p) = a(v)s_j(p) \qquad (6.5)$$

that in spherical harmonics becomes $x_j(v, \ell m) = a(v)s_j(\ell m)$. Neglecting the details that could come from the instrument characteristics (beams, response, etc), the observation with a detector is given by

$$y_i(p) = \sum_j x_j(v_i, p) + n_i(p) \qquad (6.6)$$

where $n_i(p)$ is the noise contribution for the detector i. A matrix-vector form could be used for a set of detectors:

$$\mathbf{y}(p) = \mathbf{A}\mathbf{s}(p) + \mathbf{n}(p) \ . \qquad (6.7)$$

In the latter equation, $\mathbf{y}(p)$ represents the map-set observed with all detectors, while $\mathbf{s}(p)$ is the unobserved component, that contains one template map

per astrophysical component. The *mixing matrix* **A** has one column per astrophysical component and one line per detector and it does not depend on pixels. The generic element of the mixing matrix is proportional to the spectrum of the source at an effective frequency, within the passband of the detector. With the detectors properly calibrated and using the CMB temperature for all the measurements, If one is trying to disentangle the CMB signal, detectors must be properly set such that each element of the column corresponding to the CMB, in the mixing matrix, must be equal to 1.

Recovering the single emission process through component separation means to invert the linear system represented by Eq. 6.7.

There is more than one way to get the results.

- If **A** is square and not singular, without additional informations, the inversion is *simple* and it is obtained by

$$\mathbf{W} = \mathbf{A}^{-1} \tag{6.8}$$

and consequently

$$\hat{\mathbf{s}} = \mathbf{A}^{-1}\mathbf{y} = \mathbf{s} + \mathbf{A}^{-1}\mathbf{n} \; . \tag{6.9}$$

This inversion is not always the best solution in terms of residual error, because of the remaining noise term **n**. Anyway, if the aim is to reject astrophysical signals, in terms of residual foreground contamination, the inversion gives an unbiased solution, even if it could be noisy. In comparison, the ILC method can produce a better result in terms of signal to noise ratio, but, as said, the results can be biased.

- If the system is redundant, i.e. there are more observations than components, and there are no prior informations about noise and signal levels, the inversion is obtained by the pseudo inverse

$$\mathbf{W} = [\mathbf{A}^{\dagger}\mathbf{A}]^{-1}\mathbf{A}^{\dagger} \tag{6.10}$$

and the estimator is given by

$$\hat{\mathbf{s}} = [\mathbf{A}^{\dagger}\mathbf{A}]^{-1}\mathbf{A}^{\dagger}\mathbf{y} = \mathbf{s}[\mathbf{A}^{\dagger}\mathbf{A}]^{-1} + \mathbf{A}^{\dagger}\mathbf{n} \; . \tag{6.11}$$

This estimator is unbiased as well, but it could get not rid of the noise and so results can show a low signal to noise ratio. It must be noted

that, since there is no noise-weighting in this method, just one bad channel could affect the whole data-set after the inversion.

- If we have more statistics informations about the noise, it is worth to build the noise correlation matrix, $\mathbf{R_n}$. The generalized least square (GLS) solution of the system represented by Eq. 6.7 is given by

$$\mathbf{W} = [\mathbf{A}^\dagger \mathbf{R_n^{-1}} \mathbf{A}]^{-1} \mathbf{A}^\dagger \mathbf{R_n^{-1}} \tag{6.12}$$

and the estimator is

$$\hat{\mathbf{s}} = \mathbf{W} = [\mathbf{A}^\dagger \mathbf{R_n^{-1}} \mathbf{A}]^{-1} \mathbf{A}^\dagger \mathbf{R_n^{-1}} \mathbf{y} = \mathbf{s} + [\mathbf{A}^\dagger \mathbf{R_n^{-1}} \mathbf{A}]^{-1} \mathbf{A}^\dagger \mathbf{R_n^{-1}} \mathbf{n}. \tag{6.13}$$

This solution is unbiased. The GLS method assumes that for each detector the noise is a realization of a random Gaussian field. Anyway, this solution is, at least theoretically, better than the ILC one, if the model holds, but there is still the need for prior informations about data.

- If further informations about the spectral content of the original signal and noise are known, then is possible to adapt the widely used Wiener filter to find a solution of the system in Eq. 6.7. Many details can be given about this filtering technic. Here I will give just a quick look regarding the solution of the system in Eq. 6.7. If the mixing matrix $\mathbf{A}$ is provided and second order statistics of the components and the noise are known [140] [15], through the Wiener filter we can obtain a solution by

$$\mathbf{W} = [\mathbf{A}^\dagger \mathbf{R_n^{-1}} \mathbf{A} + \mathbf{R_s^{-1}}]^{-1} \mathbf{A}^\dagger \mathbf{R_n^{-1}} \tag{6.14}$$

where $\mathbf{R_s}$ is the correlation matrix of the sources and $\mathbf{R_n}$ the noise one. The estimator is given by

$$\hat{\mathbf{s}} = [\mathbf{A}^\dagger \mathbf{R_n^{-1}} \mathbf{A} + \mathbf{R_s^{-1}}]^{-1} \mathbf{A}^\dagger \mathbf{R_n^{-1}} \mathbf{s} +$$

$$[\mathbf{A}^\dagger \mathbf{R_n^{-1}} \mathbf{A} + \mathbf{R_s^{-1}}]^{-1} \mathbf{A}^\dagger \mathbf{R_n^{-1}} \mathbf{n} \tag{6.15}$$

This method can not provide an unbiased estimate of the component of interest because some of the diagonal terms can differ from unity. Indeed the matrix before $\mathbf{s}$ is not the identity matrix. Furthermore, the final CMB map obtained through the Wiener filter may not be foregrounds free, since off-diagonal terms can have non-zero values.

Of course the use of one method instead another is determined by what we need to recover and by which constraints have to satisfy the component of interest.

6.2.2 Overview on different methods

Before moving to a particular blind technic of component separation, some other methods must be mentioned:

- the Maximum Entropy Method (MEM). If the observations correspond to a linear mixture of distinct emissions and the components (and noise) are Gaussian stationary random processes, the Wiener filter provides the best estimation of the maps (in terms of minimum-variance). The MEM method can invert the linear system of Eq. 6.7 assuming non-Gaussian probability distributions (see e.g. [66]). A particular implementation of MEM works in spherical harmonic domain: the separation of the components is done mode-by-mode allowing one to split a huge optimization problem into a certain number of smaller problems.
  Given that this is a non-blind method, the spectral behavior of the components must be known in advance and since the mixing matrix **A** is fixed the spectral properties of the components must be the same everywhere in the sky. However, introducing additional component can be seen as introducing small variations in the spectral properties of the sources. Finally one can note that using priors on the signals could bias the solution.

- The Generalized Morphological Component Analysis (GMCA) [14]. This is a semi-blind source separation method that aims to disentangle the components assuming that the source spatial morphology is well represented in a fixed waveform dictionary, such as wavelets. The waveform dictionary leads to a so-called *sparse representation*. This implies that the components are well defined from only few samples in the waveform dictionary. In addition, simple physical priors can be used to model Galactic foregrounds.

- The Independent Component Analysis (ICA) [67]. This method looks for the components which maximize some measure of the statistical independence of the components themselves. A recent implementation of this method [90] exploits the fact that non-Gaussianity is usually a convenient and robust measure of the statistical independence In addition, it also searches for linear combinations **y** of the input multi-frequency data, which maximize some measure of the non-Gaussianity.

This implementation consists in quantifying the non-Gaussianity with the *neg-entropy*. If $H(\mathbf{y}) = -\int p(\mathbf{y}) \log p(\mathbf{y}) d\mathbf{y}$ is the entropy associated to the distribution p, the neg-entropy is defined as neg-entrpy$(\mathbf{y}) = H(\mathbf{y}_G) - H(\mathbf{y})$, where $\mathbf{y}_G$ is a Gaussian variable and has the covariance matrix of $\mathbf{y}$. Through a non-linear mapping, the role of the higher order moments of $\mathbf{y}$ and this allows to search the maxima of the neg-entropy. The algorithm was successfully tested for CMB cleaning procedure, because the hypothesis of statistical independence is likely verified at least between CMB and diffuse foregrounds. It was tested on real and simulated data and both for temperature and polarization (for the latter only simulated data were used). In addition to the statistical independence the performance was also possible thanks to the high resolution of the available CMB observations, which provide a big amount of statistical realization (the pixels) for the method allowing the decomposition of the data into the independent components.

6.3   A blind component separation method

The idea that stands behind this class of technics is that to recover the components of a linear mixture even if the mixing matrix $\mathbf{A}$ in unknown. The advantages that could be taken from this are striking: recovering *blindly* the components it is possible to analyze data with limited or with not at all knowledge about the emission laws of the components (furthermore, multi-detector data can be analyzed all at once). This is why these technics go under the name of *blind source separation*, or also *independent component analysis* (ICA). The assumption that makes possible this way is that components are statistically independent.

6.3.1   SMICA

Owning to the class of methods just presented, SMICA [41, 40, 28] stands for Spectral Matching Independent Component Analysis. It is a living software, in the sense that it is continuously updated and implemented through the integration of new options and functions, with a consequent increase of its performances.
This tools ensemble is mainly realized by the ADAMIS group at APC in Paris.
I started to use SMICA during my first stage in Paris, as part of the program

of the IDAPP doctorate, and I kept using it in Bologna to complete the analysis on the IRIS maps, that will be explained in the next chapter.

SMICA is a component separation software that does not work in the pixel space but rather in Fourier space (the spectral domain). In particular it is based on spectral statistics.

To first order, the sky is modeled by a superposition of emission processes (CMB, Galactic foregrounds, SZ, etc.), so an observation with a detector d is given by

$$y_d(\theta, \phi) = \sum_{j=1}^{N_c} A_{dj} s_j(\theta, \phi) + n_d(\theta, \phi) \,, \tag{6.16}$$

where s_j is the emission template for the jth component, N_c is the number of components, n_d is the noise term and A_{dj} contains the emission laws and the detector properties.

In order to perform a multi-detector processing, a more useful formulation consists in joining all the observations y_d in one vector. A matrix-vector formulation is write as

$$Y(\theta, \phi) = AS(\theta, \phi) + N(\theta, \phi) \,, \tag{6.17}$$

where Y is the observations vector and S and N are built in the same way. The $N_d \times N_c$ matrix A is called the mixing matrix (N_d is the number of detectors). In Fourier space the notation is equal, but θ and ϕ are substituted by the frequency $\vec{\ell}$. It is necessary to build a spectral density matrix $\langle Y(\vec{\ell})Y(\vec{\ell})^\dagger \rangle$ that represents the power spectrum of Y. Here $\langle \rangle$ is the expectation operator and $\dagger$ the transpose-conjugation. This spectral density matrix is averaged over a certain number Q of bins on ℓ:

$$R_Y(q) = \frac{1}{n_q} \sum_{\vec{\ell} \, \epsilon D_q} \langle Y(\vec{\ell})Y(\vec{\ell})^\dagger \rangle \tag{6.18}$$

where $q = 1, ..., Q$ are the bins, D_q is the set of frequencies contributing in the bin q and n_q is the number of these frequencies. Hence the linear model is newly written as

$$R_Y(q) = AR_S(q)A^\dagger + R_N(q) \tag{6.19}$$

with $R_S(q)$ and $R_N(q)$ are made in the same way of $R_Y(q)$. SMICA is a blind method, so the statistical independence is required on the emission vectors and it takes the form

$$R_S(q) = \mathrm{diag}(C_1(q), ..., C_{N_c}(q)) \,, \tag{6.20}$$

where

$$C_j(q) = \frac{1}{n_q} \sum_{\vec{\ell} \in D_q} C_j(\vec{\ell})$$ (6.21)

is the binned power spectrum for the j-th component and $C_j(\vec{\ell}) = \langle |s_j(\vec{\ell})|^2 \rangle$ is the spatial power spectrum of the same component. If the noise is uncorrelated, its structure depends on N_d parameters

$$R_N(q) = \text{diag}(\sigma_1^2, ..., \sigma_{N_d}^2) .$$ (6.22)

In this way, the model depends on Q spectral density matrices $R_Y(q)$, that depend on $A, C_j(q)$ and σ_d^2. The estimation of these parameters is made by finding the best match between the $R_Y(q)$ matrices and a set of equal number of empirical spectral density matrices $\hat{R}_Y(q)$ defined by

$$\hat{R}_Y(q) = \frac{1}{n_q} \sum_{\vec{\ell} \in D_q} Y(\vec{\ell}) Y(\vec{\ell})^\dagger ,$$ (6.23)

the non parametric estimates of the corresponding $R_Y(q)$. In particular, the unknown parameters are found by minimizing the *spectral mismatch* defined as

$$\phi(\beta) = \sum_q n_q K(\hat{R}_Y(q), R_Y(q, \beta)) ,$$ (6.24)

where $\beta = \{A, \{C_j(q)\}, \{\sigma_d^2\}\}$ and $K(\hat{R}, R)$ is Kullback-Leibler divergence, a measure of the difference between two positive matrices. It must be noticed that minimizing this kind of mismatch is equivalent to maximizing the likelihood of the data in a model where all components are Gaussian, stationary and have constant harmonic spectra over the bins. Furthermore, the flexibility in the choice of the parameters allows to aim to different goals on the basis of their choice: SMICA can be adapted for different kinds of data processing.

Anyway, in this method, in some cases, there is an issue: a factor of degeneracy. When all the parameters in β are free to be determined, two *problems* turn out: the mixing matrix cannot be recovered better than up to a column permutation (basing the results only on the spectral mismatch), so the components in the model cannot be ordered; for each component j, a scalar factor can be exchanged between the j-th column of A and $C_j(q)$ and this factor cannot be determined only from the data.

After minimizing the mismatch and once the parameters are recovered, the maps are reconstructed by the Wiener filter.

The SMICA package is one of the component separation methods that will be used during the reduction of the data that will be collected by the *PLANCK* satellite. From a recent challenge on component separation technics [83], it turned out that different methods result to be effective in cleaning the CMB maps from contaminations, in reconstructing maps of the diffuse Galactic emissions and in detecting point-sources and thermal SZ effect signals. Therefore, the final component separation pipeline for *PLANCK* will involve a combination of the methods tested.

In the next chapter, it will be presented the work done on the IRIS map-set [98] about removing a contamination signal: Zodiacal Light Emission (ZLE) residuals. In this re-processing I used a basic version of SMICA in order to recover and identify the emission template and the spectral behavior of these residuals.

Chapter 7

Subtracting the residuals of ZLE in far-infrared maps

7.1 Introduction

The work I did in the context of removing foregrounds consists in the subtraction of the residuals of a foreground emission from a IR data-set.

The entire IRIS map-set [98] was re-processed, in order to remove the foreground residuals related to the Zodiacal Light Emission (ZLE). Indeed, what is visible in these maps is not a *pure* foreground signal, it is a residual of a previous subtraction. The same Zodiacal Light model realized for the DIRBE data-set was used for the original realization of the IRAS maps, the map-set from which was derived the IRIS set. Indeed, both in DIRBE and in IRIS all sky maps, when displayed in Galactic coordinate, is well visible a *stretched S* shaped pattern having reference to the ZLE pattern.

After highlighting briefly the results of the IRAS mission and the realization of the IRIS map-set, the whole process and the results I obtained aiming to clean the entire IRIS map-set from the ZLE residuals it will be discussed in details.

7.2 The IRAS satellite

The Infrared Astronomical Satellite IRAS [5], was a joint project of the US, UK and the Netherlands. The mission had a major impact on almost every area of astronomy. From January to November 1983, the satellite completed the primary mission, performing a survey of 98% of the sky at four wavelengths: $12, 25, 60, 100$ μm.

When IRAS ceased operation, it had already collected data to deliver: a catalog of infrared point sources, a catalog of extended sources smaller

than 8′, a catalog of low-resolution spectra and an atlas of absolute surface brightness images of the entire infrared sky. These catalogs give the characteristics of some 250,000 point sources and 20,000 small extended sources down to a limiting flux density, away from confused regions of the sky, of about 0.5 Jy at 12, 25 and 60 μm and about 1.5 Jy at 100 μm for point sources, and about a factor of three brighter than this for small extended sources. The angular resolution of the instrument varied between about 0.5′ at 12 μm to about 2′ at 100 μm. The positional accuracy of sources detected by IRAS depends on their size, brightness and spectral energy distribution but is usually better than 20″.

Moreover, the IRAS satellite made a significant contribution to our understanding of Galactic diffuse emission by revealing some strange structures in the sky, that can be observed in any direction [88]: the map at 100 μm is dominated by filaments known as *infrared cirrus* which, although concentrated near the Galactic plane, can be found almost all the way up to the Galactic poles. The primary, deleterious effects of the cirrus are that it can generate well-confirmed point and small extended sources that are actually pieces of degree-sized structures rather than isolated, discrete objects and this can corrupt the 100 μm channel, and occasionally the 60 μm one, in the measurements of true point sources.

From the first release of extended emission maps (the SkyFlux atlas) realized along with the IRAS point source catalog, it was clear that significant improvements of the sensitivity and photometric accuracy could be obtained based on acquired knowledge of the instrument. These became real through the second generation processing, which increased the sensitivity by a factor up to five, lead to the IRAS Sky Survey Atlas (ISSA) published in 1991 and 1992 [69].

Since its publication, the ISSA has been widely used to study various aspects of Galactic and extragalactic diffuse emission and it became an essential data set for any multi-wavelength analysis of the interstellar medium. However, the ISSA plates still suffer from defects (striping, calibration, zero level, Zodiacal light) that can significantly limit their use. The aim of the Improved Reprocessing of IRAS Survey (IRIS) was to deliver a data set with a better Zodiacal light subtraction, a calibration and a zero level compatible with DIRBE, and a better destriping.

7.3 The IRIS map-set

The IRIS [98] data set is composed by 4 full-sky maps at different wavelength: 12, 25, 60 and 100 μm (see FIg. 7.1). The thermal dust emission is particularly well visible in this frequency range and thanks to the ~ 4 arcmin resolution of the IRAS satellite, this would be a optimal set of maps to study variations and characteristics of dust properties on all scales.

The necessity of a re-processing of the whole map set arises from the fact that the ISSA plates suffer from calibration, zero level and striping problems and these not allow a safe use of the maps. Further, a non-physical related pattern is well visible at almost all wavelength: this is a residual of the initial contribution of the ZLE component. These remaining features include fine structure in the Zodiacal cloud (the Zodiacal dust bands, for instance), planets, unknown asteroids and orbital debris that escaped the artifact removal process.

This ZLE residual is well visible at 25 μm, where it reaches the maximum of its contribution and, also for this reason, this channel has a particular role in our analysis. The cleanest channel of the set is the 100 μm channel: here the ZLE residual is totally negligible.
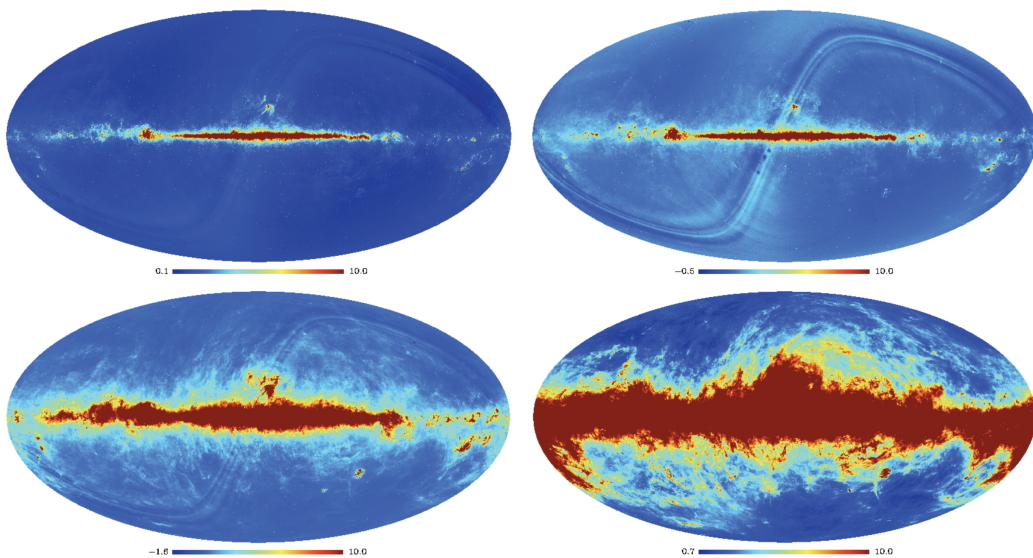
Figure 7.1: Full IRIS map-set. The flux is limited to 10 MJy/sr in order to emphasize the ZLE related structure. Top-left: 12 μm; top-right: 25 μm; bottom-left: 60 μm; bottom-right: 100 μm.

7.4   The data-set used

The whole IRIS map-set was involved in the analysis. In addition to this, in order to *tune* the subtraction process, a preliminary analysis was done using some of the DIRBE map-set [68],[73]. The reason is that this data set contains four maps at the same frequency as the IRIS map set, but its frequency coverage is wider: the DIRBE map-set spans from 1.25 to 240 μm in ten frequency bands.

In the context of component separation methods, or in a more general way, in the context of modeling and removing foregrounds, increasing the number of frequency bands of observation would bring a better understanding of the spectral behavior of an emission process and so a more precise identification and *separation*. So, before performing the analysis at the IRIS frequency, some tests were done including also the 3.5, 4.9, 120 and 240 μm (in addition to the four common channels) maps of DIRBE. Moreover, the lower resolution of the DIRBE maps allowed us to start to work with *lighter* maps without the need to degrade the maps themselves.

Further cross-analysis were done between IRAS, IRIS and DIRBE maps at each common frequency, in order to collect useful informations for the analysis, like zero levels and differences due to de-striping between IRAS and IRIS.

After this first phase and tests, I started the preliminary operations that the IRIS map-set needed and, in this discussion, I will focus on this data-set, neglecting further comments on the DIRBE maps, when possible.

7.4.1   Preliminary operation

Before doing any kind of analysis it is necessary to setup the maps properly. First thing to notice is a small number of undefined pixels in the IRIS maps and this makes any kind of calculation impossible to be performed. We decided to fix the missing values of the undefined pixels by giving to these pixels the average value of the neighbors pixels, in order to avoid to supply them a flagging value and to have a kind of consistency for the diffuse sources component separation process (point sources, like point holes, are not well treated by SMICA as I used it).

After that operation, I looked for point sources (PS) subtraction. To have a complete PS mask, I built a map in HEALPix format (with nside=1024), using the complete IRAS PS catalog. All the pixels corresponding to sources

were set to zero in the PS mask. After that, I smoothed this map with a Gaussian beam of FWHM = 4 arcmin (that is about the lowest resolution reached in the IRIS map-set) and included in the mask all the pixels under a threshold level equal to 0.95 (the values in the mask map go from 0 to 1). Only after that I masked all the PSs on the whole set with the mask described above.

At this point there is the need to choose a strategy for the Galactic plane treatment. This phase is very delicate and potentially it has a key-role in the whole process. That is because of the strong dependence I encountered in the SMICA processing in relation with the choice of the masked input maps supplied.

In order to make an optimal choice, I tested several different masks on the maps, in order to find a good Galactic cut and at the same time to satisfy a series of requirements.
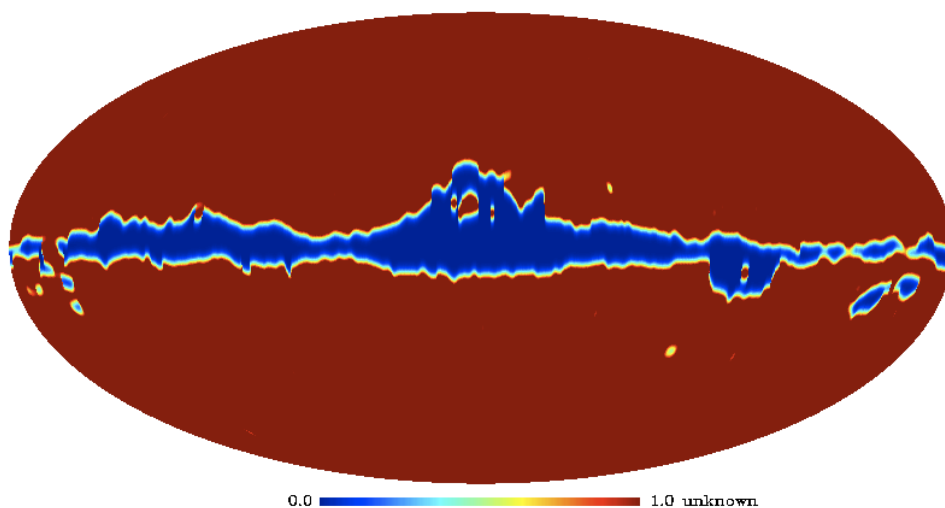
Figure 7.2: The kp2 mask used to cut Galactic plane structures.

First of all, the Galactic mask determines the fraction of uncut input map. This aspect has a double face: on one side it controls the amount of Galaxy that is going to take part in the process, on the other, delimitating the Galactic plane shape, it puts some constraints also on the ZLE pattern, because of the crossing of this component on the Galactic plane. Because of the weight that the used mask has on the component separation process, I decided to choose the *right mask* working on the 25 μm map: the most ZLE-dirt channel of the set.

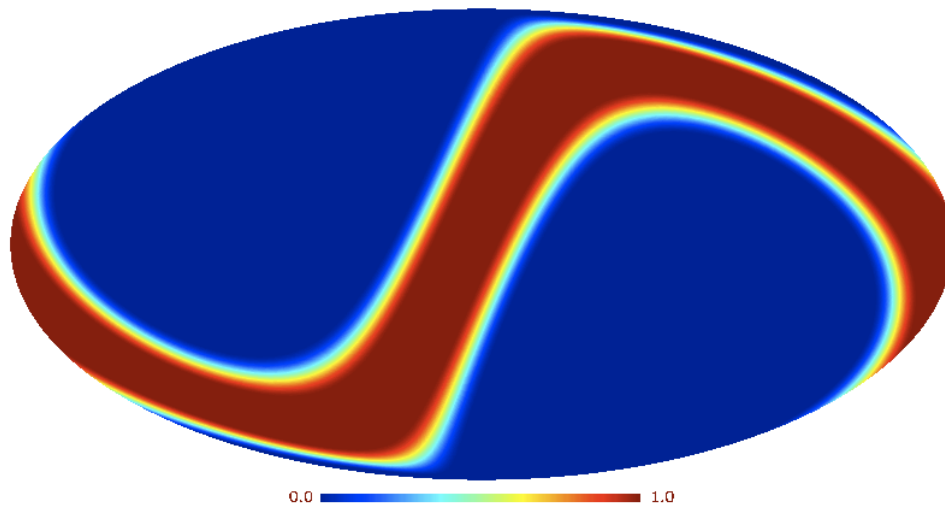This choice (Fig. 7.2) permitted me to identify, with good precision, the big

Figure 7.3: The 20 degrees zodiacal mask used to select the region with the ZLE related residual oscillations.

oscillations of the ZLE residual pattern.

I noticed also two compact sources along the ZLE pattern. This confined regions of the sky doesn't carry any problem for what concern the identification of the component in the SMICA processing, but they were crucial during the reconstruction of the maps: SMICA works in the Fourier space, so once the components are recovered the maps are reconstructed through a filtering process and newly set in the original format. During this phase, harmonic transforms generate spurious 2 oscillations around these two compact sources, giving a non-physical and non-negligible contribution to the rebuilt map of the component of interest.

At this point, the maps are full of holes, related to the cut Galactic regions and to the subtraction of point sources. I filled these holes with a diffusive filler: it diffuses the values of the border regions surrounding the holes. After this process, the SMICA input maps look like the one in Fig. 7.4.

7.5 The analysis process

7.5.1 Phase I: SMICA

Several runs were performed with SMICA, with different composition of maps, masks and boundary conditions. I also tried multi-detector analysis in SMICA: we built a data-set including the IRIS map set and same maps of the DIRBE map-set. The analysis with DIRBE map-set alone was very useful to understand which was the best method to follow in order to separate
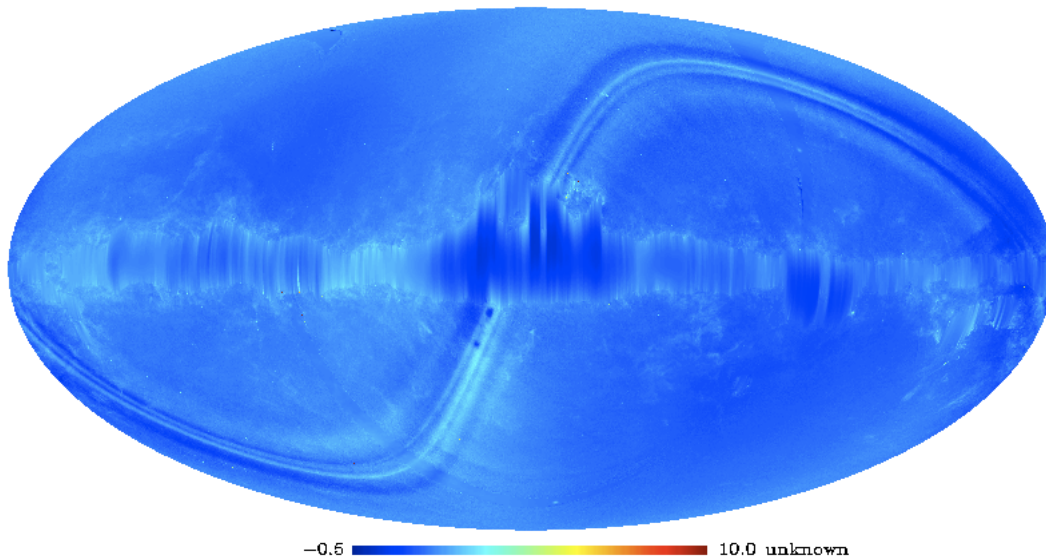
Figure 7.4: The 25 μm channel of the IRIS mapset after removing Galactic plane structures and point sources and after filling the holes with the diffusive filler. This is a typical map used as input map for a SMICA run.

the ZLE contribution to the maps. The DIRBE map-set is wider than the IRIS one, ranging from 1.25 to 240 μm, and this fact hides two potential advantages: on one side, having a wider frequency range, it is possible to make a more detailed reconstruction of the spectral emission of the Zodiacal Light, while on the other, one can perform runs in SMICA setting a model with more than 4 components (with the IRIS data-set you cannot go over 4 components, because you have only 4 different channels).

We found out that with 4 component SMICA reaches the best estimation of the ZLE template and power, even if a very light signal of this component is still present in another map of the SMICA outputs. Anyway we verified that this further residual is totally negligible on the whole map-set. A 3 component model works quite well too, but in this case the results show a well visible Galactic contamination in the map of the ZLE component, so we discarded this option and focused on a 4 component model.

We tuned our analysis running several times SMICA with medium resolution maps (nside=512 in HEALPix format) and we did the final processing chain with higher resolution maps, nside=1024. The IRIS realization of maps at higher resolution (nside=2048), shows some inconsistency due to several undefined pixel, that were causing spurious oscillations during more than one step of the processing chain.

So, once the components separation process ended, we picked up the SMICA

output map of the ZLE component and prepared it for the subtraction. The aim of this phase is to *clean* the component map in order to leave on the map itself only what have to be *really* subtracted from the original map. In other words, we act on the component map with masks: one for the Galactic plane, because even if it was masked on the original maps some residual of the diffusive filling is still visible on output, and the other mask for the ZLE residual. This last mask is a sort of *safety mask*: it is shaped on the ZLE pattern and its task is to force to zero the regions around the ecliptic poles, in order to not subtract any power from the original maps in that regions (see Fig. 7.3).

After this operations, we can easily subtract the unwanted component from the original map set.
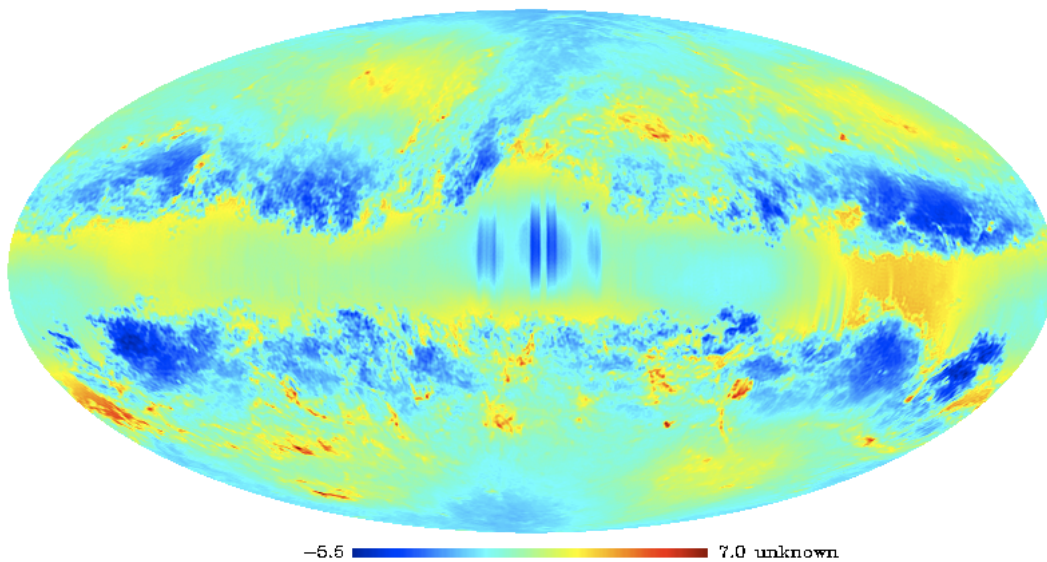
Figure 7.5: This is one of the SMICA output maps (the components separated). Galactic structures are well visible, while the ZLE pattern is totally missing.

7.5.2   Phase II: Filtering

Even if we had good results by subtracting the ZLE residuals from the IRIS map-set, after the SMICA analysis, in some maps, there is still some contamination from the unwanted component. This persisting traces are probably due to a non optimal estimation of the ZLE pattern and/or power. The source of this discrepancy could lie in the difficulty by SMICA in separating Galactic and ZLE contribution beyond a certain level and could be also caused by a degeneracy between these two components near the center of the Galactic plane, just when the ZLE cross the Milky Way disc
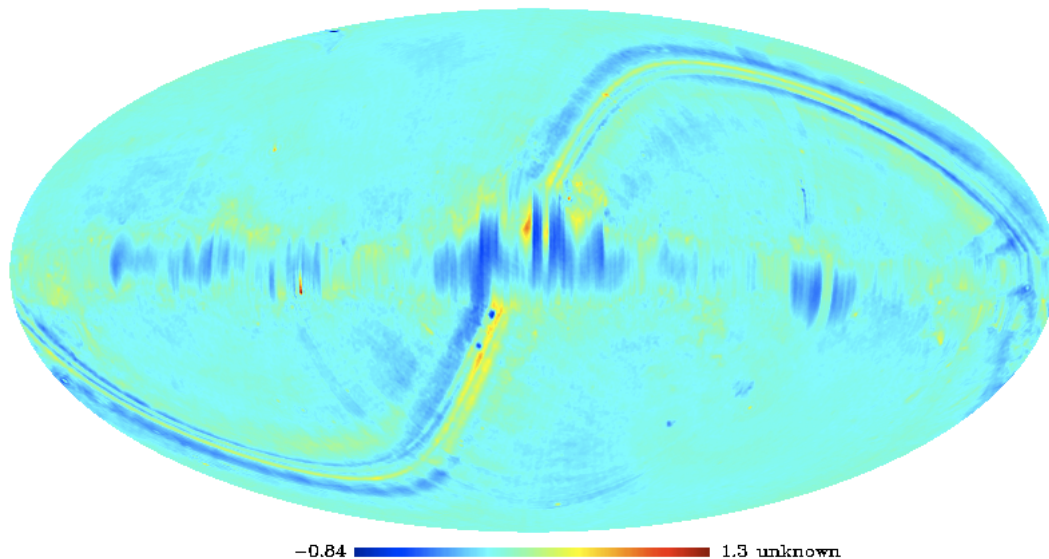
154

Figure 7.6: The SMICA output map corresponding to the ZLE residual oscillations. It is possible to see some residual contamination from unwanted contributions, in particular along the edge of the masked regions.

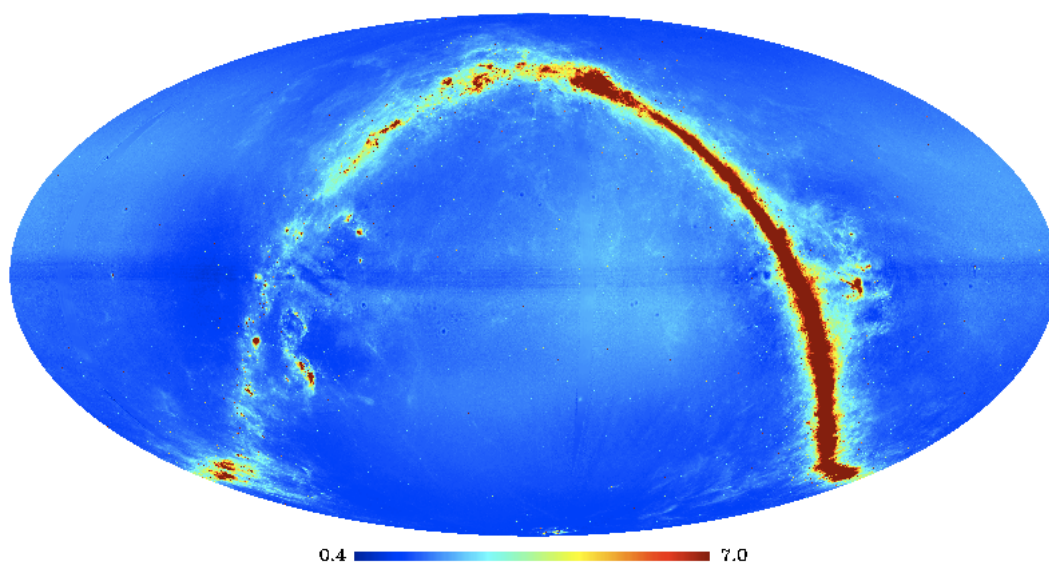in the line of sight of the Galactic center.

Figure 7.7: The 25 μm map in ecliptic coordinates, ready for the FFT filtering. In the map, the contribution of the ZLE emission recovered from a fist run with SMICA have just been subtracted. Flux is constrained to make well visible the residuals along the ecliptic plane.

Because of that, we decided to build a filter able to clean in a more efficient way the maps after the subtraction. The original idea is that

to fit the ZLE residual oscillation with some function, in a narrow stripe perpendicular to the ecliptic, and to minimize the distance of each pixel from the fitting function (that is nothing but the actual averaged value of the pixels) to the linear fit set up between the pixels values at the high and low latitude border of the stripe. After spending some time trying to fit the ZLE oscillation with polynomial functions, we decided to leave the pixel space and to try fixing this in the Fourier space. So the idea remains the same, but the fitting function is substituted by a *filtered Fourier transform* of the map in the stripe considered. In details we do like this: we project the map from Galactic to ecliptic coordinates and we scan the ecliptic plane cutting it into limited stripes binning on 0.1 degree in longitude. Of course, the stripes are centered on the ecliptic plane and they have a height ranging from 0.12 rad and 0.17 rad, depending on the features of the ZLE residuals pattern (these further residuals have a non constant position with respect to the ecliptic plane, so it is necessary to work on delimited regions).

In order to work in the Fourier space, we use the FFT function in IDL environment. In the harmonic space we do define a variable filter, that can be used both for highpass filtering and for lowpass filtering:

$$F = \frac{1}{1 + (y/\lambda)^\mu} \tag{7.1}$$

where λ and μ are parameters that set the frequency cutoff of the filter, while y is the array, with constant values, on which the filter is built.
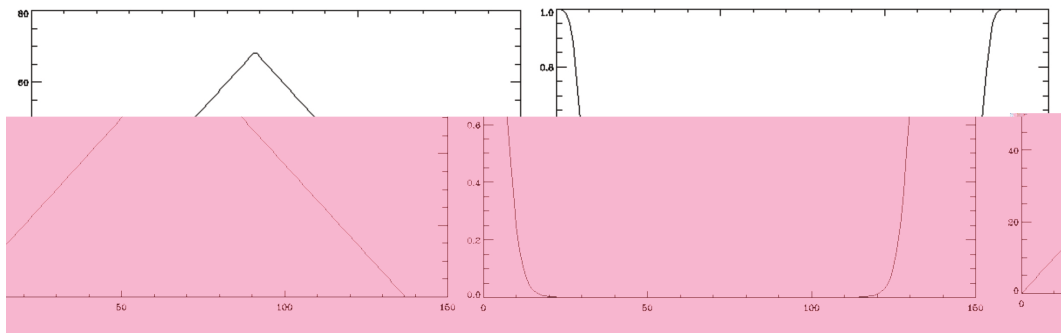

Figure 7.8: Left panel: plot of the array y used to build the filter in Eq. 7.1. Right panel: plot of the filter F itself.

We tried first to use the filter for highpass filtering, setting the cutoff

frequency just above the ZLE residual oscillations correspondence frequency. Such a thing permits to keep features that correspond to small scale structures, discarding all the large scale structures with frequency, in the harmonic space, below the cutoff frequency (the ZLE oscillations). Of course, this method rejects also the monopole power, so there is the need of defining a *compensation tool* in order to rise back the monopole power of the map. The simplest (and well working) thing capable of that is a linear fit from edge to edge of the considered stripe.

After some tests, it turned out that highpass filtering was not so good for all the maps: it works great for the highest frequency map, while it doesn't fit at all our needs on the 60 μm map. Given that, we decided to proceed in a different way for this map: we set a lowpass filter, with the same cutoff frequency of the highpass filter, but instead of rejecting the frequency over the cutoff, we subtract the passing frequencies (low frequencies) from the map, leaving the highest and then compensate for the subtraction of the monopole power.
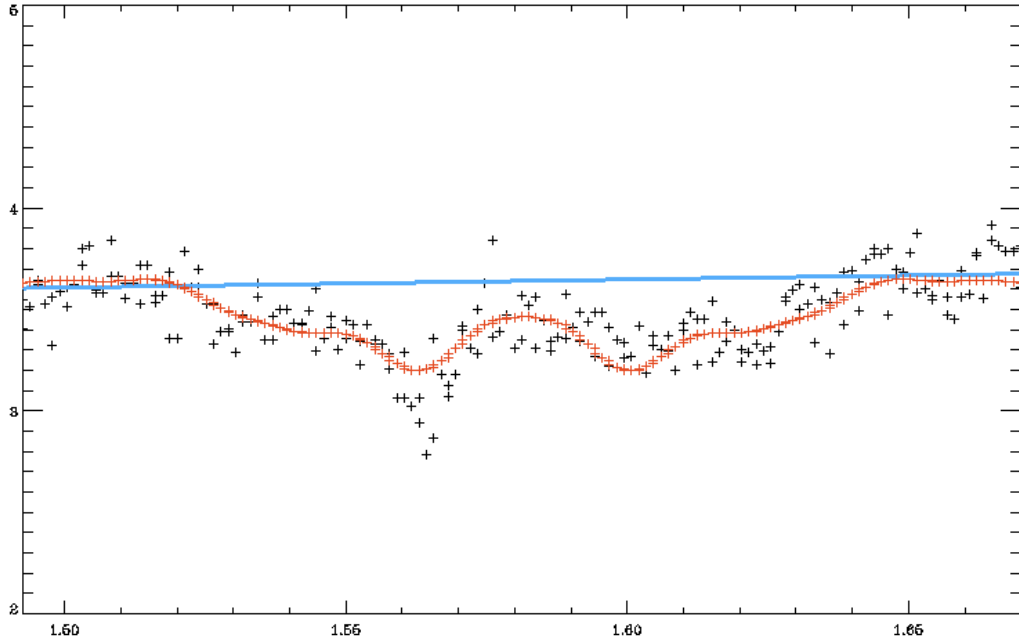
Figure 7.9: A snapshot of how the FFT filter works on the map: the black points represent the pixels values in the stripe of the input map considered, the red points are the Fourier anti-transform (back in pixel space) after the application of the low-pass filter (in Fourier space), while the blue line is the correction to apply in order to recover the medium emission level of the considered region. See text for more details.

7.6 Results obtained

The maps that we obtain after this chain of processes show a significant quality improvement. The large scale structure of the ZLE was mainly already subtracted during the realization of the IRAS and the IRIS map-sets, using the DIRBE model of Zodiacal Light. In this analysis we assumed the ZLE large scale structures as completely subtracted and we focused on its medium scale spurious signals.

Medium scale features of ZLE residuals showed a power comparable to that of discrete structures in our own Galaxy and this affects any kind of precise analysis that can be performed on the IRIS maps. As it is visible in Fig. 7.10, plotting the map power versus Galactic latitude, the residuals presented a clear oscillating pattern. This is not constant at all and varies in amplitude and shape along the ecliptic plane in a non predictable way. Indeed, an ecliptic projection of the ZLE components (or the map itself, see e.g. Fig. 7.8) shows that the residuals have variable ecliptic latitude. This complicated the filtering phase, that could not be generalized for a all-sky analysis, because the integration interval is set through ecliptic coordinates and a variation of
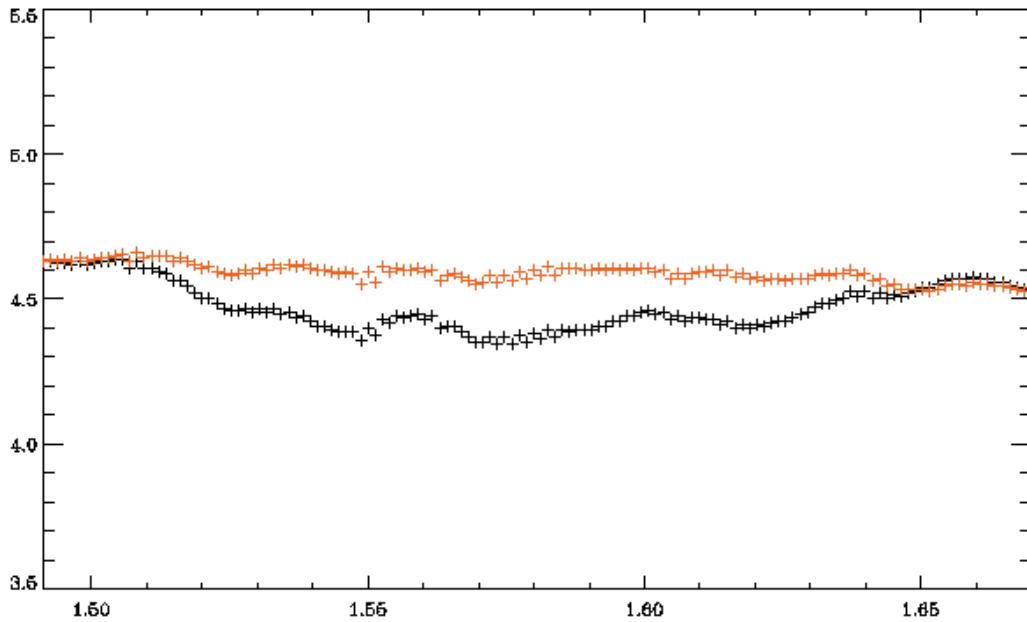
Figure 7.10: A snapshot of how the FFT filter works on the map: the black points represent the pixels values in the temporary stripe of the input map considered, the red points represent the map after the filter correction. For clarity, for this plot, was chosen a region in which the IRIS maps were completed through the DIRBE maps at the same frequency. The minor resolution of the DIRBE maps, permits to have a more clean view of the values distribution of the pixels.

this (e.g. if one extreme of the interval in the ZLE oscillation pattern and not just out of it, as it has to be) leads to a biased non-optimal frequency cut operated by the FFT filter.

We have not encountered relevant features of the ZLE at small scales.

After two different phase of analysis, the oscillations that were visible in the original maps have been recognized and subtracted from the IRIS map-set, with great precision, leaving untouched the rest of the map.

The cleaned map-set here showed would be part of the ancillary data for many kind of astrophysical analysis. In our case, the IRIS map-set is an optimal *companion* to associate to the future measurement that the HFI instrument, aboard the *Planck* satellite, will provide. Indeed, the highest frequencies of HFI are mainly devoted to the observation of the foregrounds and its frequency coverage terminates (857 GHz) almost where the IRIS frequency range starts (3 THz).

At these frequencies the main emission mechanism is thermal dust. The HFI channels well provide a great measure on which one could base a spectral analysis in order to recover a better spectral behavior of the dust emission, with respect to what we have now. Following this way, the IRIS map-set

could provide a great support to such analysis and could help to obtain a more detailed spectral emission, since the dust emission is still strong and well visible in the maps themselves.

The results obtained will be presented in [97]. Furthermore, in the same work, a stronger subtraction of the ZLE residuals will be presented, in which a further ZLE large scale structure subtraction is performed.
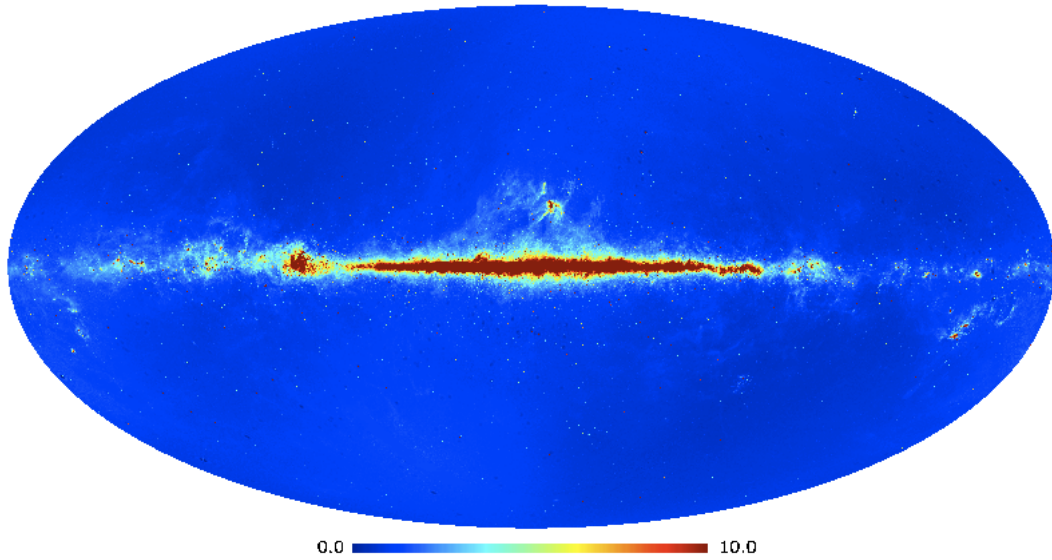

Figure 7.11: The 12 μm final map after the re-processing through SMICA and the FFT filter.
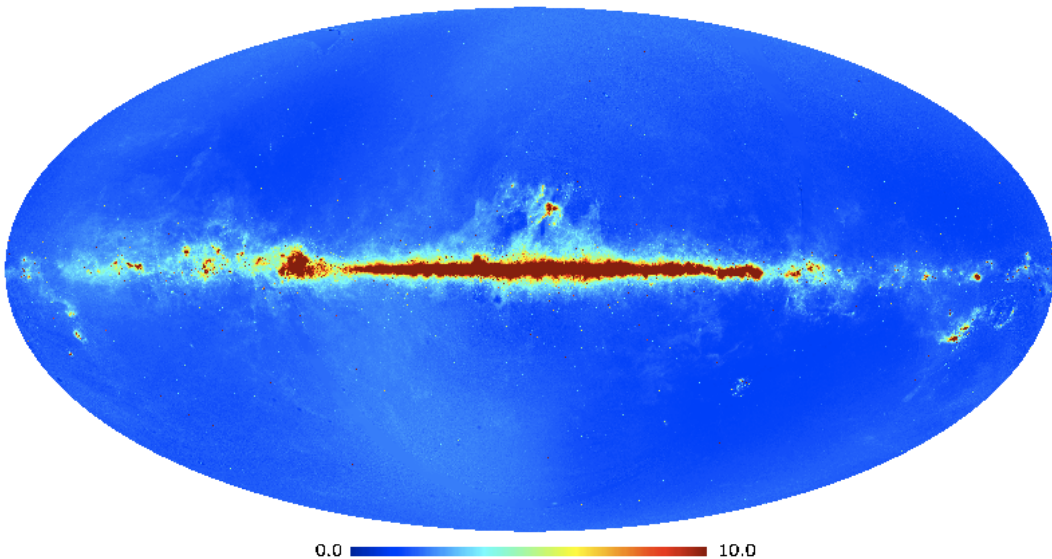
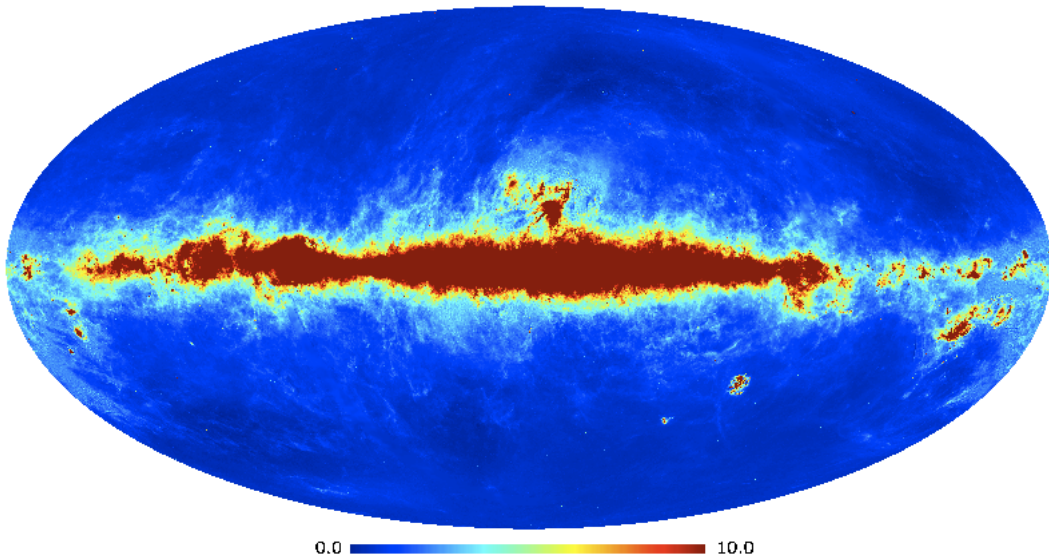Figure 7.12: The 25 μm final map after the re-processing through SMICA and the FFT filter.

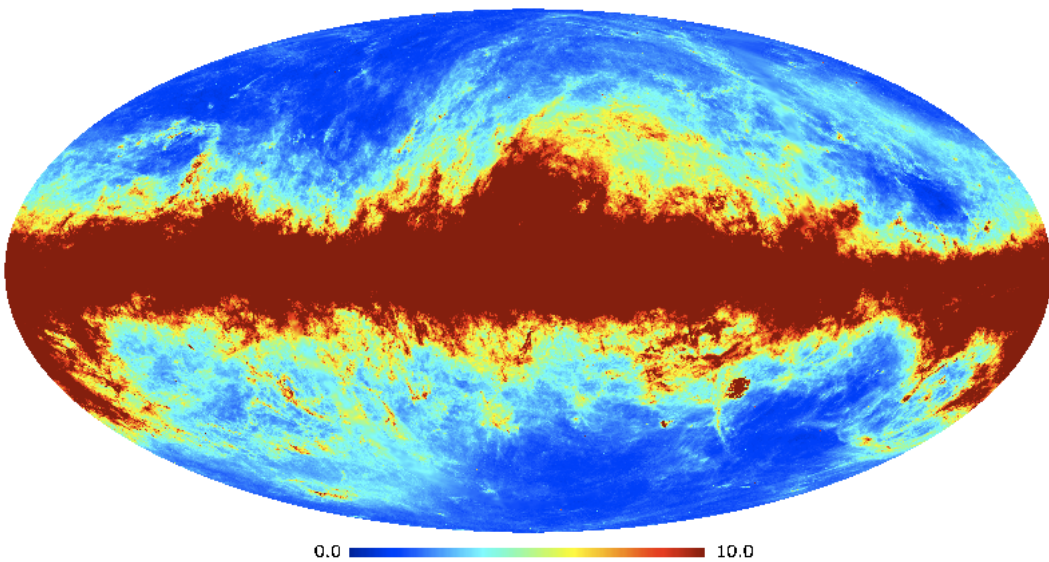Figure 7.13: The 60 μm final map after the re-processing through SMICA and the FFT filter.

Figure 7.14: The 100 μm final map after the re-processing through SMICA and the FFT filter.

7.6.1 A more detailed view on improvements

In order to better appreciate the improvements obtained, it is worth zooming on some regions in the sky and to enhance the contrast scale. The regions here showed were selected on the basis of the contamination level before the ZLE residual subtraction. The channel at 25μm was chosen for this comparison test, because of the high level of contamination by the ZLE residuals. On the other hand, in Fig. 7.18, a patch of the 100μm map was

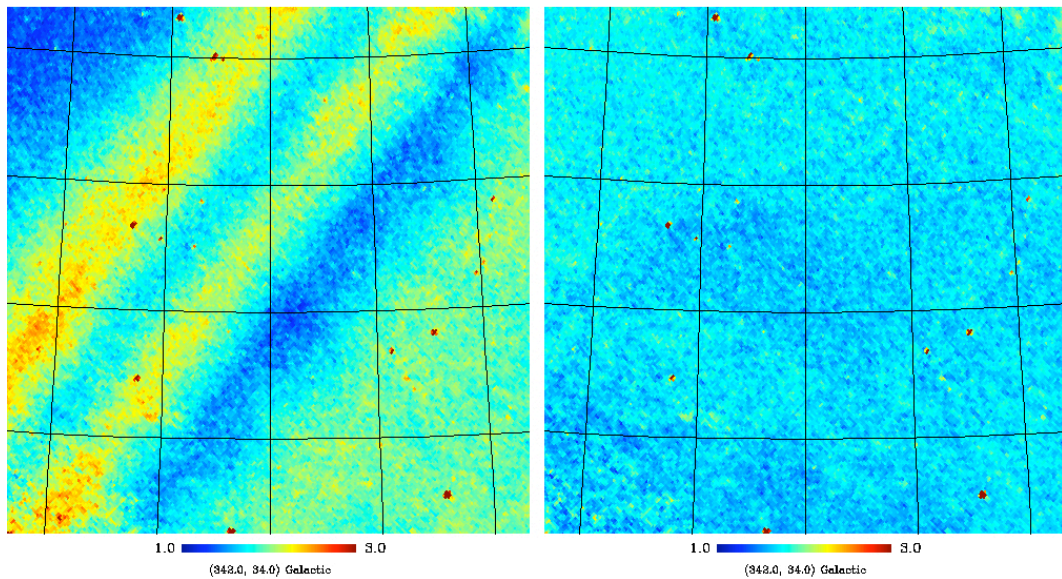displayed, in order to verify the negligibility of the contamination in this channel.

Figure 7.15: Left panel: a patch in the 25 μm map, in which the ZLE residuals are clearly visible. Right panel: the same patch of the final map at 25 μm, after the re-processing through SMICA and the FFT filter.
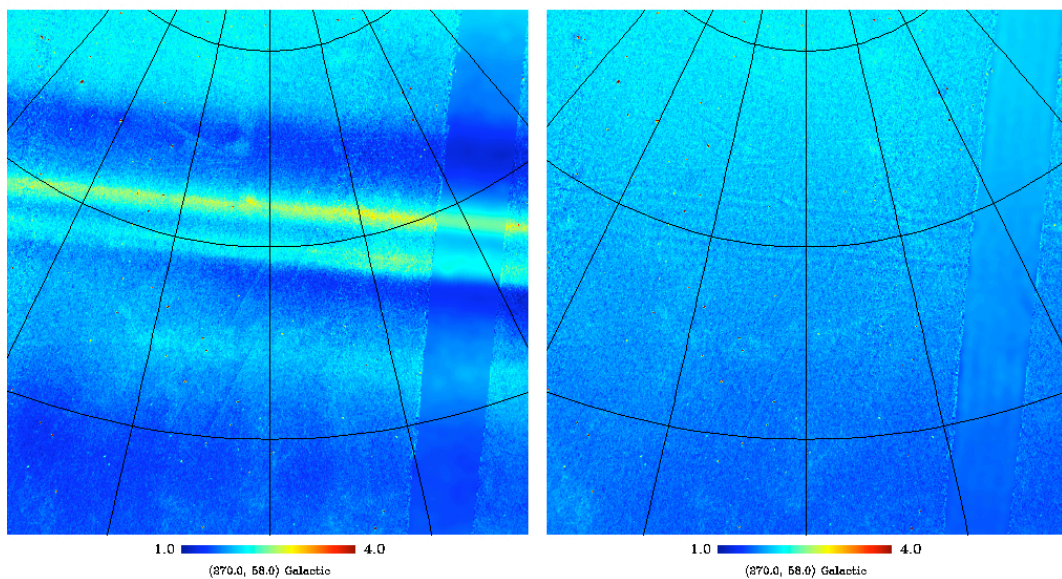

Figure 7.16: Same of Fig. 7.15, but for a different patch in the sky. The low resolution stripe comes from the DIRBE map at the same frequency. The DIRBE data represents the 2% of the sky of the IRIS maps [98].
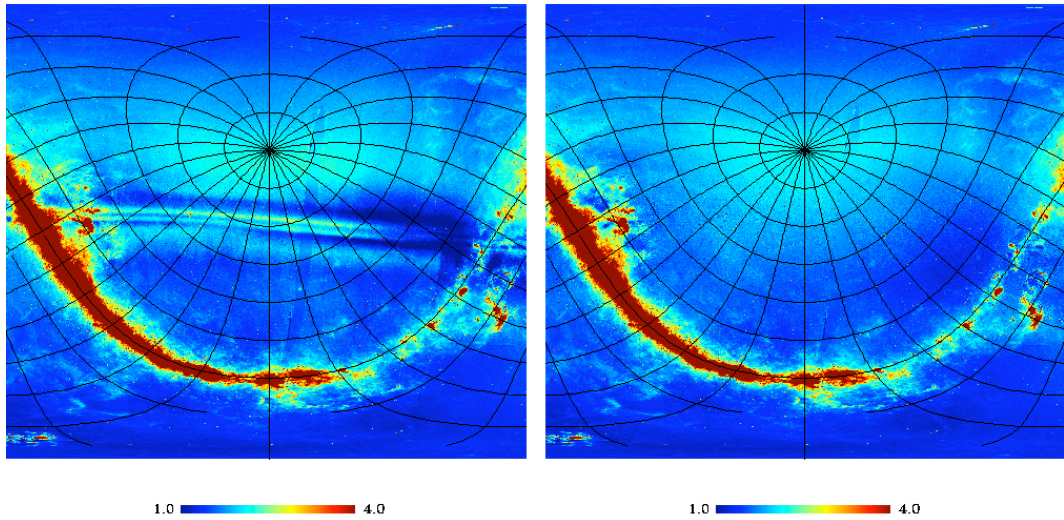
Figure 7.17: Same kind of comparison as of Fig. 7.15, but a wider region in the sky is here displayed. The big horizontal power oscillations are part of the ZLE residuals (left panel map) that have been removed (right panel).
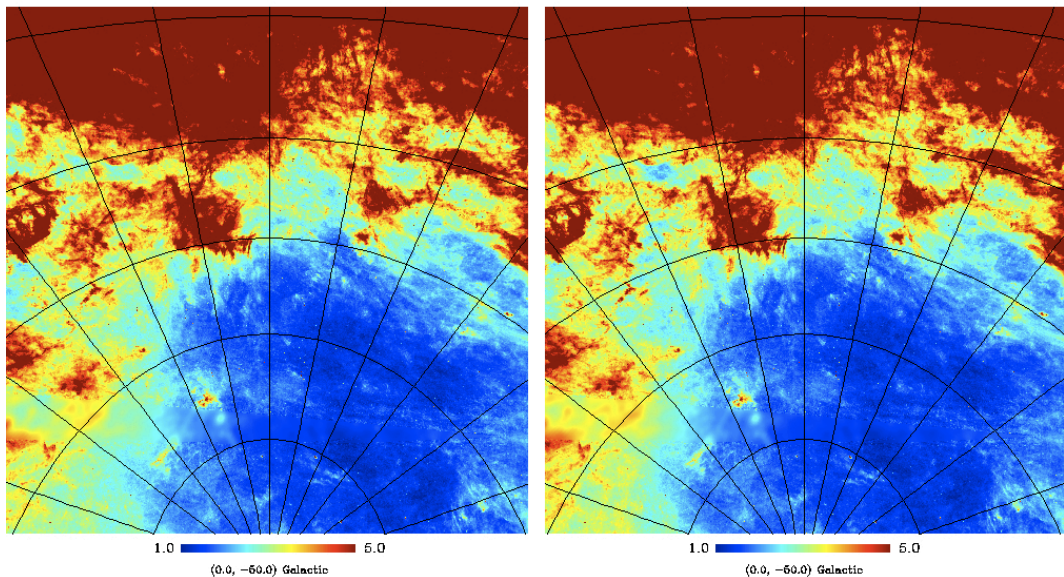

Figure 7.18: Same kind of comparison used for the previous figures, but at 100μm. It is clear that the contamination was negligible in this channel.

7.6.2 A preliminary statistical analysis of the reprocessed maps

An alternative and more quantitative estimate of the obtained results involves a statistical analysis of the maps. In particular, a multifrequency angular power spectrum analysis of the maps is in progress and here some of the preliminary results are presented.

In Chap. 2 we saw how many informations about CMB temperature anisotropies it is possible to recover from the temperature power spectrum.

The same principle it is here applied in order to compare the IRIS maps with the reprocesses maps: differences in the power spectra will indicate at any scale the excess of power due to the ZLE residuals. Further, comparing the spectra, it is possible to verify if the detection of the ZLE residuals involved only reasonable angular scales for what concerns the emission processes. That means that if the detection is good, the high multipole region in the power spectra of the cleaned maps must result the same of that of the original maps. In other words, a good component subtraction leaves the small scale structures unchanged.
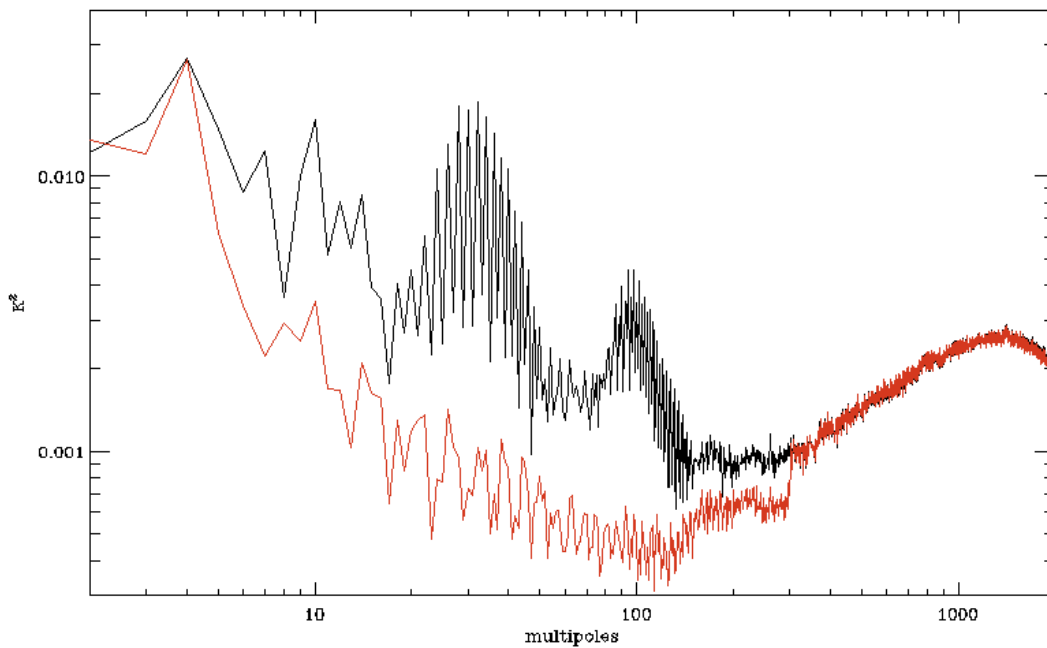

Figure 7.19: Comparison between the angular power spectrum of the original IRIS map at 25μm (black line) and the aps of the same map after the reprocessing. A Galactic cut of $|b| \leq 30°$ is performed on both the maps.

From the differences of the spectra in Fig 7.19 appears clear the improvement obtained. The power at large and medium scale is lower in the reprocessed maps. At $\ell \sim 30$, the spectrum of the cleaned map is ~ 50 mK^2 weaker than the spectrum of the original map. It is also well visible the multipoles interval in which the subtraction had effects. At $\ell \sim 300$ there is a neat break of the quantity of power subtracted to the original maps: under this angular scale, the contribution of the ZLE residuals was totally negligible and the small structures were not involved in the process. In Fig 7.21 it is shown the absolute difference in K^2 between the spectrum of the

164

original map and the spectrum of the cleaned map, at 25μm.

Anyway, further investigations are needed in order to verify with an high level of confidence the results obtained.
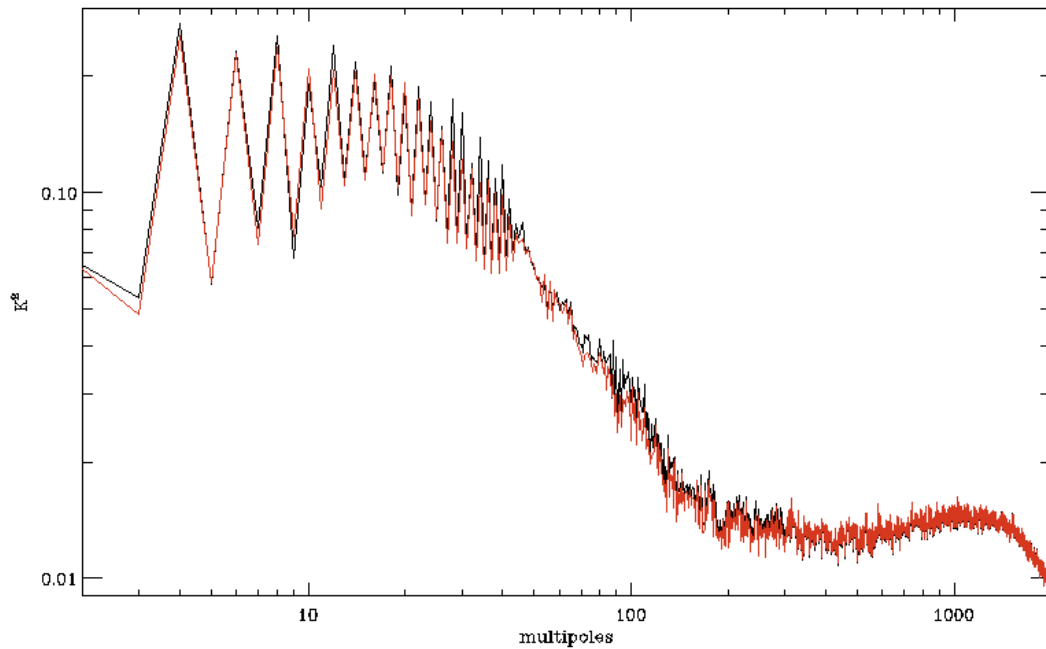

Figure 7.20: Comparison between the angular power spectrum of the original IRIS map at 25μm (black line) and the aps of the same map after the reprocessing. No Galactic cut is applied.
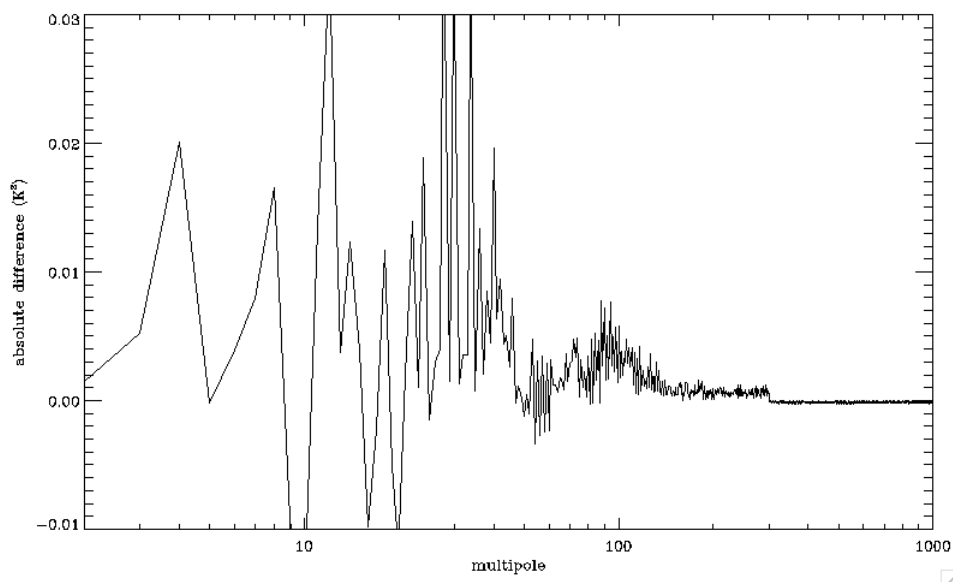

Figure 7.21: Absolute difference between the spectra showed in Fig. 7.20. Precisely the spectrum of the cleaned map is subtracted from the spectrum of the original map.

Chapter 8

Conclusions

The richness and the amount of informations that it is possible to recover through the observations of the Cosmic Microwave Background (CMB) are of tremendous impact on the modern cosmology. Through the new generation satellite missions, we are reaching great precision in determining the cosmological parameters of the standard model.

All the CMB observables are full of informations regarding different phases of the evolution of the Universe and each of them gives us information on different aspects of several primordial epochs. Even if not yet observed, the CMB spectral distortions potentially provides informations from very early to late stages of the Universe. A code, named KYPRIX, was developed in order to compute the evolution of the photon distribution function through the Kompaneets equation in cosmological context. In this thesis, the updating work done on the code, some tests and some cosmological applications are shown.

The update and the implementations on the code KYPRIX were completely performed. The details on the update are presented in Section 3.3, while the physical implementations in Section 3.4. The robustness of the code, its stability and its precision are well proved by the tests done on critical quantities, like the energy conservation test. Details on some important tests are shown in Section 3.5. The code is capable to simulate and predict spectral distortions that could be generated in the primordial Universe and/or during its late stages of evolution, like chemical potential distortions in the first case and distortions related to a reionization of the Universe in the latter case.

The results of the simulations presented in Section 3.6 clearly show that KYPRIX can predict CMB spectral distortions with an accuracy that dedicated experiments will not overtake in the next two/three decades. Further, the code can take into account different cosmological scenarios:

it is now implemented to take into account the cosmological constant contribution, more options are provided for what concerns recombination and reionization processes, allowing to get more constraining results ever updated with the precious informations that high resolution CMB observer like *Planck* can provide on these processes.

Unfortunately, foreground emissions affects the CMB signal on any observables. In order to study the cosmological signals it is necessary to subtract any unwanted emission from the observation. During this phase, it is crucial to know as better as possible the spatial and spectral characteristics of the foreground emission considered. Sensitive multifrequency observations are the fundamental brick on which one builds an accurate model for any astrophysical emission. It is hard to have a complete frequency coverage at all the desired frequencies, so it is usual to extrapolate the emission laws deduced by observations to frequencies in which there are not observations.

The Planck Sky Model (PSM) is a collection of tools able to simulate or predict several realization of the sky in the context of CMB experiments and one of its main applications consists in testing component separation technics on it. It is clear that the PSM must be continuously updated and tested. In Section 5.6 the results of some tests performed on the PSM are showed. In particular, the tests involved the last two realization of Galactic emissions of the PSM. In order to verify and validate the models, each of them was compared in temperature and polarization with the Galactic foreground templates and maps recovered from the WMAP data through a MEM component separation technic, at all the five WMAP frequencies. The most crucial channel was the low frequency one, the W band (centered at 23 GHz). From the analysis of the temperature maps of the PSM Galactic emission, it turned out that the only weakness of the new Galactic model (with respect to the previous one) lies in the emission templates in the W band. The test shows the need of some implementations of the Galactic emission, especially for what concerns compact sources on the Galactic plane. In the other channels, the new Galactic model improved the precision of predictions and simulations. For what concerns polarization, the new model presented big improvements with respect to the previous one at all the frequencies tested.

The PSM it is necessary to be a performing tool, not only because it had to simulate the sky we will see through the *Planck* satellite, but, as said, also

because many softwares are being tested on it. Indeed, about component separation technics, big leaps forward have been done and in these years more than in any other time. In this context, SMICA is one of the component separation tools that will be used to extract CMB data from the *Planck* satellite observations. In Chap. 7 a practical example of foreground subtraction process is showed. To be precise, the dataset used, the IRIS maps, was affected by residuals of a foreground, not by the foreground itself. More in details, the IRIS maps suffered from a non-optimal Zodiacal Light Emission (ZLE) subtraction and the spurious signal well visible in the 12 and 25 μm maps represents the residuals of this subtraction. In Section 7.5 the phases of the reprocess of the IRIS maps are described. These consist of two separated stages: the first one is performed through SMICA, it permits the identification of pattern and power of the ZLE residuals with great precision at all the frequencies of the mapset; the second part of the process consists in filtering delimited regions of the maps, in which the subtraction was not optimal. For this task, a Fast Fourier Transform filter was purpose-made. The results obtained are showed in the same chapter and big improvements are visible just by eye, comparing the IRIS maps with the reprocessed set.

A further deeper analysis is in progress. Through a statistical analysis of the reprocessed maps, it is possible to quantify the improvements obtained at all the angular scale and to verify that the component separation process involved only the component of interest, the Zodiacal Light Emission residuals.

The reprocessed mapset is of crucial importance in the context of the *Planck* experiment. In particular the High Frequency Instrument aboard the satellite will observe Galactic contamination at frequency near to these of the IRIS set, that in this case would be extremely useful during the modeling of the high frequency Galactic foreground.

Bibliography

[1] http://arcade.gsfc.nasa.gov/cmb_spectrum.html.

[2] http://background.uchicago.edu/~whu/araa/araa.html.

[3] http://background.uchicago.edu/~whu/physics/tour.html.

[4] http://lambda.gsfc.nasa.gov/.

[5] http://lambda.gsfc.nasa.gov/product/iras/.

[6] http://map.gsfc.nasa.gov/mission/observatory_freq.html.

[7] http://www.astro.ucla.edu/~wright/cosmo_01.htm.

[8] C. Baccigalupi et al. Power spectrum of the polarized diffuse galactic radio emission. *A.&A.*, 372:8, 2001.

[9] J. Bahcall and R. Wolf. Fine-structure transitions. *Ap. J.*, 152:701, 1968.

[10] A.J. Banday, K.M. Gorski, C.L. Bennet, G. Hinshaw, A. Kogut, and G.F. Smoot. Noncosmological signal contributions to the cobe dmr 4 year sky maps. *Ap. J. L.*, 468:85, 1996.

[11] A. Benoît et al. The cosmic microwave background anisotropy power spectrum measured by archeops. *A.&A.*, 399:L19, 2003.

[12] A. Benoît et al. First detection of polarization of the submillimetre diffuse galactic dust emission by archeops. *A.&A.*, 424:571, 2004.

[13] M. Bersanelli and N. Mandolesi. Design concept of the Planck-LFI instrument. *Ap. L. & C..37..171B*, 2000.

[14] J. Bobin, J-L. Stark, and J. Fadili. IEEE transaction on image processing. *In press*, 2007.

[15] F. Bouchet and R. Gispert. Foregrounds and cmb experiments i. semi-analytical estimates of contamination. *New Astronomy*, 4:443, 1999.

[16] W.N. Brouw and T.A.Th. Spoelstra. Linear polarization of the galactic background at frequencies between 408 and 1411 mhz. reductions. *A.&A.S.S.*, 26:129, 1976.

[17] C. Burigana, L. Danese, and G. DeZotti. Analytical description of spectral distortions of the cosmic microwave background. *A.&A.*, 303:323, 1995.

[18] C. Burigana, L. Danese, and G. De Zotti. Formation and evolution of early distortions of the microwave background spectrum - a numerical study. *A.&A.*, 246:49, 1991.

[19] C. Burigana et al. Constraints on the cosmic star formation history from the far-infrared background. *MNRAS*, 287:L17, 1997.

[20] C. Burigana et al. Beam distortion effects on anisotropy measurements of the cosmic microwave background. *A.&A.S.S.*, 130:551, 1998.

[21] C. Burigana et al. PLANCK LFI: Comparison between galaxy straylight contamination and other systematic effects. *A.&A.*, 373:345, 2001.

[22] C. Burigana, L. La Porta, P. Reich, and W. Reich. A statistical analysis of a galactic all sky survey at 1.4 ghz. *Astronomische Nachrichten*, 327:491, 2006.

[23] C. Burigana, A. De Rosa, L. Valenziano, G. Morgante, F. Villa, R. Salvaterra, P. Procopio, and N. Mandolesi. Spectral distortions of cmb. *Observation of the Universe from the Moon - LNF INFN*, 2007.

[24] C. Burigana, A. De Rosa, L. Valenziano, R. Salvaterra, P. Procopio, G. Morgante, F. Villa, and N. Mandolesi. Future experiments from the moon dedicated to the study of the cosmic microwave background. *9th ILEWG International Conference on Exploration and Utilisation of the Moon*, 2007.

[25] C. Burigana and R. Salvaterra. What can we learn on the thermal history of the universe from future cosmic microwave background spectrum measurements at long wavelengths? *MNRAS*, 342:543, 2003.

[26] C. Burigana, R. Salvaterra, and A. Zizzo. Cosmological implications of future CMB spectrum experiments. *AIP Conference Proceedings*, 703:397, 2004.

[27] C. Burigana, L. Valenziano, A. De Rosa, R. Salvaterra, P. Procopio, G. Morgante, F. Villa, and N. Mandolesi. Perspectives for future experiments and studies on cosmic background radiation from the moon. *Italian Vision for Moon Exploration Observation of the Universe from the Moon Studio Osservazione dell'Universo dalla Luna*, 2007.

[28] J-F. Cardoso et al. Component separation with flexible models. application to the separation of astrophysical emissions. *astro-ph/0803.1814*, 2008.

[29] J.S. Chang and G. Cooper. *J. Comput. Phys.*, 6, 1970.

[30] E.J. Copeland, M. Sami, and S. Tsujikawa. Dynamics of dark energy. *arxiv.org/abs/hep-th/0603057v3*, 2006.

[31] B. Crill et al. Boomerang: A balloon-borne millimeter-wave telescope and total power receiver for mapping anisotropy in the cosmic microwave background. *Ap. J.S.*, 148:527, 2003.

[32] F. Cuttaia et al. Analysis of the pseudocorrelation radiometers for the low frequency instrument onboard the planck satellite. *MSDA*, 5498:765, 2004.

[33] L. Danese and C. Burigana. Theoretical aspects of the cmb spectrum. *1994LNP...429...28D*, 1994.

[34] L. Danese and G. De Zotti. On distortions in the rayleigh-jeans region of the cosmic background radiation spectrum. *A & A*, 84:364, 1980.

[35] L. Danese and G. De Zotti. The relic radiation spectrum and the thermal history of the universe. *Rivista del nuovo Cimento*, (7):277, 1977.

[36] L. Danese and G. De Zotti. Double compton process and the spectrum of the microwave background. *A.&A.*, 107:39, 1982.

[37] P. de Bernardis et al. Detection of anisotropy in the cosmic microwave background at horizon and sub-horizon scales with the boomerang experiment. *ARXIV:astro-ph/0011468*, 2000.

[38] P. de Bernardis et al. Multiple peaks in the angular power spectrum of the cosmic microwave background: Significance and consequences for cosmology. *Ap. J.*, 564:559, 2002.

[39] G. De Zotti. The spectrum of the microwave background as a probe of the early universe. *PrPNP*, 17:117, 1986.

[40] J. Delabrouille and J.-F. Cardoso. Diffuse source separation in cmb observations. *ARXIV 2007astro.ph..2198D*, 2007.

[41] J. Delabrouille, J-F. Cardoso, and G. Patanchon. Multi-detector multi-component spectral matching and applications for cmb data analysis. *MNRAS*, 346:1089, 2003.

[42] J. Delabrouille et al. A full sky, low foreground, high resolution cmb map from wmap. *submitted to A.&A.*, arXiv:0807.0773v1 [astro-ph], 2008.

[43] C. Dickinson et al. High-sensitivity measurements of the cosmic microwave background power spectrum with the extended very small array. *MNRAS*, 353:732, 2004.

[44] B.T. Draine and A. Lazarian. Diffuse galactic emission from spinning dust grains. *Ap. J. L.*, 494:L19, 1998.

[45] A.R. Duncan. Polarimetric investigations of the galactic plane at ghz frequencies. *ADS - 1999ASPC..168...66D*, 1999.

[46] H.K. Eriksen et al. Cosmic microwave background component separation by parameter estimation. *Ap. J.*, 641:665, 2006.

[47] D.P. Finkbeiner. A full-sky Hα template for microwave foreground prediction. *Ap. J.S.S.*, 146:407, 2003.

[48] D.P. Finkbeiner, M. Davis, and D.J. Schlegel. Extrapolation of galactic dust emission at 100 microns to cosmic microwave background radiation frequencies using firas. *Ap. J.*, 524:867, 1999.

[49] D.J. Fixsen and E. Dwek. The zodiacal emission spectrum as determined by cobe and its implications. *Ap. J.*, 578:1009, 2002.

[50] D.J. Fixsen et al. Calibration of the cobe firas instrument. *Ap. J.*, 420:457, 1994.

[51] D.J. Fixsen et al. *Ap. J.*, 47:576, 1996.

[52] D.J. Fixsen et al. The cosmic microwave background spectrum from the full cobe firas data set. *Ap. J.*, 473:576, 1996.

[53] D.J. Fixsen et al. The spectrum of the extragalactic far infrared background from the cobe firas observations. *Ap. J.*, 508:123, 1998.

[54] D.J. Fixsen et al. Arcade 2 measurement of the extra-galactic sky temperature at 3-90 ghz. *arXiv0901.0555F*, 2009.

[55] D.J. Fixsen, A. Kogut, S. Levin, et al. The temperature of the cosmic microwave background at 10 ghz. *Ap. J.*, 612:86, 2004.

[56] D.J. Fixsen and J.C. Mather. The spectral results of the far-infrared absolute spectrophotometer instrument on cobe. *Ap. J.*, 581:817, 2002.

[57] J.E. Gallegos et al. Cosmosomas: a circular scanning instrument to map the sky at centimetric wavelengths. *MNRAS*, 327:1178, 2001.

[58] B. Gold et al. Five-year wilkinson microwave anisotropy probe observations: Galactic foreground emission. *eprint arXiv:0803.0715*, 2008.

[59] K.M. Gorski et al. HEALPix: A framework for high-resolution discretization and fast analysis of data distributed on the sphere. *Ap. J.*, 622:759, 2005.

[60] R.J. Gould. The cross section for double compton scattering. *Ap. J.*, 285:275, 1984.

[61] H.P. Gush, M. Halpern, and E. Wishnow. Rocket measurement of the cosmic-background-radiation mm-wave spectrum. *PRL*, 65:537, 1990.

[62] A. Guth. The inflationary universe : the quest for a new theory of cosmic origins. *Addison-Wesley*, 1998.

[63] M.M. Hedman et al. A limit on the polarized anisotropy of the cosmic microwave background at subdegree angular scales. *Ap. J.*, 548:L111, 2001.

[64] S.R. Hildebrandt et al. Cosmosomas: a circular scanning instrument to map the sky at centimetric wavelengths. *arXiv:0706.1873v1*, 2007.

[65] G. Hinshaw et al. Five-year wilkinson microwave anisotropy probe (wmap) observations: Data processing, sky maps, and basic result. *Ap. J.S.*, Feb-2009 (accepted).

[66] M.P. Hobson, A. Jones, A. Lasenby, and F. Bouchet. Foreground separation methods for satellite observations of the cosmic microwave background. *MNRAS*, 300:1, 1998.

[67] A. Hyvarinen. *IEEE Signal Processing Letters*, 6:145, 1999.

[68] The infrared and submillimetre sky after COBE; Proceedings of the NATO Advanced Study Institute. *Preliminary results from the FIRAS and DIRBE experiments on COBE*, 1992.

[69] Ipac. *IRAS Sky Survey Atlas (ISSA)*. Jet Propulsion Laboratory (IPAC), 1994.

[70] N. Kaiser and J. Silk. Cosmic microwave background anisotropy. *Nature*, 324:529, 1986.

[71] W.J. Karzas and R. Latter. Electron radiative transitions in a coulomb field. *Ap. J.S.*, 6:167, 1961.

[72] B.G. Keating et al. A limit on the large angular scale polarization of the cosmic microwave background. *Ap. J. L.*, 560:L1, 2001.

[73] Thomas J. Kelsall et al. Investigation of the zodiacal light from 1 to 240 um using cobe dirbe data. *Proc. SPIE*, 2019:190, 1993.

[74] A. Kogut. Diffuse microwave emission survey. *astro-ph/9607100*, 1996.

[75] A. Kogut. Spatial correlation between hα emission and infrared cirrus. *Astron. J.*, 114:1127, 1997.

[76] A. Kogut. Wmap polarization results. *New Astronomy Review*, 47:977, 2003.

[77] A. Kogut et al. Wmap first year observations: Te polarization. *Ap. J.S.*, 148:161, 2003.

[78] E. Kolb and M. Turner. The early universe. *Addison-Wesley*, 1990.

[79] E. Komatsu et al. Five-Year Wilkinson Microwave Anisotropy Probe (WMAP) Observations: Cosmological Interpretations. *arXiv:0803.0547v2 [astro-ph]*, 2008.

[80] A.S. Kompaneets. *Zh.E.T.F.*, 31:816, 1956.

[81] J.M. Kovac et al. Detection of polarization in the cosmic microwave background using DASI. *Nature*, 420:772, 2002.

[82] L. La Porta and C. Burigana. A multifrequency angular power spectrum analysis of the leiden polarization surveys. *A.&A.*, 457:1, 2006.

[83] S.M. Leach et al. Component separation methods for the planck mission. *A.&A.*, 2008.

[84] E.M. Leitch et al. DASI Three-Year Cosmic Microwave Background Polarization Results. *Ap. J.*, 624:10, 2005.

[85] A.P. Lightman. Double compton emission in radiation dominated thermal plasmas. *Ap. J.*, 244:392, 1981.

[86] A. Linde. Inflation and quantum cosmology. *Academic Press, Boston*, 1990.

[87] M. Longair. On the interpretation of radio source counts. *MNRAS*, 133:421, 1966.

[88] F.J. Low. Infrared cirrus and zodiacal dust bands. *Bulletin of the American Astronomical Society*, 16:511, 1984.

[89] F. Lucchin. Introduzione alla cosmologia. *Zanichelli*, 1998.

[90] D. Maino et al. All-sky astrophysical component separation with fast independent component analysis (FASTICA). *MNRAS*, 334:53, 2002.

[91] M. Maris, C. Burigana, and S. Fogliani. Zodiacal light emission in the planck mission. *A.&A.*, 452:685, 2006.

[92] J.C. Mather et al. Spectra and sky maps from the cobe far infrared spectraphotometer (firas). *Bulletin of the A.A.S.*, 22:1216, 1990.

[93] J.C. Mather et al. Measurement of the cosmic microwave background spectrum by the cobe firas instrument. *Ap. J.*, 420:439, 1994.

[94] J.C. Mather, D.J. Fixsen, et al. Calibrator Design for the COBE Far-Infrared Absolute Spectrophotometer (FIRAS). *Ap. J.*, 512:511, 1999.

[95] A. Mennella et al. Analysis of thermally-induced effects in planck low frequency instrument. *AIP Conference Proceedings*, 616:229, 2002.

[96] A.R. Mitchell and D.F. Griffiths. *The finite difference method in partial differential equations*. Wiley, Chichester, 1980.

[97] M.-A. Miville-Deschênes, J. Delabrouille, P. Procopio, et al. *in preparation*, 2009.

[98] M.-A. Miville-Deschênes and G. Lagache. IRIS: a new generation of IRAS maps. *Ap. J.S.S.*, 157:302, 2005.

[99] T.E. Montroy et al. A Measurement of the CMB ¡EE¿ Spectrum from the 2003 Flight of BOOMERANG. *Ap. J.*, 647:813, 2006.

[100] G. Morgante et al. Two hydrogen sorption cryocoolers for the planck mission. *AIP Conference Proceedings*, 616:298, 2002.

[101] P. Naselsky and L.-Y. Chiang. Late reionizations of the universe and their manifestation in the wmap and future planck data. *MNRAS*, 347:795, 2004.

[102] M.R. Nolta et al. Five-year wilkinson microwave anisotropy probe (wmap) observations: Angular power spectra. *arXiv:0803.0593v2 [astro-ph]*, 2008.

[103] L. Page. The map satellite mission to map the cmb anisotropy. *Proc. of IAU General Assembly XXIV, Manchester*, 2000.

[104] L. Page et al. Three-year wilkinson microwave anisotropy probe (wmap) observations: Polarization analysis. *Ap. J.S.*, 170:288, 2007.

[105] B. Partridge. 3k: The cosmic microwave background radiation. *Cambridge Astrophysics*, 1995.

[106] J. Peebles. Principles of physical cosmology. *Princeton University Press*, 1993.

[107] S. Perlmutter et al. *Ap. J.*, 517:565, 1999.

[108] N. Peyraud and J. Peyraud. Quasi-statistical theory of a partially ionized plasma with partial radiation losses. *J. Physique*, 30:773, 1969.

[109] N. Ponthieu, J. F. Macías-Pérez, M. Tristram, et al. Temperature and polarization angular power spectra of galactic dust radiation at 353 ghz as measured by archeops. *A.&A.*, 444:327, 2005.

[110] L. Popa, C. Burigana, and N. Mandolesi. Radiative effects by high-z uv radiation background: Implications for the future cmb polarization measurements. *New Astronomy*, 11:173, 2005.

[111] L. Popa, C. Burigana, N. Mandolesi, R.C. Butler, F. Cuttaia, F. Finelli, E. Franceschi, M. Galaverni, A. Gruppuso, M. Malaspina, G. Morgante, F. Paci, P. Procopio, M. Sandri, L. Stringhetti, L. Terenzi, L. Valenziano, F. Villa, and J. Zuccarelli. Planck-lfi scientific goals: Implications for the reionization history. *New Astronomy Review*, 51:298, 2007.

[112] W.H. Press, B.P. Flannery, S.A. Teukolsky, and W.T. Vetterling. *Numerical Recipes*. Cambridge Univ. Press, 1982.

[113] P. Procopio and C. Burigana. Accuracy and performance of a numerical code for the solution of hte kompaneets equation in cosmological context. *Internal Report IASF-BO/420/2005*.

[114] P. Procopio and C. Burigana. Cosmological applications of a numerical code for the solution of the kompaneets equation. *In preparation*.

[115] P. Procopio and C. Burigana. Cosmological applications of a numerical code for the solution of the kompaneets equation. *Internal Report IASF-BO/421/2005*.

[116] P. Procopio and C. Burigana. Updating a numerical code for the solution of the kompaneets equation in cosmological context. *Internal Report IASF-BO/419/2005*.

[117] P. Procopio and C. Burigana. A numerical code for the solution of hte kompaneets equation in cosmological context. *A & A (to be submitted)*, 2009.

[118] M. Ram and P.Y. Wang. Calculation of the total cross section for double compton scattering. *P.R.L.*, 26:1210, 1971.

[119] C.L. Reichardt et al. High resolution cmb power spectrum from the complete acbar data set. *Ap. J.*, 2008 (submitted).

[120] A.G. Riess et al. *Astron. J.*, 116:1009, 1998.

[121] A.G. Riess and others [SST collaborators]. *Ap. J.*, 607:665, 2004.

[122] G.B. Rybicki and A.P. Lightman. *Radiative processes in astrophysics*. ed. John Wiley & sons, Inc., 1979.

[123] R.K. Sachs and A.M. Wolfe. Perturbations of a cosmological model and angular variations of the microwave background. *Ap. J.*, 147:73, 1967.

[124] R. Salvaterra and C. Burigana. Construction of a Database of CMB Spectrum Observations. *arXiv:astro-ph/0206350*, 2002.

[125] M. Sandri et al. Planck low frequency instrument: Beam patterns. *AIP Conference Proceedings*, 616:242, 2002.

[126] M. Sandri et al. Straylight analysis and minimization strategy in planck low frequency instrument. *SPIE Proc.*, 5962:575, 2005.

[127] M. Seiffert et al. 1/f noise and other systematic effects in the planck-lfi radiometers. *A.&A.*, 391:1185, 2002.

[128] U. Seljak and M. Zaldarriaga. Polarization of microwave background: Statistical and physical properties. *eprint arXiv:astro-ph/9805010*, 1998.

[129] J. Silk and A. Stebbins. *Ap. J.*, 269:1, 1983.

[130] J. Singal et al. The ARCADE 2 Instrument. *arXiv0901.0546S*, 2009.

[131] G. Sironi et al. The absolute temperature of the sky and the temperature of the cosmic background radiation at 600 mhz. *Ap. J.*, 357:301, 1990.

[132] G.F. Smoot. Galactic free-free and h-alpha emission. *arXiv:astro-ph/9801121v2*, 1998.

[133] G.F. Smoot et al. Structure in the cobe differential microwave radiometer first-year maps. *Ap. J. L.*, 396:L1–L5, 1992.

[134] D.N. Spergel et al. First-Year Wilkinson Microwave Anisotropy Probe (WMAP) Observations: Determination of Cosmological Parameters. *ApJ Suppl. Series*, 148:175, 2003.

[135] C. Stanghellini, C.P. O'Dea, S.A. Baum, D. Dallacasa R. Fanti, and C. Fanti. A vlbi study of ghz-peaked-spectrun radio sources. *Kluwer Academic Publishers*, 1996.

[136] R. Stompor et al. Cosmological implications of the maxima-1 high resolution cosmic microwave background anisotropy measurement. *Ap. J. L.*, 561:L7, 2001.

[137] R.A. Sunyaev and J. Chluba. The richness and beauty of the physics of cosmological recombination. *2008ASPC..395...35S*, 2008.

[138] R.A. Sunyaev and Y.B. Zel'dovich. Distortions of the background radiation spectrum. *Nature*, 223:721, 1969.

[139] M. Tegmark. Doppler picks and all that: Cmb anisotropy and what they can tell us. 1996.

[140] M. Tegmark and G. Efstathiou. A method for subtracting foregrounds from multifrequency cmb sky maps. *MNRAS*, 281:1297, 1996.

[141] M. Tegmark, D.J. Eisenstein, W. Hu, and A. de Oliveira-Costa. Foregrounds and forecasts for the cosmic microwave background. *Ap. J.*, 530:133, 2000.

[142] L. Terenzi, F. Villa, A. Mennella, M. Bersanelli, R.C. Butler, F. Cuttaia, O. D'Arcangelo, E. Franceschi, S. Galeotta, D. Maino, M. Malaspina, N. Mandolesi, G. Morgante, M. Sandri, L. Stringhetti, M. Tomasi, L. Valenziano, C. Burigana, F. Finelli, M. Galaverni, A. Gruppuso, F. Paci, L. Popa, P. Procopio, and J. Zuccarelli. The planck lfi rca flight model test campaign. *New Astronomy Review*, 51:3005, 2007.

[143] J.C. Testori, W. Reich, and P. Reich. A large-scale radio polarization survey of the southern sky at 21cm. *2004mim..proc...57T*, 2004.

[144] F. Tricomi. *Equazioni a derivate parziali*. ed. Cremonese, 1957.

[145] M. Tucci, E. Carretti, S. Cecchini, R. Fabbri, M. Orsini, and E. Pierpaoli. The angular power spectra of polarized galactic synchrotron. *New Astronomy*, 5:181, 2000.

[146] L. Valenziano et al. The 4k reference load for the planck low frequency instrument. *AIP Conference Proceedings*, 616:291, 2002.

[147] L. Valenziano, M. Sandri, G. Morgante, C. Burigana, M. Bersanelli, R.C. Butler, F. Cuttaia, F. Finelli, E. Franceschi, M. Galaverni, A. Gruppuso, M. Malaspina, N. Mandolesi, A. Mennella, F. Paci, L. Popa, P. Procopio, L. Stringhetti, L. Terenzi, M. Tomasi, F. Villa, and J. Zuccarelli. The low frequency instrument on-board the planck satellite: Characteristics and performance. *New Astronomy Review*, 51:287, 2007.

[148] F. Villa et al. High performance corrugated feed horns for space applications at millimetre wavelengths. *Experimental Astronomy*, 14:1, 2002.

[149] M. Wolleben et al. The drao 26-m large scale polarization survey. *arXiv:astro-ph/0402365v1*, 2004.

[150] M. Zaldarriaga. An introduction to cmb anisotropies.

[151] Y.B. Zel'dovich, A.F. Illarionov, and R.A. Sunyaev. Influence of energy release on the radiation spectrum in the hot model of the universe. *Soviet Phtsics*, 35:643, 1972.

[152] Y.B. Zel'dovich and E.V. Levich. Stationary state of electrons in a non-equilibrium radiation field. *JETP Lett*, 11:35, 1970.